DEVELOPMENT OF AN IMAGING SYSTEM FOR NEUTRON REMOTE SENSING

Thesis submitted for the degree of
Doctor of Philosophy
at the University of Leicester

by

Massimiliano Canali

Department of Physics and Astronomy
University of Leicester
May 2019

University of Leicester

DEVELOPMENT OF AN IMAGING SYSTEM FOR NEUTRON REMOTE SENSING

Massimiliano Canali

Abstract

This thesis is concerned with the design, modelling and characterisation of a Charge-Coupled Device (CCD) camera imaging system and the prediction of the camera's performance in applications with Micro-Channel Plate (MCP) optics.

The development and optimisation of analogue CCD readout electronics are described and its extension to a fully digital CCD readout method with its dedicated analogue front-end processing stage is presented. The mechanical and the optical design of the camera are presented and a performance model of the camera system from scintillator to detector is expressed by means of a system gain model.

A noise mathematical model of the analogue chain of the CCD readout electronics is developed and compared to Spice simulations. A shaping filter method is proposed and implemented to generate noise time series from a given noise power spectral density. The method is adopted to build a time domain simulation model of the CCD camera system. The model allows investigation of the impact that different noise sources have on the performance of CCD readout methods and to drive the design criteria of the system.

Characterisation of the CCD camera system by means of photon transfer curve theory is presented. Calibration of the system for X-ray detection, followed by the derivation of a quantitative model and relative comparison with real measurements in terms of scintillator light yields are presented. The resolution of the system is quantified by means of Modulation Transfer Function (MTF).

A model of the performance of MCP optics is discussed and specific performance parameters such as gain and surface brightness are presented. An extension of their use for focusing neutrons is considered and the development of a neutron telescope concept using MCP optics for investigation of hydrogen distribution on a planetary surface at higher resolution that can be achieved with current instruments is presented.

Declaration

I hereby declare that that no part of this thesis has been previously submitted to this or any other university as part of the requirement for a higher degree. The work described herein was conducted solely by the undersigned except for those colleagues and other workers acknowledged in the text.

Massimiliano Canali

May 2019

Acknowledgements

There are many people I would like to acknowledge for their help and encouragement over the duration of my thesis work without whom this thesis would have been impossible.

Thanks to all the staff of the Space Research Centre for their technical assistance in and out of the lab and for their general chat and friendship. Thanks in no particular order to Tony Crawford, Dave Vernon, John Holt, Duncan Ross and Chris Bicknell for their assistance to setup the laboratory and quickly fix faults at the most odd times of the day. Also thanks to Piyal Samara, John Sykes and Paul Houghton for their help with the mechanical design.

My gratitude goes to Jim Pearson, Adrian Martindale, Charly Feldman, Pippa Molyneux and Dick Willingale to provide the best education in Monte Carlo simulation and ray tracing software I could have hoped for. I am grateful to Ian Hutchinson who provided me with a replacement sensor when every hope was lost and to Graeme Hansford for his help with the sensor calibration.

Also thanks to Mark Sims and my external examiner David Smith for their insightful and helpful comments and suggested revisions to the thesis which have greatly improved it.

Special thanks to my supervisor Richard Ambrosi for his guidance, advice and gentle pushing in the right direction. For his help and support I will always be grateful.

Thanks to Manolis Georgoulis, Aldo Rona and Alessandro Battaglia for their friendship, methodological advices and continuous support.

Finally, my endless gratefulness and love to my family for believing me, to my wife and baby for their patience to bear the burden of my frequent absences from home.

Table of Contents

List of Tables

List of Figures

List of Acronyms

ADC	Analogue to Digital Converter
ADU	Analogue to Digital Unit
APS	Active Pixel Sensor
ASIC	Application Specific Integrated Circuit
AST	Applied Scintillation Technologies
CDS	Correlated Double Sampling
CCD	Charge-Coupled Device
CIC	Clock Induced Charge
CID	Charge Injection Devices
CMOS	Complementary Metal Oxide Semiconductor
DCDS	Digital Correlated Double Sampling
DQE	Detection Quantum Efficiency
EMCCD	Electron Multiplying Charge Coupled Device
FIR	Finite Impulse Response
FOV	Field Of View
GCR	Galactic Cosmic Rays
IDMA	Internal Direct Memory Access
MCP	Micro-Channel Plate
MTF	Modulation Transfer Function
OTF	Optical Transfer Function
PLL	Phase Locked Loops
PPS	Poly Phenylene Sulphide
PTC	Photon transfer Curve
QE	Quantum Efficiency
ROI	Region Of Interest
SEM	Scanning Electron Microscope
SNR	Signal to noise Ratio
TEC	Thermoelectric Cooler

1. Introduction

The work presented in this thesis concerns the design, modelling and characterisation of a Charge-Coupled Device (CCD) camera imaging system and the prediction of the camera's performance in applications with Micro-Channel Plate (MCP) optics.

1.1 Image Sensors

Photographic silver halide film was the main competitor to the electronic sensor as an imaging detector, being sensitive to a broad range of wavelengths and a low cost technology had widespread use in science, medical and space applications. Electronic sensors had to compete also with image tube type of detector but especially for the dimension, degradation in time and readout method the electronic imaging sensors became the dominant technology (Janesick, 2001).

Resolution, charge transfer inefficiency and quantum efficiency where the main issues for the first CCD sensors, but under the needs of NASA for space mission detectors the collaboration between Texas Instruments and Jet Propulsion Laboratory paved the way to the scientific CCD we know today. CCD sensors in the latest years are facing competition by Complementary Metal Oxide Semiconductor (CMOS) imagers (Yadid et al., 2004), a technology that is assuming major importance in the science and space sector and that has already conquered the commercial market.

At their first experimentation CMOS imagers adopted one amplifier per column or per row with Signal to Noise Ratio (SNR) of discrete entity, the second generation implemented a source follower per pixel commonly known as Active Pixel Sensor (APS).

Positive characteristics of CMOS imagers are (Bigas et al., 2006):

- CMOS imagers have a smaller pixel size with positive effect on the resolution
- They need one supply voltage, instead of CCDs needing different bias and clock voltages
- Integration of functionalities in the same silicon integrated chip, as for instance ADCs and data compression units
- Random access and high-speed imaging

- Blooming and smearing effects do not affect CMOS sensors

Disadvantages of CMOS sensors over CCDs:

- Sensitivity: because of a limited fill factor CMOS pixels have lower sensitivity to incident light and consequently lower quantum efficiency (QE)
- Dynamic range has a lower value than in CCDs
- Image quality is lower than CCD, e.g. uniformity of response between pixels

In space missions CMOS sensors found application in, up to now, robotic and navigation cameras, imagers for Earth observation, lander and rover imagers often as a low cost replacement to CCDs for instance as in CubeSat programs for Sun sensing and horizon detection (CubeSense, 2016).
For X-ray mission a detector should achieve high QE and good energy resolution (Yibin Bai et al., 2008).
The readout noise of monolithic CMOS imagers is relatively higher than CCDs, related to the capacitance of the sense node CMOS pixel and lower conversion gain. Researchers (Takayanagi et al., 2008) have developed the four transistor (4T) pixel with on chip CDS processing reaching a noise level lower than 2 electrons r.m.s..
Another important limiting factor for CMOS imagers is the QE. Back illuminated CMOS imagers are a viable solution to improve QE. One of the latest experimentations in the EUV/soft X-ray range (Stern et al., 2011) gave encouraging results with QE values comparable to measurements of CCDs and are quite practical for use in future space-borne solar physics or astrophysics missions. CMOS imagers have also been proposed as near UV imagers coupled with an MCP image intensifier (Ambily et al., 2016).
It could be possible to introduce other imaging devices such as flat panel detectors, photodiode imaging arrays, charge injection devices (CID) (Miller et al., 2004) with their high radiation tolerance and intensified MCP for high speed photon counting, without considering direct detection detectors of energy particles, but CCDs still play a major role in high quality and low sensitivity applications.

The possibility to implement avalanche multiplication in the CCD output channel merits particular interest. It was developed by Texas Instruments (Hynecek, 2001) and e2v (Jerram et al., 2001) which allows detection of low level signal with improved signal to noise under determinate conditions.
The impact of avalanche multiplication on the image quality for radiography applications has been assessed for instance in Kuhls-Gilcrist et al. (2008) with a resolution at 10% contrast of 4 cycles per mm, whose meaning will be explained in Chapter 5 a lower value than the one achievable at good signal intensities and with no avalanche multiplication.

Just to name a few space missions where CCDs plays a fundamental role: Hubble Space Telescope Wide Field/Planetary I (Trauger, 1989), and more recently Euclid (Szafraniec et al., 2014) and Plato (Endicott et al., 2012).
The CCD readout method adopted determines the level of noise introduced in the image and will be introduced in the following paragraph.

1.2 CCD Readout Methods

The ultimate level of sensitivity achievable by the CCD sensor depends on the noise level introduced by the readout method.
The CCD itself introduces noise amplified by the following stage to be finally processed by the correlated double sampling (CDS) and then converted to a digital value by the ADC converter. Traditionally two methods are implemented: the sample and hold and the dual slope integration method (Janesick, 2001). The methods have had well established theoretical treatments since 1980s (Hopkinson et al., 1982).
Recently, with the advent of higher quality and low noise analogue to digital converters, several research groups (Gach et al., 2003), (Smith et al., 2013), (Stefanov et al., 2014), (Clapp, 2012) and the group of Cancelo et al. (2012) have developed digital readout methods, characterising the system and specifying the limits.
Analogously, in the present work, after the characterisation of the dual slope analogue readout method, a digital electronic readout method has been designed and implemented.

Relying on a static model of an imaging sensor, CCD or CMOS, introduced in Konnik et al. (2014), it was thought to extend it to include a time domain representation of the CCD signal waveform. A CCD time domain noise simulation model was implemented by proper generation of noise time series from given noise power spectrum.

The static model allows introduction of most of the noise sources that a CCD can be affected by, e.g. signal shot noise, dark signal shot noise, fixed pattern noise and so on

The simulation model shares a common part with the static model and its philosophy can be introduced by explaining the scheme reported in Figure 1 adapted from Konnik et al. (2014).

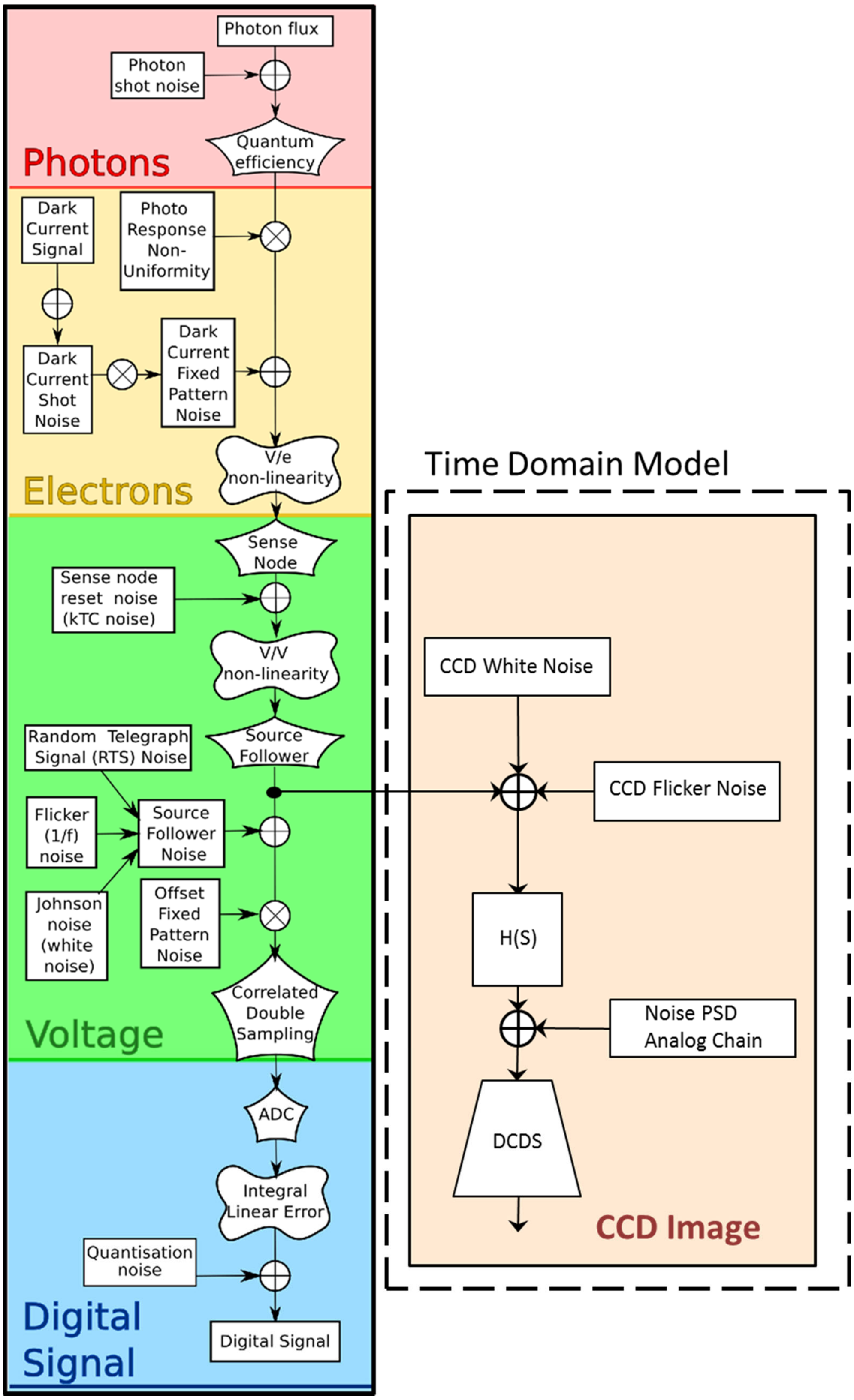

Figure 1 CCD Time Domain Simulation Scheme

Starting from a static matrix representation of the irradiance levels on the pixels representing the scene photon flux, a voltage matrix is obtained by the electron to voltage conversion in the sense node. The output from the source follower is processed by the time domain engine which transforms each static pixel voltage level in a time domain representation both for the pedestal value and the signal charge level.
The discrete time samples are processed at each time step by the transfer function $H(s)$ of the front-end analogue processing chain. The samples at the output are processed by the digital correlated double sampling (DCDS) scheme to complete the readout process and assess the noise performance. In the time domain simulation the different noise sources can be selected independently and their effect can be detected directly on the time representation of the CCD signal waveform. Parameters such as the size of the image, the pixel frequency rate, the number of signal samples per pixel period can be configured as well.
The advantage of this simulation model stands in the possibility of simulating at the same time the behaviour of the analogue electronic chain together with the CCD characteristics and of driving the design phase to optimise the circuit parameters, such as analogue bandwidth, gain and op-amp characteristics, for different readout conditions, such as temperature, pixel frequency and photon flux.
Such an approach allows investigation of the impact that different noise sources have on the performance of the CCD readout method, such as the noise introduced by the analogue chain or the effect of low frequency noise components at longer pixel time periods.
Furthermore, the performance of a specific readout processing method can be assessed before adopting them in the real circuit. The behaviour for different design choices and filtering algorithms can be verified with important hints about its capability to improve the noise performance addressing specific noise components. In the case of this thesis the simulation has included a differential averager or DCDS which can be considered as the analogue of the dual slope integration method (Janesick, 2001), the same identical method used for the camera characterisation in the laboratory.
The results from the simulations were also compared with the findings from the above mentioned research groups. Particularly, Gach et al. (2003) evaluated the distribution weight at samples during the pixel period time concluding that for long pixel periods it is

convenient to weight more the samples near the serial transfer charge time. The algorithm adopted in this thesis weights the samples equally as the weighting approach proposed by Gach et al. was not consistently proven by other groups. Clapp (2012) developed an analytical model for noise calculation of the electronic processing circuit and of the DCDS transfer function. In this work a similar circuit noise calculation was followed but the two mentioned works reached different conclusions regarding the contribution of the low frequency noise.

Stefanov et al. (2014) gave an analytical model for the DCDS transfer function putting in relation the analogue parameters of the processing electronics and gave terms of comparison with the analogue dual slope integration method. The present work compared their findings and reached similar conclusions.

Smith et al. (2013) decomposed the spectral frequency contribution of the DCDS algorithm as a function of the number of samples. In the scope of this thesis the same findings were shown by a different method.

Finally, a shaping filter is proposed to model noise time series from noise power density which can be exploited to implement a Kalman filtering algorithm to estimate and reduce the low noise frequency components with the same aim as demonstrated in Cancelo et al. (2012).

1.3 Micro-Channel Plates and Focusing Systems

Micro-Channel Plates (MCP) initially were conceived as image detectors and intensifiers (Wiza, 1979).

Subsequently they were proposed as X-ray grazing incidence telescopes exploiting the reflectivity property of X-rays at the walls of the plates (Angel, 1979).

In the scope of this thesis MCPs will be treated at first as focusing devices to increase the photon flux in a small area, estimating by means of a mathematical model and simulation their performance with X-rays and then for neutrons.

A similar experiment has already been carried out by a number of research groups (Peele et al., 1996) for X-rays and using analogous device by Allman et al. (1999) for neutrons.

Following the exhaustive theoretical treatment given in Chapman et al. (1991), an analytical evaluation model was implemented and supported by Monte Carlo simulations.
The considered MCP optic has already been characterised in the laboratory at University of Leicester by Price et al. (2002) for different X-ray energies. The results from this simulation have been weighted with Price's experimental findings to forecast the gain value at 17.5 keV and for thermal neutron focusing, comparing the results with Allman et al. (1999).
Neutron scattering spectrometers, small angle neutron scattering and time-of-flight spectroscopy experiments require a high intensity gain. Use of an MCP is one of the approaches that could be followed to reach higher intensity gains. Usually toroidal mirrors are used to focus neutrons (Alefeld et al., 1989).
Other solutions can be proposed such as elliptical neutron optics based on super-mirror technology, refractive and magnetic lenses (Desert, 2013).
For instance gain values achieved adopting different methods such as capillary optics or aspherical super-mirrors with layers of NiC/Ti reached a gain of 52 (Nagano et al., 2012) or adopting Kirkpatrick–Baez micro-focusing optics (Ice, 2005) achieved a gain of 27.
Another interesting method of focusing neutrons relies on (Khaykovich et al., 2011) axisymmetric mirror systems configured in a Wolter mirror configuration nesting nickel mirror pairs.
This method achieved an experimental gain of 3 ± 0.5, whereas the corresponding ray-tracing simulations predicted a gain of 8 ± 1.
Their approach to adopt Wolter mirror configuration for neutron focusing has similarities with the proposed method in this thesis for high resolution neutron remote sensing.

1.4 Neutron Remote Sensing

Planetary neutron spectroscopy has gained importance among the available methods for remote geochemical analysis. Orbital neutron spectroscopy from orbital distances of 30–500 km relies upon the interaction of galactic cosmic rays (GCR) hitting the surfaces of airless or nearly airless planetary bodies initiating nuclear spallation reactions that liberate high-energy neutrons. Elastic and inelastic collisions with planetary nuclei create an equilibrium energy flux spectrum in energy ranges of fast, epithermal, and thermal neutrons (Lawrence et al., 2010).

Measurement of the composition of the neutron flux between thermal, epithermal, and fast neutrons allows information indicative of the underlying near-surface chemical composition to be observed. For example, a strong measurement of hydrogen at a planetary surface can be correlated to a decrease in the flux of epithermal neutrons, as for instance at the lunar poles as measured by the Lunar Prospector spacecraft and at Mars from the Mars Odyssey spacecraft. Thermal neutrons have been used to measure the abundance of the rare earth elements at the Moon (Elphic et al., 2000) and also CO_2 concentration at Mars (Prettyman et al., 2004).

Spatial resolution obtained for the measurement of the neutron flux up to now has not reached a resolution greater than 10 km. The reason for this stands in the adoption of nearly omni-directional neutron sensors, e.g. in Messenger the effective field of view (FOV) has hemispherical response (Goldsten, 2007) or for instance in the neutron detectors on-board Lunar Prospector and Mars Odyssey, the optimum spatial resolutions were 54 and 600 km respectively (Maurice et al., 2004) (Prettyman et al., 2004).

Spatial resolution is the key to resolving the origin of the signal that is observed. In response to this need to obtain better spatial resolution, the LEND instrument on-board Lunar Reconnaissance Orbiter (LRO) is a collimated neutron detector system with a 10 km diameter (FWHM) footprint at the nominal 50 km orbital altitude (Mitrofanov, 2010).

In order to improve the detection and sensitivity limits of spatially resolved neutron measurements, a neutron imaging telescope is proposed relying on the geometry of MCP structures as a conical approximation to the Wolter type I geometry (Willingale et al., 1998).

1.5 Overview of the Thesis

Chapter 2 describes the development and optimisation of the analogue CCD readout electronics developed at the Space Research Centre (SRC) University of Leicester, the optimisation and digital design of the FPGA coming under the scope of this thesis.

Furthermore, the design of a fully digital CCD readout method with its analogue front-end processing stage is described.

Chapter 3 describes the mechanical as well the optical design of the camera. A performance model for the overall chain from scintillator to detector and electronics will be presented as an analytical verification for the results presented in chapter 5.

Chapter 4 describes firstly a noise mathematical model of the amplifiers and filters of the analogue chain of the digital readout electronics, and is compared to Spice simulation results. Secondly, a time domain noise method will be proposed which will be adopted to build a time domain model of the CCD camera system. Comparisons of the readout performance with the corresponding analogue domain processing methods are shown.
Finally, the characterisation of the CCD camera system based on the e2v CCD 97 by means of photon transfer curve theory is presented.

Chapter 5 describes the calibration of the system for X-ray detection, followed by the derivation of a quantitative model and relative comparison with real measurements in terms of light yields. The resolution of the system is quantified by means of Modulation Transfer Function (MTF).
Secondly, a model of the performance of the MCP is discussed and specific performance parameters are introduced. An analytic derivation and simulation is considered.
Finally, a simulation model of the focusing optics for neutrons is presented and its possible applications in space science discussed.

2. Electronic System Engineering Design

2.1 Introduction

The electronic engineering design plays a crucial role in the development of modern detection systems both in terms of performances, reliability and power consumption.
The advent of CCDs, developed by W. S. Boyle and G. E. Smith in 1969 at Bell Laboratories (Boyle et al., 1970) as a solid state memory device and then as an imaging device, paved the way to a consistent proliferation, both commercially and scientifically, to a variety of applications of CCD based detection systems in different fields such as space exploration, medical imaging, video applications and diagnostic industry analysis.
The development of different techniques for the readout of imaging devices has had a big acceleration in the last twenty years of the twentieth century especially in terms of integration with efforts towards Application Specific Integrated Circuit (ASIC) design aiming to low noise and power consumption especially in the case of space applications. Most of the electronic designs have usually relied on analogue processing schemes to recover the pixel charge value basically on a sample and hold scheme or a dual slope integration of the pixel reference value and the charge pixel value realised by CDS (Hopkinson et al., 1982). Despite the technological advances in analogue to digital conversion methods, recent designs for highly demanding applications, e.g. the forthcoming Euclid (Szafraniec et al, 2014) space mission for dark matter and energy investigation and the PLATO mission (Endicott et al., 2012), still rely on analogue schemes precluding the possibility of adopting advanced digital signal processing algorithms.
In the present chapter the development and optimisation of the analogue CCD readout electronic developed at the Space Research Centre University of Leicester will be shown. The optimisation and the digital design of the FPGA are presented in this thesis. Furthermore, the design of a fully digital CCD readout method with its analogue front-end stage is described.

2.2 CCD Analogue Readout Electronics

The CCD replacement electronics project was conceived to produce a modern version of the existing laboratory electronics. The design fulfilled the requirements of at least four SRC projects and becomes the laboratory research 'workhorse' replacing Acorn driven STE bus and XMM flight electronics boxes, and Xcam and Osprey PC based systems. These units had replaced previous CAMAC modular rack systems controlled by PCs or Acorn machines. The aim was to demonstrate low noise CCD readout in photon-counting mode at a speed of at least 1 MHz, through two nodes, using a range of CCDs. High voltage clocks to support the new design of e2v CCD97 are also provided. In addition, the design can demonstrate embedded processing of CCD X-ray events via ADSP and FPGA designs and demonstrates the use of FPGA based clock sequence generation, which is a preferred method for space use because of flexibility, rad-hardness and power consumption. Additional requirements were that the design could be maintained in-house and use standard PC interfaces and good availability of platform independent support software

The projects that required the design were:

1. ExoMars Lander XRD/Crest – low power readout, medium speed, demonstrator of embedded CCD processing
2. Gamma Camera – high throughput, avalanche multiplication CCD, embedded processing
3. 'Standard CCD camera' for X-ray interferometer project – use for optical and X-ray imaging
4. Replacement for obsolete laboratory equipment.
5. CityScan for high throughput optical spectrometer

The camera system is controlled by a USB interface to a Windows XP® PC running a proprietary GUI that allows easy fine tuning of the operating parameters. Camera system parameters are: vertical and horizontal clock sequencing times and delays, clock and bias voltages, image dimensions, pixel binning and system gain.

2.3 External Interfaces

The electronics is designed to be run off a single 12 V power supply, and have a single interface to a PC. The PC runs the IDL programming language and controls the electronics through a USB2 interface. A single 40-way edge connector carries CCD clock and bias signals. A range of plug-in cards was manufactured to conform to the various laboratory configurations. Mechanically the plug-in adaptor has a front panel on which the CCD connector is mounted. This card can provide optional rise-time control resistors that allow to shape the clock waveforms for better noise performance. The signal connections are made with two SMA connectors with a linkable option to collect the signals from the CCD connector (four in the case of double stacked data acquisition). An auxiliary front panel interface provides CCD temperature measurement with 100 Ω and 1000 Ω PRTs, plus two spare 0 - 2.048 V monitoring ADC inputs.

2.3.1 Internal Interfaces

The Cypress USB2 peripheral controller device is on a sub-board plugging into the main electronics motherboard board and has a ROM containing the QuickUSB functions, which makes the IDL to CCD electronics interface reasonably transparent. An alternative method of communication would have been to use the native Cypress libraries, but this was thought to be too difficult at the onset of the project. If it is found that the QuickUSB structures interfere with future applications, the system can be disabled with a couple of U-links and custom drivers programmed into the CCD electronics. Further flexibility at the computer interface is provided by the ability to swap the USB interface for a different one such as Ethernet.

The various devices on the motherboard are controlled from an I2C interface from the USB controller. The Actel FPGA has a JTAG programming interface and a separate Actel flash programmer is used to set it up off-line. The FPGA is at the heart of the data flows and can be programmed to act as a straight path of the data acquisition ADC to the computer interface (the default setup) or additional FIFOs can be created or the data can be routed via the on-board DSP device. The initial configuration uses the DSP as the CCD clock sequence generator with the FPGA acting as a peripheral controller for the DSP and feeding the clock signals to the programmable level translators. The code running on the

DSP is provided by the I2C bus which is converted in the FPGA to an Internal Direct Memory Access (IDMA) boot loader for the DSP. The same interface allows the DSP code to be modified on the fly, e.g. delays can be changed without having to restart the clock sequencer.
The I2C bus also controls the DACs used to provide programmable clocks and biases for the CCD, and controls the main power supplies. A return path from the I2C bus to the USB interface can read the contents of the DSP, and also provides power and temperature monitoring of the power board. There are several I2C addresses decoded by the FPGA to control data acquisition, power converter synchronisation and control bits for the CDS signal processing. The I2C bus also feeds the DACs used for signal offsets.

The diagram shown in Figure 2 shows how the various functional blocks are related.

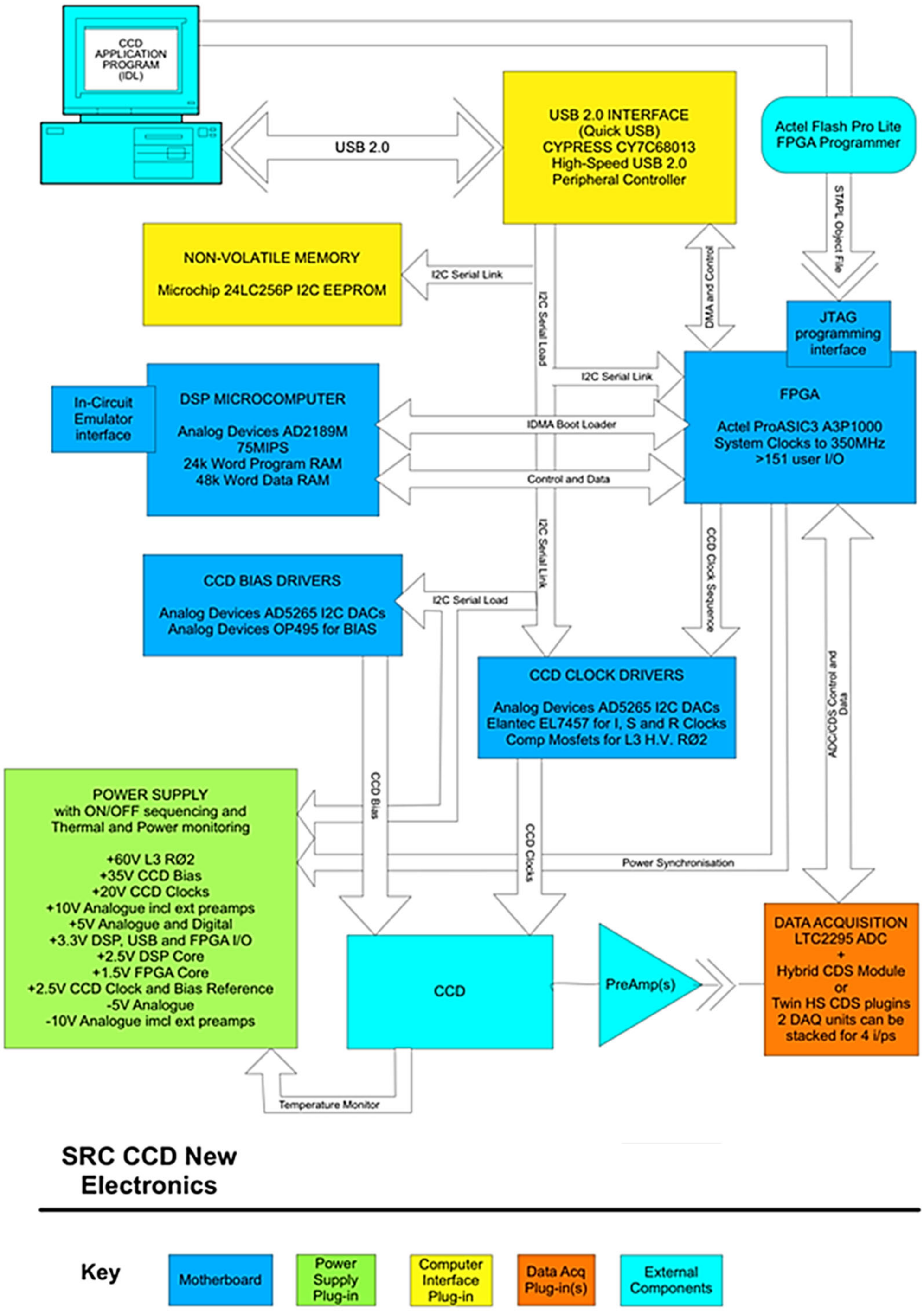

Figure 2 SRC CCD Electronics

2.3.2 Functional Logic Design

The heart of the working logic of the system is implemented in the Actel ProASIC3 A3P1000. The code is written in VHDL and apart from the implementation of the Phased Locked Loops (PLL) for clock generation, no proprietary IP blocks are adopted including the I2C and Serial Port Interface (SPI) blocks. This approach paves the way for a future implementation on a different platform or to evaluate the possibility of designing the system as an ASIC for a forthcoming space project.

The diagram shown in Figure 3 shows the principal modules implemented in VHDL and how they are interrelated.

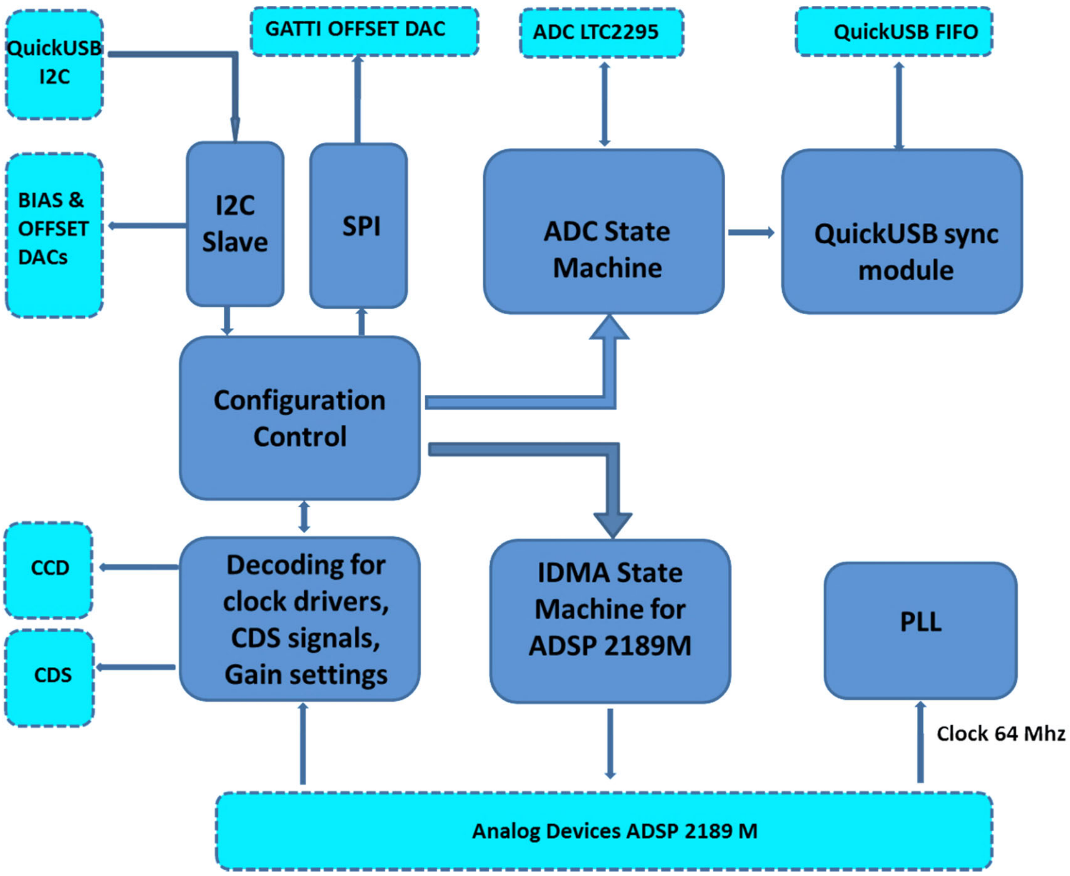

Figure 3 FPGA Functional Diagram

The main clock comes from the ADSP 2189M at 64 MHz and all necessary clocks are generated by the PLL module.

The I2C slave module is necessary to communicate with the QuickUSB module in order to load the program memory code for the DSP, i.e. the sequencer for the CCD. It is also necessary to store the settings for the CDS and the values of the offset for the DACs converters. All the communication via I2C is managed by the Configuration Control module which, depending on the type of request, determines the start of a specific state machine or configuration of control registers.
The SPI module is necessary to communicate with the DAC converter for the so called Gatti offset, named after the research by Gatti (1963) in electronic methods for nuclear spectroscopy pulse high analysis which provides a very fine resolution of the ADC offset adjustment and improvement of differential linearity of the ADC.
The DSP code, written in assembler, performs the functions of sequencing the operation of the CCD and is loaded via I2C. The IDMA state machine module allows the DSP to boot via the IDMA interface.
Logic signals for clock drivers, which will subsequently be amplified by the clock drivers and then delivered to the CCD interface, are received from the DSP and decoded via the FPGA through the decoding module; the same approach is followed for the control signals of the CDS.
The digital acquisition of the pixel signal, after processing by the CDS circuit, is synchronised through an ADC strobe signal coming from the sequencer. The VHDL module named "QuickUSB sync VHDL" takes care of handshaking the sample between different clock domains and writing the sample value to the memory in the QuickUSB chip via the Slave FIFO mode of operation.

2.3.3 Clock Sequencing

The various electrode phases of the CCD are biased high and low in sequence to integrate the CCD image and then transfer it to the output amplifier.
The sequence of clocking events used to generate and read out a CCD image is written in assembler code by the user as a series of loop operations that are executed in the ADSP 2189M signal processor.

The DSP is connected to the FPGA that in turn controls the clock drivers EL7457 that amplify the signals required to clock the CCD. A number of custom sequencer programs for the CCD97 were developed, which will be discussed in the chapter four.

The first row of pixels is transferred into the serial register by calling the first parallel clock loop. All rows in the image become shifted down by one row during this operation.

Before the serial transfer, the charge in the output node capacitor is reset to a reference charge level by the activation of the reset FET with the signal Φ_R and is defined by the potential applied to the reset drain (V_{RD}) as shown in Figure 4, typically of the order 17 V. All potentials cited are with respect to the clock low level of 0 V. The reference signal is a dual slope integrator system. In this instance, the reference level is integrated for a fixed period and held.

The electrodes in the serial register, now holding all the charge packets of the bottom row, perform a similar sequence to the parallel transfer to move the charge packets one-by-one to the output amplifier. The charge applied to the node capacitance causes a potential shift. This is coupled to the output FET (assuming a single stage output circuit as shown in Figure 4) causing a change in V_{DS}, thereby altering I_{DS} and hence the potential difference across the external load resistance, thereby generating an output voltage signal.

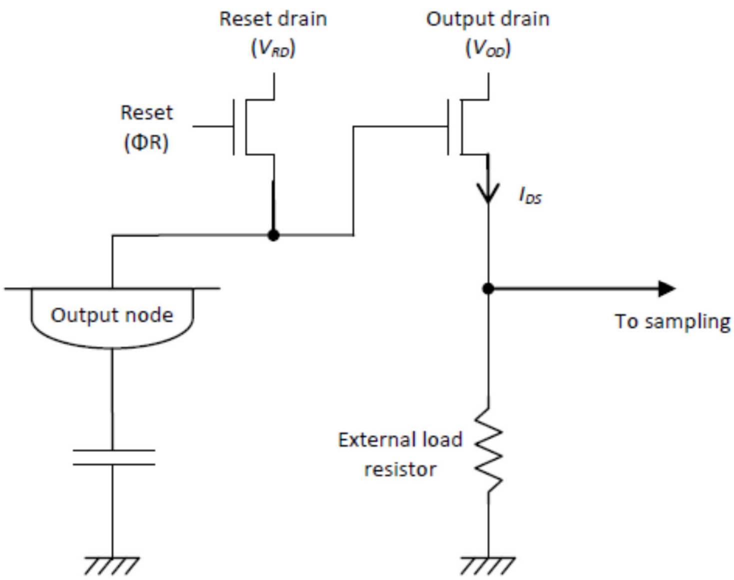

Figure 4 CCD Source Follower (Janesick, 2001)

This is then sampled by the ADC at the request of an enable clock signal (ENB) indirectly from the DSP but generated by the FPGA (ADC_EN). The output node is then reset and the next pixel charge packet is clocked in with the same serial transfer loop.

Once the entire row of pixel charge packets has been sampled by the ADC the parallel clock sequence is called to transfer the next row of the image into the serial register for sampling. The process is repeated until every pixel in every row has been sampled and recorded.

2.3.4 Clock and Bias Voltages

Clock voltages are programmed via the GUI to output between –5 V and +15 V, following e2v recommendations for CCD97. The range of settable voltage values is reported in Table 1 where the value in parenthesis represents the minimum voltage value for the specific voltage. The potential biases applied to the CCD during operation are provided internally to the camera drive electronics by a power supply module. The camera system allows the adjustment of these values in the reference range using a DAC converter to the bias potentials needed for the particular application and CCD.

Signal	V-	V+
Dump Gate 2	-5	5
Dump Gate	5	15
IØ4	5 (-5)	15(5)
IØ3	5 (-5)	15(5)
IØ2	5 (-5)	15(5)
IØ1	5 (-5)	15(5)
Reset 2	-5	5
Input Gate 2	-5	5
Reset 1	5	15
Input Gate 1	5	15
Reset HR	5	15
Reset LS	-5	5
SØ4	5(-5)	15(5)
SØ3	5(-5)	15(5)
SØ2	5(-5)	15(5)
SØ1	5(-5)	15(5)
NC		
RØ2 HV	20 (0)	50 (10)

Signal	V-	V+
RØ6	5(-5)	15(5)
RØ5	5(-5)	15(5)
RØ4	5(-5)	15(5)
RØ3	5(-5)	15(5)
RØ2	5(-5)	15(5)
RØ1	5(-5)	15(5)
Output Drain B	0	35
Reset Drain B	0	25
Auxilliary B	0	35
Reset Drain A	0	25
Output Gate B	0	5
Guard Ring	0	25
Input Diode	0	25
Diode Drain	0	25
Output Drain A	0	35
Auxiliary A	0	35
Substrate	0	10
Output Gate A	0	5

Table 1 CCD Clock and Bias Voltages

Of particular importance for the study presented in this thesis is the RØ2 HV signal used to trigger avalanche multiplication in CCDs such as the CCD97.

2.3.5 Image Pixels and Pixel Binning

The number of pixels in the image is input by the user via the GUI and is forwarded to the sequencer program as variables for the number of row and column loops to perform.

Pixel binning allows the summation of neighbouring pixels in the image array, allowing for images with effectively larger pixels but at a cost to spatial resolution. The binning operation is performed by including additional charge transfers in both directions between pixel resets.

2.3.6 CCD Image Acquisition

The camera system automatically runs the sequencer program as an infinite loop, such that pixels are constantly being sampled by a 14-bit ADC at 10 MS/s. DSP output flags are used to identify the beginning of the frame (Frame-Sync) and the start of each row (Line-Sync) before the first pixel is clocked into the output amplifier. Upon request of an image, sampled values from the ADC begin to be stored in the USB chip buffer. The PC runs the IDL programming language and controls the electronics through a USB2 interface. The IDL application program (ccd_src.pro) communicates with the board via a set of drivers provided by Bitwise Systems in the US. The system is called QuickUSB and provides a set of DLLs callable from within IDL to store internally the image.

A histogram function enables the user to plot the pixel values from either the entire image or a user specified region of interest (ROI). In X-ray applications, such a plot provides the energy spectrum of the photons incident on the CCD.

A Gaussian fitting routine from the IDL library can be used to ascertain statistics within the histogram plot to derive the mean and standard deviation of the signal plot that can be used to calibrate an energy scale for the system to evaluate the noise (electrons r.m.s.) and energy resolution (eV/Channel).

The analysis software also includes a statistical histogram tool to detect different types of X-ray events: single event, corner event, bipixel, tripixel, quadripixel and over 5 pixel events. Such features will not be used in the context of this thesis.

2.3.7 Correlated Double Sampling

Correlated double sampling (CDS) is a method to eliminate the reset noise from the signal, also known as KTC noise. For every pixel, the initial reset charge of the output node is

sampled before the pixel charge packet is added onto the output node and is referred to as the reset reference level. The pixel charge packet is then clocked into the output node and is the difference between the current value and the reset reference level (White et al, 1974).
Reset and the clocking operations can be superimposed onto the output waveform via capacitive coupling; such peaks are referred to as clock feed-through. Proper delays in the sequencer code via GUI configuration allow mitigation of such unwanted signals. Furthermore a proper PCB design and cable shielding provides good signal integrity and help preventing such interferences.
The CDS method used is the dual slope integrator shown in Figure 5, which uses an average of the CCD output over a period of time for both the reference and the signal levels (Janesick, 2001).

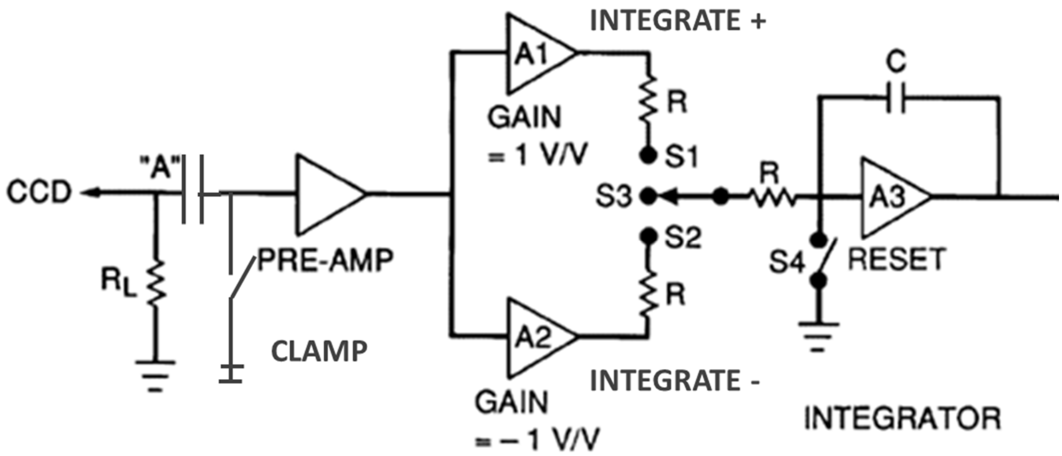

Figure 5 Dual Slope CDS Scheme, adapted from (Janesick, 2001)

The CCD video signal is input to a preamplifier stage; the signal is then clamped to ground during the pixel reset (CLAMP signal) that sets a reference point for the integrator. The pixel reference potential level is then integrated negatively across the capacitor C for the periods that switch INTEGRATE- is closed due to the -1 gain of the amplifier. This causes the output of the integrator to slope negatively (down) with a linear gradient for the period in which INTEGRATE- is closed.
Before activation, the serial transfer of the pixel charge packet into the CCD output, switch INTEGRATE- is opened, freezing the reference level at the output of the integrator. After

adding the pixel charge packet to the output node, signal INTEGRATE+ is then activated integrating the pixel charge onto the reference level. Switch INTEGRATE + is then closed and the value of the pixel is stored at the output of the integrator. Shifting the level and applying in case a Gatti offset value (Gatti, 1963), the voltage signal is then sampled by the ADC. Finally, during the CCD pixel reset, the CLAMP switch is closed to reset the reference level and an INTEGRATOR RESET switch shorts the feedback capacitor of the integrator to discharge it in time for the next pixel.

To note is the presence of four different gain/bandpass configurations for the front-end amplifier as well as four different choices for the gain of the integrator, namely the value of the time constant. The choice of capacitors made of polyphenylene sulphide (PPS) film assures good charge holding properties necessary for this type of application.

The possible configurations are summarised in Table 2 and Table 3.

Gain Setting	Gain Amplifier	F_{-3dB}
0	2	50 MHz Limited by AD8065 F_{-3dB}
1	2	312 kHz
2	6.29	10 MHz Limited by AD8065 F_{-3dB}
3	6.29	268 kHz

Table 2 Gain Setting for Preamplifier

CDS Setting	Integration Time Constant (s)
0	47E-9
1	239.7E-9
2	940E-9
3	4.7E-6

Table 3 Integration Time Constant Setting for Dual Slope CDS

The spectral power density of the dual slope CDS process can be expressed as (Pimbley et al., 1991), (Hopkinson et al., 1982):

$$|H_{CDS}|^{2} = 4 \cdot \frac{sin^2(\pi f \tau)}{(\pi f \tau)^2} \cdot sin^2(\pi f \tau + \pi f \tau \Delta) \tag{2.1}$$

Where τ is the integration time of the slope, Δ is the fraction of time between the two integration slopes and f is the frequency. In an ideal case Δ can be assumed to be zero. It is also assumed that the time constant of the integrator is equal to the integration time of the slope.

In such a situation the transfer function H_{CDS} of the CDS, with τ = 5 µs and considering a gain G_{CDS} expressed as:

$$G_{CDS} = \frac{\tau}{\tau_{RC}} \tag{2.2}$$

given by the ratio of the integration time of the slope to the time constant of the integrator circuit which is usually chosen close to unity, is represented by the graph shown in Figure 6.

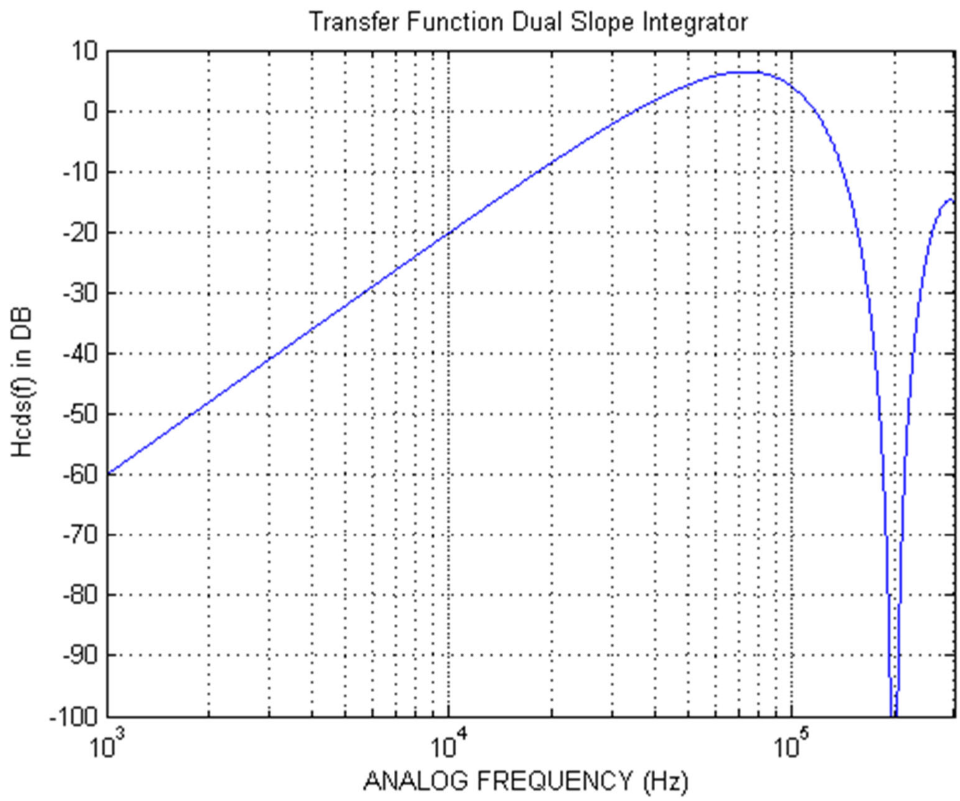

Figure 6 Transfer Function Dual Slope Integrator

The graph in Figure 6 shows how well the dual slope integrator attenuates $1/f$ noise and its passband behaviour limits the broadband white noise generated by thermal noise in the system. For more detailed analysis the reader is referred to Pimbley et al. (1991). In the configuration plotted, the integration time equals half the pixel time period, $\Delta = 0$, the noise bandwidth for the dual slope CDS can be considered as the pixel frequency.

2.3.8 System Gain and Calibration

From a performance point of view two parameters that are important to evaluate are the system gain and the noise in electrons r.m.s..
As shown in Figure 7 adapted from Holst (1998) an incident photon on the active area of the CCD is transformed via a charge sensitive capacitor to a voltage at the output node.

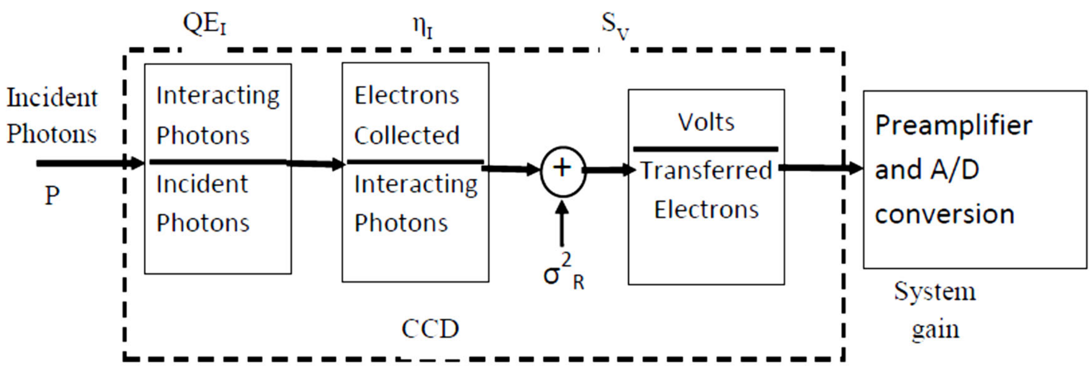

Figure 7 CCD Photon Conversion Diagram

In the case of the CCD97 there are two possible values of CCD gain, G_{CCD}, for the output amplifiers on the chip:
Large Signal (LS) amplifier G_{CCDL} = 1.1 μV/electron;
High Responsivity (HR) amplifier G_{CCDH} = 5.3 μV/electron.
Subsequently, this output voltage will be amplified by the first amplifier, processed by the CDS and converted by the ADC to a digital number, often referred to as ADC channels or Analogue to Digital Unit (ADU).
In the scheme of analogue CDS processing the theoretical gain, G_{sys}, can be evaluated following the flow diagram shown in Figure 8.

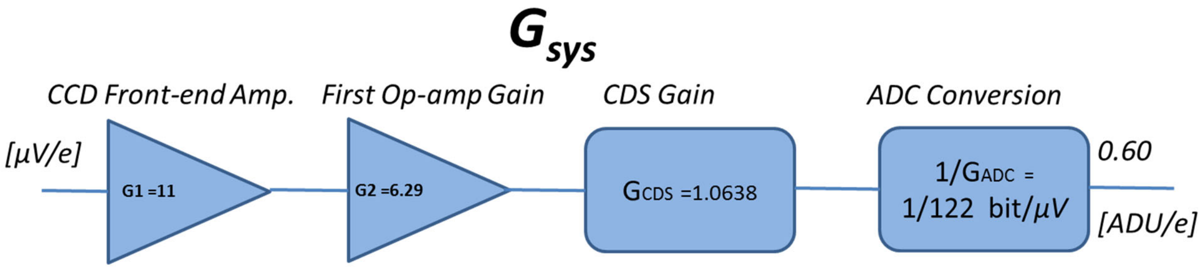

Figure 8 Analogue Readout Method Gain

G1 represents the gain of the CCD front-end amplifier that is placed in the camera head in vacuum. It is an AD829 amplifier in a non-inverting configuration with an F_{-3dB} of 10 MHz and a gain G1 = 11.

G2 represents the gain of first amplifier in the CCD electronic box, mini-CDS plugin, first entry point of the CCD signal preceded by the clamp switch.

CDS gain is considered in a configuration with integration time of 5 µs and an integration time constant of 4.7 µs.

The ADC LTC 2295 is configured with a full scale of 2 V over 14 bits of resolution, which corresponds to 122 µV/bit.

The value of amplification G_{sys} expressed in ADU/electron is 0.6.

Considering the two possible output amplifiers of the CCD97 it corresponds to final gains of respectively for the LS and HR outputs:

$Gain_L = G_{CCDL} \cdot G_{sys} = 0.66$ ADU/electron or in terms of the typical gain for X-rays spectroscopy 1.51 eV/ADU

$Gain_H = G_{CCDH} \cdot G_{sys} = 3.18$ ADU/electron or in terms of the typical gain for X-rays spectroscopy 0.31 eV/ADU.

The camera system noise is measured in electrons r.m.s. in terms of the uncertainty on the signal. The standard deviation σ in electron r.m.s. can be measured by a variety of different methods. The standard deviation can be obtained by calculating the value in the over-scan region of the CCD, sequencing the serial register for a number of columns greater than the effective dimensions of the CCD and reading out the relative pixels

Alternatively, it can be measured calibrating the camera with a known photon energy, usually an Fe55 source producing Mn-Kα (5,898 eV) photons, and converting into the noise equivalent signal by dividing by the quantum yield for silicon, namely the energy required to generate 1 e-h pair which has an average value of 3.65 eV at 293 K. Gaussian curves can be fitted to spectral peaks observed at a) the background and b) the known X-ray energy to determine the peak location (in number of channels) and σ. The known energy (e.g. 5,898 eV) is divided by the number of ADUs between the two peak locations. The ratio, eV/ADU, gives the energy conversion scale with 0 eV at the background peak location.

Subsequently, σ for the background peak is multiplied by the energy conversion scale to determine its value in eV. Finally, this value can be divided by the quantum yield for silicon to convert it into the noise equivalent signal in electrons.

The last method considered is the photon transfer curve (PTC) (Janesick, 2007) consisting of a plot of the standard deviation of back to back images with monotonic exposure as a function of the average effective signal. Such a curve provides both the conversion gain and the readout noise for a CCD.

The measure of the standard deviation includes all the noise contributions from internal sources such as thermal noise and power supply noise as well as external induced effects such as EMI from the environment.

The results of the PTC method will be shown in chapter 4, regarding the camera characterisation.

2.4 CCD Digital Readout Electronics

It was thought that the analogue electronic system developed could be leveraged to design a fully digital system with the aim to pave the way to evaluate digital signal processing methods to improve the noise performance, as in Rawley (2016), and to optimise the operations in specific conditions as for instance in presence of radiation damaged CCDs.

The driving design goals to achieve were:

- Maximum leverage of the existing design
- Minimise the number of electrical connections required
- Make the electronic design and acquisition software as simple as possible

- Make use where possible of evaluation boards without compromising performance

As shown in Figure 9, the GUI IDL software and the CCD electronic box are retained due to their capabilities of driving the CCD and easily changing the parameters of the sequencer. The assembler code running on the DSP has been changed for the digital acquisition due to a polarity change of the electronic switches adopted.
The acquisition and configuration software runs on a different machine and is based on a program written in C language relying on a DLL library compatible with function calls on the USB Cypress chip developed by Digilent, producer of the FPGA evaluation board Atlys based on a Xilinx Spartan6 LX45, and connected via USB to the computer for loading the firmware and transmitting data.

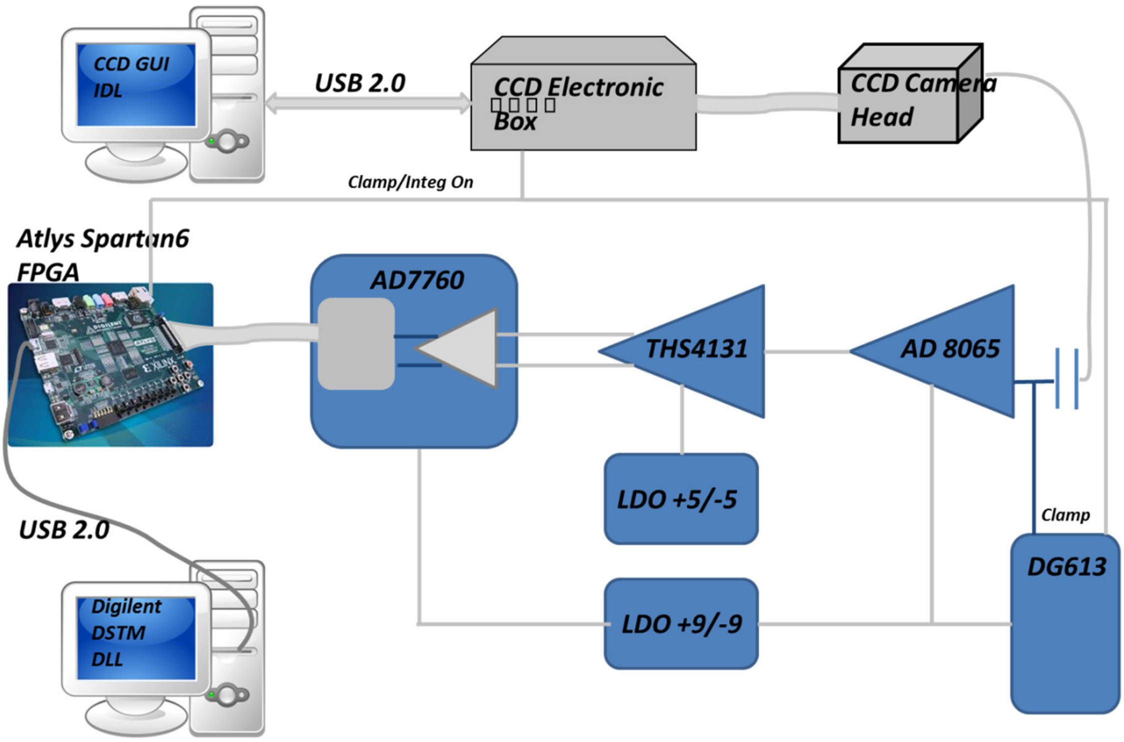

Figure 9 CCD Digital Readout Method Functional Scheme

To minimise the number of connections, and consequently modifications to the existing CCD electronics, it was chosen to connect only to two digital signals. Depending on the operating mode of the digital electronics, these signals are: the CLAMP signal necessary to determine the start of the pixel period and to operate the switch DG613, necessary to DC restore the AC coupled signal coming from the CCD camera head, and INTEGRATE PLUS or INTEGRATE ON depending on the trigger setting of the ADC AD7760. The former is used by the analogue CDS to signal the duration of the integration period during the pixel period and the latter is a signal normally connected to a LED that indicates the start and finish of the exposure time of the CCD.

The AC coupled CCD signal, after DC restoration through the switch, is amplified by a FET input amplifier, AD8065. In order to achieve best performances by the ADC the input signal should be differential, and for this purpose the fully differential amplifier THS4131 transforms the signal from single ended to differential. At this stage the differential CCD signal is fed to the on chip fully differential amplifier of the AD7760 to normalise its range to the maximum digital code.

The AD7760 evaluation board is connected to the FPGA via an IDE cable and a BBmod adapter connector. Apart from the FPGA, which uses its own power supply, all the other systems are powered through four linear drop regulators on separate PCB boards, LM78xx and LM79xx. Such a choice disregards power consumption to the benefit of the lowest power supply noise.

Finally, once the image is acquired on the computer via USB, the samples are processed via a Matlab program which synchronises the samples in the pixel period relative to the CLAMP signal and the delay introduced by the ADC and processes them depending on the algorithm implemented to calculate the pixel charge value. The data matrix obtained then is transformed into an image via ImageJ.

2.4.1 Functional Logic Design

The FPGA code running on the Spartan6 is written in VHDL and apart from the implementation of the PLLs and the FIFOs no other proprietary IP blocks are adopted. This approach paves the way for a future implementation on a different platform and the possibility to design the system in an ASIC.

Figure 10 shows the principal modules implemented in VHDL and how they are interrelated.

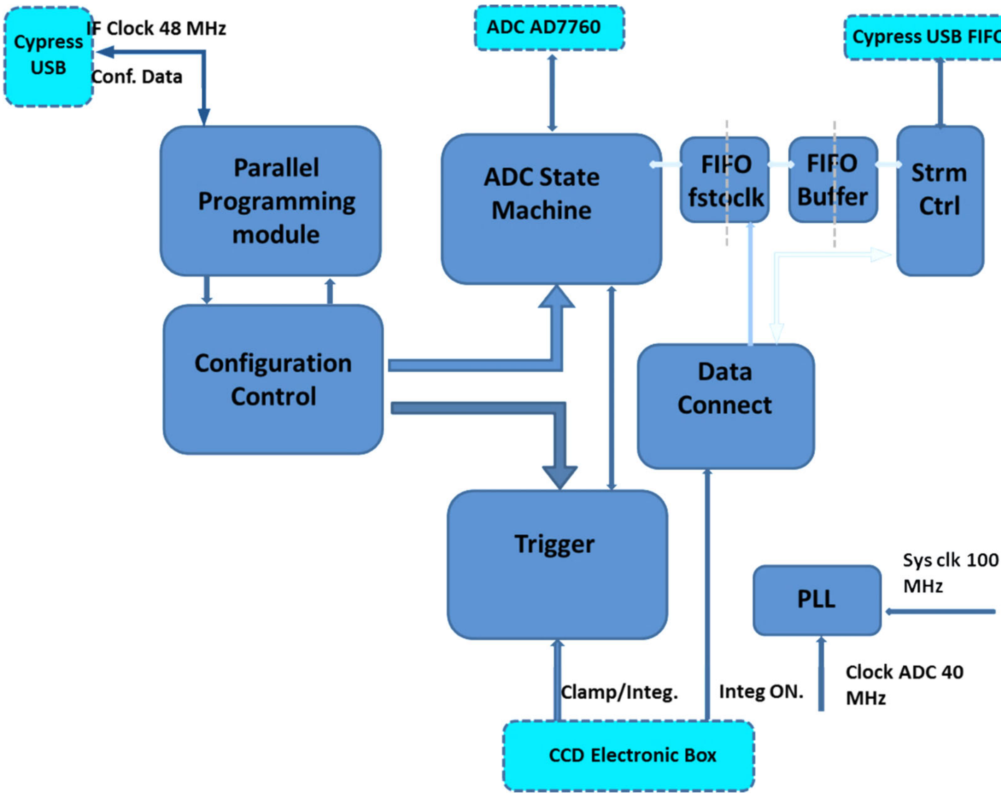

Figure 10 FPGA Functional Design for CCD Digital Readout Method

The main clock comes from the on board 100 MHz of the FPGA as well the clock of 40 MHz coming from the ADC board that is used to synchronise with the data flow and configuration for the ADC. Communication via USB is implemented through a Cypress chip, CY7C68013A-56, both for ADC data transmission and configuration setting running at an internally generated clock of 48 MHz.

The parallel programming module implements a sort of parallel interface to the Cypress chip, adapted from a code released by Digilent named "DPIMREF", to write and read back registers which contain the settings - control registers - and start/run configuration bits for the state machines to set the standby mode for the acquisition process. The proper decoding and synchronisation of these control settings is implemented by the Configuration Control module.

The ADC State Machine implements the logic to write the configuration registers for the AD7760. This ADC offers optimum performance in terms of noise and resolution using a delta-sigma conversion method with a high resolution of 24 bits up to 2.5 MHz in fully filtered mode at the expense of a more complicated implementation. The same module, depending on the bits set by the Configuration Control module, implements the logic to read the sample converted by the ADC. To operate the ADC, it is first necessary to write to control register 0x0001 and then set the sampling rate and digital cut off filter writing to register 0x0002.

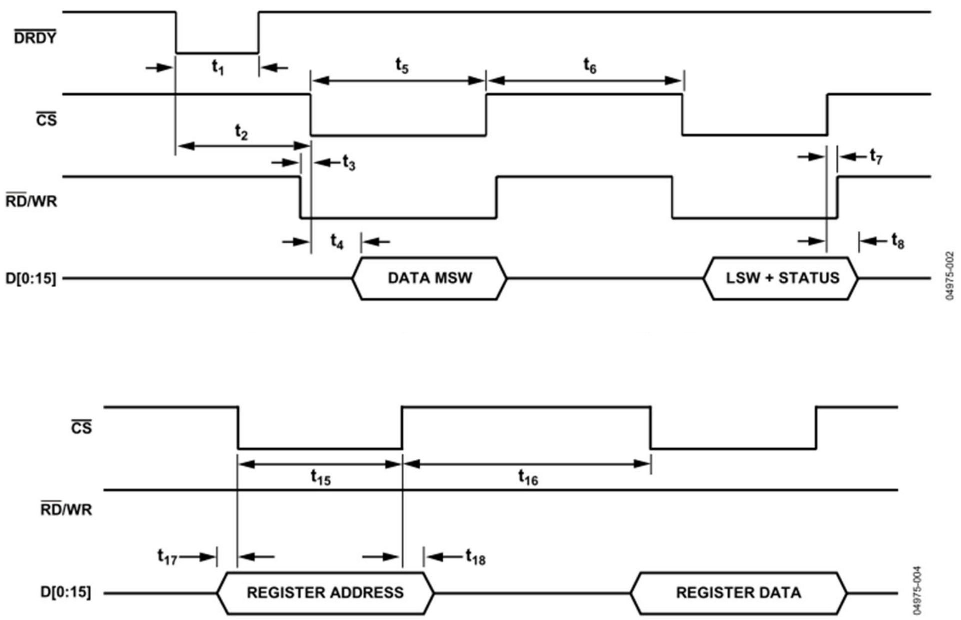

Figure 11 Timing Diagram AD7760

Figure 11 shows the timing sequence that the state machine in the firmware module follows to drive the ADC converter. The top diagram is for the sample reading process; when a new sample is available the converter pulses the DRDY signal and the FPGA logic generates the CS and $\overline{\text{RD}}/\text{WR}$ signals with stringent timing and the latching logic to acquire the sample.
The bottom diagram is followed in the case of setting the configuration registers.
The Trigger module is used to set the acquisition mode for the ADC; namely it can be continuous or it can be set to acquire a specified number of samples after an event on a trigger signal or acquire samples during the high state of a trigger signal. All these

parameters can be set through the Parallel Programming module. The signals that can be used as trigger coming from the CCD electronic box can be INTEGRATE PLUS or INTEGRATE ON as explained above.

The Data Connect module is at the heart of the logic to synchronise the acquisition process with the status of the CCD, specifically the falling edge of the INTEGRATE ON signal triggers the state machine to start the acquisition process and, depending on the trigger setting, enables the writing to the FIFO fstoclk which holds the samples coming from the ADC. Subsequently, the data samples crossing the domain clock from fsclock at 40 MHz to clk at 100 MHz are passed to the FIFO Buffer, which is a large FIFO in order not to lose samples from the ADC given the different speeds between the ADC and the Cypress chip, and crossing the clock domain from the clk at 100 MHz and IF Clock at 48 MHz of the USB chip.

Finally, the samples from the FIFO can be written to the Cypress chip via the logic implemented in the Strm Ctrl VHDL module that implements a slave FIFO synchronous transmission mode to the USB chip. Such a method expects the size of the data requested by the routine written in C language and running on the computer to be a multiple of 512 bytes to commit the total data to the computer. To do this the Data Connect module implements a padding mode to write dummy data after the end of the CCD data samples to use up any empty bytes.

2.4.2 Circuit Description

Following the above general description, a more detailed explanation of the analogue circuit will be given concerning the choice of the components.

In the schematic circuit shown in Figure 12 the AD829 amplifier is part of the camera head circuit and as such can only be changed with difficulty, although an optimisation could be achieved at least reducing the bandwidth of the circuit.

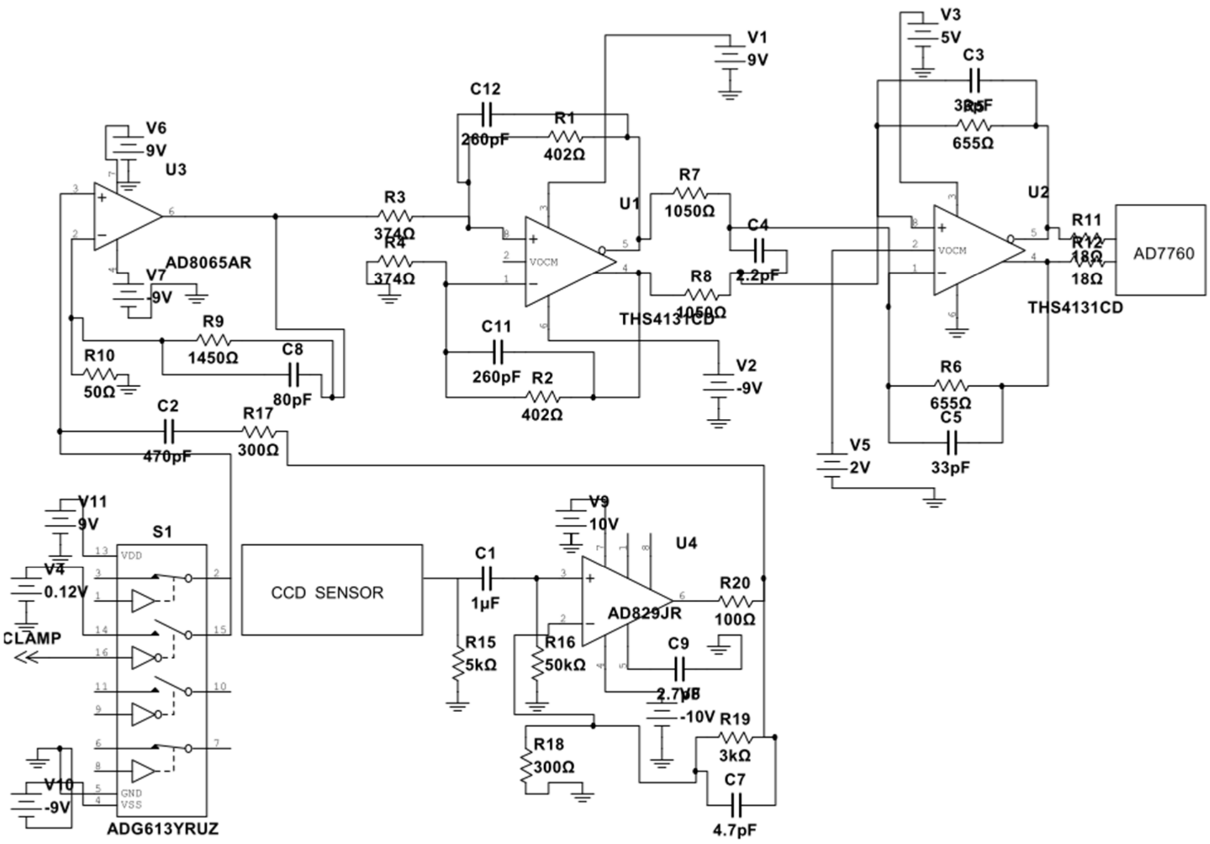

Figure 12 Analogue Processing Circuit for CCD Digital Readout Method

The AD8065 amplifier is AC coupled and the signal value is DC restored during the reset pulse of the CCD to avoid a floating value of the DC content of the signal depending on the DC signal blocked by capacitor C2 that varies with time. Such a problem was experienced in the first release of the system in which the first stage was an op-amp OPA690, coupled via a large capacitor of 20 μF to avoid the blocking of low frequency signals.

The decision to choose the AD8065 is driven by the low noise performance of the amplifier, low input bias current being a FET input amplifier, the good dynamic performance in settling time, and 3_{dB} bandwidth with high gain values such the value of 30 adopted.

The presence of the switch DG613 becomes necessary not only to restore the DC value, as already stated, but also because in using a FET input amplifier the bias current, although very small, would increase the charge on the capacitor and after few seconds the stage would be in saturation. The restoration point of the DC signal has been chosen such that the output voltage will be at around 3.5 V just before the AC signal will be connected at the clamping off of the capacitor to give a higher dynamic range to the signal and optimise the analogue voltage range at the converter inputs. The Vishay DG613 family can be considered one of the best fast switches given its very low Ron resistance of the order of few Ωs, fast switching time at 12 ns, low propagation delay of 40 ns as shown in Figure 13 and very low charge injection and leakage current, in the order of the pA, the most important parameter for this type of application.

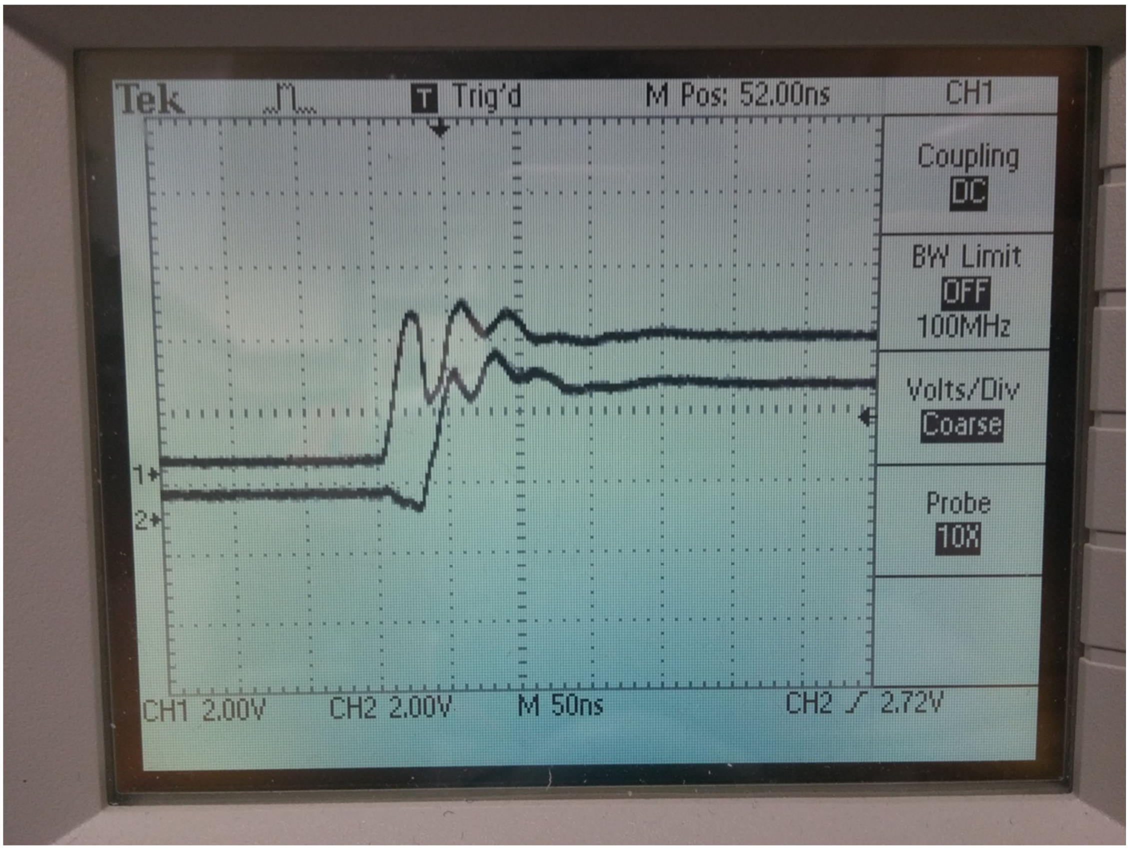

Figure 13 DG613 Delay

The THS4131 is a fully differential amplifier with a high bandwidth, appropriate settling time, low noise performance, an easy to configure single ended to fully differential configuration and the availability of an evaluation board.

Apart from the THS4131 the preceding circuits have been built on custom made PCB boards.

The AD7760 converter is a 24 bit delta-sigma converter with exceptional performance (Schreier et al., 2005). It can be configured in a variety of modes with an output rate up to 20 MHz in the modulator mode where the internal digital filtering is bypassed. The advantage of the converter is evident from Figure 14.

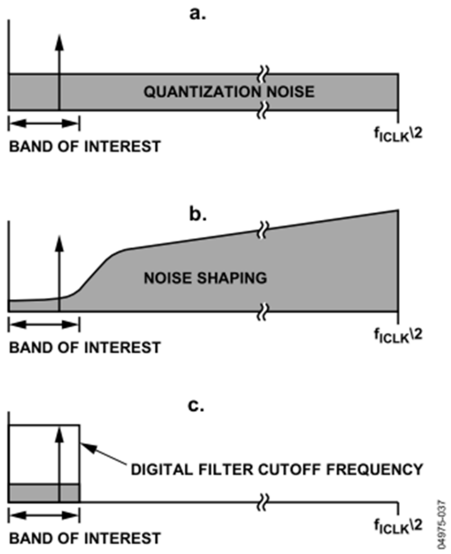

Figure 14 Noise Shaping ADC AD7760

This type of converter shapes the quantisation noise in an uneven mode such that the digital cut-off filter is configurable by setting default registers or by downloading a custom one that can cut much of the noise in the band of interest. The SNR improvement over the standard ratio of a non-oversampling ADC, ratio limited by the quantisation noise and the number N of decoding bits, is given by the processing gain related to the ratio between the oversampling frequency F_s and the signal band of interest B_W. $SNR_{\Delta\Sigma}$ is expressed as:

$$SNR_{\Delta\Sigma} = 6.02 \cdot N + 1.76 + 10 \cdot \log_{10}\left(\frac{F_s}{2 \cdot B_W}\right) \tag{2.3}$$

The ADC configuration chosen in this work is summarised in Table 4.

Output Data Rate (Msample/s)	2.5
Signal-to-Noise Ratio (dB)	99 typical
Computational Delay (µs)	4.6
Cut-off Frequency (kHz)	562.5

Table 4 ADC AD7760 Settings

The frequency of 562.5 KHz is appropriate considering a pixel frequency of 70 kpix·s^{-1}, the cut of frequency being advised to be 6 to 8 times the pixel frequency (Clapp, 2012). Such a choice is a compromise between cutting-off out of band noise and representing properly the CCD output waveform in terms of rise and fall time, as also confirmed by simulation adopting the time domain simulation model developed in this thesis.

The evaluation board provides the on chip differential amplifier in a first-order antialias filter configuration, the 10 dB attenuation at the first alias point of 19 MHz, necessary considering that the oversampling clock works at 40 MHz.

The chosen configuration of the gain and the default setting of the internal digital gain register of the ADC establish a full scale input range at the converter of +/-5.3 V, namely 10.6 V peak to peak. Considering the clamping process of restoring the DC to a value of 3.5 V it means that the maximum signal of pixel charge, which is negative, is given by:

- (-5.3 V - 3.5 V) = 8.8 V

2.4.3 System Gain

Proceeding as already done for the analogue readout electronics it is important to calculate the gain of the system, G_{sys}, the system gain readout being shown in Figure 15.

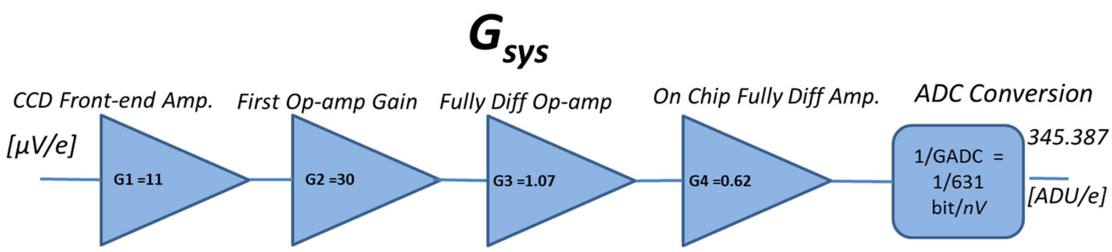

Figure 15 System Gain CCD Digital Readout Method

G1 represents the gain of the CCD front-end amplifier that is placed in the camera head in vacuum and is identical to the analogue case being part of the CCD camera head.

G2 represents the gain of first operational amplifier, the AD8065, with a gain of 30.

G3 is the gain of the THS4131 in a single ended to differential configuration with a gain of 1.07.

The on chip fully differential amplifier on the AD7760 is configured to give a gain of 0.618.

The AD7760 ADC is configured with a full digital scale corresponding to a signal at the input of the on-chip differential amplifier of +/- 5.3 V over 24 bits of resolution, which corresponds to 0.6318 μV/bit.

G_{sys} expressed in ADU/electron is 345.387 and considering the two possible output amplifiers of the CCD97 it corresponds to final gains of:

$Gain_L = G_{CCDL} \cdot G_{sys} = 379.9257$ ADU/electron or in terms of the typical gain for X-rays spectroscopy 0.002632 eV/ADU.

$Gain_H = G_{CCDH} \cdot G_{sys} = 1830.55$ ADU/electron or in terms of the typical gain for X-rays spectroscopy 0.5462E-3 eV/ADU.

The camera system noise, as in the case of the analogue readout electronics, is measured in electrons r.m.s. in terms of the uncertainty on the signal. The standard deviation σ in electrons r.m.s. will depend on the algorithm used to evaluate from the acquired samples the effective pixel charge value by processing the pixel reset value and the pixel charge value.

Direct implementation of the digital counterpart of the CDS dual slope integrator in the analogue domain is offered by the differential averager digital signal algorithm (Stefanov et al., 2014) and in Smith et al. (2013) and already deployed successfully in a number of scientific projects as in Bredthauer et al. (2013).

The verification of the gain and system noise can follow similar procedures as already described for the analogue readout electronics.

Details of the possible processing algorithms and the first results obtained under the work of this thesis are presented in chapter 4.

3. Camera System Design

3.1 Introduction

The camera has been designed at the University of Leicester leveraging the experience built with a camera for medical imaging applications as a gamma ray detection camera (Lees et al., 2011).

The camera is a scintillator coupled detection system using the electronics described in the previous chapter for the readout of a CCD detector.

The scintillator is coupled to an e2v CCD97 back-thinned device to improve sensitivity. The incorporation of avalanche multiplication in the serial register, especially in the case of low photon flux applications, reduces the relative detrimental effects of readout noise.

The CCD detector needs to be cooled in order to reduce the effects of dark noise to a temperature of -70 °C requiring that the system is maintained in vacuum.

In the present chapter a view of the mechanical as well optical design of the camera will be given and a performance model for the overall signal chain from scintillator to detector and electronics will be presented as an analytical verification for the results presented in chapter 5.

3.2 Mechanical and Thermal Design

The mechanical design of the camera head started from a previous project for a gamma ray camera, which used a directly coupled scintillator and a single Peltier stage to cool the CCD.

The design had to be modified to allow the CCD to work as an optical camera device for the exact focus distance of a C-mount lens, namely a lens flange to CCD image plane distance of 17.52 mm.

The back of the CCD, in a first release of the design, was thermally coupled to a thermoelectric cooler (TEC) allowing, with a water cooling method on the cold side of the TEC, the CCD to be operated at temperatures down to -10 °C.

For the type of applications foreseen and from simulation studies this operational temperature was insufficient and as such a new camera design was started. In order to detect single photons in an Electron Multiplying Charge Coupled Device (EMCCD) regime, the detection limit is set by the number of ‘dark’ background events. These events consist of both residual thermally generated electrons and Clock Induced Charge (CIC) electrons estimated to be in the order of 1 electron/s/frame at a temperature of -55 °C as reported in the CCD97 datasheet. In order to get to this single photon detection regime there must be sufficient cooling, to obtain significantly less than 1 event per pixel; the second design considered the use of a liquid nitrogen cooling system with a spider structure at the base of the camera head and a cold finger at the centre of the spider touching the CCD via a series of springs the back surface of the device. Figure 16 shows the assembled camera.

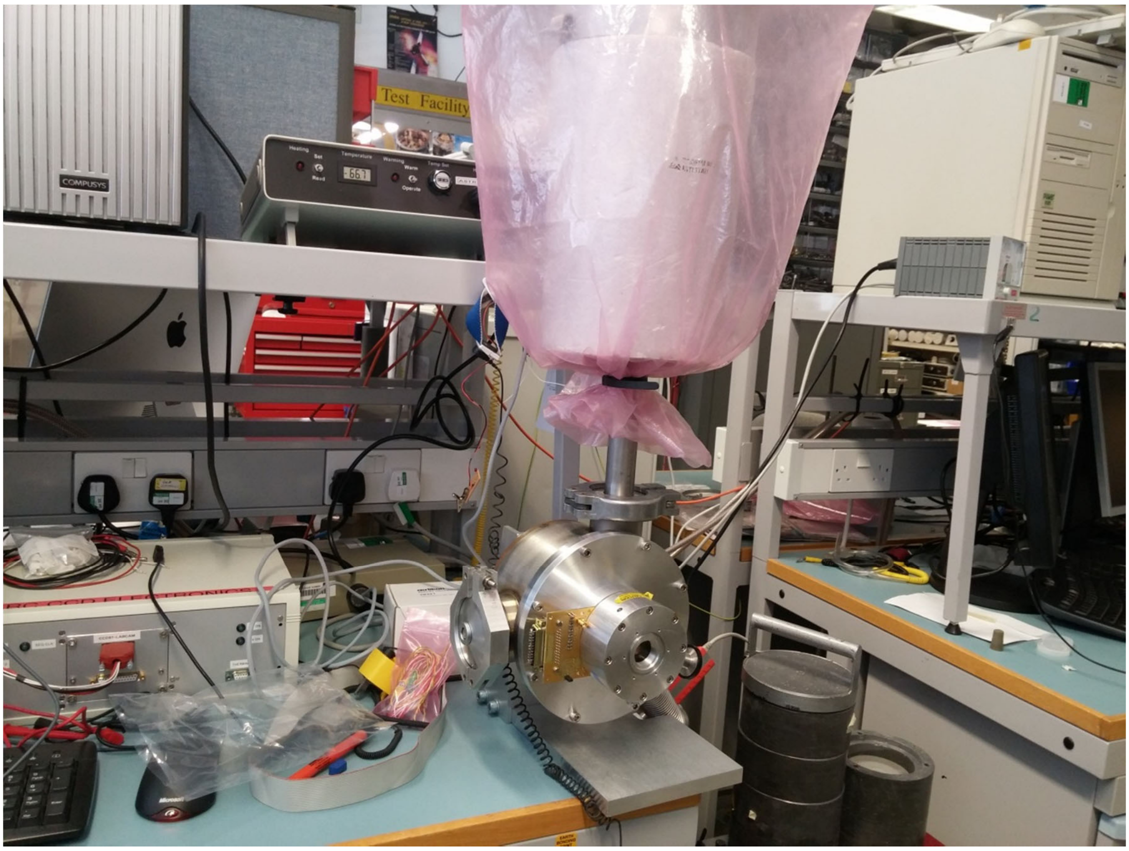

Figure 16 Camera Cooling System View

Figure 17 shows the surface of the copper cold finger on which the CCD will be mounted on; the couple of wires are for the PRT in charge of controlling the temperature of the system.

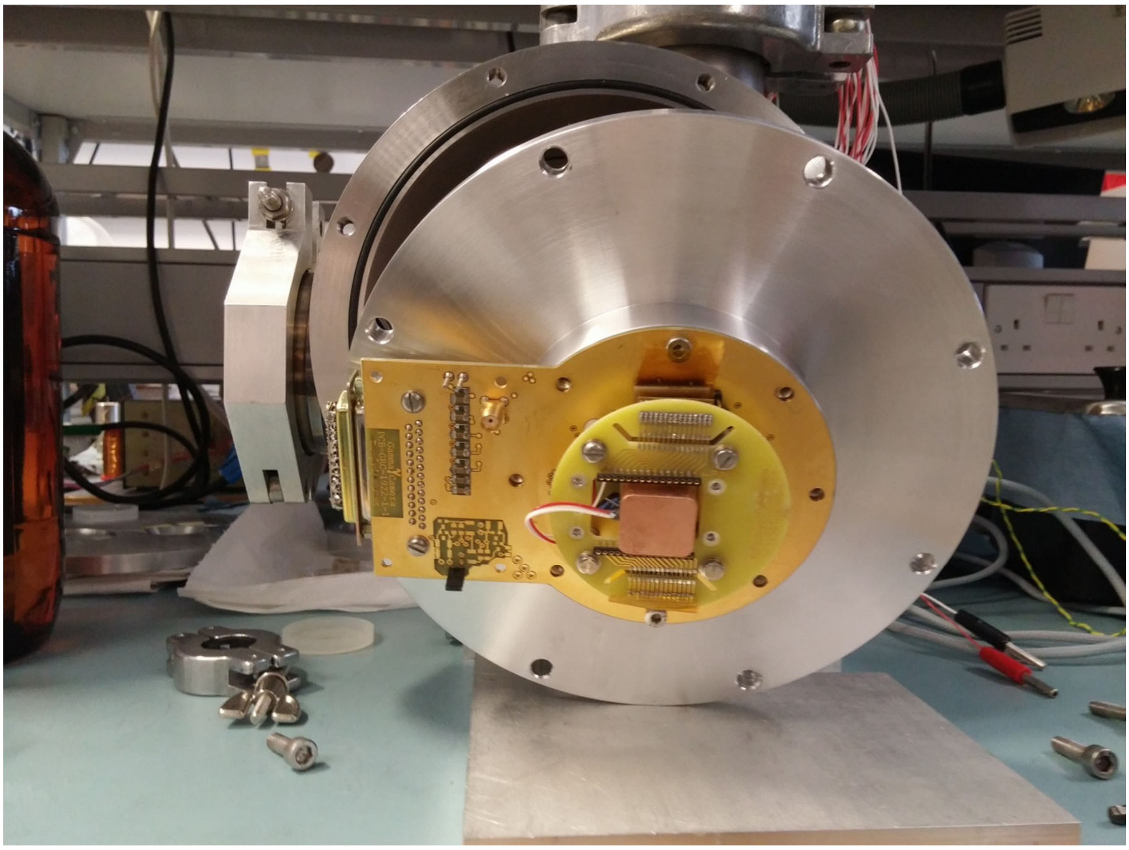

Figure 17 Cold Finger View

The temperature gets controlled automatically with a PID controller, which switches on the metal case resistor attached to the cold finger as shown in Figure 18.

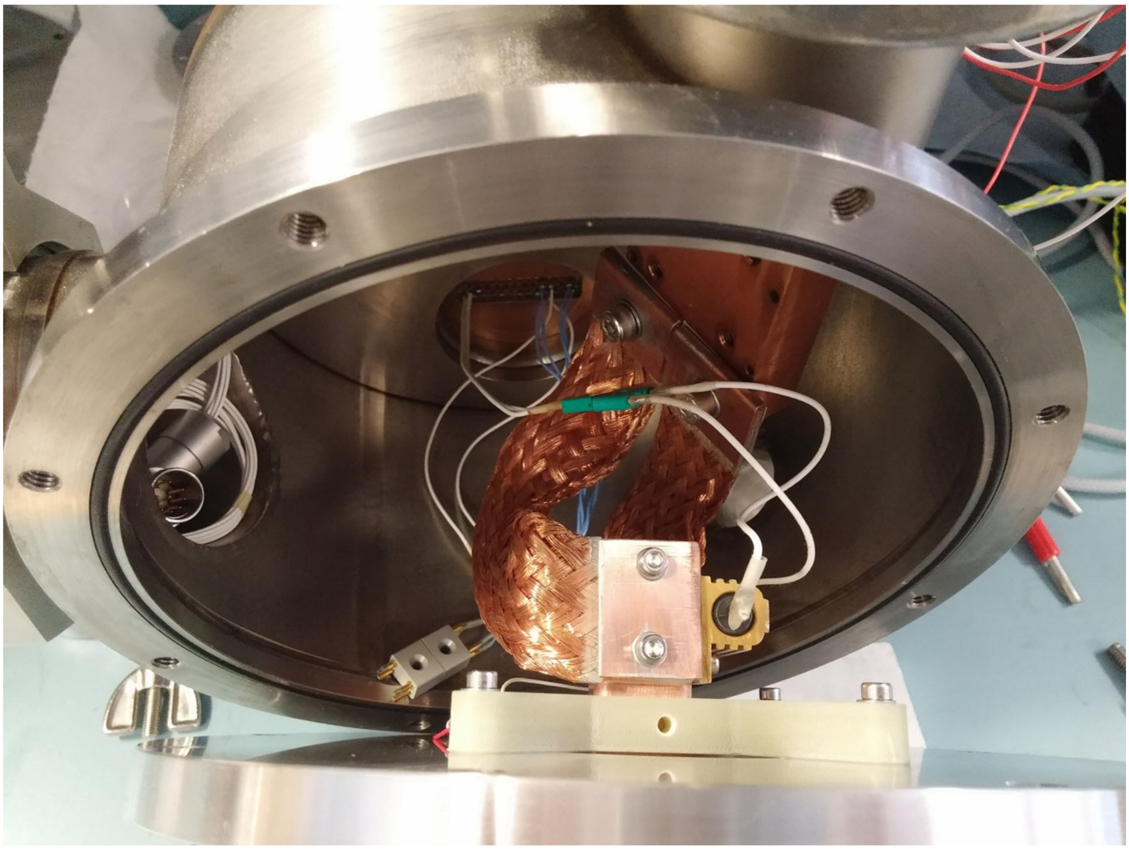

Figure 18 Thermal Strap View

The thermal connection to the liquid nitrogen tank and its copper cold finger is assured by two copper thermal straps.

The cold finger gets pushed toward the back surface of the CCD through a spider system and springs as can be observed in Figure 19.

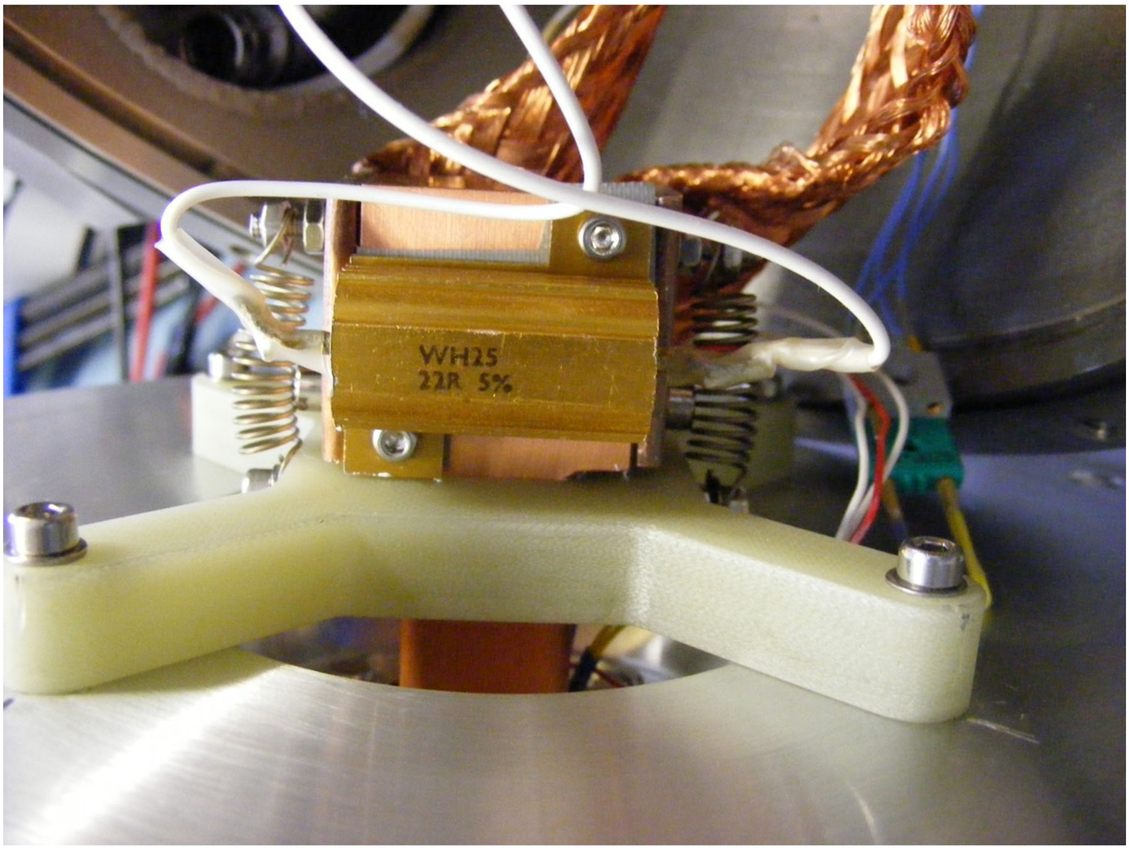

Figure 19 Spider and Springs View

The verification of the cooling capability of the system required consistent testing.

At first a PRT was placed directly on the surface of a damaged CCD, as shown in Figure 20, to understand the difference between the setting temperature of the regulator and the effective CCD temperature. The sensed temperature read externally was found to be 5 °C different.

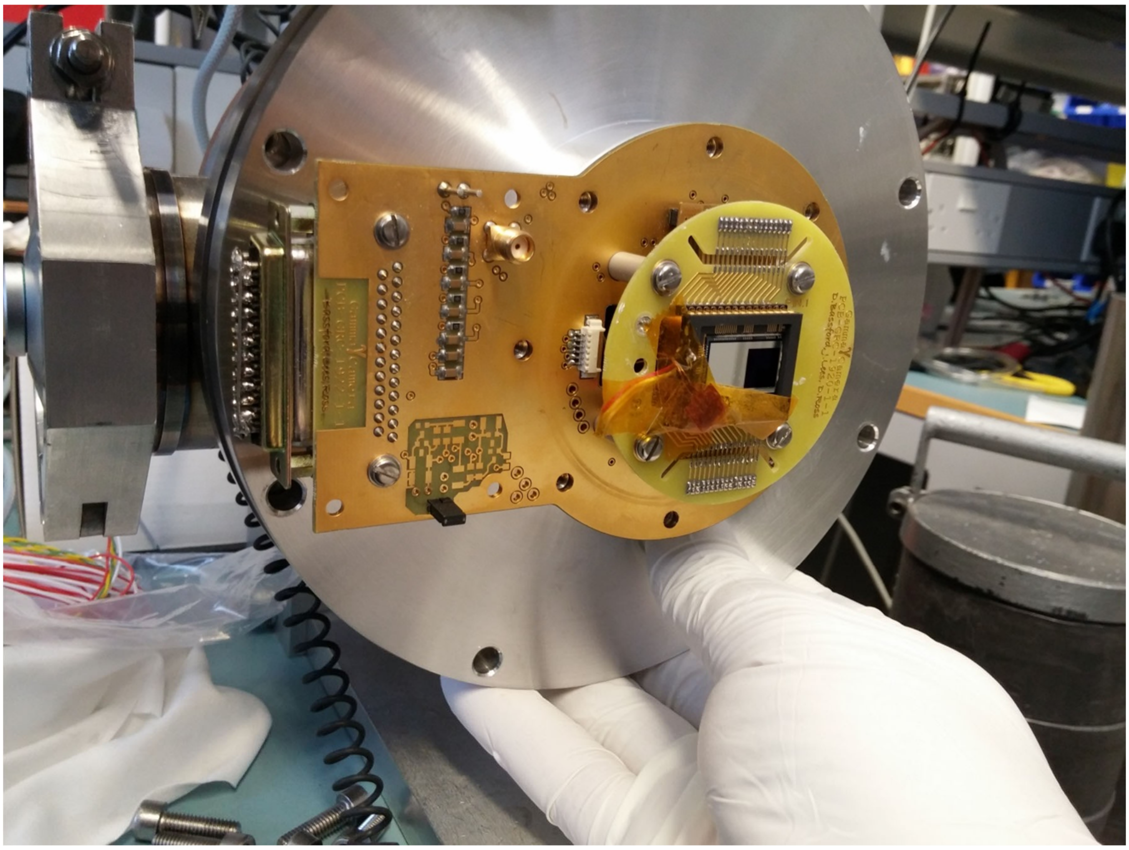

Figure 20 CCD Thermal Sensor Setup

A second problem was found in that there was a point between -40 and -65 °C that the detector temperature deviated from the cold finger temperature as shown in Figure 21.

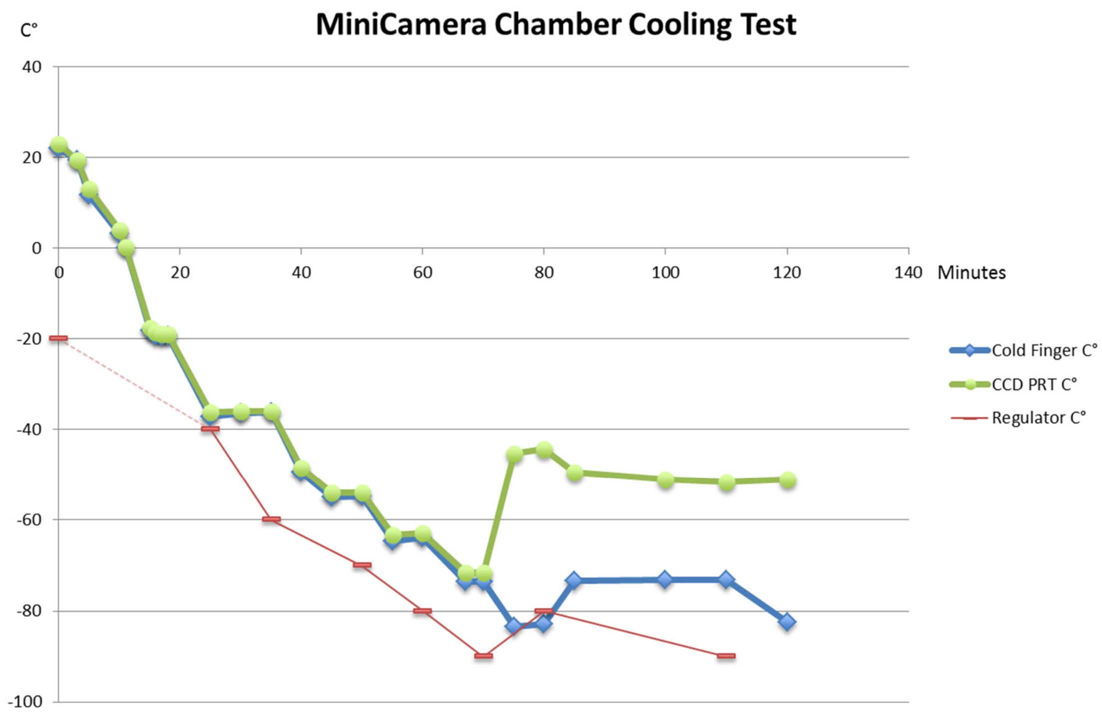

Figure 21 Camera Cooling Test

The solution to the problem was to replace the thermal paste between the cold finger and the CCD with one capable of functioning at cryogenic temperatures. The problem was solved adopting Apiezon N grease as thermal paste.

3.3 Camera / Scintillator Systems

Scintillators are materials - solids, liquids, gases - that produce sparks or scintillations of light when ionizing radiation passes through them (Tsoulfanidis, 1990). Depending on the type of ionising radiation, as well as the chosen type of light collection method and behaviour in terms of hygroscopicity, a different type of scintillator must be selected. In the following discussion only the scintillation parameters related to the light yield and the final gain of the camera system are of interest. More extensive details are given in chapter 5. A scintillator's light can be amplified by a device known as a photomultiplier tube (or phototube or intensifier). Its name denotes its function: it accepts a small amount of light, amplifies it many times, and delivers a strong pulse of electrons at its output.

Amplification can also be achieved through the use of avalanche multiplication directly on the silicon detector like using a CCD97 as proposed in the following work.
The different types of scintillators are divided into three groups:

1. Inorganic scintillators
2. Organic scintillators
3. Gaseous scintillators

Different characteristics of the scintillators adopted and a comparison between them will be given in the chapter 5.
The operation of a camera system based on scintillators may be divided into two broad steps:
1. Absorption of incident radiation energy by the scintillator and production of light photons $g(E)$, light yield, per absorbed X-ray quanta $\alpha(E)\cdot Q(E)$ in its characteristic spectral photon emission $d\theta(\lambda)/d\lambda$. Where $\alpha(E)$ is the X-ray absorption and $Q(E)$ is the X-ray flux function of energy.
2. Collection of light and transformation by the detector in photo-electrons then voltage and subsequently converted to ADC channels.

A list of the characteristics of some inorganic scintillators is reported in Table 5 (Eijk, 2004).

	Density ($g\ cm^{-3}$)	ρZ^4_{eff} (10^6)	Attenuation length at 511 keV (mm)/ prob. phot. eff. (%)	Hygro- scopicity	Light yield (photons/ MeV)	Decay time (ns)	Afterglow (% after 3 ms/100 ms)	Emission maximum (nm)	$\Delta E/E$ (FWHM) at 662 keV (%) PMT read-out	Δt (ps) /BaF_2 /^{60}Co
CsI:Na	4.51	38	22.9/21	Yes	40 000	630		420	7.4	
CsI:Tl	4.51	38	22.9/21	Slightly	66 000	800–>6×10^3	>2/0.3	550	6.6 (PMT)/ 4.3 (SDD)[a]	
$CaWO_4$	6.1	89	13.6/32	No	20 000[b]			420	Integrating mode	
$YTaO_4$:Nb	7.5	96	11.8/29	No	40 000[b]			410	Integrating mode	
Gd_2O_2S:Tb	7.3	103	12.7/27	No	60 000[b]	1×10^6		545	Integrating mode	
Gd_2O_2S:Pr,Ce,F	7.3	103	12.7/27	No	35 000[b]	4×10^3	<0.1/<0.01	510	Integrating mode	
Gd_2O_2S:Pr (UFC)	7.3	103	12.7/27	No	50 000[b]	3×10^3	0.02/0.002	510	Integrating mode	
$Y_{1.34}$,$Gd_{0.60}O_3$:$(Eu,Pr)_{0.06}$[c] (Hilight)	5.9	44	17.8/16	No	42 000[b]	1×10^6	4.9/<0.01	610	Integrating mode	
$Gd_3Ga_5O_{12}$:Cr,Ce	7.1	58	14.8/18	No	40 000[b]	140×10^3	<0.1/0.01	730	Integrating mode	
$CdWO_4$	7.9	134	11.1/29	No	20 000[b]	5×10^3	<0.1/0.02	495	6.8	
Lu_2O_3:Eu,Tb	9.4	211	8.7/35	No	30 000[b]	$>10^6$	>1/0.3	611	Integrating mode	
$CaHfO_3$:Ce	7.5	139	11.6/30	No	~10 000[b]	40		390	Integrating mode	
$SrHfO_3$:Ce	7.7	122	11.5/28	No	~20 000[b]	40		390	Integrating mode	
$BaHfO_3$:Ce	8.4	142	10.6/30	No	~10 000[b]	25		400	Integrating mode	
NaI:Tl	3.67	24.5	29.1/17	Yes	41 000	230		410	5.6	
$LaCl_3$:Ce	3.86	23.2	27.8/14	Yes	46 000	25 (65%)		330	3.3	224
$LaBr_3$:Ce	5.3	25.6	21.3/13	Yes	61 000	35 (90%)		358	2.9	385
$Bi_4Ge_3O_{12}$ (BGO)	7.1	227	10.4/40	No	9 000	300		480	9.0	
Lu_2SiO_5:Ce (LSO)	7.4	143	11.4/32	No	26 000	40		420	7.9	
Gd_2SiO_5:Ce (GSO)	6.7	84	14.1/25	No	8 000	60		440	7.8	
$YAlO_3$:Ce (YAP)	5.5	7	21.3/4.2	No	21 000	30		350	4.3	
$LuAlO_3$:Ce (LuAP)	8.3	148	10.5/30	No	12 000	18		365	~15	
$Lu_2Si_2O_7$:Ce (LPS)	6.2	103	14.1/29	No	30 000	30		380	~10	

Table 5 Inorganic Scintillators

Light yield is expressed in photons/MeV. In reality there is a variation of the light yield with incident photon energy as well as a variation in X-ray absorption with energy.

A typical spectral photon emission $d\theta(\lambda)/d\lambda$ for Kodak Lanex Regular is represented in Figure 22.

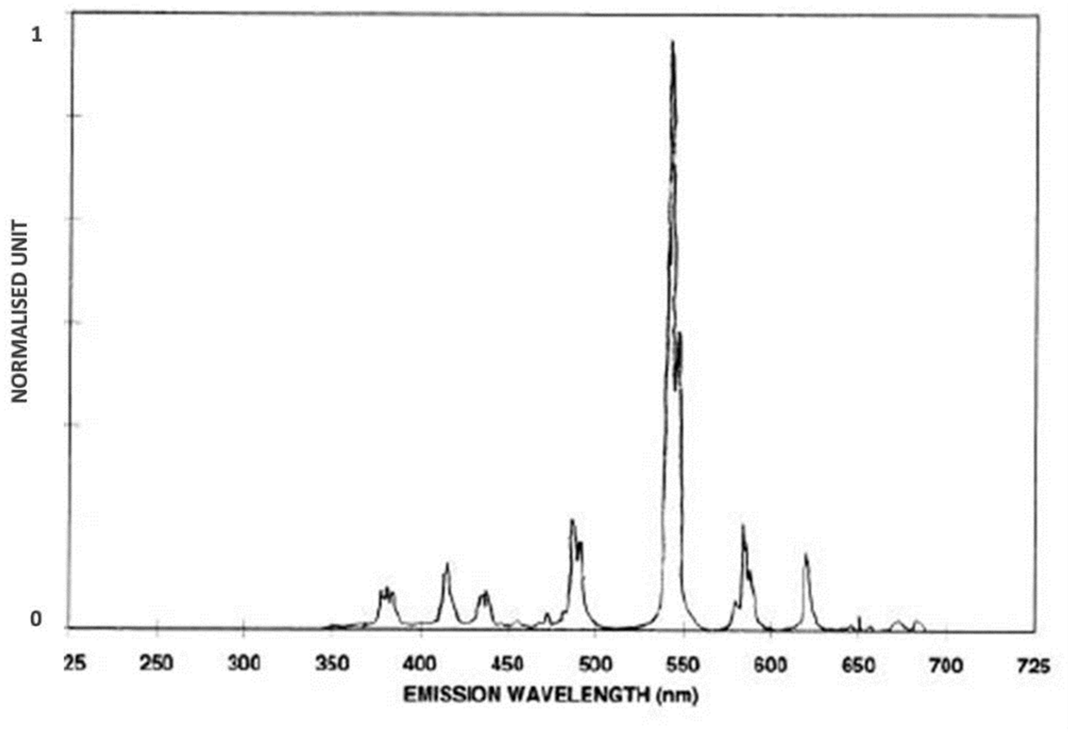

Figure 22 Lanex Spectral Emission

The emission spectrum can be integrated numerically to get an estimate of the light photons emitted and to calculate the matching with the spectral response of the CCD. This process will be shown for the types of scintillators adopted in chapter 5.

The analytical model to calculate the number of photons emitted by the scintillator, G_{Screen}, should follow the approach as in Hejazi et al. (1997):

$$G_{Screen} = \left(\frac{\int \frac{dQ(E)}{dE} \cdot \alpha(E) \cdot dE}{\int \frac{dQ(E)}{dE} \cdot dE} \right) \cdot \left(\frac{\int \frac{dQ(E)}{dE} \cdot \alpha(E) \cdot g(E) \cdot dE}{\int \frac{dQ(E)}{dE} \cdot \alpha(E) \cdot dE} \right) \tag{3.1}$$

Where $dQ(E)/dE$ is the X-ray energy spectrum as a function of energy E and so the first term corresponds to the absorption of the scintillator screen and the second term is the number of photons emitted per interacting X-ray; G_{Screen} can be considered to be the number of photons emitted per absorbed X-ray.

The value of gain introduced is not a constant and can introduce a variation given statistically by a standard deviation around G_{Screen} +/- σ_{Screen}

The standard deviation takes into account the structure of the scintillator, in some cases the matrix of the structure, which could be eliminated in the final image by flat fielding and the statistical shot noise related to the random process of generation of the photons. Usually this latter number can be neglected given the large number of photons emitted per X-ray.

3.3.1 Neutron Radiography Systems

A similar approach from a camera system point of view can be adopted for neutron radiography. A neutron beam penetrating a specimen is attenuated by the sample material and detected by a two dimensional imaging device. Contrary to X-rays, neutrons are attenuated by some light materials, such as hydrogen, boron and lithium, but penetrate many heavy materials. Neutrons can be used to distinguish between different isotopes and neutron radiography is an important tool for studies of radioactive materials (Ambrosi, 2000).

Typical neutron radiography detectors are:

- X-ray film/converter plate assemblies
- Track - Etch films
- imaging plates
- scintillator / CCD camera
- amorphous silicon (a-Si) or flat panel detectors

Neutrons behave differently depending on the energy they carry and can be distinguished as follows:

- Thermal neutrons are neutrons with kinetic energy related to the temperature of their surroundings with kinetic energy of around 0.025 eV.
- Neutrons with sufficient energy to be transmitted through a cadmium foil are called epithermal neutrons and have kinetic energies from 0.5 eV to 10 keV.
- Fast neutrons have energies above 10 keV.
- Cold neutrons have energies below around 0.005 eV.

The probability of neutron absorption in a nucleus increases with the decrease of neutron kinetic energy, explaining why thermal neutrons are usually the reference choice for neutron radiography.

Typical scintillator materials are ZnS(Ag)-^{6}LiF or ZnS(Cu)-^{6}LiF. The first step of the detection mechanism for these scintillator materials is an (n,α) reaction:

$$^6_3\mathrm{Li} + \mathrm{n} \rightarrow {}^3_1\mathrm{H} + {}^4_2\mathrm{He} + 4{,}78\ \mathrm{MeV}$$

Then these emitted α particles cause a secondary converter emission in the form of optical light photons.

Table 6 reports the most commonly used scintillator materials neutron radiography.

Material	Isotope	Abundance (%)	Reaction	Thermal Neutron Cross Section (barns)	Half Life (#)	Use (*)
LiF	Li-6	7.5	$^{6}Li(n,\alpha)^{3}H$	940	NA	D,R
H_3BO_3	B-10	19.8	$^{10}B(n,\alpha)^{7}Li$	3838	NA	D
Metal	Rh-103	100	$^{103}Rh(n,\gamma)^{104}Rh$	140	42s	D
			$^{103}Rh(n,\gamma)^{104m}Rh$	11	4.5m	D,I
			$^{103}Rh(n,n')^{103m}Rh$	--	57m	D,I
Metal	Ag-107	51.8	$^{107}Ag(n,\gamma)^{108}Ag$	37	2.4m	D
	Ag-109	48.2	$^{109}Ag(n,\gamma)^{110}Ag$	170	24.5s	D
			$^{109}Ag(n,\gamma)^{110m}Ag$	4	254d	I
Metal	Cd-113	12.3	$^{113}Cd(n,\gamma)^{114}Cd$	19,600	NA	D
Metal	In-115	95.7	$^{115}In(n,\gamma)^{116}In$	155	54m	D,I
			$^{115}In(n,\gamma)^{116m}I$	42	14s	D
Metal or Oxide	Sm-149	13.8	$^{149}Sm(n,\gamma)^{150}Sm$	42,000	NA	D
	Sm-152	26.7	$^{152}Sm(n,\gamma)^{153}Sm$	210	47h	D
Metal or Oxide	Eu-151	47.8	$^{151}Eu(n,\gamma)^{152m}Eu$	3,200	9.2h	D,I
Metal or Gadolinium Oxysulfide	Gd-155	14.9	$^{155}Gd(n,\gamma)^{156}Gd$	61,000	NA	D,R
	Gd-157	15.7	$^{157}Gd(n,\gamma)^{158}Gd$	255,000	NA	D,R
Metal or Oxide	Dy-164	28.2	$^{164}Dy(n,\gamma)^{165}Dy$	900	2.35h	D,I
			$^{164}Dy(n,\gamma)^{165m}Dy$	1800	1.25m	D
Metal	Au-197	100	$^{197}Au(n,\gamma)^{198}Au$	98.8	2.695d	D,I

NA in those cases in which emission used for film exposure is "prompt" or emitted immediately after neutron interaction
* D (Direct) - screen and film together during neutron exposure
I (Indirect or Transfer) - screen exposed without film in the neutron beam and then transferred to the film after exposure
R (Real time) - screen used with an image intensifier to produce real time or CRT images

Table 6 Scintillators for Neutron Radiography

3.4 Optical Design

A camera system device that detects neutrons or ionizing radiation by light emission from a scintillator needs to be coupled optically to the emission surface of the scintillator.

Depending on the type of application the best choice in terms of resolution and sensitivity needs to be selected.

Three different approaches can be followed:

1. Direct coupling of the scintillator to the CCD
2. Lens coupling
3. Fibre optic coupling

The first approach can be used in situations in which the radiation of interest would not disturb the light photo-electrons or whose energy could be well separated by the visible energy collected by the CCD, e.g. it would not be recommended for neutron detection in case of direct impact of neutrons on the CCD. This approach would give the best efficiency and is widely adopted for gamma rays (Bugby et al., 2016). The disadvantage is the high cost of implementation and the possible application in space environment could be problematic for the type of glues usually used for direct contact to the CCD.

In the case of lens coupling, the collection of light from a scintillating screen in the form of a Lambertian source can be expressed as (Swindell, 1991):

$$\eta_L = \frac{T_L}{1 + 4 \cdot F_{\#}^2 \cdot (1+m)^2} \tag{3.2}$$

Where $F_{\#}$ is the *f* number of the lens, m is the demagnification factor and T_L is the transmission factor of the lens.

The advantage is the low cost and readiness of implementation. It also gives more flexibility in terms of field of view, which is especially useful in prototyping the design of the camera. For this reason it is the choice adopted in the work presented.

The emission of photons from a panel with Lambertian source can be expressed for a tapered fibre optic bundle as a mean for collecting photons on the CCD detector by the transmission efficiency, η_{TF0}, as (Kapany, 1967):

$$\eta_{TF0} = \left(\frac{1}{m}\right)^2 \cdot \left(\frac{\left(n_2^2 - n_3^2\right)^{1/2}}{n_1}\right)^2 \cdot T_F \cdot \left(1 - L_R\right) \cdot F_c \tag{3.3}$$

Where n_1, n_2 and n_3 are the refractive indices of the source medium, the fibre core and the cladding, respectively. Also m is the demagnification factor and T_F is the transmission of the fibre core, L_R represents losses due to Fresnel reflection and F_c is the fibre core fill factor.

The two equations above are plotted in Figure 23 for comparison as a function of the demagnification factor m. It can be seen that the fibre optic approach gives around 6 to 8 times higher coupling efficiency.

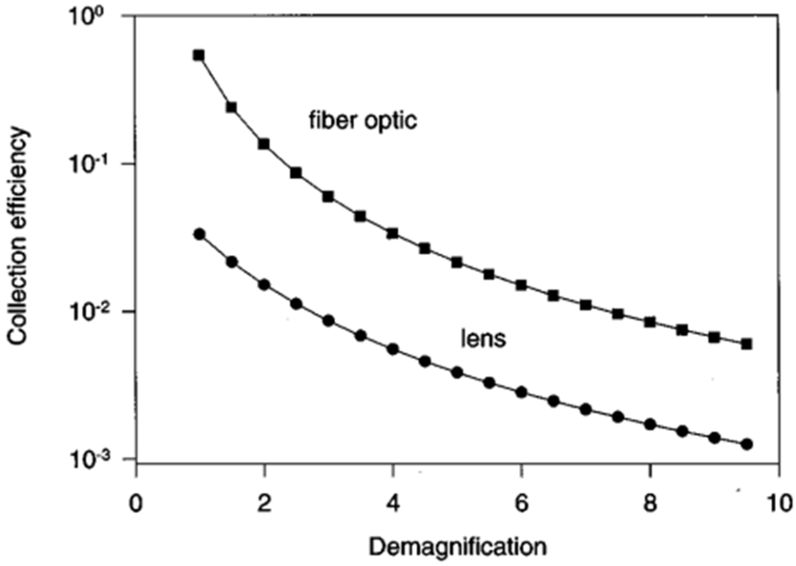

Figure 23 Fibre Optic and Lens Coupling Efficiency

Despite the high costs of implementation, fibre optic coupling would be the optimal solution in a final revision of the presented project.

As mentioned above the lens coupling method is the one adopted for the presented work and illustrated in Figure 24.

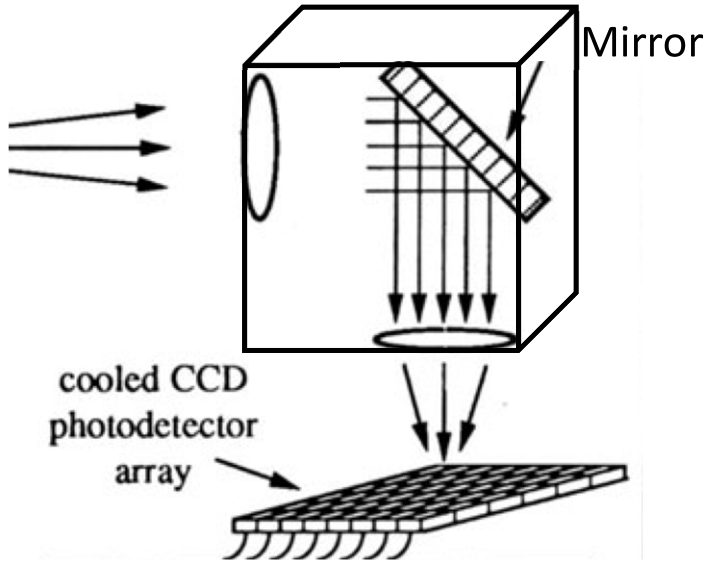

Figure 24 Lens Coupling Scheme

An L shaped black box of plexiglass was realised containing the frame to support the scintillator and the opening for the camera head. At the centre of the box a mirror was placed, which directed the light at an angle of 90° to the lens.

The lens is in C mount format, which required particular attention in the process of obtaining the right focusing distance from the flange to the CCD image plane of 17.52 mm. The lens chosen, which is easily changeable, is a Pentax 25 mm $F_{\#}$ 1.4 and given the distance from the lens to the scintillator of 180 mm, gives a measured demagnification factor of m = 6.83. A transmission factor for the lens of around 0.95 was considered, assuming negligible the optical absorption from the mirror.

In Figure 25 the blackout box made of black plexiglass is shown whose internal walls have been completely covered by special black velvet to avoid internal scattering of light. It is also possible to see on the left the X-ray tube whose rays impact on a wheel target to generate secondary fluorescence, the vacuum chamber for X-ray propagation, the liquid nitrogen tank and the vacuum pump attachment for the camera.

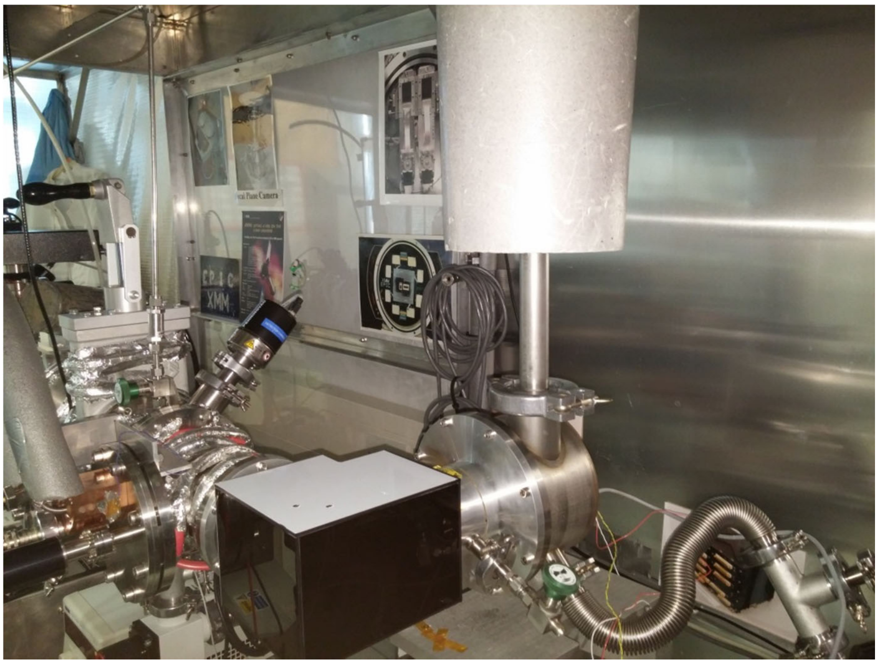

Figure 25 Laboratory Test Environment

3.5 CCD Detectors

A CCD is composed of a matrix of MOS capacitors formed by gate electrodes structures separated by silicon channels of different doping polarity and by a thin oxide layer. During the charge collection period a potential well is generated below each MOS structure that becomes a sink for any locally photo-generated electric charge. The amount of charge stored depends on the intensity of light incident on the CCD surface and exposure time. Charge packets are transferred, one row at a time, by a sequence of image parallel clocks from the image area to a storage area, in case of frame transfer device as shown in Figure 26, and subsequently each row is transferred by applying a sequence of storage parallel clocks into a serial register.

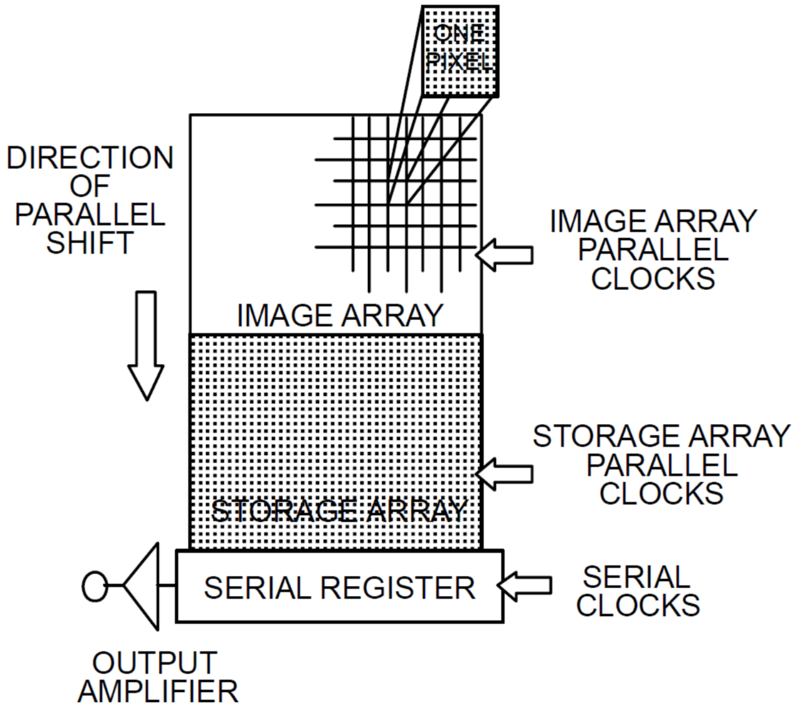

Figure 26 Frame Transfer CCD

The charge is then transferred to an output node by applying a sequence of serial clocks to the serial register. The signal at the output of the CCD can be considered as a sequence of voltage values corresponding to a discrete mapping of the photon distribution over the active area of the CCD.

To increase the performance of sensors in low light conditions, CCDs with avalanche multiplication in the serial register were introduced by Texas Instruments (Hynecek, 2001) and e2v (Jerram et al., 2001). An EMCCD features an extended serial register as shown in Figure 27, known as a multiplication register, where a gain process by avalanche multiplication is applied in the charge domain prior to the charge to voltage conversion.

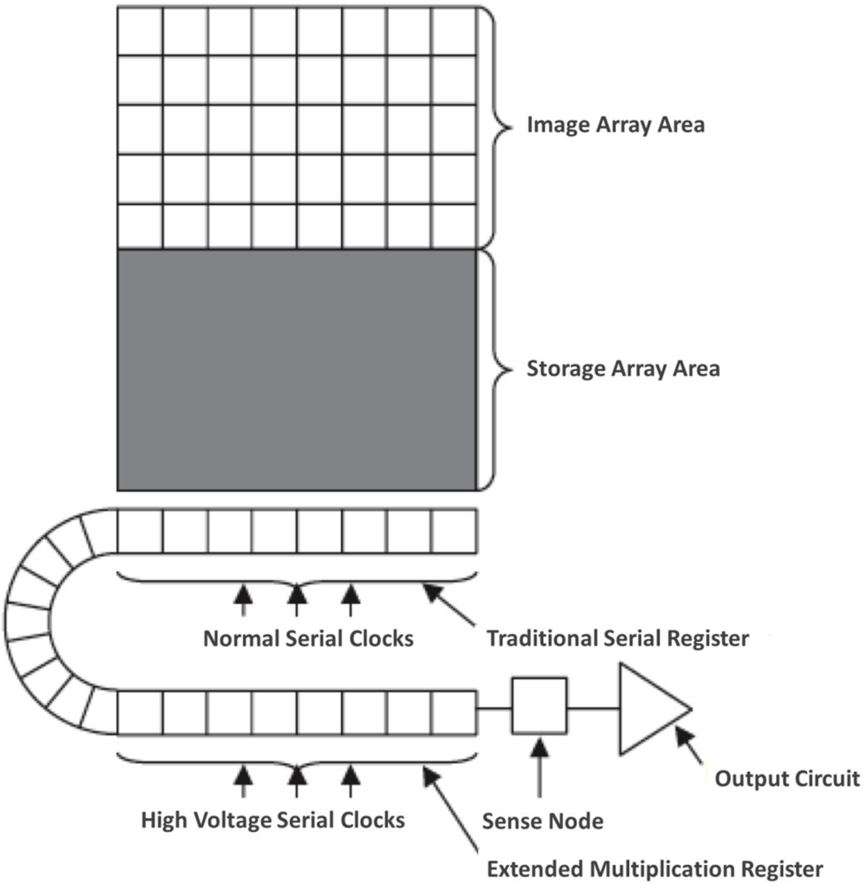

Figure 27 Electron Multiplying CCD Structure

Electrons are accelerated from pixel to pixel in the multiplication register by applying high voltage serial clocks, in the CCD97 are applied via the signal RØ2 HV, which are related to the timing of the second phase RØ2 of the standard serial register. Accelerated electrons reaching sufficient energy generate secondary electrons via an impact-ionization process. The multiplication gain M is function of the secondary-electron generation probability, g, and the number of pixels, N, in the multiplication register and can be expressed as:

$$M = (1+g)^N$$

Adopting EMCCD technology is particularly useful for low level incident flux, offering a sub-electron readout noise, with disadvantages for photometric applications, because of the stochastic multiplication process, and for applications requiring high spatial resolution, because of the spreading of charge between adjacent pixels of the multiplication horizontal register during the multiplication process and horizontal transfer of the charge.

To increase the detection efficiency of the device a number of different approaches have been adopted by manufacturers such as suppression of thermal noise via inverted mode operation, back thinned illumination, tri-level voltage operation for parallel clocks, and mini-lenses above the photo collection diodes. Of particular importance in terms of performance is the quantum efficiency (QE) of the device to the radiation spectrum.
Figure 28 shows a CCD97 mounted on the camera head with the PRT attached to one side of the sensor.

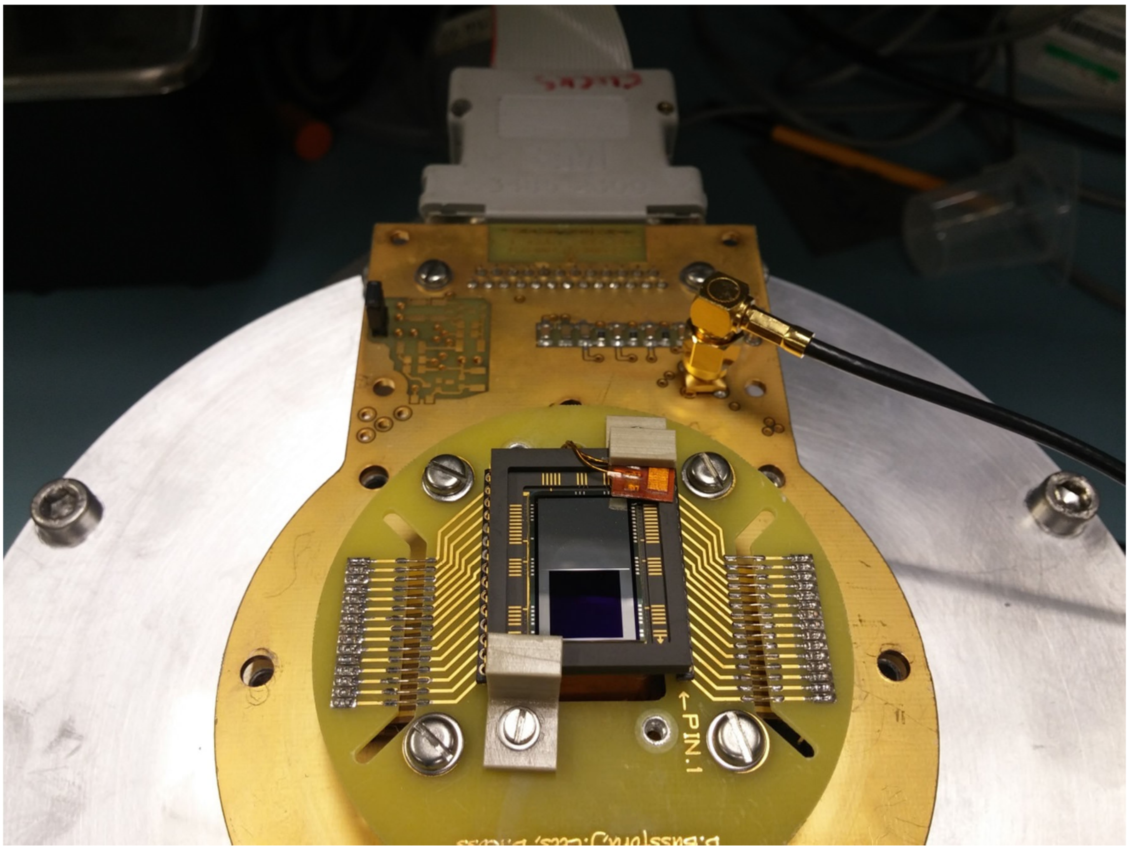

Figure 28 CCD Sensor Camera Head

3.5.1 Quantum efficiency

Quantum efficiency is a measure of the fraction of the number of incident photons that generate signal charge within the CCD, expressed as a percentage. The $QE(\lambda)$ is presented as a graph of values measured over a broad range of wavelengths, termed the spectral response. Figure 29 shows the CCD97 QE.

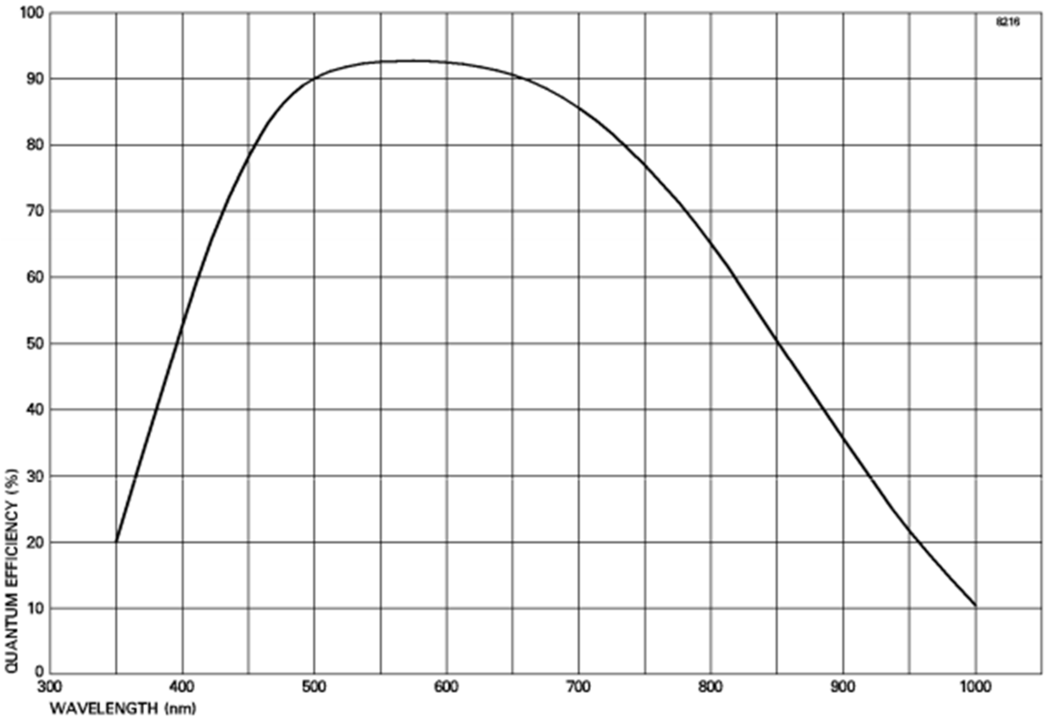

Figure 29 CCD97 Quantum Efficiency from e2v

Typically a value of around 50% is common for front illuminated CCD. The CCD97 reaches values in the order of the 93% in the green region of the spectrum. Difference due to the presence of MOS gates at the front of the CCD that limit incident light absorption. The spectrum together with the photon spectra of emission of the scintillator give a matching efficiency expressed as:

$$\eta_{CCD} = \left(\frac{\int \frac{d\theta(\lambda)}{d\lambda} * QE(\lambda) * d\lambda}{\int \frac{d\theta(\lambda)}{d\lambda} * d\lambda} \right) \tag{3.4}$$

3.5.2 Signal Measurement

The stored charge is converted to a voltage at the end of the serial register by means of a capacitor formed by an area of n+ silicon; the conversion is represented by a gain G_{ccd}

expressed in µV/electron This capacitor is reset between one pixel charge and the next by the reset voltage pulse Φ_R to a reference voltage V_{RD}.

The output circuit comprises a MOSFET amplifier and reset FET that are connected to the output node capacitance. The potential applied to the gate by the charge stored in the output node capacitor controls the flow of electrons from the source to the drain potential. The output circuit of the CCD97 is shown in Figure 30

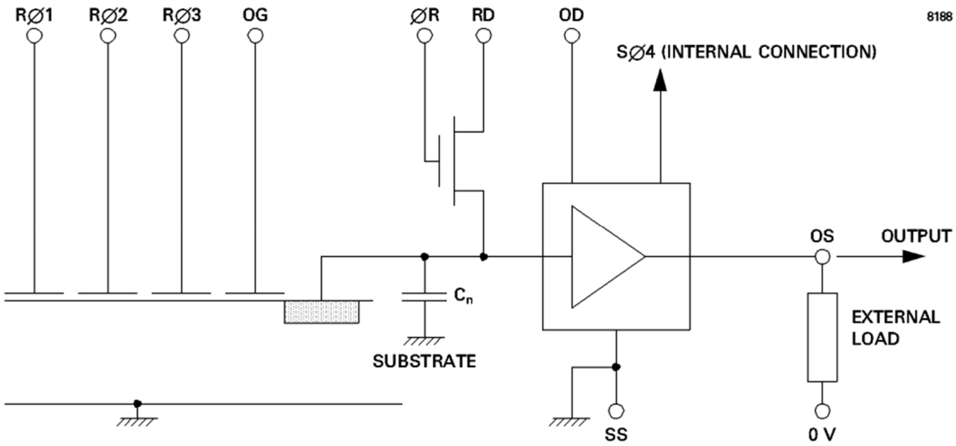

Figure 30 CCD97 Output Circuit

The gate of the reset FET induces a feed-through, because of the capacitive coupling with the output circuit, disturbing the output waveform. It is not the only capacitive coupling among the inner structures of a CCD but reset feed-through is the one with the greatest amplitude onto the CCD output. A reset settling time is necessary to avoid sampling the reset voltage during the transient period. In Figure 30 a line DC restore signal internal to the device is also indicated by the SΦ4 phase.

3.5.3 Noise Sources

Dark current and reset level noise are the two major contributors to the noise, both of which must be minimised for good performance. Other important noise sources are shot noise, given by the nature of arrival of photons, and in the case of avalanche multiplication devices the excess noise factor. At very low temperature clock induced charge (CIC) also becomes important and at very low average signal level the intrinsic Fano factor becomes important (Janesick, 2007).

In summary, a list of possible noise sources is as follows:

- Shot Noise
- Dark Current
- Reset Noise
- Excess Noise Factor
- Cosmic rays
- Pixel Non-Uniformity or Fixed Pattern Noise, namely the variation in the output between pixels when a uniform input is applied.
- Fano Noise
- On-Chip CCD Read Noise
- Off-Chip CCD Camera Noise
- Electronic Interference

Some of them of particular interest are explained below; an exhaustive explanation is presented in Janesick (2001).

3.5.3.1 Shot Noise

The nature of the arrival of photons in time is the intrinsic reason for shot noise. Every photon is an independent event and is a random event; the probability of a photon's arrival is governed by a Poisson distribution. Detection of a small number of photons is shot noise limited, although if working directly with X-rays the lower intrinsic limit is given by the Fano noise at soft X-rays energies. Collecting more photons with longer exposure or summing up more images can reduce this noise. Shot noise, σ_{Shot}, is given by:

$$\sigma_{Shot} = (N_s)^{1/2} \tag{3.5}$$

Where N_s is the number of photo-electrons detected.

3.5.3.2 Dark Current

Brownian motion can excite electrons into the conduction-band of a silicon atom and is termed ‘dark current’. This charge cannot be distinguished from the photo-generated signal charge, so cooling systems are needed to mitigate the generation of dark current. Its effect in terms of noise can be considered as a Poisson noise contribution.

Q_d is the dark charge per unit time t per pixel, T_{int} is the frame integration time giving an expression for the dark current, σ_{Dark}, as follows:

$$\sigma_{Dark} = (Qd \cdot T_{\text{int}})^{1/2} \tag{3.6}$$

The dark current can be estimated analytically following the thermal agitation driven by Boltzmann statistics in semiconductors (Janesick, 2001) to have a dark signal per pixel per second (electron/pix·s) expressed as:

$$D[electron/(pix \cdot s)] = \frac{C \cdot J_D \cdot T^{1.5} \cdot E^{-\frac{E_G - E_T}{2 \cdot K \cdot T}} \cdot A_{Pix}}{q} \tag{3.7}$$

With a value of the current density J_D equal to 10 pA/cm^2 and considering the variation of the bandgap energy E_G with temperature T and a pixel area A_{Pix} for the CCD97, the dark current per pixel can be evaluated at -70 C° to be 0.0016 electron/(pix·s).

This value is consistent with experimental results as for example in the Princeton Instrument camera (ProEM-HS, 2016).

3.5.3.3 Excess Noise Factor

Excess noise factor is the additional noise introduced by avalanche multiplication CCDs because of the statistical nature of the multiplication gain in the extended serial register. An excess noise factor F can be expressed as (Hynecek, 2001):

$$F^2 = \frac{\sigma_{out}^2}{M^2 \cdot \sigma_{in}^2} \tag{3.8}$$

Where M is the mean gain and σ^2_{in} and σ^2_{out} are the variances of the input and output signals. The impact of the excess noise factor on the system gain and noise is shown in paragraph 3.6.

3.5.3.4 Reset Noise

Reset noise, σ_R is caused by the Johnson noise in the reset FET. The signal charge packet of a pixel is added to the reset level held in the output node during the serial clocking operation. Therefore both the reset level and 'clocked' signal level contain exactly the same reset noise component. The same KTC noise can be generated by a low pass RC filter; as explained in the previous chapter this noise, in the subtraction of the pixel charge value from the reset, can be eliminated by correlated double sampling (Janesick, 2001).

3.5.3.5 Cosmic Rays

Heavy ions and high energy protons from the Sun and other celestial sources that interact with the Earth's stratosphere generating secondary particles as well as secondary radiation from nuclear reactions from spacecraft parts generate cosmic rays that can be observed by the CCD (Janesick, 2001).

3.6 System Gain Model

Following the same process as described in chapter 2 for the gain of the electronic system, an overall parameter that describes the system gain can be given.
Considering all the efficiencies and gain introduced in the preceding paragraphs the overall system gain G in ADC counts per X-ray can be expressed as:

$$G = M \cdot G_{CCDL} \cdot G_{sys} \cdot \eta_L \cdot G_{Screen} + / - \sigma \tag{3.9}$$

$$\sigma = M \cdot \sqrt{(G_{sys}{}^2 \cdot F^2 \cdot \sigma'^2 + \sigma_{ADC}^2 / M^2 + \frac{\sigma_{Read}^2}{M^2})} \tag{3.10}$$

$$\sigma' = \sqrt{(G_{CCDL}{}^2 \cdot \eta_L{}^2)(G^2{}_{Screen} \cdot Q + Q^2 \cdot \sigma_{Screen}^2) + \sigma_{Dark}^2} \tag{3.11}$$

Where Q is the number of X-ray events, G_{Screen} can be defined as the number of visible photons per detected radiation event and σ^2_{Screen} is the statistical noise introduce by the scintillator. M is the multiplication gain of the EMCCD as previously introduced and F is the excess noise factor, which is $\approx \sqrt{2}$ for $M > 10$ (Robbins et al., 2003).

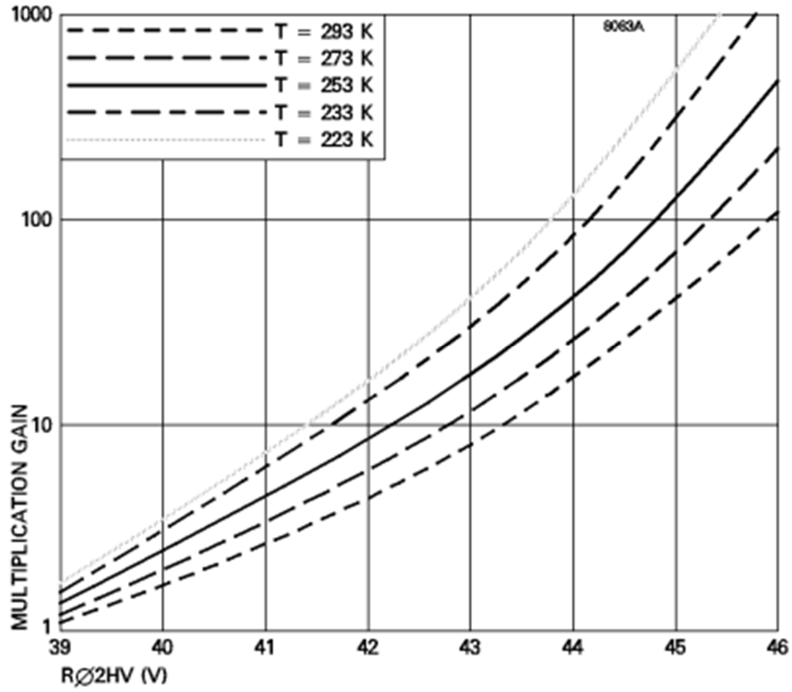

Figure 31 Multiplication Gain

Figure 31 features the variation of the multiplication gain M with the high voltage serial register clock and its dependence with temperature.

It is important to highlight the presence of the multiplication noise F and multiplication gain M in the system gain expressions as this reduces drastically the readout noise. The effective signal level can be assumed to be equal to the signal leaving the image region of the CCD and so the effective readout noise is reduced by the multiplication gain.

4. Camera Electronic Simulation and Characterisation

4.1 Introduction

Simulation of the electronic performance of CCD camera electronics is a fundamental tool to forecast the impact that different design approaches can have on the overall system performance.

The aim of this chapter is to present a characterisation model of the noise of the single electronic modules in the system as described in the previous chapter and of the CCD sensor performance not only as a static computational model of the noise but to unify its frequency domain characterisation with a time domain noise analysis.

Relying upon a static model of a CCD sensor as introduced in Konnik et al. (2014), a time domain model of the CCD sensor and of its readout electronics has been developed allowing simulation of the amplified waveform from the sensor, corrupted by noise sources, and to assess the performance of several readout processing methods.

The model allows investigation of the impact that different noise sources have on the performance of CCD readout methods and to assess the performance of noise reduction algorithms. The developed model is necessary to drive the design criteria of the system.

Firstly, a noise mathematical model of the amplifiers and filters for the analogue chain of the digital readout electronics is introduced and compared with Spice simulation. Secondly, a time domain noise method is introduced which is adopted to build a time domain model of the CCD camera system, comparisons of the readout performance with the corresponding analogue domain processing methods are shown.

Finally, the characterisation of the CCD camera system based on the e2v CCD97 by means of photon transfer curve theory is presented.

4.2 Circuit Noise Model

The operational amplifiers presented in the previous chapter have been modelled in their non-inverting configuration and single ended to fully differential for the THS 4131 amplifier.

In the presented analysis, the contribution from the ADC AD7760 and its on chip fully differential amplifier have not been modelled but their impact has been assessed experimentally by measurement of the standard deviation of the voltage in Data Numbers (DN) units, short circuiting the ADC inputs, with a value of σ = 51 DN units of ADC equivalent to 32 µV. A partial plot is shown in Figure 32.

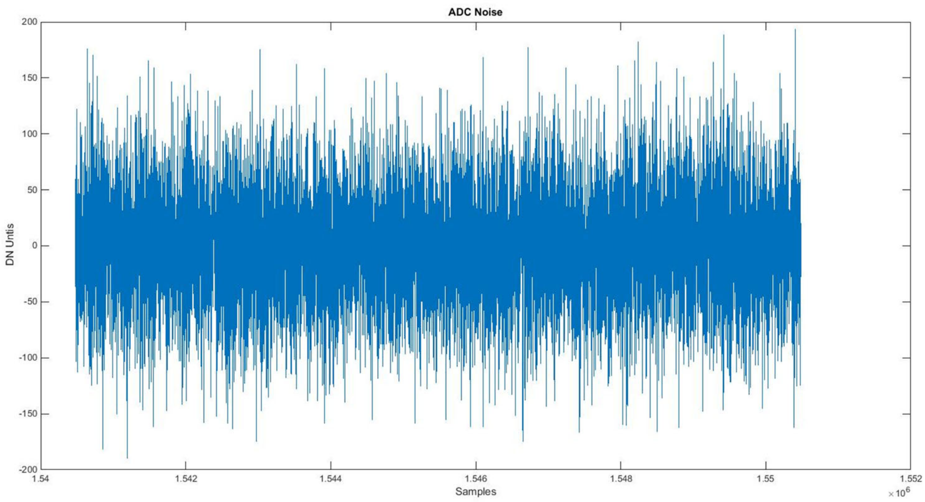

Figure 32 ADC Noise Contribution

In the same way, the noise contribution due to power supply noise has not been considered in the discussion given the high value of Power Supply Rejection Ratio (PSRR) and the use of linear drop regulators.

The open loop gain transfer function for the operational amplifiers has been modelled as a two pole model (Franco, 1990) and its behaviour included in the closed loop transfer equation:

$$H(f) = \left(1 + \frac{Z_2(f)}{R_1}\right) \cdot \left[\frac{1}{1 + \left(\frac{1}{A(f) \cdot \beta(f)} \right)} \right] \tag{4.1}$$

Where *A(f)* is the open loop gain and *β(f)* is the so called noise gain and $Z_2(f)$ is the feedback impedance.

A different approach has been followed for the fully differential amplifier THS4131 being considered as two inverting amplifiers and is shown later.

The parameters for the amplifiers have been deduced from datasheets and, especially for the second pole definition, by the available Spice model. The operational amplifier noise generator parameters, namely the *K* and *C* constants to express respectively the flicker and white noise components of the voltage and current power spectral densities, have been derived from datasheet values using the method described in SLVA043B (2007).

Table 7 summarises the findings.

Amplifiers	**Flicker Noise K_V (V^2)**	**White Noise C_V (V^2/Hz)**	**Flicker Noise K_I (A^2)**	**White Noise C_I (A^2/Hz)**
AD829	147.5e-18	2.89e-18	114.4e-24	2.25e-24
AD8065	143510e-18	49e-18	Not Applicable	0.64e-30
THS4131	576e-18	1.69e-18	314.9e-24	1e-24

Table 7 Noise Amplifiers

Where the parameters follow the well-known expression for spectral noise density:

$$V_n(f) = C_V + \frac{K_V}{f} \tag{4.2}$$

expressing the white noise component and flicker noise component, similarly for current noise generators.

The amplifier noise model follows the schematic shown in Figure 33, showing the noise current sources on each input and the contribution from the thermal current of the resistors.

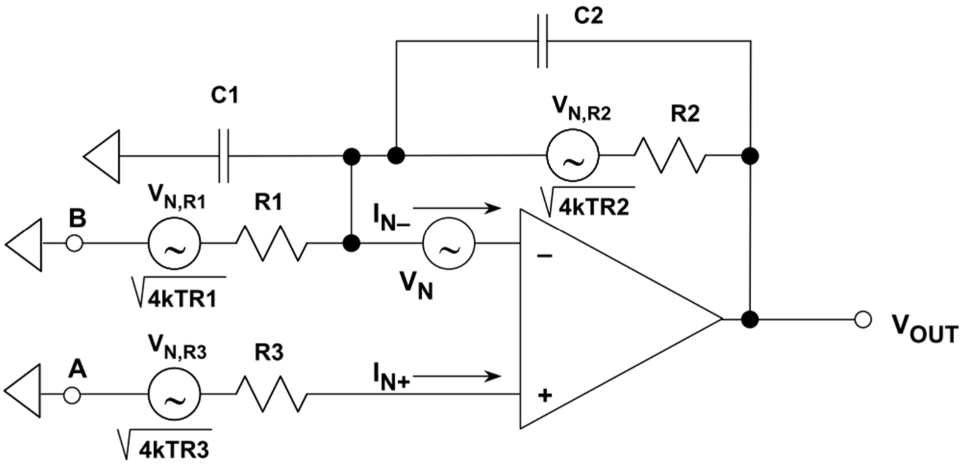

Figure 33 Amplifier Noise Generators (MT-050, 2008)

The actual circuit for the digital processing of the CCD signal presented in chapter 3 is more complicated as it requires consideration of the high pass behaviour of the filter in front of the AD829 and AD8065 as shown in Figure 34, as well as the noise introduced by the network itself.

Figure 34 shows the AD829 front-end network with thermal noise generation due to the resistors.

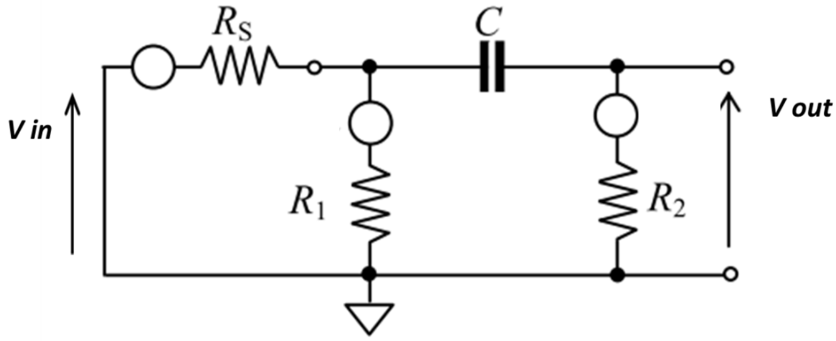

Figure 34 High Pass Input Circuit

R_s would represent the CCD R_{out} resistor assumed to be 250 Ω.

The noise introduced by the network is expressed by $PSD_{HighPass}(f)$, power spectral density (PSD), and it can be shown to be (Serrano-Finetti et al., 2014):

$$PSD_{HighPass}(f) = 4 \cdot K \cdot T \cdot \left[R_S \cdot |H_{Pass}|^2 + R_1 \cdot |H_1|^2 + R_2 \cdot |H_2|^2 \right] \quad (4.3)$$

Where H_{Pass} is the transfer function of the high pass circuit, which is a function of frequency, as seen from the left input to the output, namely the op-amp non-inverting input of the AD829. H_1 and H_2 represent the transfer functions seen by R_1 and R_2 respectively to the output of the network.

The transfer function H_{Pass} in the Laplace domain can be shown to be (Gray Meyer, 2001):

$$H_{Pass}(s) = \frac{s \cdot R_2 \cdot C}{(1 + \frac{R_s}{R_1}) \cdot (1 + s \cdot \tau)} \quad (4.4)$$

Where $s = j \cdot \omega$ and $\tau = C \cdot (R_2 + \frac{R_1 + R_s}{R_1 \cdot R_s})$

Similar expressions have been derived for H_1 and H_2.

Interesting to note is that the behaviour in terms of added noise of an AC coupled amplifier, as described in Serrano-Finetti et al. (2014) and in Vargas et al. (1994), compared to the case of a DC coupled amplifier is that it could be minimised by setting the F_L high pass frequency of the signal at a later stage other than the front-end amplifier because of the additional noise introduced by the high pass network and current noise generator.

The main point stands in the different frequency transfer function seen by the signal and current noise generator. Summarising the results from the two above mentioned papers, a large ratio $K= F_L/ F_C$, with F_C the high pass cut frequency determined by the front-end network and F_L the high pass band of the signal, demonstrate that relatively large K values yield a total noise closer to the noise floor of a DC coupled amplifier, allowing bipolar op-amps to achieve lower noise than FET amplifiers despite the higher current noise, assuming that the value of resistor R_1 allows proper biasing of the bipolar amplifier as in the AD829. In the actual circuit the ratio K is far from achieving a factor higher than the unity because of the high input impedance of the FET amplifier; the front-end bipolar transistor amplifier AD829 in the camera head is part of the head electronics and its elimination from the circuit would have been difficult, otherwise a better approach would have been to directly interface the CCD with the FET op-amp using an adequate high pass network interface.

The high pass behaviour of the circuit is shown in Figure 35 and the marked point shows a value close to the F_{-3dB} point at around 3 Hz.

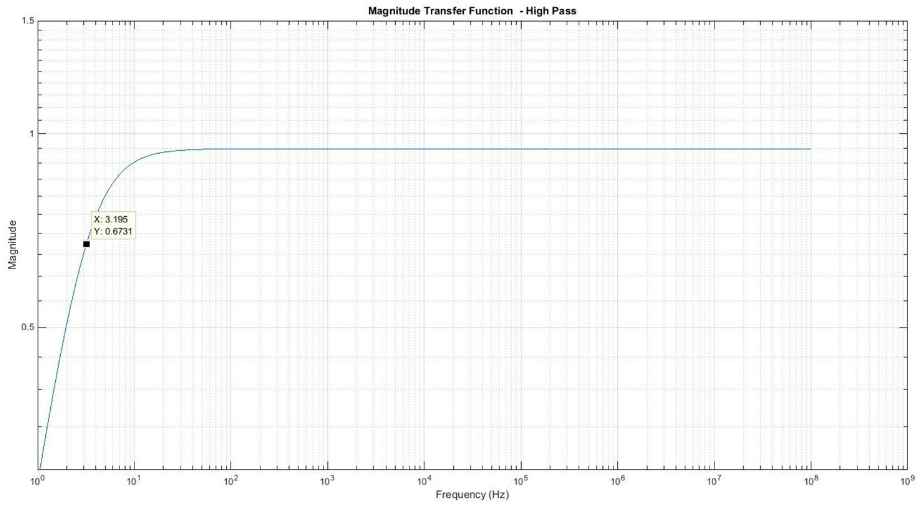

Figure 35 High Pass Input Front-End Transfer Function

The overall noise introduced by the first amplifier in the chain, using the theory as explained in Motchenbacher (1993), can be shown to have a PSD of:

$$PSD_{AD829}(f) = |H(f)|^2 \cdot [PSD_{HighPass}(f) + V_n(f) + |Z_S(f,R_4,C_4,R_3)|^2 \cdot \frac{4 \cdot K \cdot T}{R_3} + \\ + |Z_S(f,R_4,C_4,R_3)|^2 \cdot I_n(f) + |Z_{HpassOut}(f)|^2 \cdot I_n(f)] + |Z_P(f,R_4,C_4)|^2 \cdot \frac{4 \cdot K \cdot T}{R_4} \tag{4.5}$$

The resistors and capacitor presented in the equation corresponds to the following components of Figure 12:

- R_s= CCD R_{out} equivalent resistance
- R_1= R_{15}
- R_2= R_{16}
- C_1=C_1
- R_4=R_{19}
- C_4=C_7
- R_3=R_{18}

Where:

- $|H(f)|^2$ is the square module of the closed loop op-amp transfer function
- $PSD_{HighPass}(f)$ is the noise PSD introduced by the high pass network
- $V_n(f)$ represents the voltage flicker and white noise components introduced by the op-amp
- $|Z_S(f,R_4,C_4,R_3)|^2\cdot(4\cdot k\cdot T/R_3)$ represents the noise introduced by the gain resistor R_3 at the inverting input of the op-amp, $Z_S(f,R_4,C_4,R_3)\cdot$is the impedance of the series between $R_4//C_4$ and R_3
- $|Z_S(f,R_4,C_4,R_3)|^2\cdot I_n(f)$ represents the noise introduced by the op-amp current noise components at the inverting input
- $|Z_{HpassOut}(f)|^2\cdot I_n(f)$ represents the noise introduced by the op-amp current noise components at the non-inverting input, $Z_{HpassOut}(f)$ being the impedance of the high pass circuit shown in Figure 34 as seen by V_{out}
- $|Z_P(f,R_4,C_4)|^2\cdot(4\cdot k\cdot T/R_4)$ represents the thermal noise introduced by the feedback loop resistor R_4 low pass filtered by capacitor C_4, $Z_P(f,R_4,C_4)$ being the parallel of R_4 and C_4

A similar approach has been followed to calculate the noise introduced by the AD8065 amplifier stage and its high pass network, namely the power spectral density PSD_{AD8065}.One difference stands in the modelling of the effect of the current noise generator on the non-inverting input of the amplifier.

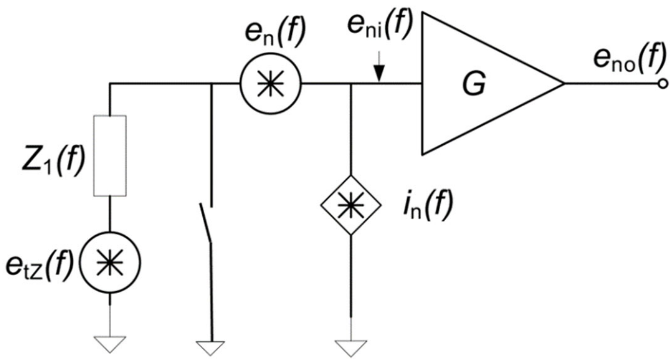

Figure 36 AD8065 Input Circuit

The presence of the switch, to accomplish to the function of DC restore, shown in Figure 36 could be considered as resetting the statistics of the current noise $I_n(f)$ and its contribution to the output noise. Such behaviour has been modelled as the transfer function seen by the current noise generator does see the $Z_1(f)$ impedance, modified by a shaping filter, $H_{Shape}(f)$, such to place a zero near the pixel frequencies of interest. In accordance with the concept that low frequency noise components have an effect on the output signal if the observation time or measurement time is higher than the inverse of the frequencies of interest of the output signal. Such shape filter in the Laplace domain can be expressed by the following equation:

$$H_{Shape}(s) = \left| \frac{s \cdot \tau_1}{(1 + s \cdot \tau_1)} \right|^2 \tag{4.6}$$

Where τ_1 can be expressed as $1/(2 \cdot \pi \cdot F_{pix})$ and F_{pix} is the readout frequency in pix·s^{-1}.

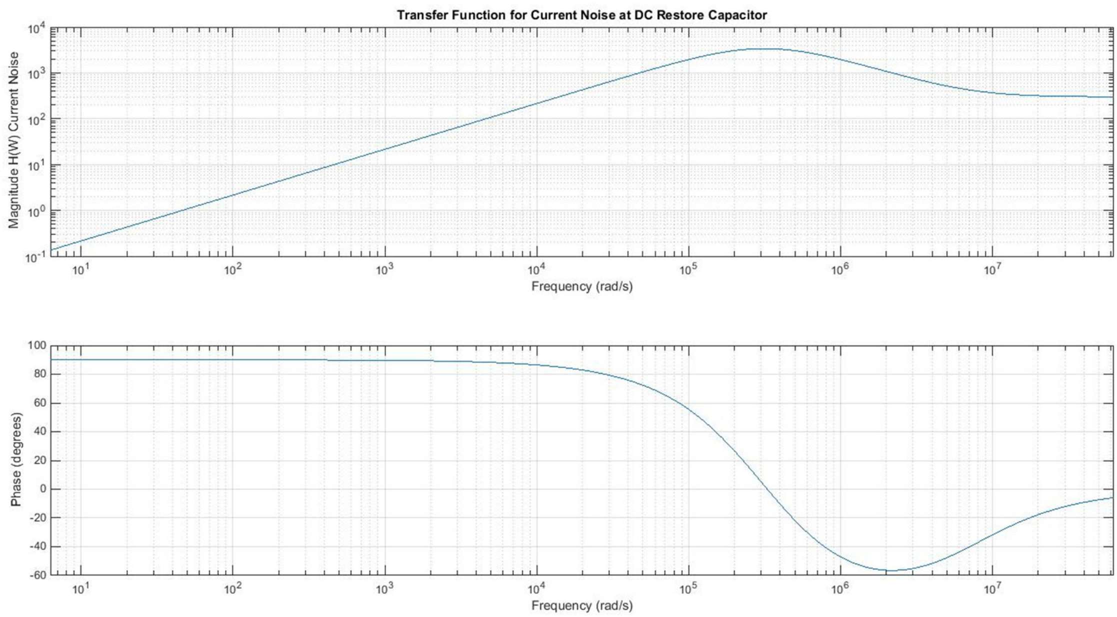

Figure 37 Transfer Function seen by Input Current Noise Generator

Figure 37 shows the magnitude of the transfer function as seen by the current noise generator.

The chain composed of the AD829 and AD8065 amplifiers has been simulated in Spice for noise analysis and compared to the results of the mathematical model implemented in Matlab. The noise PSD of the chain, $PSD_{AD829toAD8065}$, can be expressed as:

$$PSD_{AD829toAD8065}(f) = \left|H_{AD8065}(f)\right|^2 \cdot \left|H_{HPassAD8065}(f)\right| \cdot PSD_{AD829}(f) + PSD_{AD8065}(f) \qquad (4.7)$$

Where:

- $PSD_{AD829}(f)$ is the noise PSD of the AD829 amplifier
- $|H_{AD8065}(f)|^2$ is the square module of the closed loop op-amp transfer function of the AD8065 amplifier
- $|H_{HPassAD8065}(f)|^2$ is square module of the high pass transfer function in front of the amplifier AD8065
- $PSD_{AD8065}(f)$ is the noise power spectral density introduced by the second stage, similarly calculated as $PSD_{AD829}(f)$

Figure 38 shows the results from the Spice simulator, which are to be compared with the results from the Matlab simulation shown in Figure 39.

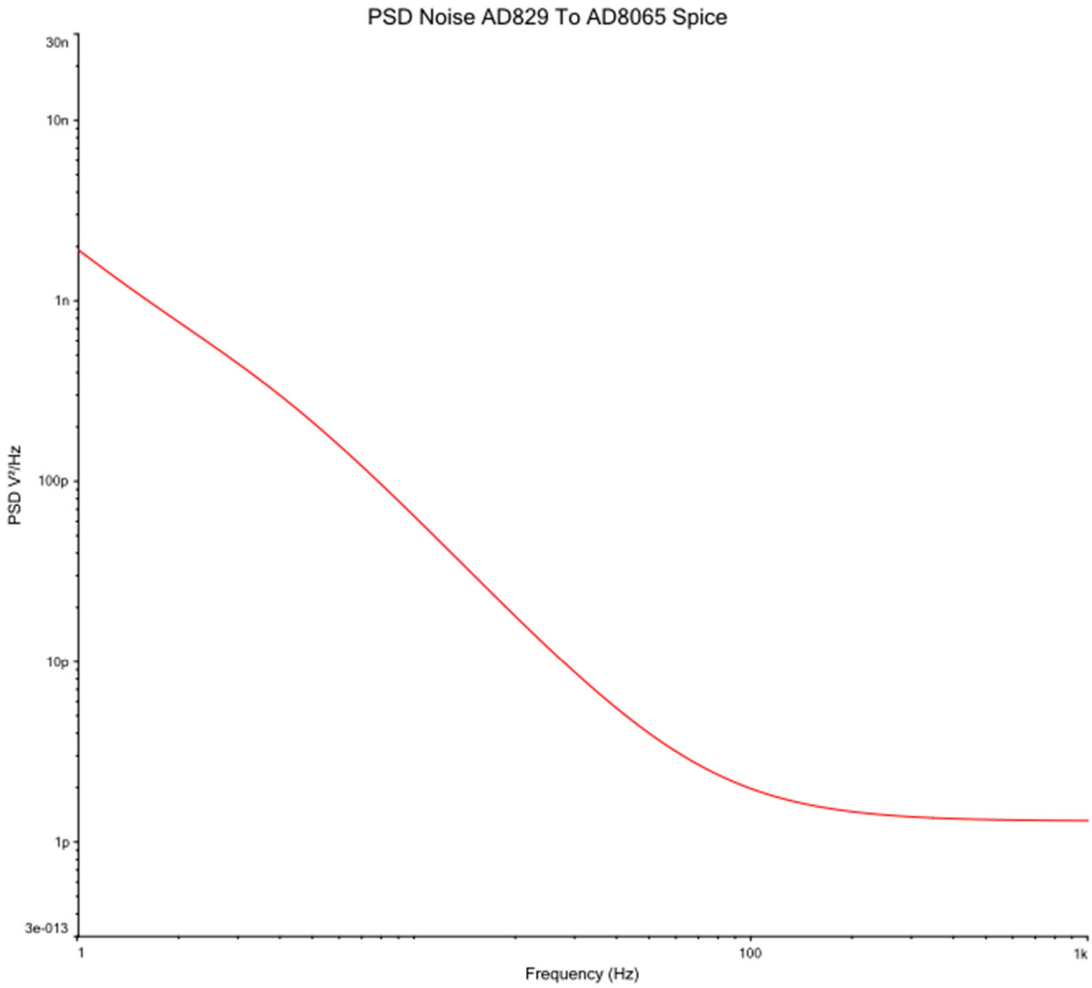

Figure 38 PSD Noise Spice Simulation

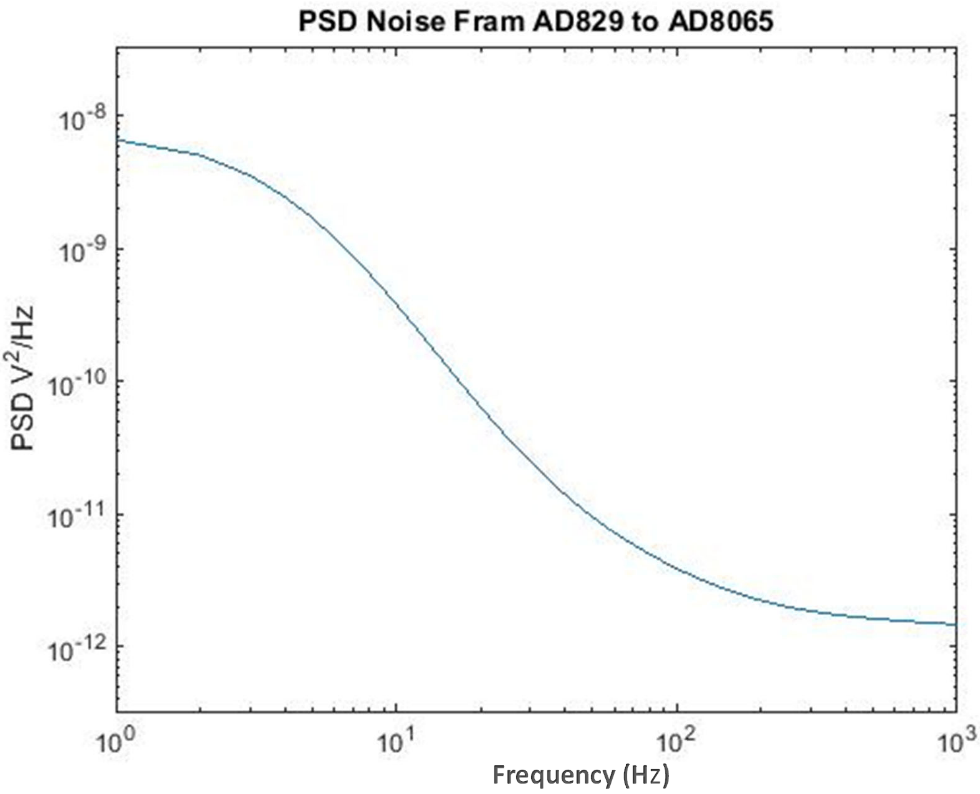

Figure 39 PSD Noise Matlab Simulation

The comparison shows that the mathematical model in Matlab gives around four times bigger values of noise PSD below the lower frequencies of 10/15 Hz, meaning flicker noise at low frequencies is better represented in Matlab compared to the Spice simulation as confirmed also in Clapp (2012). The Matlab simulation model for the flicker noise components of the amplifiers is derived by means of a shaping filter approximation method, which will be explained in the following paragraph. The shaping filter model is in good agreement with the flicker noise analytical formulation:

$$V_{n\,flicker}(f) = \frac{K_V}{f} \tag{4.8}$$

Interestingly, the calculation of the r.m.s. voltage noise, namely integrating the power spectral density in frequency, gives a very good agreement between the models.

Figure 40 shows the plot of r.m.s. voltage noise from Spice simulation.

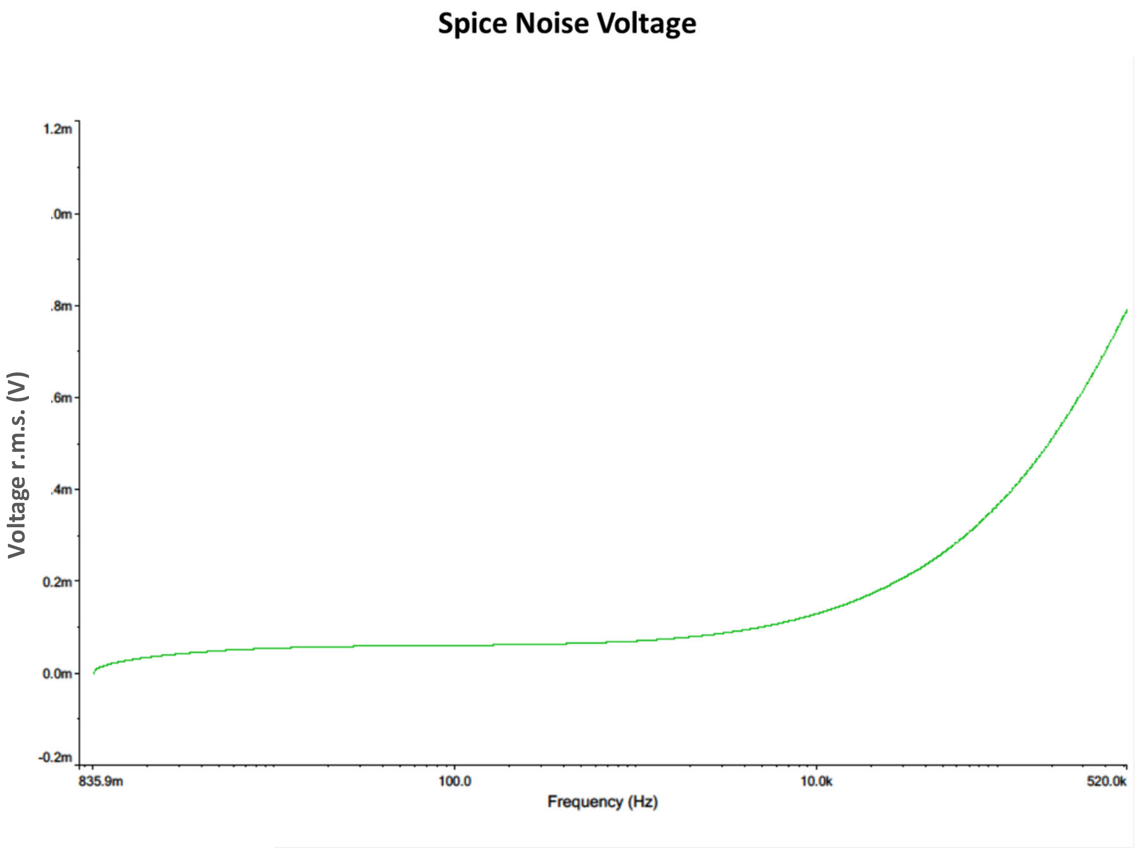

Figure 40 Spice Simulation of r.m.s. Voltage Noise

The noise at 500 kHz is close to 800 μV r.m.s. practically the same result obtained by the Matlab simulation.

The last part of the analogue chain is the single ended to fully differential amplifier, the Texas Instruments THS4131.

The noise analysis here followed a different approach considering it in principle as two inverting amplifiers, adapting the analysis as presented in SLOA054D (2002), the noise PSD introduced by the differential amplifier with the noise generators presented in Figure 41 can be calculated.

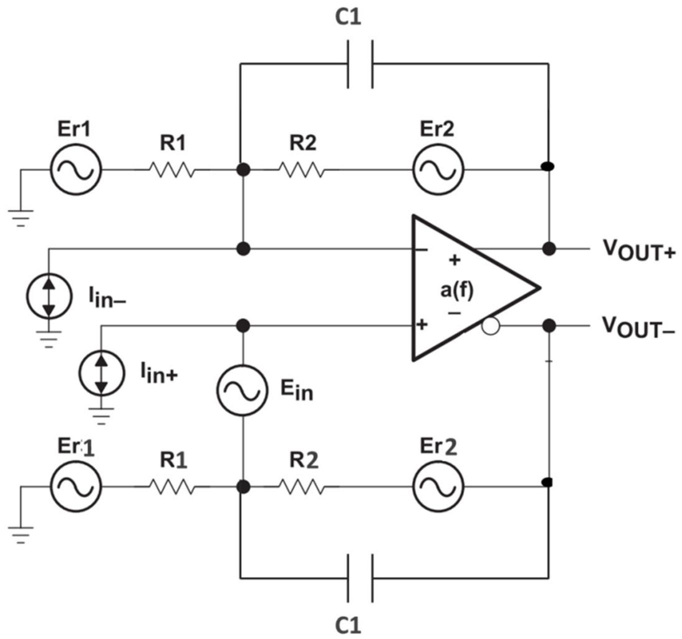

Figure 41 Fully Differential Amplifier

$PSD_{THS}(f)$ can be calculated as:

$$PSD_{THS}(f) = \left|H_{diffnoiseG}(f)\right|^2 \cdot [V_n(f) + +2 \cdot \left|Z_S(f, R_2, C_1, R_1)\right|^2 \cdot I_n(f)] + \\ + \left|H_{diff}(f)\right|^2 \cdot 8 \cdot K \cdot T \cdot R_1 + \left|Z_P(f, R_2, C_1)\right|^2 \cdot \frac{8 \cdot K \cdot T}{R_2} \tag{4.9}$$

Where:

- $H_{diffnoiseG}(f)$ is the noise gain expressed in Laplace transform as:

  $$1 + \frac{R_2}{R_1 \cdot (1 + S \cdot C_1 \cdot R_2)}$$

- $V_n(f)$ represents the voltage flicker and white noise components introduced by the op-amp
- $8 \cdot k \cdot T \cdot R_1 \cdot |H_{diff}(f)|^2$ is the thermal noise due to resistor R_1 and $H_{diff}(f)$ is the transfer function of the fully differential amplifier expressed in Laplace transform as:

  $$\frac{R_2}{R_1 \cdot (1 + s \cdot C_1 \cdot R_2)}$$

- $|Z_S(f,R_2,C_1,R_1)|^2 \cdot I_n(f)$ is the noise due to the current noise generator of the amplifier, where $Z_S(f,R_2,C_1,R_1)$ is the series between R_1 and the parallel of R_2 with C_1
- $|Z_P(f,R_2,C_1)|^2 \cdot (8 \cdot k \cdot T/R_2)$ represents the thermal noise introduced by the feedback loop resistor R_2 low pass filtered by capacitor C_1, $Z_P(f,R_2,C_1)$ being the parallel of R_2 and C_1

Finally, considering that each PSD introduced by an amplifier gets amplified by the square module of the transfer function of the successive stages, the noise PSD of the chain of the three amplifiers can be expressed as:

$$PSD_{Amps}(f) = \left|H_{diff}(f)\right|^2 \cdot PSD_{AD829toAD8065}(f) + PSD_{THS}(f) \tag{4.10}$$

4.3 Time Domain Noise Generation

To derive a model to simulate the effect of noise on the CCD signal in the time domain it is necessary to generate noise time series which conserve the spectral characteristics of the underlying noise stochastic process.

From a survey of the methods to generate noise time series, from a given power spectral density especially used in circuit simulation models at transistor level, two methods have been considered for the sake of comparison with the shaping filter method proposed in this thesis. The first method generates a noise time series from a given noise PSD spectrum through a sum of N sine-waves with arbitrary phase. Each sinusoidal component has a power equal to the area of the power spectral density in a determined frequency range, i.e. frequency bin. Analytically it can be expressed as (Fornasari et al., 2009):

$$V_{Noise} = \sum_{i}^{N} a_i \cdot \sin\left(2\pi i \frac{f_{MAX}}{N} t + \varphi_i\right) \tag{4.11}$$

Where N is the total number of sine waves chosen for the frequency decomposition, i is the specific frequency component with φ_i the relative arbitrary phase and a_i the amplitude related to the power of the frequency bin in the PSD.

A sample of the adopted Matlab code to generate the noise is reported below:

```
Area=y(1:N).*Fs/(2*N);
Ampl=Area;
Phases=2*pi*rand(1,N);
u=0:1/Fs:(2 -(1/Fs));
for i=1:length(u)
spectral_component=(sqrt(2*Ampl).*sin(2*pi*[1:N]*Fs/(2*N)*u(
i)+Phases(1:N)));
out(i)=sum(spectral_component);
end;
```

Where the variable y represents the PSD and F_s the sampling frequency, which in Matlab corresponds to the simulated number of samples per second; in the above example the noise time series has been generated for two seconds. Note that from a simulation point of view, a noise time series with a length of 2 seconds can require computational times longer than two hours.

The second method (Rudolph, 2004), usually referred to as 'whitening method', consists of creating perfect white noise by generating random phases in the frequency domain, i.e. a phasor with random phases, then multiplying it by the given magnitude of the PSD. The whitened magnitude spectrum gets inverse fast Fourier transformed and the real part represents the noise time series sought after. From a computational point of view this method is more efficient with results tested evaluating the power and power spectral estimation from the generated time series and its similarity with the starting PSD.

Research into a method to filter the CCD signal waveform to reduce noise, revealed a possible candidate would be the implementation of a Kalman filter (Brown et al., 1998) which has already been demonstrated to be a valid method to reduce specific components of long memory noise such as the flicker noise that affects for instance the global clock accuracy, in terms of jitter, in satellite navigation systems (Davis et al., 1986).

One of the steps required to define a valid dynamic model of the system is to apply a Kalman filtering algorithm to derive a matrix state-space representation of the physical system. A set of recursive filter equations needs to be derived under the assumption of white noise forcing functions and a method is required to transform non-white forcing functions, and in some cases also non-white measurement noise, to the white-sequence assumption. Such a method is referred to as the method of augmenting the state vector (Brown et al., 1998).

Such transformation can be accomplished by conceiving a shaping filter that projects a white noise PSD to the desired noise power spectral density as illustrated in Figure 42.

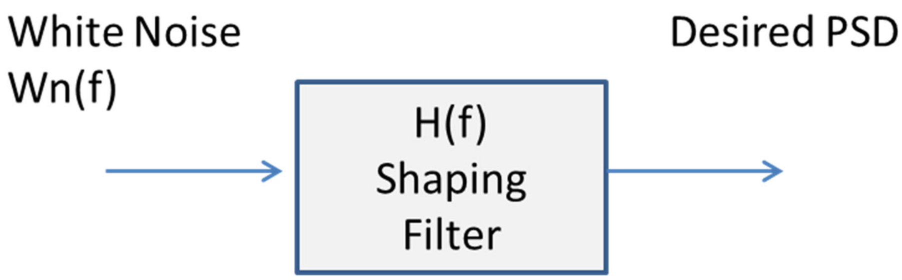

Figure 42 Conceptual Shaping Filter

The power spectral density of interest is the representation of flicker noise, expressed by:

$$PSD(f) = \frac{K_V}{f} \tag{4.12}$$

Alternatively it can be expressed as:

$$PSD(f) = \frac{W_n \cdot F_{cn}}{f} \tag{4.13}$$

Where W_n is the white noise specification and F_{cn} is the frequency corner noise (Meyer, 2001).

In the paper by Jeremy (1995) a method for discrete generation of noise time series is proposed. The discrete spectral density is found via:

$$S_d(f) = \frac{Q_d \cdot \Delta_t}{(2 \cdot \sin(\pi f \Delta_t))^{\alpha}} \tag{4.14}$$

Where $\alpha = 1$ represents flicker noise and Q_d is the variance of the input noise process of an independent and identically distributed (IID) noise sequence with autocorrelation $E_{wmwl} = Q_d\, \delta_{ml}$. The above equation, as described in the above mentioned paper, has been derived through the Z transform of discrete time transfer function $H(Z)$ of a first order Markov process generalization of a random walk.

For frequencies below the Nyquist frequency the equation can be approximated to:

$$S_d(f) \cong \frac{Q_d \cdot \Delta_t^{1-\alpha}}{(2\pi f)^\alpha} \tag{4.15}$$

The spectral density sought after is $Q/(2\pi f)^\alpha$ and hence the variance is:

$$Q_d = \frac{Q}{\Delta_t^{1-\alpha}} \tag{4.16}$$

The last equation shows how Q_d should be chosen. In the paper the filter coefficients to generate noise of the desired power law characteristics are derived in a recursive manner:

$$h_0 = 1 \tag{4.17}$$

$$h_k = (\frac{\alpha}{2} + k - 1) \cdot \frac{h_{k-1}}{k} \tag{4.18}$$

The above equations have been implemented in Matlab and the filtering process implemented by multiplication of fast Fourier transform of the filter coefficients and the white noise input sequence as shown from a sample of the code:

```
alpha = 1;
wk_sigma = qrt(2*pi*k1/2); % Generate white noise for
the sequence wk.
wk = wk_sigma * % Generate the coefficients hk.
hk = zeros(1,N);
hk(1+ 0) = 1;
for k = 1:N-1
hk(1+ k) = (k - 1 + alpha/2) .* (hk(1+ k-1) / k);
end;
hk_fft = fft(hk);
wk_fft = fft(wk);
yk_fft = wk_fft .* hk_fft;
```

The results of using this code show better representation of the noise time series to the originating PSD as the number of the coefficients h_k grow; the number of these coefficients also determines the number of generated noise time series samples.

Thinking of the realization in hardware (FPGA) of a real time Kalman filter using this type of shaping filter, in the procedure of augmenting the state in the state space matrix representation of the filter, the large number of necessary coefficients h_k in the recursive equations would pose a demanding computational cost in terms of size of matrix and relative arithmetic operations.

As pointed out in In Soo (1986) flicker noise is not decomposable into a product of arbitrary functions and according to linear system theory (Chen, 1970) the system cannot be realised by a finite-dimensional linear system. The dimension of the system must be infinite as confirmed by the above mentioned approximation related to the number of coefficients h_k. Any model of flicker noise with finite-dimension must be an approximation. The envisaged method to generate a shaping filter for flicker noise relies on the previous theoretical analysis but attempts to shape the $1/f$ spectral characteristics via a parallel combination of low pass filters, whose F_{-3dB} cut-off frequency and amplitude shapes the desired noise power spectral density. The advantage of this method is that the number of coefficients or matrix dimensions, and hence computational time, necessary to implement the filter in case of an implementation in hardware for real time processing, a necessity given the amount of data generated over the order of the GB, would be lower. The final form of the state transition matrix for the Kalman filter would benefit from an easier representation and a lower computational cost, given the diagonal structure, and the steps would be similar to the ones explained in In Soo (1986).

The shaping filter for the flicker noise $PSD(f) = \frac{K_V}{f}$ assumes the structure shown in Figure 43.

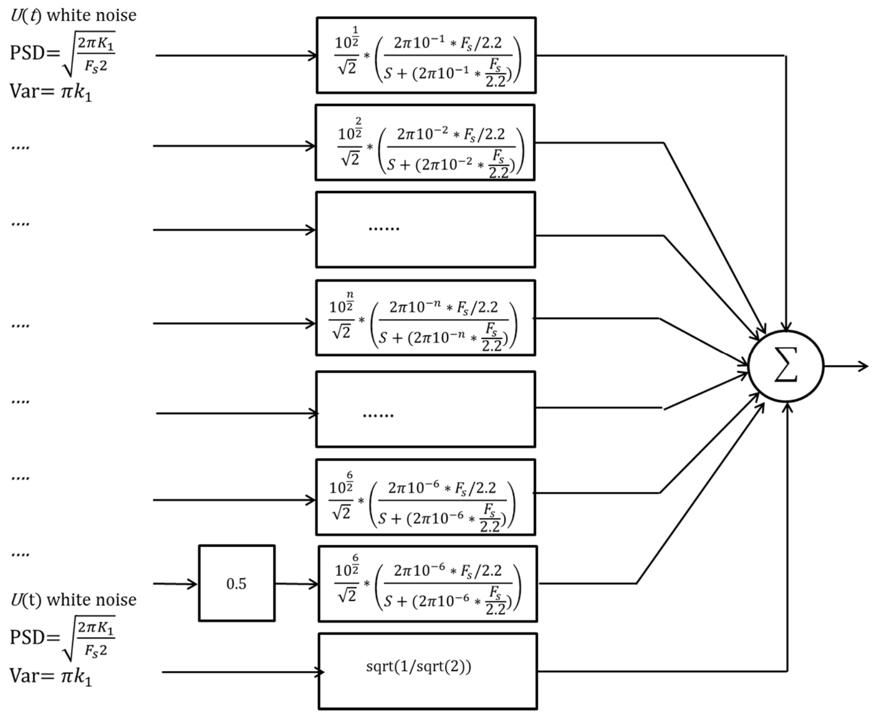

Figure 43 Shaping Filter Implementation

Where independent Gaussian noise processes are input to each filter with the following characteristics:

U(*t*) white noise

PSD= $\sqrt{\frac{2\pi K_1}{F_s 2}}$

Variance= πk_1

In agreement with the concept that if the spectral density sought after is $Q/(2\pi f)^{\alpha}$ the variance should be chosen as:

$$Q_d = \frac{Q}{\Delta_t^{1-\alpha}} \text{ for } \alpha = 1. \tag{4.19}$$

The single shaping filter transfer function $H(s)$ in the Laplace s domain has the structure:

$$H(s) = \frac{10^{\frac{n}{2}}}{\sqrt{2}} \cdot \left(\frac{2\pi 10^{-n} \cdot F_s/2.2}{S + (2\pi 10^{-n} . \frac{F_S}{2.2})}\right) \tag{4.20}$$

Where:

- n is the order
- $\frac{10^{n/2}}{\sqrt{2}}$ is the scaling factor for magnitude shaping
- F_s is the sampling frequency, which in Matlab simulation would correspond to the sampling interval of the simulated noise time samples

The number of filter elements considered was varied from n=1 to n=6, increasing the order allowing the simulation to better model the very low noise frequency components.
Comparison with the analytical equation for the noise power spectral density gives a better understanding of this relationship; remaining in the domain of the frequency the output power spectral density has been simulated for two conditions, respectively for F_s = 20 MHz and F_s = 2.5 MHz, considering the flicker noise for the AD829 K/f.

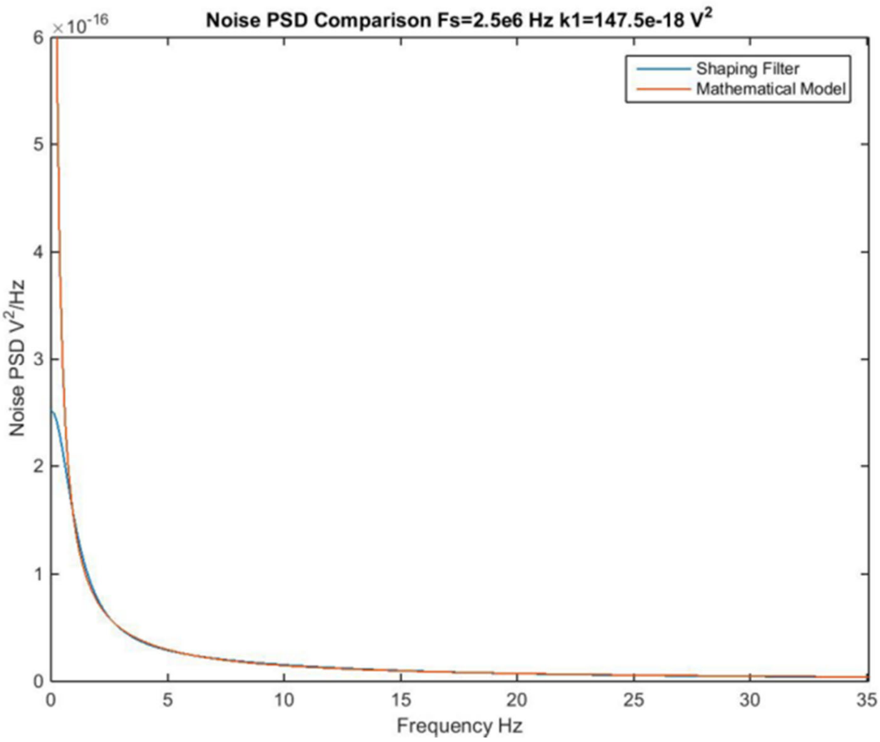

Figure 44 Noise PSD Comparison for 2.5 MHz Rate

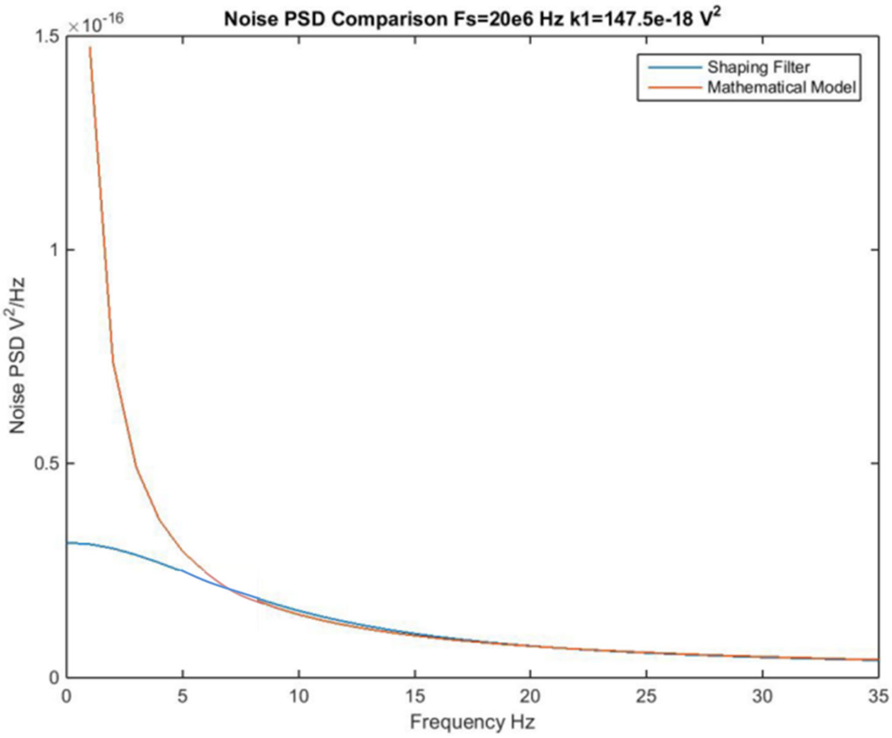

Figure 45 Noise PSD Comparison for 20 MHz Rate

From the graphs shown in Figure 44 and Figure 45 of the reconstructed noise PSD the simulation accurately reconstructs up to frequencies to a fraction of the Hz in case of $F_s =$ 2.5 MHz and a few Hz, around 7.5 Hz, for $F_s =$ 20 MHz. The effect that specific frequency noise components have on a physical process or signal depends on the timescale of the observation/measurement process. Low frequency noise components would start to affect the measurement process when the observation/measurement time is approximately longer than about 1/100th the period of the noise frequency components under consideration. In terms of a CCD waveform, assuming a pixel frequency of 50 kHz, a 7 Hz frequency noise component would start to affect the CCD signal after an observation time of 1.4 ms, namely after around 70 pixel period times. Unless a hypothetical filtering algorithm could exploit the low frequency noise correlation characteristics above the duration of 70 pixels worth of time, the simulation/verification of the goodness of the algorithm at reducing noise would not be affected by the approximation presented. Should the necessity arise, modification of the shaping filter choosing a different sampling frequency, such as F_s = 2.5 MHz, or including higher n order shaping filters would allow the simulation to meet the requirements.

A similar approach and discussion has been followed in Terry (2004) but with different choices of shaping filter and relying on different stochastic process considerations.

The above discussion was limited to the frequency domain. To generate a noise time series for simulation it is necessary to convert the shaping filter to its analogous digital filter; it has been accomplished via a bilinear transform (Oppenheim et al., 1999) and then transformed to a realisable filter via a direct Finite Impulse Response (FIR) form realization. The eight independent white noise time series input sequences get filtered by the respective digital filters and summed at the output. This calculation method has been implemented in Matlab.

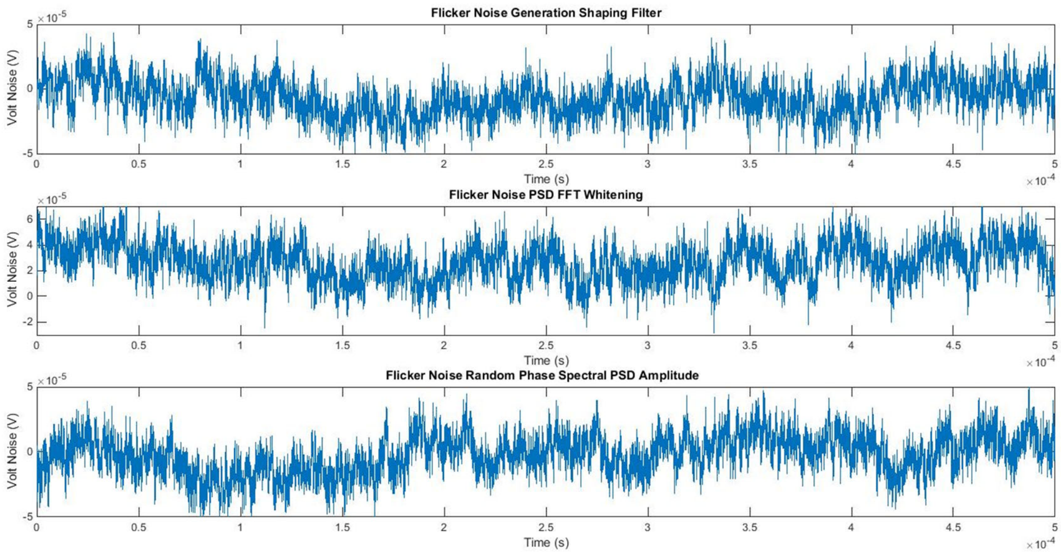

Figure 46 Noise Time Series Comparison

The output time series is the first row in Figure 46, which shows a comparison with the other two methods implemented and presented at the beginning of the chapter.

Power and spectral characteristics are in good agreement between the methods and the typical low frequency noise pattern can be observed as well.

Verification of the performance of the method has been carried out by considering a CCD noise PSD, $Noise_{CCD}(f)$, as input to the analogue chain $H(s)$ of the CCD digital readout model. The calculated power of the time series at the output was compared with alternative methods, which is explained as follows.

The CCD noise can be expressed as (Janesick, 2001):

$$Noise_{CCD}(f) = W_{fCCD} \cdot (1 + \frac{F_{cn}}{f}) \tag{4.21}$$

Where W_{fCCD} represents the white component and F_{cn} is the corner noise frequency of the flicker noise component.

At first, the noise time series generated in the time domain with the proposed method have been filtered through the transfer function $H(s)$ of the analogue processing chain; the power of the time series has therefore been calculated.

The respective value has been compared with the PSD estimate by the Welch method (Bendat et al., 1986) of the noise time series and multiplying it by the square module of $H(s)$. The Hann window has been used for the spectral estimate giving superior performance for noise spectral measurements (Heinzel et al., 2002). A second comparison has been made with the mathematical expression of the CCD noise PSD and multiplying it by the square module of $H(s)$.

The scheme reported in Figure 47 represents the explained simulation.

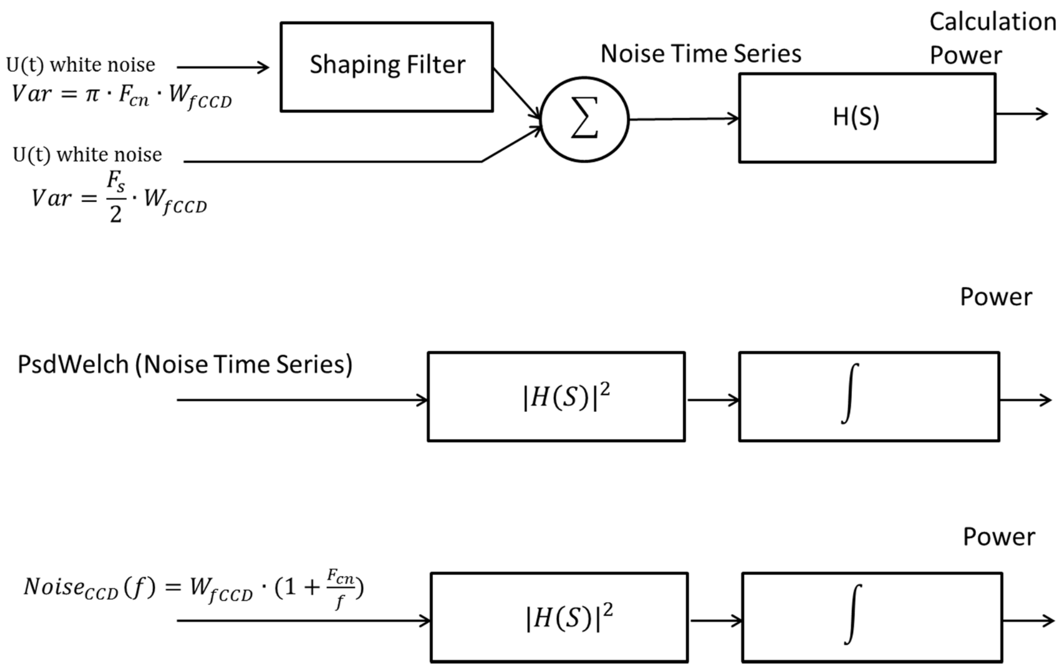

Figure 47 Time Domain Noise Validation Scheme

$H(s)$ is the transfer function of the analogue chain composed of the three amplifiers composed of the transfer functions introduced in paragraph 4.2 and a sample of the top level Matlab code is as follows:

```
%%transfer function of the chain
hshighpassFE=Hpass(250,5000,50000,1e-6);
hsopa829=gen_nonideal_notinv(90000, 2*pi*7500,
2*pi*200000000,300,3000,4.7e-12);
hsHpassad8065=Hpassad8065(300,1000e+9,470e-12);
hsopa8065=gen_nonideal_notinv(17783, 2*pi*3650,
2*pi*334000000,50,1450,100e-12);
hsHdiff= Hdiff(402,260e-12,374);
hs=hshighpassFE*hsopa829*hsHpassad8065*hsopa8065*hsHdiff;
```

whose magnitude transfer function is shown in Figure 48.

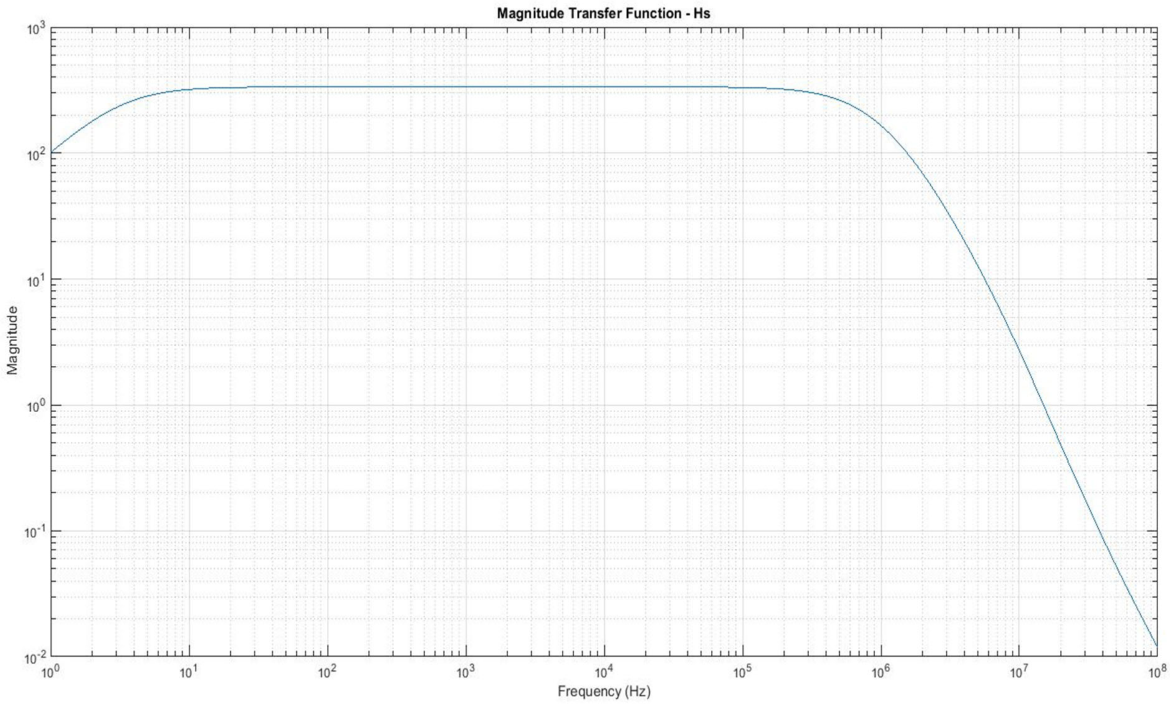

Figure 48 Magnitude Transfer Function Analogue Processing Digital Readout Method

A lower F_{-3dB} frequency at 620 kHz is simulated which is in good agreement with the values experimentally measured in the real circuit.

The values of power from the three mentioned methods are in very good agreement and are respectively:

- Power noise time series = 4.13e-5 V^2
- Power estimated via Pwelch method = 4.10e-5 V^2

- Power calculated analytically = 4.20e-5 V^2

The two graphs shown in Figure 49 and Figure 50 report the power $V^2_{r.m.s.}$, function of the frequency, and the spectral estimate of the noise time domain sequence in comparison with the analytical noise PSD respectively.

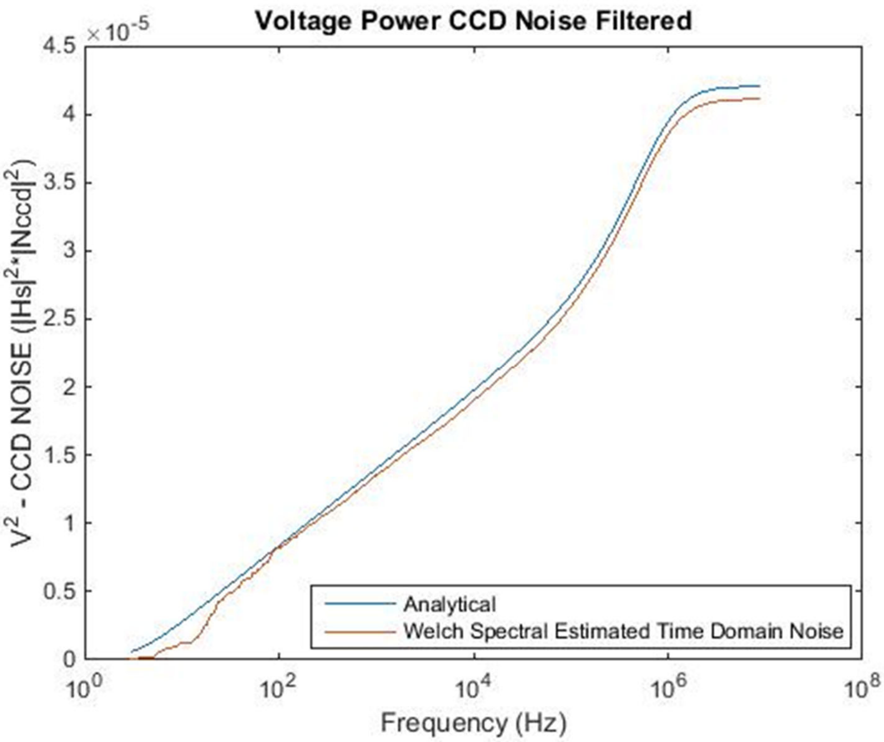

Figure 49 Power V^2r.m.s. - Welch Estimate versus Analytical

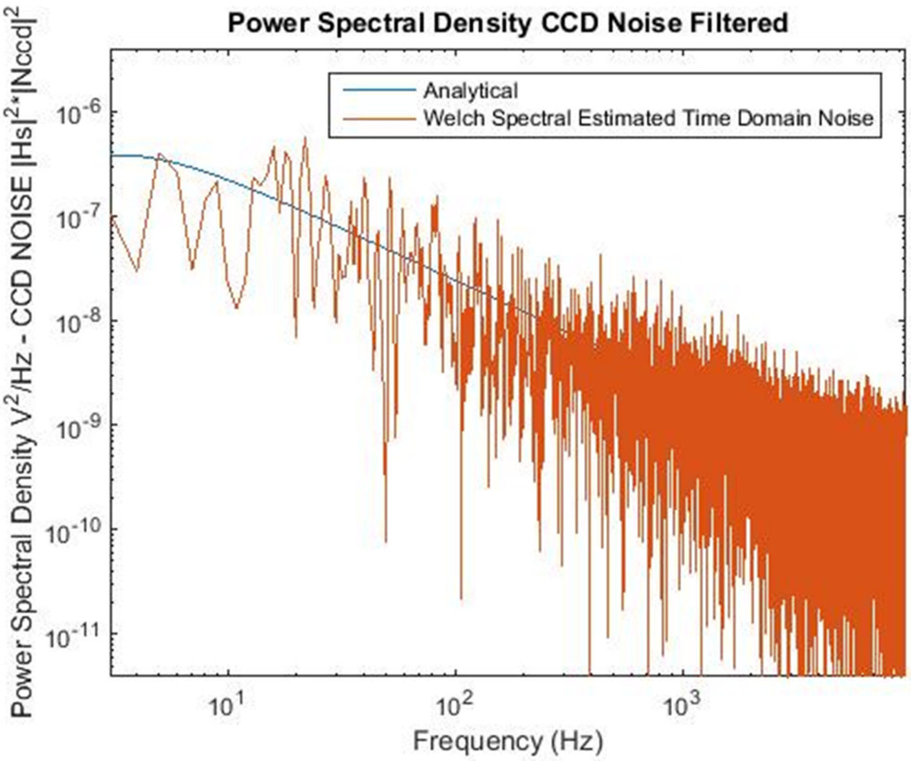

Figure 50 Power Spectral Density - Welch Estimate vs Analytical

The last comparison has been carried out with a Spice simulation of the overall noise introduced by the analogue chain, as described at end of the previous paragraph for the equation of $PSD_{Amp}(f)$ where each noise source of the amplifier has been modelled in the frequency domain with the shaping filter introduced. The result for the Spice simulation of the noise reports a value at 562 kHz of 857.9 μV r.m.s. while for the model introduced the simulation reported a value of 852.8 μV r.m.s.. The Spice results are shown in Figure 51.

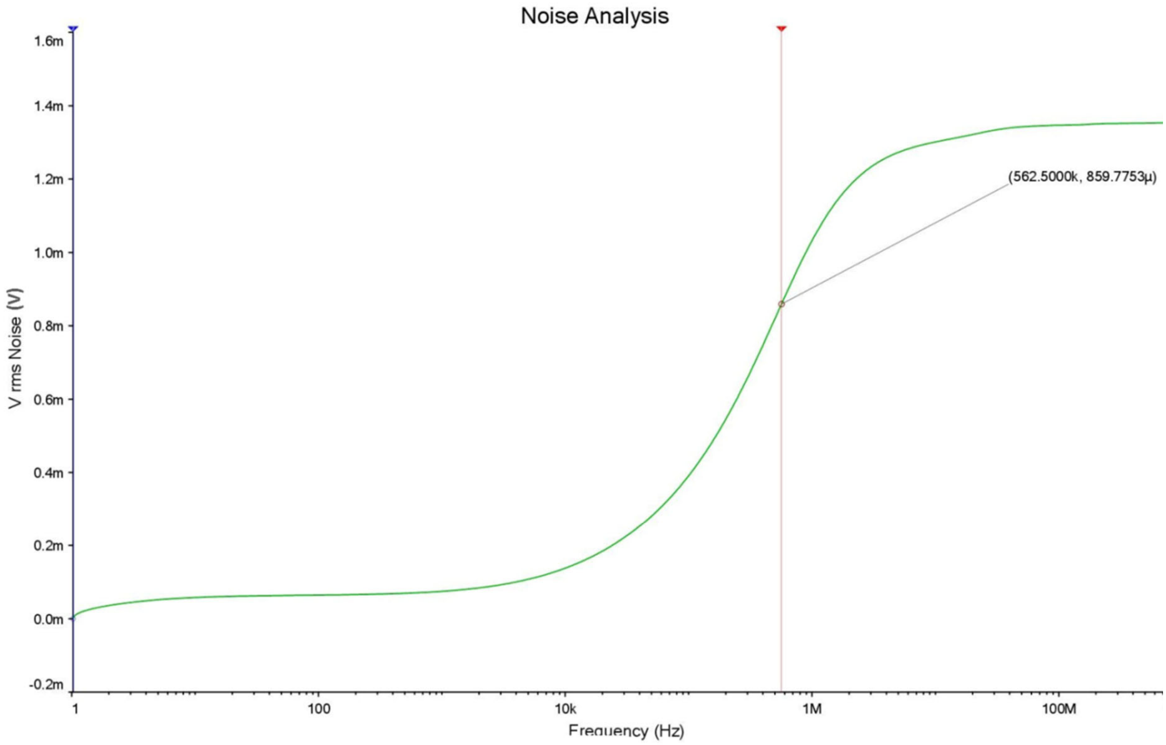

Figure 51 Spice r.m.s.Voltage Noise

4.4 CCD Time Domain Simulation

4.4.1 Introduction

The work undertaken described in the preceding paragraphs has suggested a method to introduce noise in the time domain superimposed on the time waveform of a signal whose content represent the information to be measured.

As introduced in chapter one, a time domain simulation of the CCD signal waveform was developed relying on the static model proposed by Konnik et al. (2014).

The static model takes into consideration the generation of an image N by M pixels given a determined irradiance matrix. For the purpose of the validation of the model it was preferred to consider a uniform illuminated image as in the condition required for carrying out measurements for a photon transfer curve. A real image could have been processed by scaling the pixels' matrix of the real image with the irradiance factor to obtain a representative irradiance matrix.

Reset noise was added at each pixel reset reference value using inverse Gaussian distribution statistics from pixel to pixel. The reason of its addition to the simulation parameters stands in the validation of the readout algorithm to remove reset noise by digital correlated double sampling.

A sample of the discrete time samples, obtained by the time simulation engine as introduced in chapter 1, representing the CCD readout electronic output is shown in Figure 52.

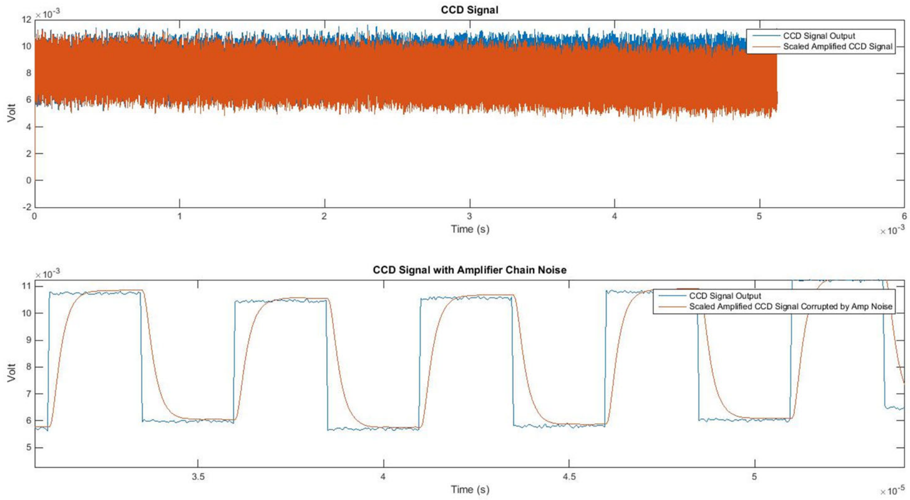

Figure 52 Sample of Simulated CCD Time Waveform

The upper two waveforms represents a portion of the readout sequence covering 5 ms of time while the lower two waveforms show a zoom in the horizontal axis in which the blue line represents the direct signal from the CCD sensor corrupted by noise and the red line the amplified signal through the analogue amplifier chain.

The simulation time engine transforms a static matrix of pixel values projecting each pixel value into two equivalent length sequences of samples simulating the sampled waveform from the ADC. The first sequence represents the pixel voltage reference period, the pedestal value, and the second sequence represents the sample pixel values carrying information about incident photons. The model does not include any characterization of reset feedthrough and serial register transfer period, but this could be introduced by envisaging a sort of shaping filter with time varying characteristics following predetermined random statistical distributions for the period of interest, e.g. of the type $e^{-\alpha n\Delta t} \cdot \cos(2\pi\beta n\Delta t)$; where α and β can be considered two random variable samples from a determined distribution extracted at intervals Δt.

In the analysis that follows the simulated readout processing algorithm does not process the samples relative to three time intervals in the pixel period, as these samples do not carry information regarding the pixel charge. This is consistent with a real CCD sequencing scheme in which the samples during the reset settling, transfer settling and settling times are not integrated by the CDS circuit. These three time intervals are indicated in Figure 53.

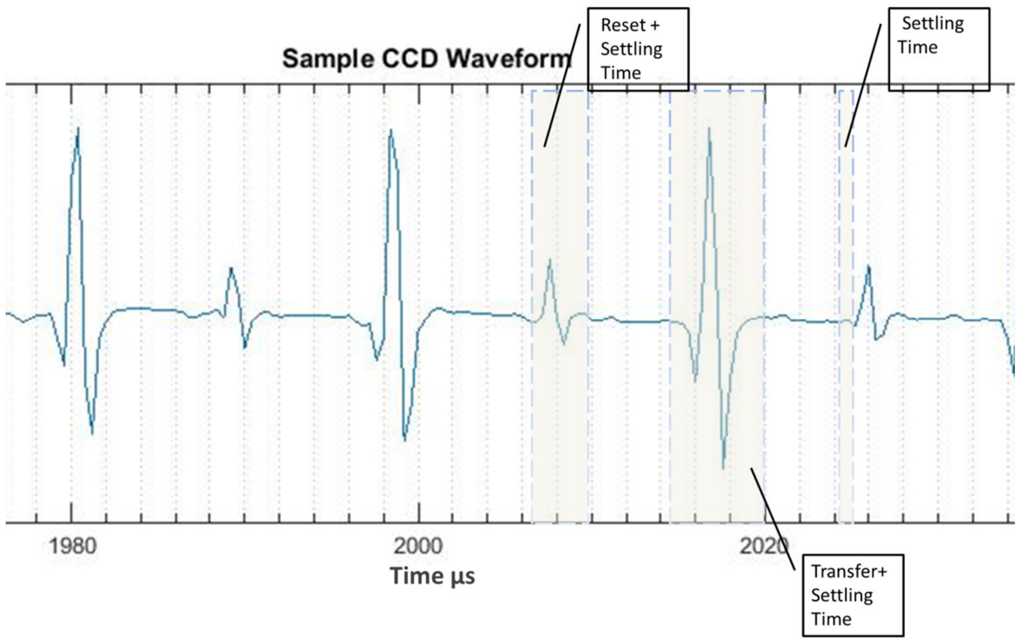

Figure 53 Settling Times in CCD Waveform

Hence, although the transients are not represented in the simulated waveform they have been taken into consideration by the readout algorithm.

In the analysis that follows the same weight in the differential averaging algorithm is given to the meaningful samples of the pixel value although for long pixel times weighting more the samples next to the serial transfer interval of the pixel could give some advantages (Gach, et al., 2003).

In the end, the results that will be shown represent the effect of noise process statistics on the CCD and readout electronic signal rather than representing all the possible interference signals that could affect the performance of a real circuit, this work being more interested in modelling and representing in time the effect of noise time series.

4.4.2 Model Description

In the simulation model developed the number of signal samples per pixel period and the ratio of samples in the pixel period among the reset settling region, the settling time and serial transfer region, as shown in Figure 53, can be configured.

In the actual version of the model a simulated ADC sampling rate of 20 Msample/s is considered, which corresponds to the actual delta modulator conversion rate of the AD7760 ADC. In the real circuit the delta-sigma ADC downsamples the sampled signal by a factor of 8 and low pass filters the signal to minimise the quantisation noise. This last process is not included in the simulation model but, in case it is needed, it could be possible to embed a model of a delta-sigma ADC such as the one developed by Brigati et al. (2009).

The time domain noise representation for the CCD noise sources follows the shaping filter generation method introduced in the previous paragraph, namely convolving in time the input white noise processes with the shaping filter as detailed in Figure 43. On the other hand, the time domain representation for the analogue electronic chain noise is obtained by first considering for each flicker noise source the noise PSD obtained by multiplying the PSD of the input white noise processes by the square module of the shaping filter transfer function, obtaining the relative flicker noise PSD, then multiplying the obtained PSD noise by the square module of the specific amplifier's transfer function; a similar methodology is adopted for the amplifier white noise components. Once the representation of the noise PSD for each amplifier is obtained, similar to the derivations in paragraph 4.2, the expression of the noise PSD for the overall chain of amplifiers, $PSD_{Amp}(f)$, can be obtained. The generated noise time series follows the procedure named as whitening method in paragraph 4.3. The reason behind this choice stands on the grounds that it would not be necessary to estimate white and flicker noise components from the PSD noise, but process directly the numerical PSD function by the algorithm in Matlab without an intermediate estimation process.

The parameters adopted to simulate the CCD noise performance have been deduced from the datasheet parameters of the CCD97, the analytical expression for reset noise and e2v publications; namely the reset noise for the HR channel is given as 50 electrons r.m.s., considering the relationship of this to the sense node capacitance C_{sn} and source follower gain as explained in Janesick (2001) and the 5.3 μV/electron value of the output amplifier responsivity for the OSH channel. Estimated values for the A_{sf}, source follower gain, of 0.688 and a value for the A_{sn} of 7.7 μV/electron were used. This was used for estimating the reset noise but would not affect the calculation involving the responsivity in V/electron of the sensor.

The other fundamental parameter to be estimated is the CCD97 sensor noise, namely white noise and flicker noise not considering other higher power law noise contributions in the analysis; the estimation relied on a datasheet parameter indicating 2.2 electrons r.m.s. of noise expressed for the OSH channel adopting a CDS at 50 kHz pixel frequency, a value inferred by design and not measured.

Considering the mathematical expression, as detailed in the above mentioned reference, the noise in electrons r.m.s. for a CDS readout method as a function of CCD white noise and for different values of flicker noise, is given by (Janesick, 2001):

$$N_{CDS}(e^-) = \frac{1}{S_V \cdot A_{CCD} \cdot \left[1 - \exp\left(-{t_s}/{\tau_D}\right)\right]} \cdot \left[\int_0^\infty \left|N_{CDS}(f)\right|^2\right]^{1/2} \tag{4.22}$$

Where $|N_{CDS}(f)|^2$ is represented by (Janesick, 2001)::

$$\left|N_{CDS}(f)\right|^2 = \left|N_{CCD}(f)\right|^2 \cdot \frac{1}{1 + (2\pi f \tau_D)^2} \cdot \left[2 - 2\cos(2\pi f t_s)\right] \tag{4.23}$$

Considering the sample-to-sample time $t_s = T_{pix} \cdot 2/5$ at 50 kHz readout rate and τ_D equivalent to a bandwidth close to twice the frequency of the pixel rate, indicated in Jerram (2016) as the minimum possible pre-sampling bandwidth, the noise electrons r.m.s. for a CDS readout method can be plotted as in Figure 54.

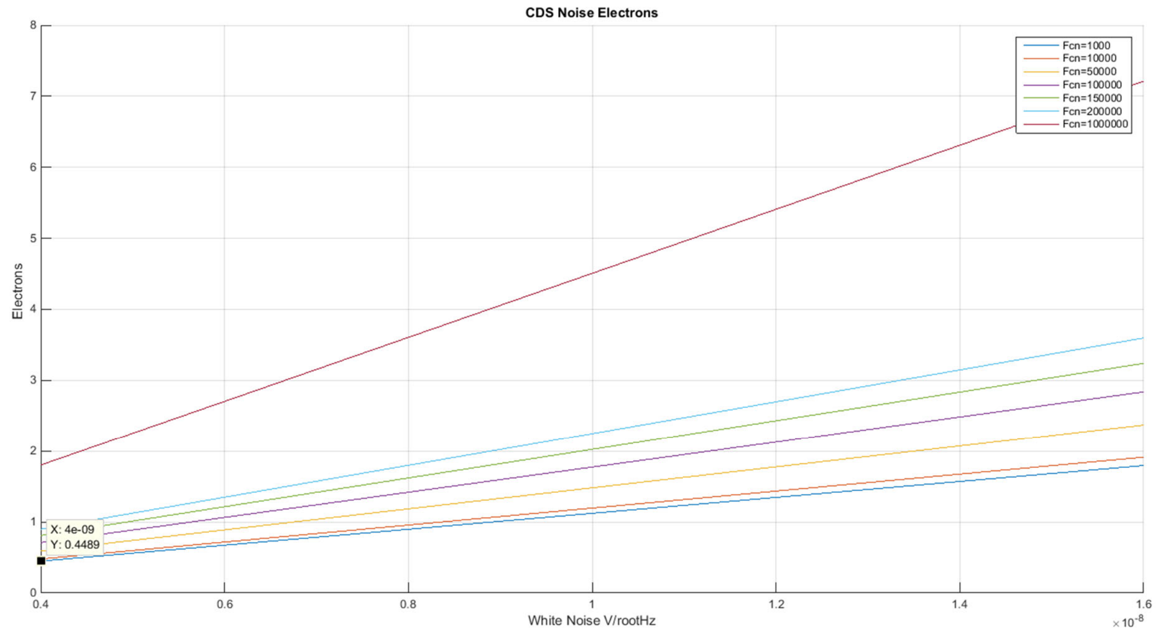

Figure 54 CDS Noise for Estimation of Real CCD97 Noise

In order to estimate the white noise components of the CCD noise a plot of the CDS noise for different values of flicker corner frequency, F_{cn}, is shown in Figure 54. Adding the consideration that usually for a CCD the flicker corner frequency, F_{cn}, can be assumed next to a value of 150 kHz (Jerram et al., 2016) and the reference parameter of 2.2 electrons r.m.s. of noise from CCD97 datasheet, it has been chosen to characterize the CCD noise with a white noise component of 12 nV/$\sqrt{\text{Hz}}$ and a flicker corner frequency of 150 kHz:

$$|N_{CCD}(f)|^2 = (12\ \text{nV}/\sqrt{\text{Hz}})^2 \cdot (1 + 150000/f) \tag{4.24}$$

The implemented model also allowed to quantify the effect that a readout pixel rate change has on the noise performance for the given circuit parameters. On one hand, for long pixel time periods the circuit shows a transient behaviour at very low signal frequencies due to the high pass time constant, given that the system is AC coupled. On the other hand, the low pass F_{-3dB} frequency at 620 kHz limits the circuit response for high frequency pixel rates. Considering the noise electron r.m.s. as the performance parameter, it was found for the simulated circuit, whose transfer function is expressed by the previously introduced

$H(s)$, that the performance is not affected for pixel rates between 6.25 kpix·s^{-1} and 100 kpix·s^{-1}.

4.4.3 Simulation Philosophy and Results

Three different types of simulation have been carried out regarding the distribution of samples in the pixel time period falling between: reset and settling time, serial transfer and settling time, settling time before reset of the next pixel. The timing is described in Figure 53 and the simulations were as follows:

1) The distribution of the number of samples in the pixel time period between the different regions follows the same ratio as between the different settling and transfer times in the real digital circuit, hence choosing a settling time proportional to the pixel period and not a constant settling time, changing the pixel period at a constant ADC sampling rate the number of samples would scale accordingly to a factor. Such a choice is useful to analyse a larger dynamic of effective samples useful for integration in the DCDS algorithm because the ratio is not limited by the specification of a constant settling time. In this analysis the DCDS is applied to the time samples directly at the output of the CCD without considering the effect of the time constants of the analogue readout electronics on the signal waveform.
2) Same conditions as described in point 1) except for the above mentioned settling times that in this scenario remain constant as it would happen in a real pixel time period, hence increasing the pixel time period would accordingly increase the number of samples useful for integration in the DCDS algorithm.
3) Same reset and settling time at the beginning of the pedestal value and same length of settling time in the second half of the pixel period corresponding to the pixel charge value; all the remaining time intervals correspond to useful samples for the integration in the DCDS algorithm. This was done to compare the results of the time domain simulation with an analytical expression for the DCDS readout method as introduced in Stefanov et al. (2014).

The first case is presented in Figure 55.

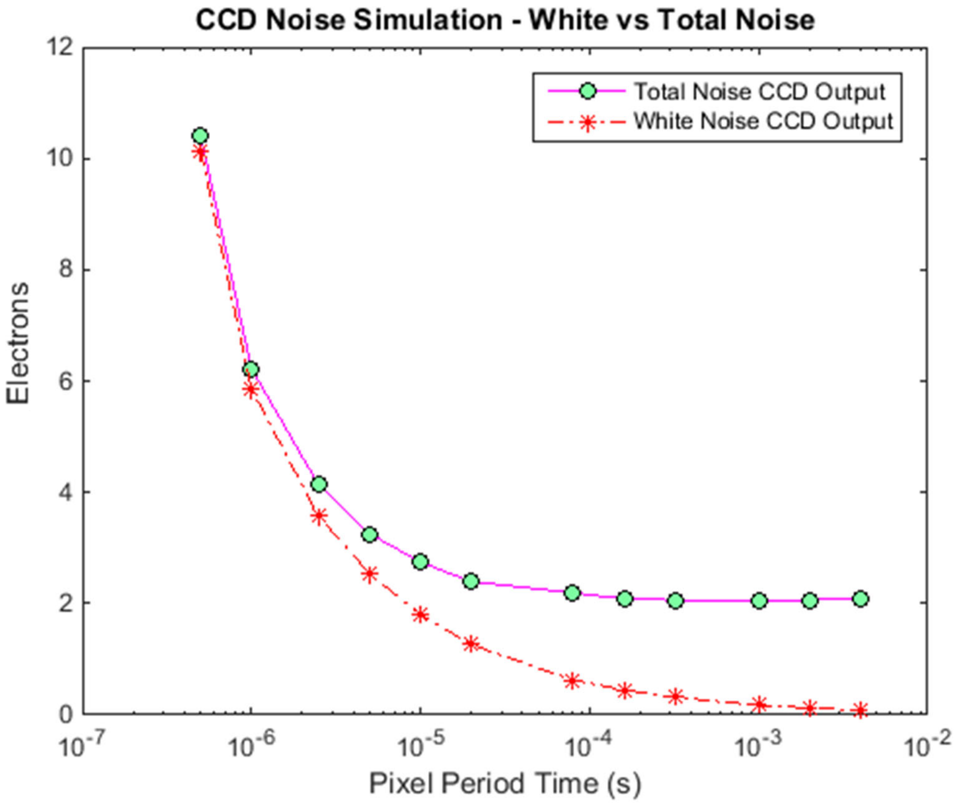

Figure 55 White and Total Noise Contribution to Readout Noise

The direct signal from the CCD output is simulated for a range of pixel frequencies from 2 Mpix·s^{-1} to 250 pix·s^{-1} corresponding to a number of effective samples integrated in the DCDS from 1 sample to 12800 effective samples and with no low pass filtering. The red curve in Figure 55 shows only the white noise component and the other one with green markers also includes the flicker noise component.

It is evident how at the increase of the integrated number of samples the reduction of the electron r.m.s. noise is consistent, confirming the statistical relationship for the DCDS noise gain of $n_{gain} = \frac{\sqrt{2}}{\sqrt{N_{sample}}}$ and reported also in Clapp et al.(2012); although, different from the derivation in the cited reference, the relationship should hold valid only for the white noise component, and the n_{gain} factor should not also be multiplying the flicker noise component in the calculation of the total r.m.s. noise contribution, because of the intrinsic correlation in time of the 1/*f* noise the noise performance reaches a plateau for pixel period times over 1 kpix·s^{-1}.

The second case presented in Figure 56 matches the settling times of the real digital acquisition circuit, which, as a reminder, operates at a decimated ADC rate of 2.5 Msample/s. The effective number of integrated samples was chosen to be between 6 and 8.

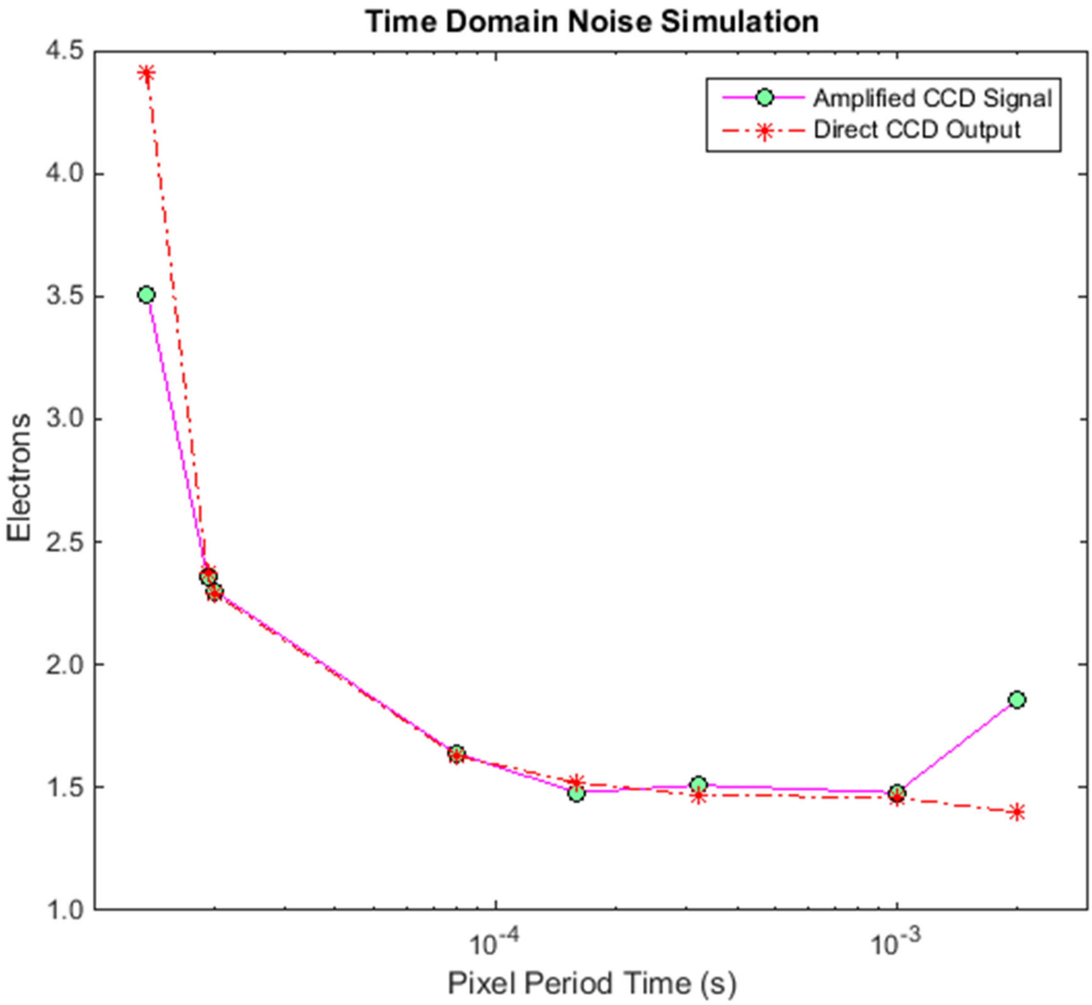

Figure 56 DCDS Noise Output

The plot compares the noise from the waveform directly from the CCD, with no low pass filtering applied, to the one processed by the analogue chain $H(s)$.

The pixel rate of interest goes from F_{pix} of 70 kpix·s^{-1} to 500 pix·s^{-1} with a corresponding number of integrated samples given in Table 8.

F_{pix} **(kHz)**	73.5	52.08	50	12.5	6.25	3.125	1	0.5
N_{sample}	8	64	72	672	1472	3072	9872	19872

Table 8 Pixel Frequency and Effective Samples

It should be noted that the simulated waveform is virtually sampled at a rate of 20 Msample/s corresponding to the actual rate of the first stage of the delta-sigma modulator of the AD7760, subsequent decimation taking the rate to 2.5 Msample/s. The second column of the table would represent the case of the real circuit if the operation of decimation by 8 could be included; such modification will be embedded in a future evolution of the model.

From the plot a range of 2.2 to 3 electrons r.m.s. noise can be estimated for the real circuit, with contributions to the noise due only to the CCD and amplifiers.

A comparison of the above estimate with the one suggested by Jerram et al. (2016) for the minimum noise achievable by a CCD readout electronic is interesting. The expression is given by:

$$Noise_{r.m.s.} \approx \frac{1}{2} \cdot \sqrt{C_n (2 + f_b / F_{cn})} \qquad (4.25)$$

Where f_b is the low frequency cut, assumed to be double the 50 kpix·s^{-1} pixel frequency and C_n, the white noise component, and F_{cn}, the flicker corner noise frequency, with the same value of the simulation model presented. This equation gives a noise of 3.72 electron r.m.s.; which is in good agreement with the estimate of the simulation model, considering that it takes into account only the noise from the CCD and amplifiers.

It is also evident at shorter pixel integration time for the direct CCD output case that there is a higher noise due to the white noise component not being filtered and an increase of noise at longer pixel times for the amplified CCD signal because of the effect of the AC droop due to the AC coupling capacitor.

The third case allows the time domain simulation results to be compared to a theoretical model developed by Stefanov et al. (2014), which helps deduce insights that allow selection of the parameters for digital readout.

The mentioned model allows calculation of the performance of the system relying on four parameters: the signal bandwidth, the settling error ε, the CCD clock frequency and the ADC sampling frequency. The equation to model the differential averager is given by (Stefanov et al., 2014):

$$|H_{DA}(f)|^2 = \frac{1}{N^2} \cdot \frac{4 \cdot \sin^2(N\pi f T_{ADC}) \cdot \sin^2((N+M) \cdot \pi f T_{ADC})}{\sin^2(\pi f T_{ADC})} \tag{4.26}$$

Where:

- M is the number of samples of settling
- N is the number of samples integrated
- T_{ADC} is the ADC sampling period

The number of samples M is related via the settling time t_{set} to the bandwidth of the circuit via the percentage settling error ε:

$$M = t_{set} \cdot F_{ADC} \text{ where } t_{set} = \tau_D \cdot |\ln \varepsilon| \tag{4.27}$$

The total number of samples in the pixel period is given by:

$$T_{pix} = 2 \cdot (N+M) \tag{4.28}$$

The equation representing $|H_{DA}(f)|$ has been assessed for a variety of conditions and compared with the results of the time domain simulation with only the noise of the CCD included, so no noise from the analogue processing chain was considered. The settling time has been chosen to be constant, hence M samples, and equal to the one used in the real digital circuit corresponding to a settling of ε = 1.60e-05.
When increasing the pixel time T_{pix} there will be a corresponding increase in the number of integrated samples with M constant; obviously changing the ADC rate all the parameters will change accordingly.

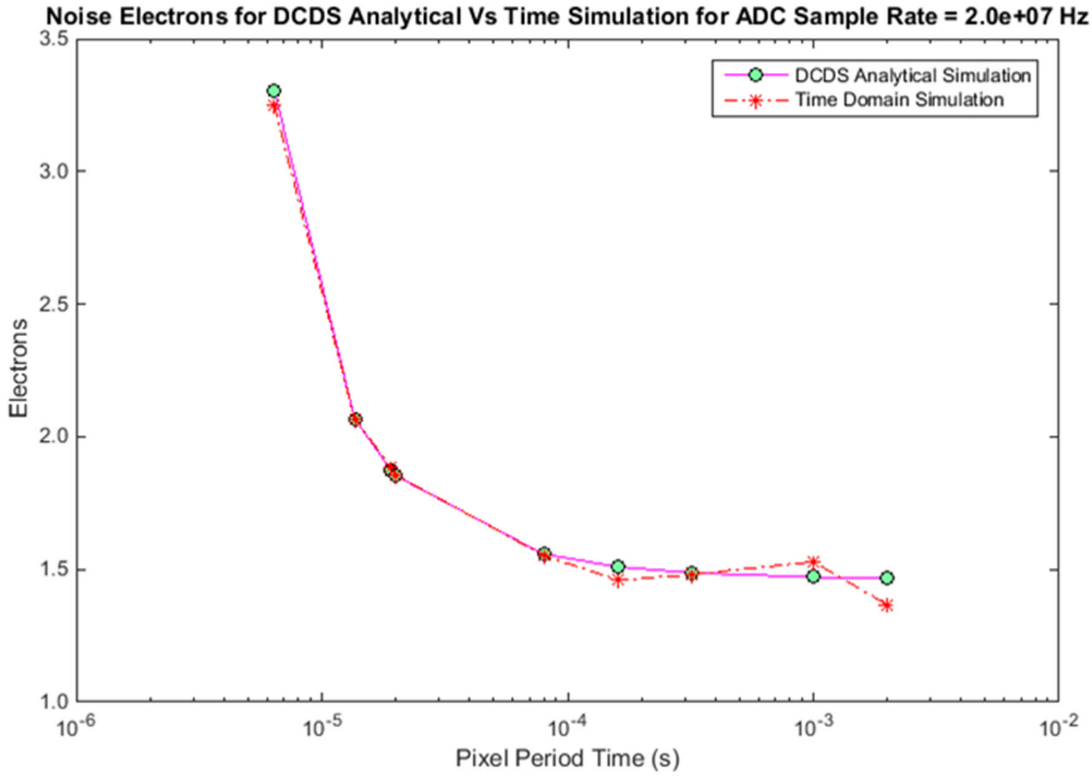

Figure 57 Comparison Analytical DCDS vs Time Domain Simulation

As can be seen in Figure 57 there is a very good match between the two derivations. Changing the sample rate of the converter does not give a big improvement once at least 8 to 16 samples have been included for the integration process as shown in Figure 58 for a pixel period of 20 μs.

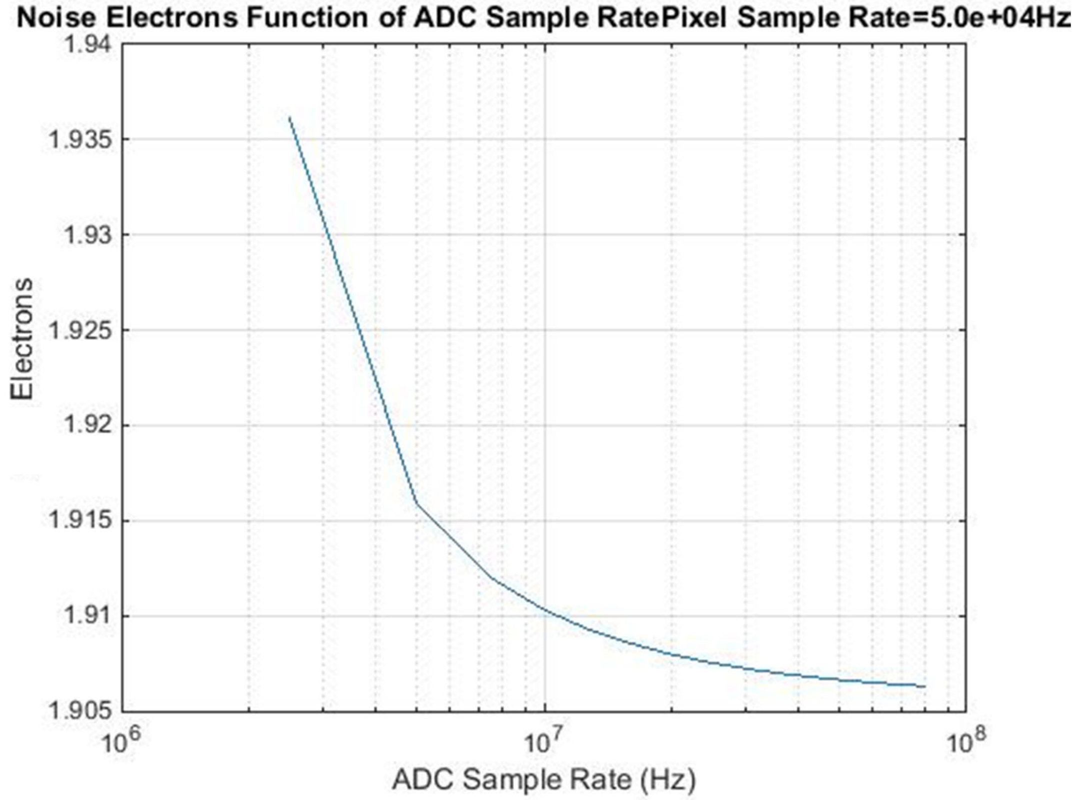

Figure 58 Noise Electron Function ADC Sample Rate

Changing the sample rate, therefore increasing the number of samples per pixel, has the effect of pushing noise aliases, created by the sampling and averaging process, to higher frequencies as explained in Smith et al. (2013).

It is therefore necessary to include an antialiasing filter to efficiently suppress these high frequency components that would alias into the passband.

To understand better the nature of these frequency components the two plots in Figure 59 and in Figure 60 represent the CCD noise spectrum processed by the DCDS for two different pixel sample rates.

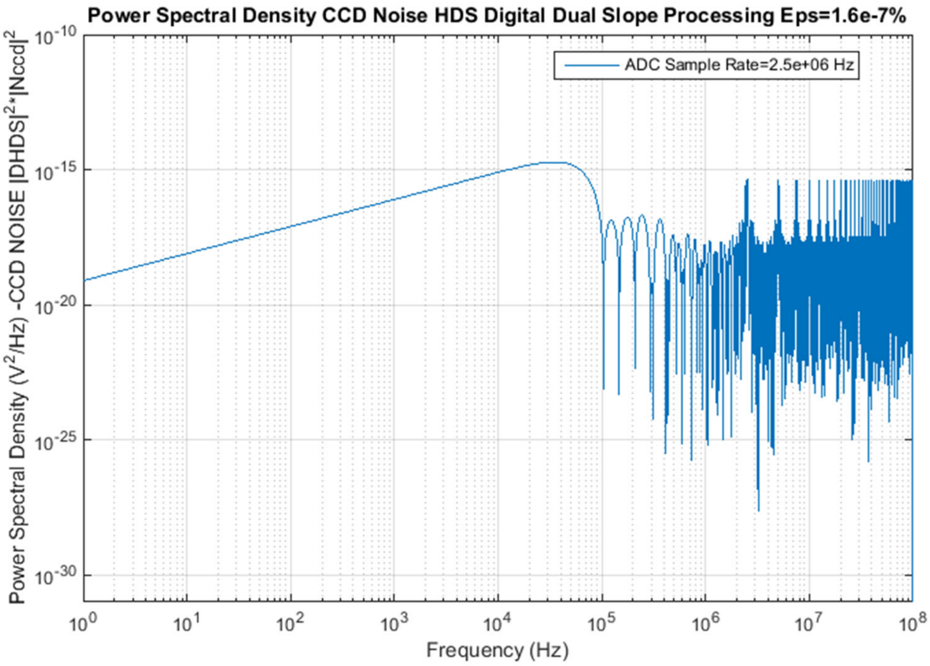

Figure 59 DCDS PSD at 2.5 MHz ADC

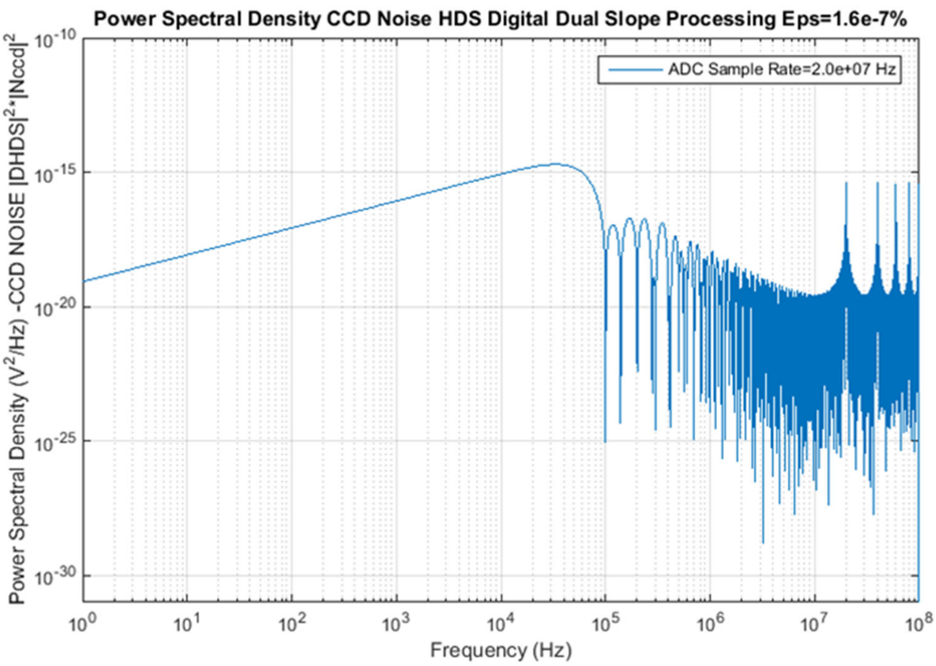

Figure 60 DCDS PSD at 20 MHz ADC

It is clear how at the increased ADC sample rate the noise peaks starting from about 2.5 MHz get shifted to 20 MHz and hence are more easily filtered out.

Including in the model representation the analogue amplification chain the noise gets shaped as shown in Figure 61 and Figure 62.

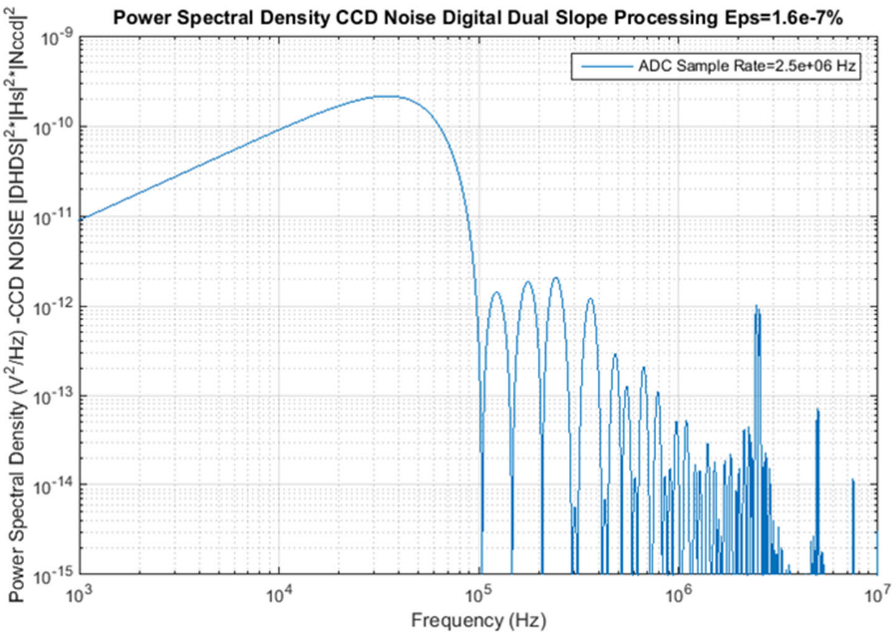

Figure 61 DCDS PSD at 2.5 MHz ADC Filtered by Analogue Front-End

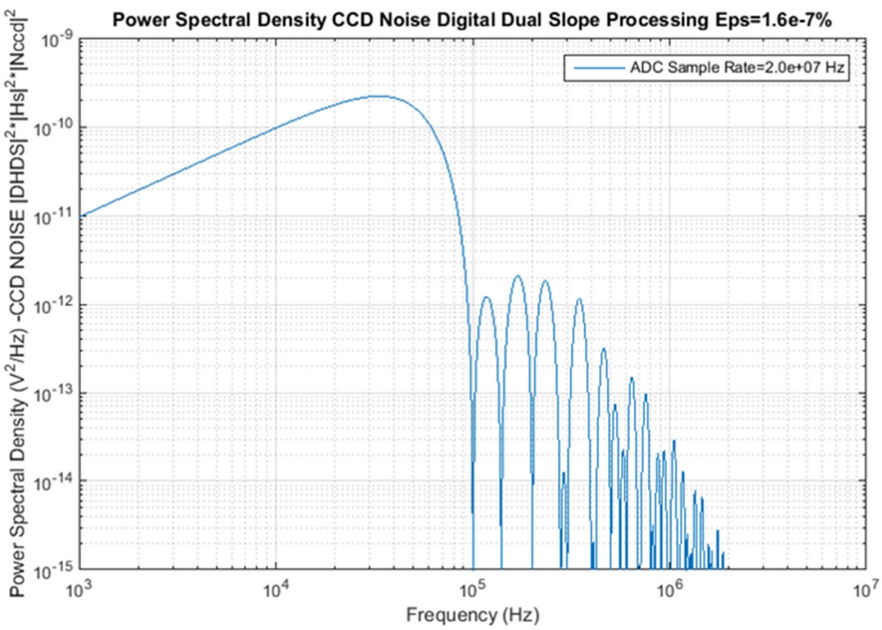

Figure 62 DCDS PSD at 20 MHz ADC Filtered by the Analogue Front-End

Figure 61 and Figure 62 show a higher contribution of noise for pixel sample frequencies above 1 MHz. Such peaks do not find correspondence in the case of the dual slope analogue integrator simulated for the same conditions and shown in Figure 63.

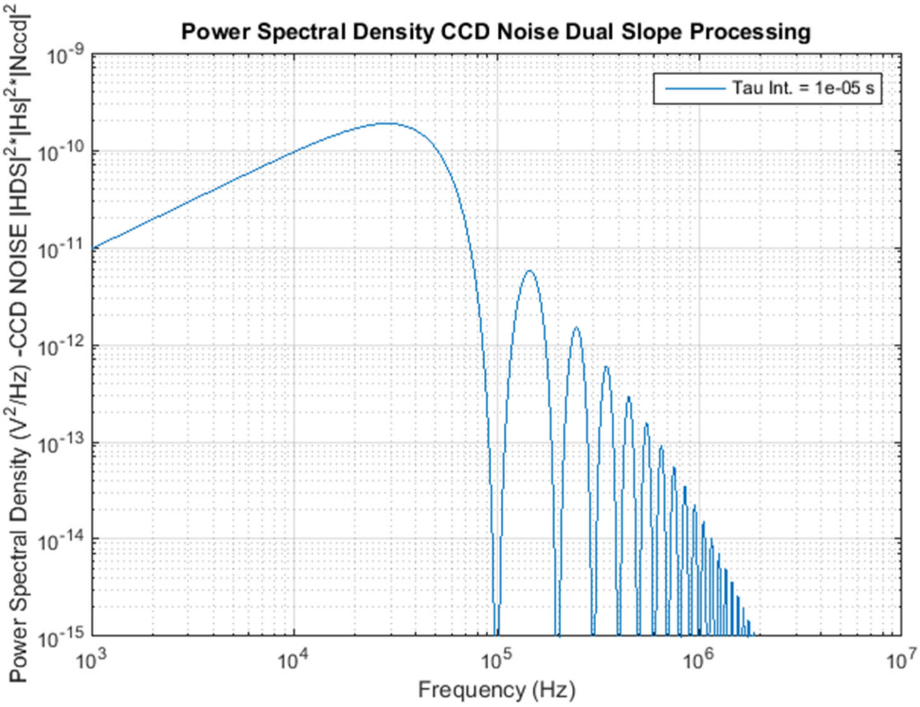

Figure 63 Analogue Dual Slope Processor

Figure 63 shows how the ideal analogue dual slope method is the optimum processor to which the DSDS can tend to. The electron r.m.s. noise for the case of the ideal dual slope with an integration period set to half the pixel time period, so that no settling times are considered, is plotted in Figure 64.

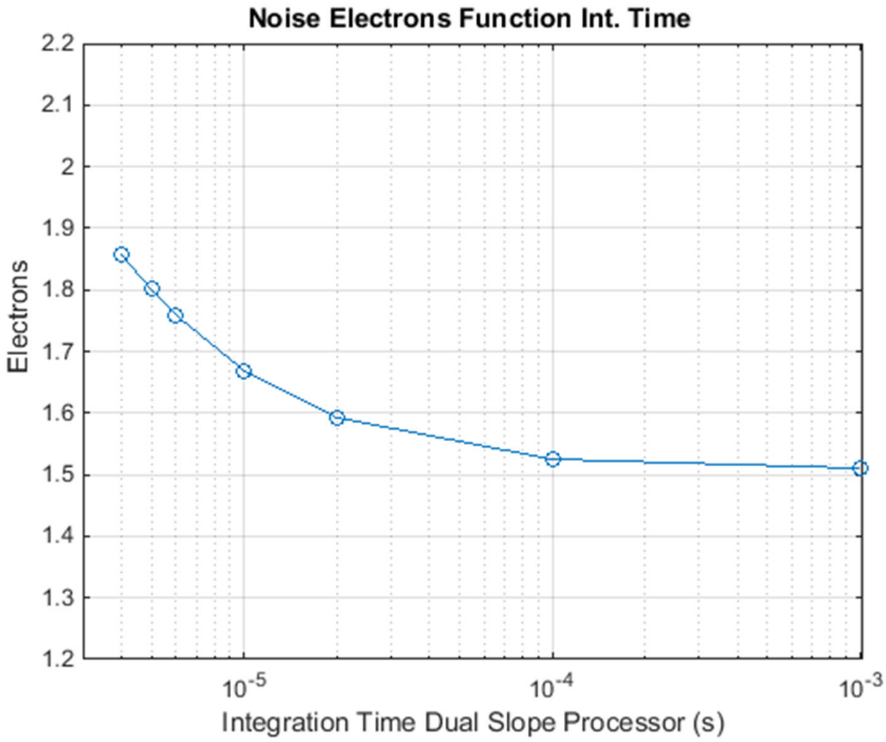

Figure 64 Noise Electrons - Analogue Dual Slope

In the end the overall effect for the DCDS method of choosing a lower F_{ADC} is a slight increase of noise for F_{pix} frequencies above the 50 kpix·s^{-1}, as shown in Figure 65 for the case of F_{ADC} equal to 2.5 MHz. Choosing a lower F_{ADC} presents similar performance for lower pixel frequencies as the square module of the noise transfer function for different sampling rate behaves similarly for low frequencies when flicker noise becomes the dominant noise contribution.

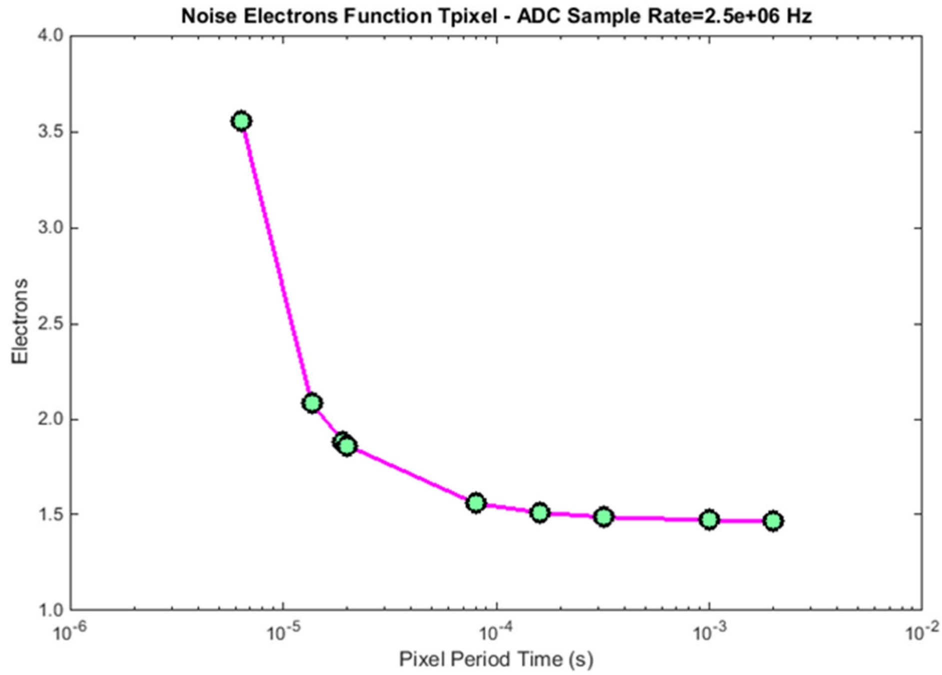

Figure 65 Noise Electrons - DCDS at 2.5 MHz

Similarly to the same conclusion reached by Smith et al. (2013) the above findings suggest that it is preferable to use a lower sample rate ADC with very good noise performance, such as the AD7760, and use a multiple pole low pass frequency amplifier to obtain a sharper cut of the high frequency aliased components. In the case of the real electronic circuit implemented, it has three poles with an overall 600 kHz F_{-3dB} followed by a further antialias filter attenuating a further 10 dB at 19 MHz.

Nevertheless, the choice of the ADC sample rate could play a role when adopting algorithms different from the DCDS and when implementing specific noise reduction methods exploiting the correlation in time of the low frequency noise. A higher number of samples per pixel could help reducing noise, optimising the conditions to reach convergence. An interesting approach is presented in Cancelo et al. (2012) exploiting the correlation in time of the low frequency noise estimated in a sample of 20 pixels and then subtracting it from the original CCD signal.

Further efforts will be dedicated to conceiving a filtering algorithm specifically to reduce the low frequency noise components which affect the CCD readout for long integration time, especially above 70 kpix·s^{-1}. Particularly, the research could focus on a Kalman filter algorithm with the construction of a state transition matrix leveraging the proposed shaping filter for flicker noise in the procedure of augmenting the state vector of the dynamic model (Brown et al., 2012).

4.5 Characterisation of Camera System

4.5.1 Introduction

In order to characterise the camera system in terms of gain and noise for comparison with the calculations and simulations presented previously it was chosen to set up a system for the measurement by photon transfer theory (Janesick, 2007).
The first step was to assemble together the equipment to reach good levels of illumination uniformity on the CCD. It was decided to procure equipment commonly utilised for macro photography. Particularly, as shown in Figure 66, a macro bellows extension kit.

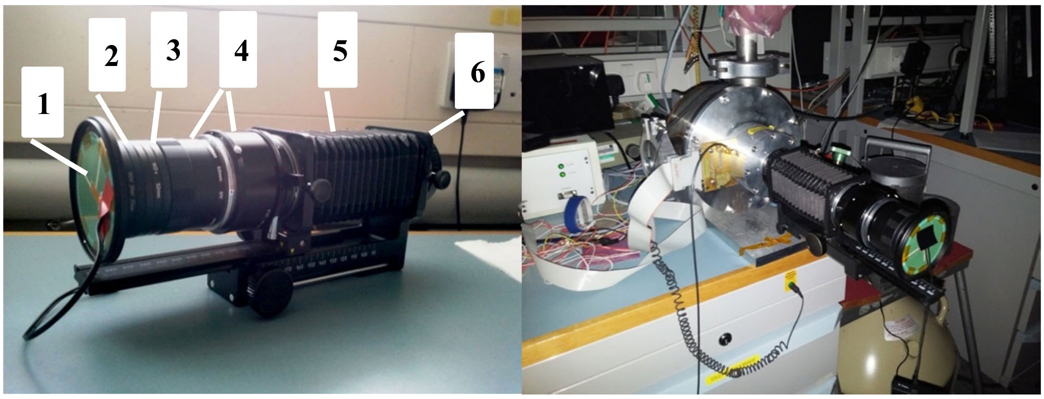

Figure 66 Photon Transfer Curve Equipment

From left to right in Figure 66 the description of the equipment is:

1. Electroluminescent circular panel, which through a DC to AC inverter can modulate the intensity of the incident light and the pattern in time from continuous to pulsed.
2. A series of neural density filters, which can be added or removed, to attenuate to the desired level the level of irradiance
3. Circular Lambertian diffusor from Edmonds

4. Extension tubes
5. Macro extension bellows
6. A Nikon to C mount adapter to attach it to the C mount thread on the camera system

The design of the illumination assembly assures a measured uniformity of 1.07% between the centre of the image and the edges of the pixel region of interest used to process the images, which is a standard value for a good measurement setup (Janesick, 2007).
To be sure that the light emitted by the electroluminescent panel matched the CCD97 in its wavelength range, a measurement of the spectrum was carried out with a Maya2000 Pro spectrometer. The collected spectrum is shown in Figure 67.

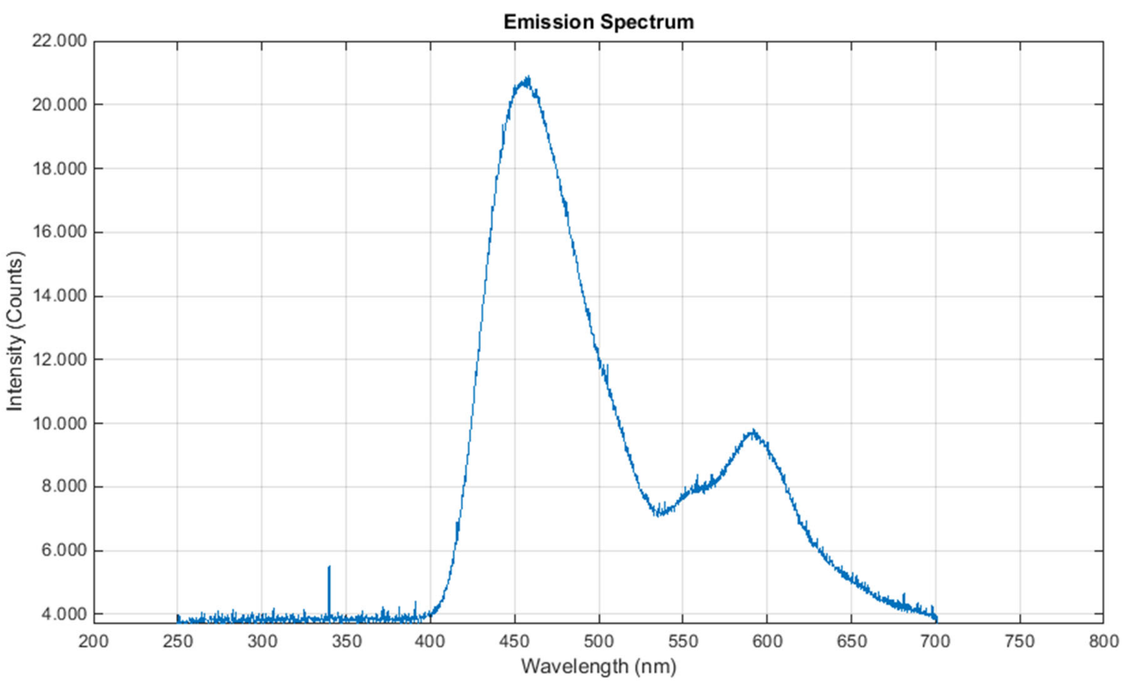

Figure 67 Electroluminescent Panel Emission Spectrum

Most of the emission is in the range 400 to 700 nm wavelength, which is a good match with the spectral response of the sensor.
This stage of the experimental work gave the opportunity to optimise the sequencer code written in assembler, run by the digital signal processor, for the analogue readout method to

sequence the operation of the CCD97. A different sequence of operation was implemented related to the pre-existing code and several versions were tested, to list some of them:

- Compliance with the CCD97 datasheet, change of vertical phases timing
- Elimination of Dump Gate sequence, but after the frame transfer phase empting the serial register with dummy cycles, this helped to reduce peaks at the beginning of the readout which, once amplified, would have affected the analogue input stage protection of the digital readout electronics compromising its safety
- Position of vertical phases and movement of serial register and reset during integration time
- Change of serial register timing to enable at request the readout of the OSL channel or the OSH channel

A similar optimisation opportunity was followed for the digital readout method in the choice of the settling parameters and number of integration samples. A sample of the Matlab code to DCDS process the collected CCD images is reported below:

```
count=count+1;
deltapixel(count)= z;
start=z+ADCdelay+Resetsettling;
for k=1:2
for M= 1:Nsanples
x(i,j,k,M)=dataset(start+M,2);
end;
start=start+Nsamples+Nserialtransfer;
end;
end;
if ((i==528) && (j==568))
break;
end;
end;
for d=1:(count-1)
deltapixelvalue(d)= deltapixel(d+1)-deltapixel(d);
end;
deltapixelvalue(count)=deltapixelvalue(1);

dimension=size(x);
pixel=zeros(dimension(1), dimension(2));
for i=1:dimension(1)
    for j=1:dimension(2)
        for k=dimension(3):-1:1
            for M=1:dimension(4)
                if (k==1)
                    pixel(i,j)=pixel(i,j)-x(i,j,k,M);
                elseif (k==2)
                    pixel(i,j)=pixel(i,j)+x(i,j,k,M);
                end;
            end;
        end;
    end;
end;
pixel=-(pixel./Nsamples);
```

4.5.2 Photon Transfer Curves

All the images were acquired at a temperature of -70°C at a pixel rate of 54 kpix·s^{-1} and to a maximum integration time of 80 s with different levels of irradiance.

A pair of images was acquired for each photometric setting, one image straight after the other. Sequences of 10 to 24 pairs of images were acquired with increasing mean pixel level for each readout method, namely:

- Analogue readout with OSH channel
- Analogue readout with OSL channel
- Digital readout with OSH channel
- Digital readout with OSL channel

Matlab routines were developed to automatically process the images given the region of interest and the overscan region for the offset calculation.
Particularly, a pixel region of {[110 420], [110 452]} rows by columns respectively for an area of (311) × (343) pixels was considered.
Following the theoretical equations and methods well explained in the above mentioned reference the standard deviation curve showing total noise, shot + read noise and shot noise were calculated; also the variance in the photon transfer curve was calculated to enable checking of the results.
A sample of two images for 5 s of integration with neutral-density filters (N_D filters) to reduce the intensity of light and at two different illumination levels is shown in Figure 68.

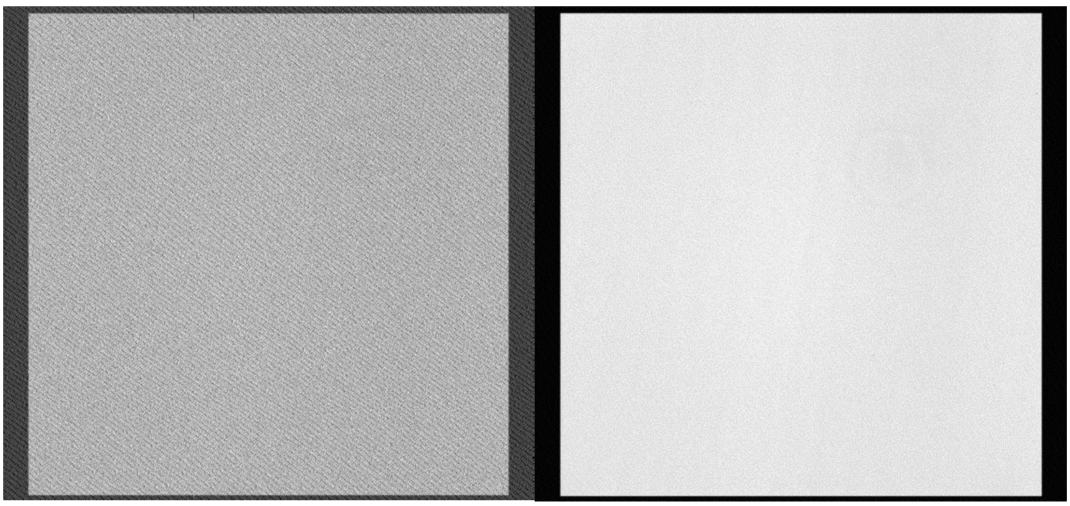

Figure 68 Sample of CCD Frames for Photon Transfer Curve

Figure 69 to Figure 72 show the standard deviation PTC curves for the four cases above. The points highlighted in the figures on the shot noise curves are necessary to calculate the conversion gain, K_{ADC}, expressed in electrons per digital number (electron /DN).

Specifically in the shot noise regime (Janesick, 2007):

$$K_{ADC}\left(\text{electron}/\text{DN}\right) = \frac{S(\text{DN})}{\sigma^2_{Shot}} \qquad (4.29)$$

Where S(DN) is the signal corresponding to the axis of abscissae in the figures and σ^2_{Shot} the square of the values on the axis of ordinates.

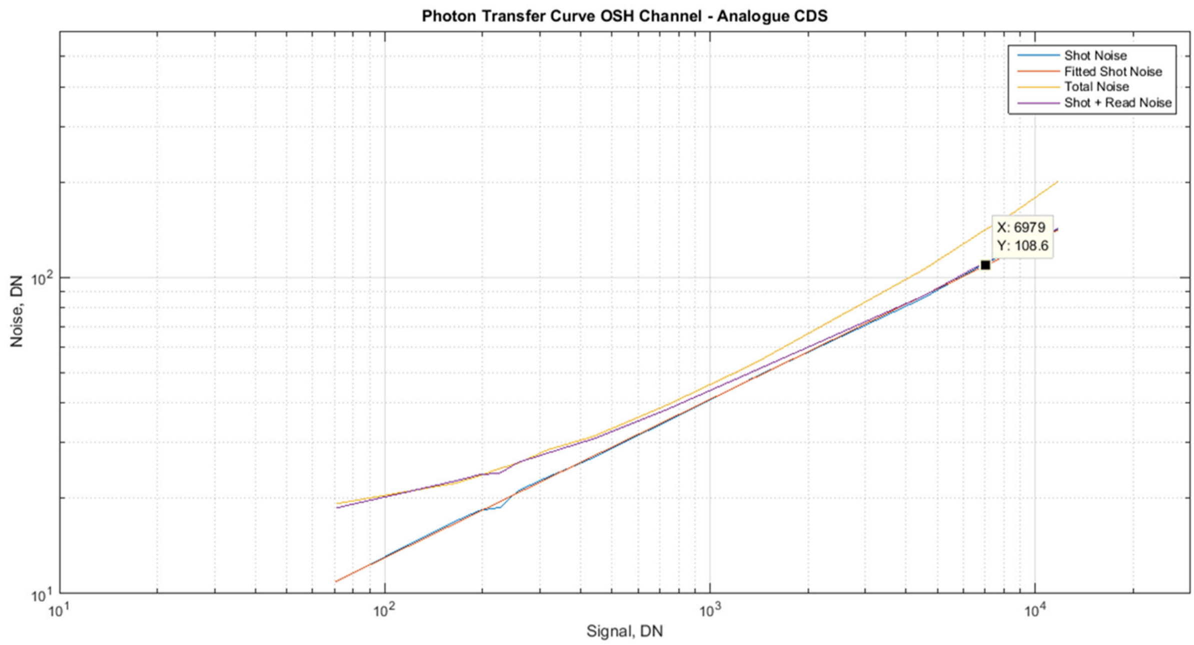

Figure 69 PTC - OSH Channel Analogue Readout

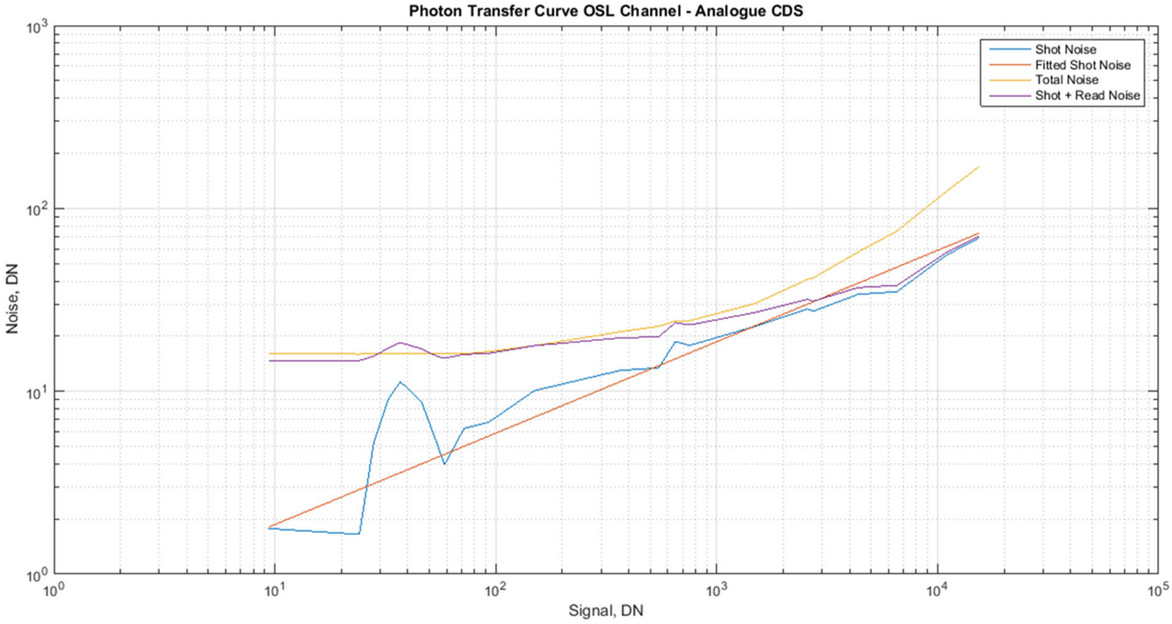

Figure 70 PTC - OSL Channel Analogue Readout

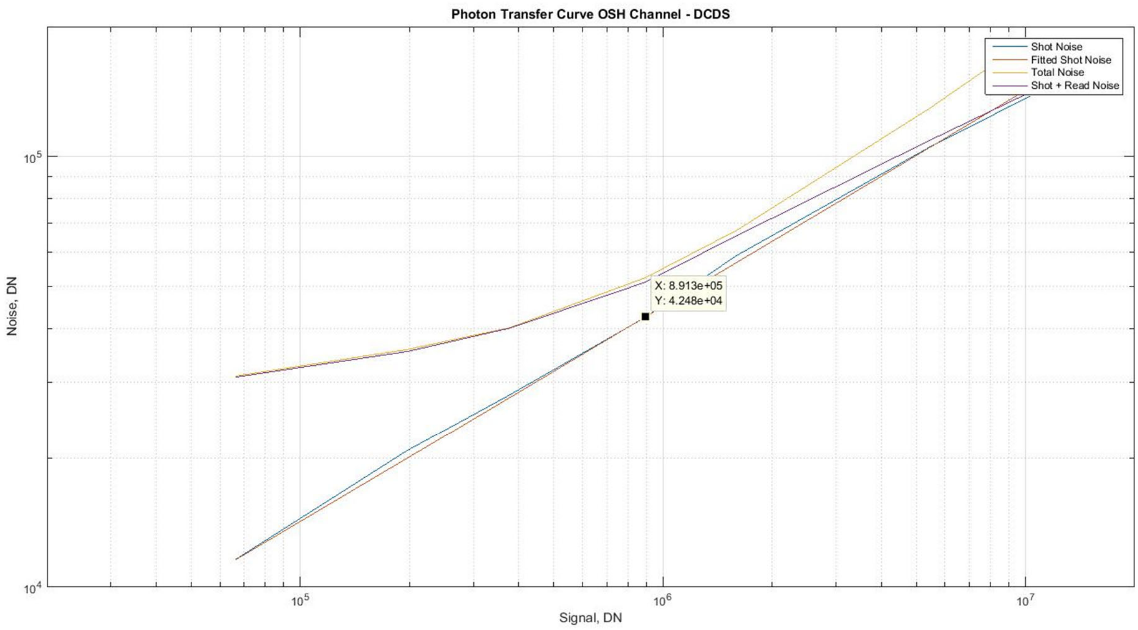

Figure 71 PTC - OSH Channel Digital Readout

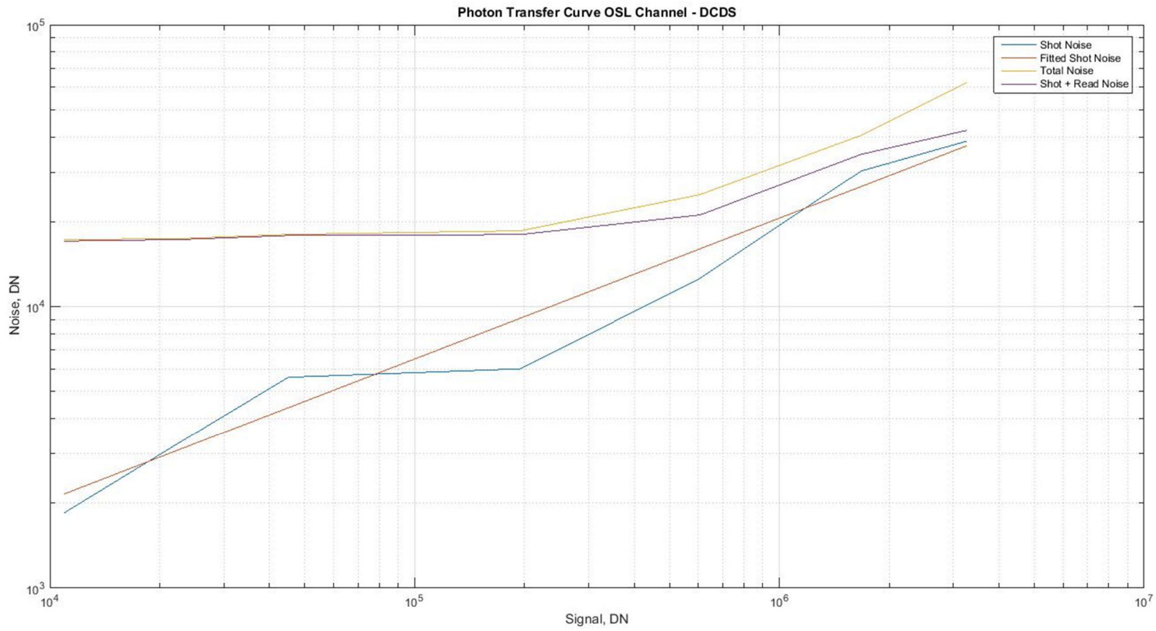

Figure 72 PTC - OSL Channel Digital Readout

For the same underlying principle, namely in the shot noise regime the noise σ_{Shot} is proportional to the square root of the signal *S*(DN), the shot noise curves shows the typical slope of ½ in logarithmic scale. Furthermore, given the limited dynamic range of the measurement up to 5000 to 7000 electrons, due to the gain of the amplification chain, nonlinearity effects are evident for the noisier OSL channel; the measurement should be carried out as close to the full well capacity of 90000 electrons as possible for the CCD97 as indicated in the datasheet. These nonlinearities for the OSL channel could also be due partially to a not perfect estimation of the offset and read noise and also reveal a problem of charge transfer when the slope is not ½ in log scale; the reader is referred to Janesick's book for a detailed explanation (Janesick, 2007).

The findings from the above calculations are summarised in Table 9.

Method/Channel	K_{ADC} (electron/DN)	Read Noise (DN)	Read Noise (electron r.m.s.)
Analogue OSH	0.59	15	8.9
Analogue OSL	2.87	14	40
Digital OSH	4.95e-4	18000	8.92
Digital OSL	2.35e-3	16980	40.02

Table 9 PTC Results

The gain electron/DN is in quite good agreement with the analytical calculations presented in this thesis; the noise is a few electrons higher than the expected. From simulations a noise of 3 to 4 electrons was expected, as no noise from power supplies or interference effects in terms of signal integrity had been taken into account.

Analysis of the sampled CCD waveform from the digital readout system reveals feedthrough of the serial register clocks affecting the signal waveform as shown in Figure 73.

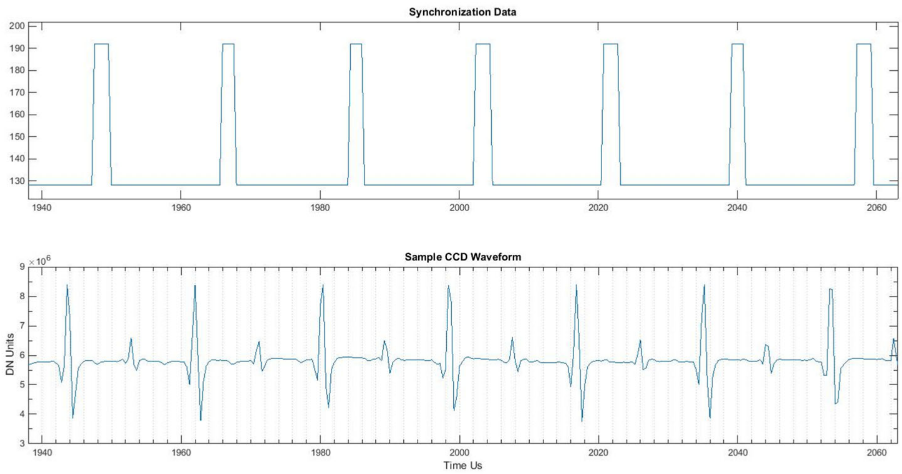

Figure 73 Real CCD Sampled Signal

The high peaks in Figure 73 correspond to the serial register charge transfer action, the smaller peaks to the reset feedthrough. Different voltage levels and timings were tested improving the performance only partially; it is believed that the problem was in the signal integrity and shielding at the camera head possibly coupled with where the serial register clocks depart from the CCD electronic box and connect to the camera head and affects the signal integrity of the CCD signal. These issues will be addressed as a follow up action to the work of this thesis.

Highlighting that the noise performance is similar for the analogue readout method and the digital one, as the conclusion of the simulation work anticipated, it is likely that the problem could happen at some stage before the readout happens. To confirm this hypothesis a test with the digital readout method was undertaken, connecting a 50 Ω resistor at the input of the AD8065 amplifier as shown in the scheme presented in Figure 74.

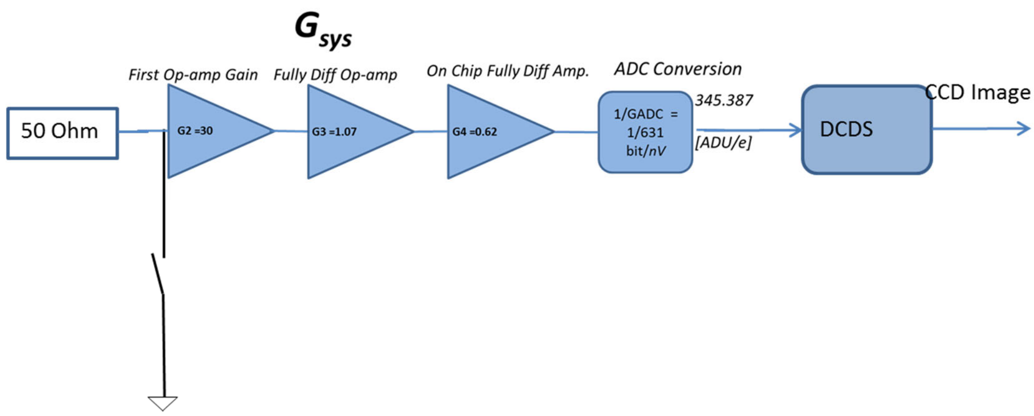

Figure 74 Test Setup Digital Noise Measurement

An image was acquired by DCDS method, in order to understand the noise introduced in the real circuit by the electronics itself. The corresponding CCD image is shown in Figure 75.

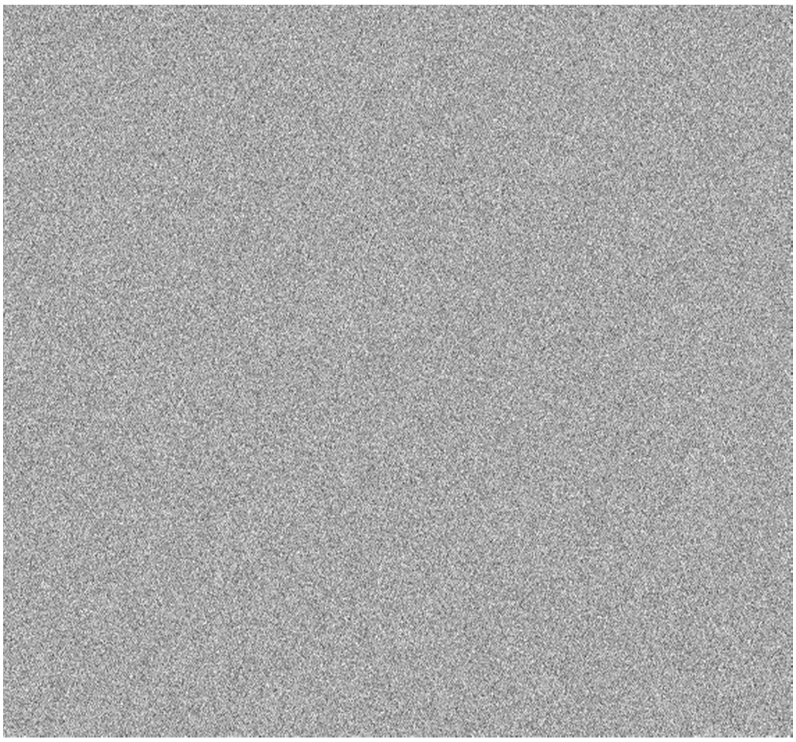

Figure 75 Digital Noise Image

The resulting image in Figure 75 has a standard deviation in pixel charge of 395 DN which using the conversion gain from the OSH digital photon transfer curve of 4.95e-4 electron/DN corresponds to a noise contribution of 0.19 electron r.m.s. to the total noise, which demonstrates that the noise added by the amplification chain, ADC converter and power supplies, is negligible, as it should be. The front-end amplifier AD829 is part of the camera head and so its noise is not of course included in this experimental result; interestingly, a simulation with the CCD time domain noise model of the amplification chain, including also the front-end amplifier AD829, was run. The calculated noise added by the complete amplification chain for the same pixel frequency as in the experimental test is equal to 0.76 electron r.m.s..

4.5.3 Multiplication Gain

This concluding paragraph will show the effect of enabling the multiplication gain on the CCD97. One of the illumination settings used to produce the photon transfer curve for the

OSL channel, 5 s of integration at minimum irradiance level and presented in Table 10 as 'Base' image, was adopted to calculate the multiplication gain at varying levels of RØ2HV.

Images	**Mean DN**	**Gain**
Base (5s integration)	22	1
Base - 60V on (Multiplication not enabled)	22	1
Base - 43.5V	2785	126.59
Base - 44V	5553	252.40
Base - 44.5V	10956	498
Base - 44.6V	12422	564.63

Table 10 Multiplication Gain

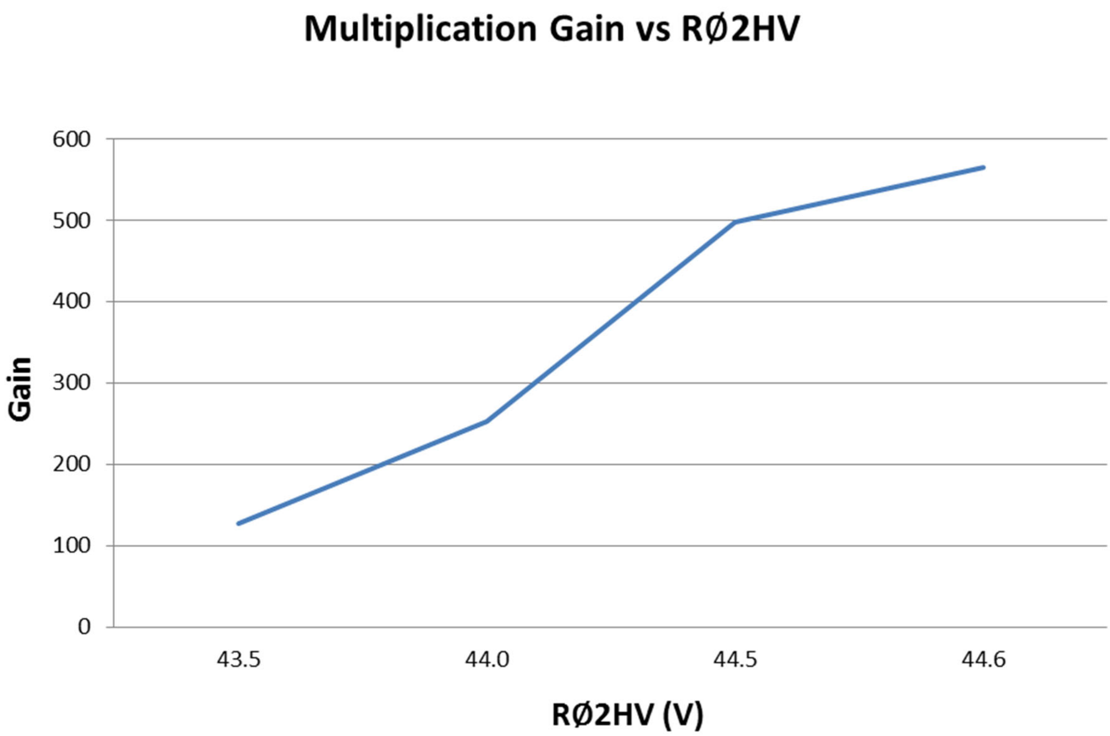

Figure 76 Multiplication Gain

Plotting the standard deviation at different voltage gain on a log log scale gives a slope of one as the region is dominated by fixed pattern noise. Given that the multiplication noise goes as $2^{1/2}$, for a given multiplication voltage and taking exposures of increasing time at a uniform illumination, the variance tends to be two times the mean value. In other words the shot noise would get multiplied by $2^{1/2}$.

The above considerations should be taken into account in assessing the SNR when adopting avalanche multiplication as a factor of F^2 would appear in the denominator as shown in paragraph 3.6 in the system gain expressions, increasing the shot noise of the image. For very low signal levels below 10 to 15 electrons the SNR with avalanche multiplication would give better results.

Future work following up the thesis will focus on evaluating the effect of the excess noise factor on the resolution of radiography like system by means of modulation transfer function and noise power spectrum as introduced in the next chapter.

5. Model of MCP Imaging, Experimental Evaluation and Applications

5.1 Introduction

The final word on the performance of the camera electronics and opto-mechanical design comes from the measurement of the performance in a real application scenario.

Camera systems for the detection of radiation are used in a vast field of applications and play a major role in medical science, non-destructive testing and space science.

X-ray radiographic imaging can be considered as a sort of compulsory test to assess the goodness of the assembly of the camera.

The aim of this chapter is to present a quantitative model of the conversion process from X-rays at the input to electrons at the CCD output, its comparison with real data from different types of scintillators and an assessment in terms of spatial resolution; the system was also operated at low temperatures, -70 °C, and for a long duration. The importance of the quantitative model stands in the possibility of using it to predict the performance of the imaging system to design changes.

This activity can be considered as necessary knowledge to model an application where the flux of the X-rays at the scintillator gets increased through the focusing of the rays via micro-channel plates (MCP). This stands as a test bed for the extension, under suitable conditions, to the focusing of thermal neutrons and its conceptual application in spatially resolved orbital neutron spectroscopy.

Firstly, calibration of the system for X-ray detection, followed by the derivation of a quantitative model and relative comparison with real measurements in terms of light yield and resolution of the system by means of Modulation Transfer Function (MTF) will be shown.

Secondly, a model of the performance of the MCP will be discussed and specific performance parameters introduced; analytic derivation and simulation will be considered.

Finally, a simulation model of the focusing optics for neutrons will be presented and its possible application in space science discussed.

5.2 Radiography Systems

Following the discussion at system level of a camera system for the detection of ionizing radiation presented in chapter 3, the experimental results and a comparative analytical model will now be shown.

The scintillators have been chosen primarily in terms of light yield performance at 17.5 keV, which is the energy at which the behaviour of an X-ray resembles that of a thermal neutron at the reflection with silicon glass (Fraser, 1993). Other selection criteria were the documented performance, spatial resolution and availability.

Specifically the four scintillators studied were:

- ZnSe(Te) 0.7 mm thickness (Ryzhikov et al., 2001)
- ZnSe(Te) 0.3 mm thickness
- Gd_2O_2S:Tb Gadox in the form of Kodak Lanex regular
- HB screen Gadox higher coating likely 134 mg/cm^2, supplied by Applied Scintillation Technologies (AST)

Aluminium holding masks were manufactured for the different sizes of scintillator. A large amount of work was required for the modification of the EPIC X-ray test facility (Turner, 2001) to accommodate the molybdenum secondary target and the camera system with scintillators.

Before proceeding to tube measurements it was necessary to know with good accuracy the photon flux in X-rays to the scintillator. To this aim a calibration facility based on a PNsensor already available in the X-ray vacuum chamber facility was setup to cover the energies of interest. Importantly the results were corrected by the QE of the detector and the attenuation of the entrance window (Hartmann et al., 1995), although the accuracy of the QE curve given by the manufacturer for energies above 10 keV is not as accurate as for lower energies because of a courser energy step resolution and a higher slope of the curve in the region which is more susceptible to quantification errors. SpecLab software was used to measure the counts for a Fe target and for a Mo target at first for the energy calibration procedure, then afterwards the real energy integration was carried out with the Mo target. The characteristic emission lines $k_{\alpha 1}$ and $k_{\beta 1}$ of the Mo and of Fe are clearly detectable in

Figure 77; the last line at around 26 keV being just an artefact from the electronic processing system of the equipment.

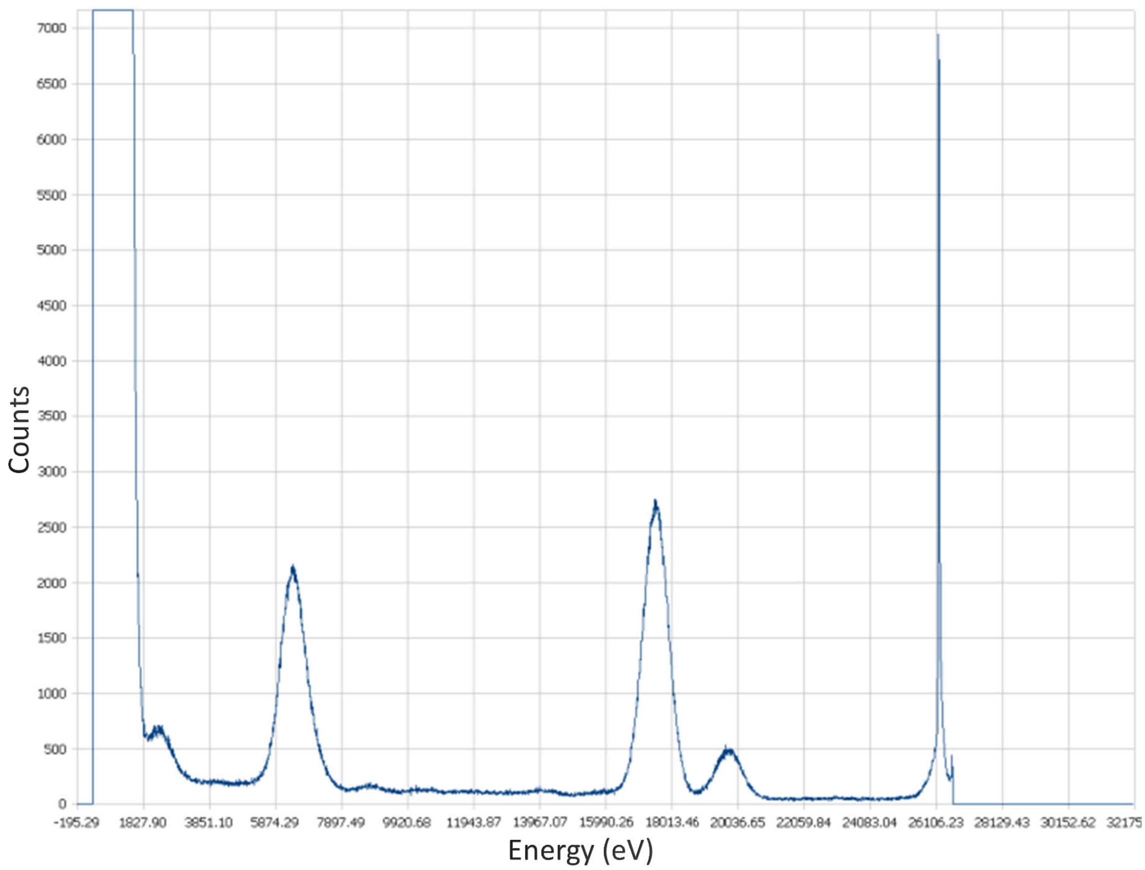

Figure 77 Calibration Spectrum for X-rays

The counts above the energy line of interest, 17.5 keV, could have been isolated using a 50 μm Mo filter that would have strongly attenuated energies above 20 keV, but such a filter was not available for use in the presented study.

In the analytical calculation, that will be shown later, it has been considered to group together the area under each of the Mo lines at the two energies of 17.479 keV and 19.471 keV. The counts from 21 to 24 keV were calculated with the SpectLab centroid utility to assign them to the energy of 23 keV and the counts from 24 to 27 keV were estimated, because of the presence of a peak at higher energy being an artefact of the PNsensor readout electronics. Likely higher energy counts could have been included because the voltage of the X-ray tube was nominally set to 40 kV, but previous measurements carried out with lower tube voltages showed a behaviour indicating a lower real value making possible higher energies contributions even less important.

The flux per mm^2 at the scintillator was calculated to be 11.83 photons·s^{-1} at the 17.479 keV line of the emission of the Mo. This was determined by geometry, in similar way as in Hansford (2012). Specifically, it was estimated from the solid angles between the source, the exposed area of the PNsensor (the detector) and the scintillator.

Energy (keV)	17.5	19.471	23	25.5
X-ray/(s·mm²)	11.83	3.10	1.45	2.02

Table 11 Theoretical X-Ray Flux at Scintillator Plane

Table 11 shows the theoretical number of X-rays that would have hit the scintillator at different energies as the vacuum chamber has a flange of 0.7 mm thickness of aluminium, hence the number of X-ray has been decreased by the relative absorption at each energy.

The analytical model to calculate $\overline{\Gamma}_{CCD}(E_j)$, the number of electrons per CCD pixel per second for each energy contribution, assuming unitary optical collection efficiency is expressed by:

$$\overline{\Gamma}_{CCD}(E_j) = \Phi_{APS}(E_j) \cdot T_X(E_j) \cdot \alpha_s(E_j) \cdot \rho_R \cdot N_{photons}(E_j) \tag{5.1}$$

Where:

- $\Phi_{APS}(E_j)$ is the number of X-rays per second in the equivalent area of a CCD pixel on the scintillator
- $T_X(E_j)$ represents the transmission attenuation by the chamber flange and eventual layers in front of the scintillator calculated for each energy and scintillator
- $\alpha_s(E_j)$ represents the absorption of the X-ray by the scintillator screen which follows the well-known exponential equation related to the mass absorption coefficient $\mu(E_j)$; it was assumed to be 0.96 for Lanex (Ginzburg, 1993) and 1 for ZnSe (Opolonin et al., 2013)

- ρ_R takes into account the contribution of the back light reflection layer of the screen and the assumption that half of the light photons are emitted in the direction of the detector (Barrett et al., 1981)
- $N_{photons}(E_j)$ is the number of optical photons emitted by the interaction of an X-ray with a given energy and takes into account the spectral matching between the scintillator and the CCD detector; it will be explained later in detail

Finally, the contributions at each X-ray energy are summed:

$$\overline{\Gamma}_{CCD} = \sum_j \overline{\Gamma}_{CCD}(E_j) \tag{5.2}$$

Γ_{CCD}, the number of electrons per pixel·s, is obtained by multiplication with the optical collection efficiency η_L:

$$\Gamma_{CCD} = \overline{\Gamma}_{CCD} \cdot \eta_L \tag{5.3}$$

η_L was introduced in chapter 3 and is the efficiency for a Lambertian source because of the similar angular dependent radiance distribution of the screen (Yu, 1997). In the actual system adopting a Pentax 25 mm $F_{\#}$ 1.4 lens and given a demagnification factor m = 6.83, η_L = 0.002. This is the most detrimental factor in the photon collection chain; a fibre optic bundle would increase the performance but in a testing stage its adoption would have limited flexibility of the system.

Considering the above assumptions the analytical model was developed in Matlab and assessed for the 0.7 mm thick ZnSe and Lanex scintillators and gave the results shown in Table 12 in terms of electron/(pix·s) for the X-ray energies considered.

Energy (keV)	17.47 & 19.47	23	25.5
ZnSe(Te) electron/(pix·s)	0.1313	0.0287	0.0488
Lanex regular electron/(pix·s)	0.0923	0.0189	0.0321

Table 12 Modelled Number of Electron/(Pix·s) for X-ray Energies

Γ_{CCD} for the Lanex screen was found to be 0.1433 electron/(pix·s).

The model allowed estimation of the number of light photons per X-ray event at the specific energy leaving the screen in the direction of the CCD detector as indicated in Table 13.

Energy (keV)	17.47	19.471
ZnSe(Te) Photons/X-ray	900	1017
Lanex regular Photons/X-ray	592.7	669

Table 13 Modelled Number of Photons Leaving the Scintillator Screen

The different values between the two scintillators are due to the different wavelengths of emission of the screens. Taking into account the calculation for the Lanex regular screen the values simulated are in very good agreement with the experimental results reported by various research groups, for instance in Ginzburg (1993) which reports a value at 17 keV of about 600 photons.

No values have been found in literature concerning a ZnSe scintillator in terms of photons leaving the side of the screen to provide a comparison.

The calculation of $N_{photons}(E_j)$ was more demanding as it had to take into consideration the spectral matching between the CCD detector and the spectral luminescence spectrum of the scintillator. In the general form it follows the integral equation reported in chapter 3 but for numerical calculation it can be expressed by:

$$N_{photons}(E_j) = \frac{1}{1239}\eta_{screen} \cdot E_j \cdot \sum_i f(\lambda_i) \cdot \eta_{CCD}(\lambda_i) \cdot \lambda_i \qquad (5.4)$$

Where:

- η_{screen} represents the conversion efficiency of the screen assumed to be 15% for lanex (Tyrrell, 2005) and 19% for ZnSe (Ryzhikov et al., 2001)
- $f(\lambda_i)$ is the normalised spectral luminescence of the scintillator

- η_{CCD} is the quantum efficiency of the detector
- λ_i the wavelength in nm

In order to calculate the above quantities a numerical integration of the spectral luminescence curves of the scintillators was carried out through visual comparison with the datasheet values and mathematical fitting at each nm interval, starting from the graphical expression for the ZnSe luminescence shown in Ryzhikov et al. (2001) and presented in Figure 78.

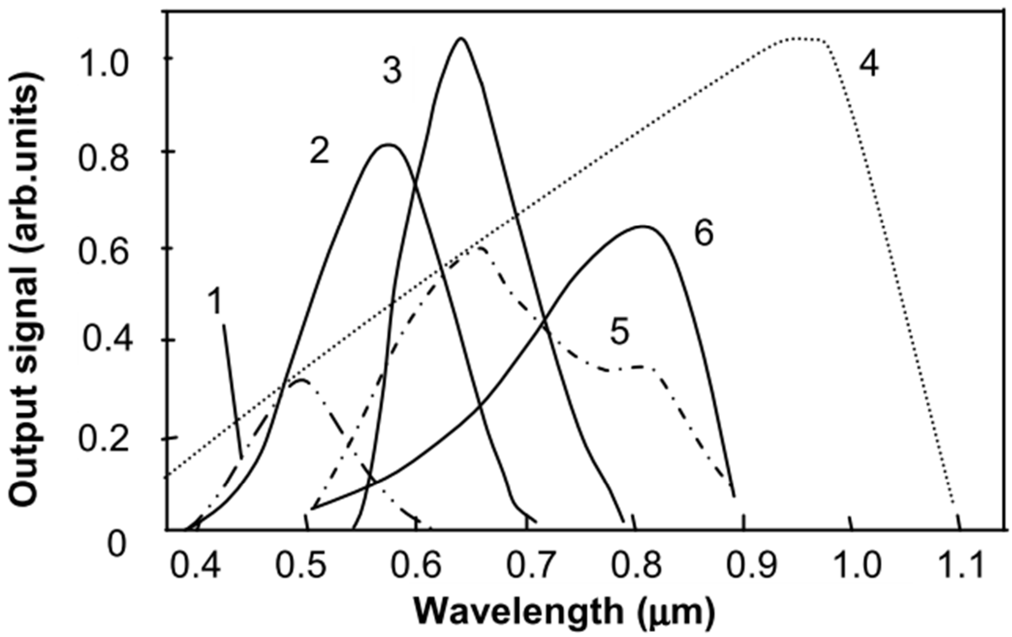

Spectral-luminescent characteristics of the scintillators: 1 - $CdWO_4$; 2 - CsI(Tl); 3 - ZnSe(Te); 4 - sensitivity of Si photodiode; 5 - sensitivity *p*ZnTe-*n*CdSe ($N_e=2.4\times10^{17}$ cm^{-3}) photodiode; 6 - sensitivity *p*ZnTe-*n*CdSe ($N_e=2.4\times10^{15}$ cm^{-3}) photodiode.

Figure 78 Relative Spectral Luminescence - ZnSe(Te)

Curve 3 in Figure 78 was reconstructed in Matlab and normalised to the total area. In reality it is reported that the peak of emission is at 610 nm and the reconstructed curve agrees with that value as shown in Figure 79.

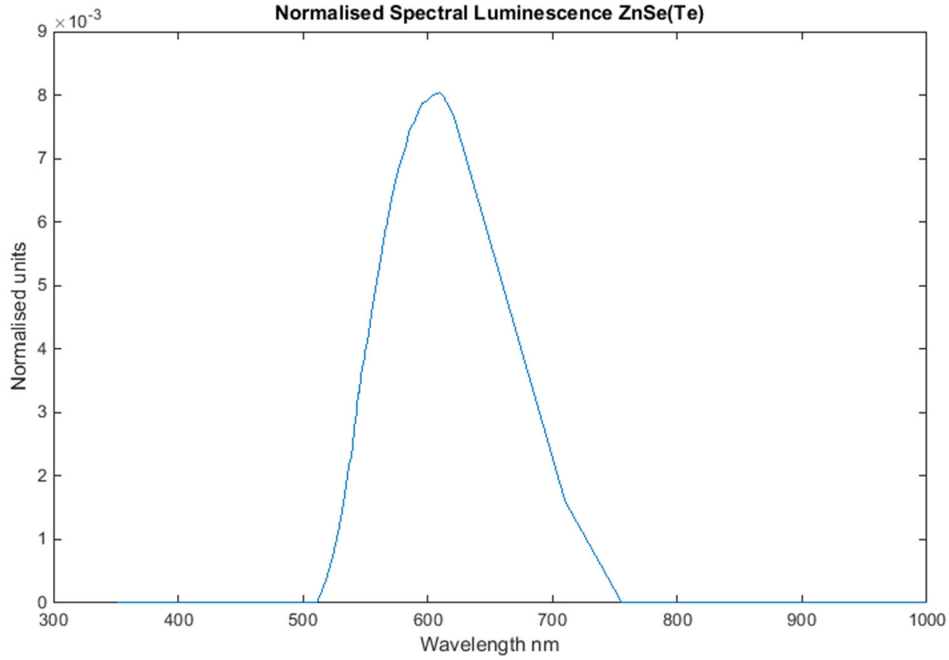

Figure 79 Numerically Estimated Luminescence - ZnSe(Te)

Similarly it was done for the Lanex scintillator, whose curve was presented in chapter 3 Figure 22, and its discrete spectra reconstruction is shown in Figure 80.

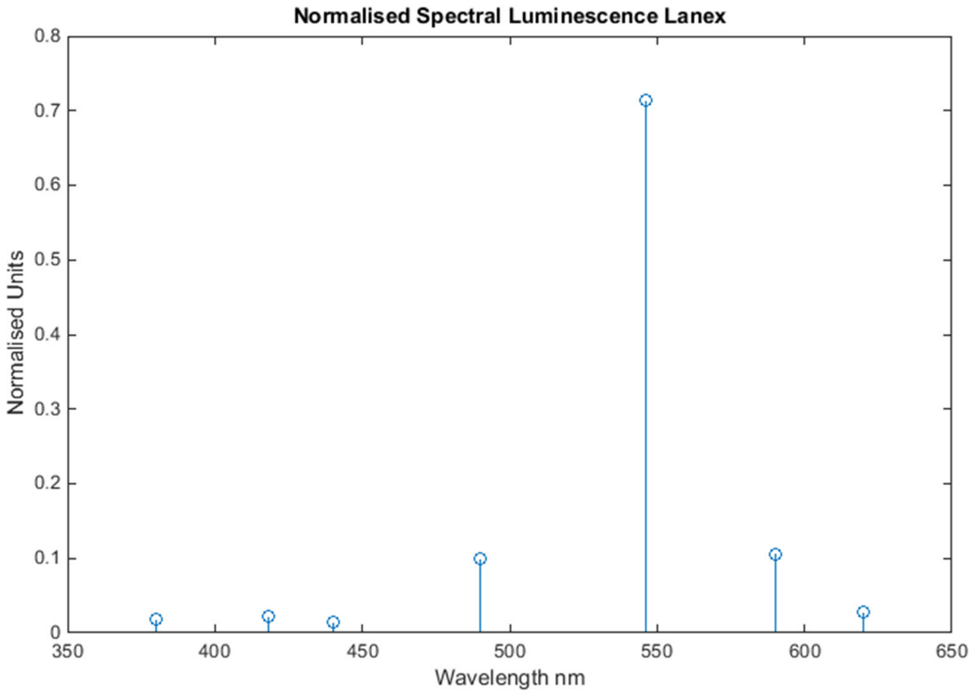

Figure 80 Numerically Estimated Luminescence - Lanex

Each wavelength of emission was weighted by the normalised area that represents the area of the curve under each discrete spectral emission line to which the spectral luminescence Lanex screen can be approximated to.

The QE curve of the sensor was also mathematically reconstructed in Matlab and is shown in Figure 81.

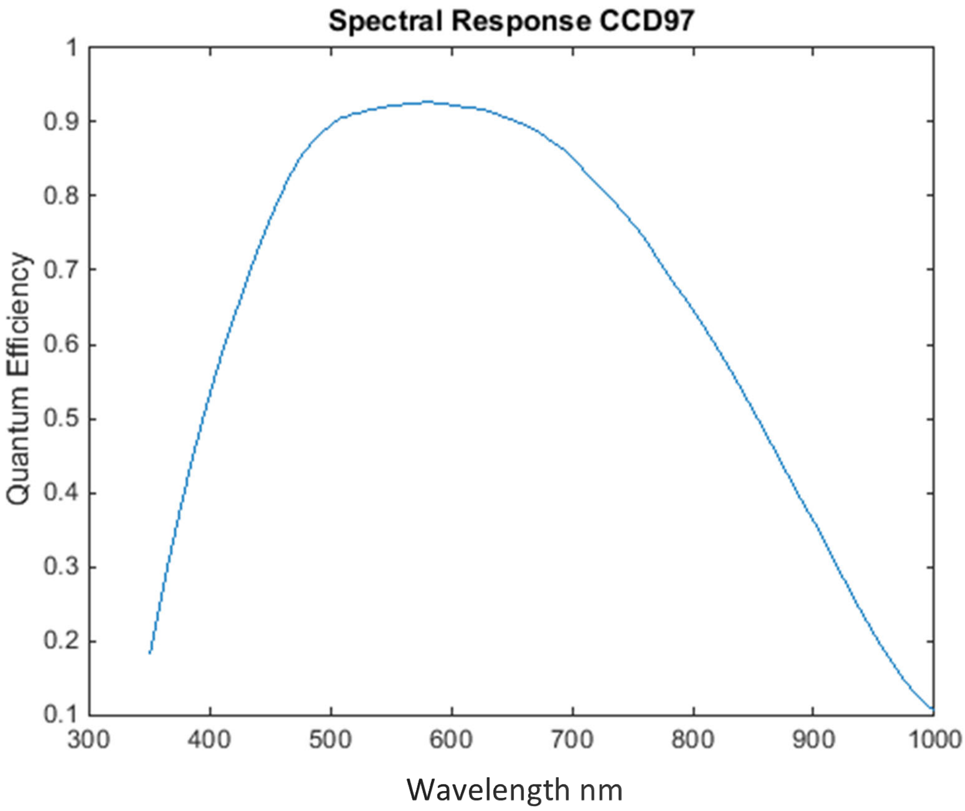

Figure 81 Numerically Estimated CCD97 Quantum Efficiency

The product of the two curves, the detector spectral response and the scintillator normalised spectral emission, gives the spectral match between the detector and the scintillator. The ZnSe spectral match is shown in Figure 82.

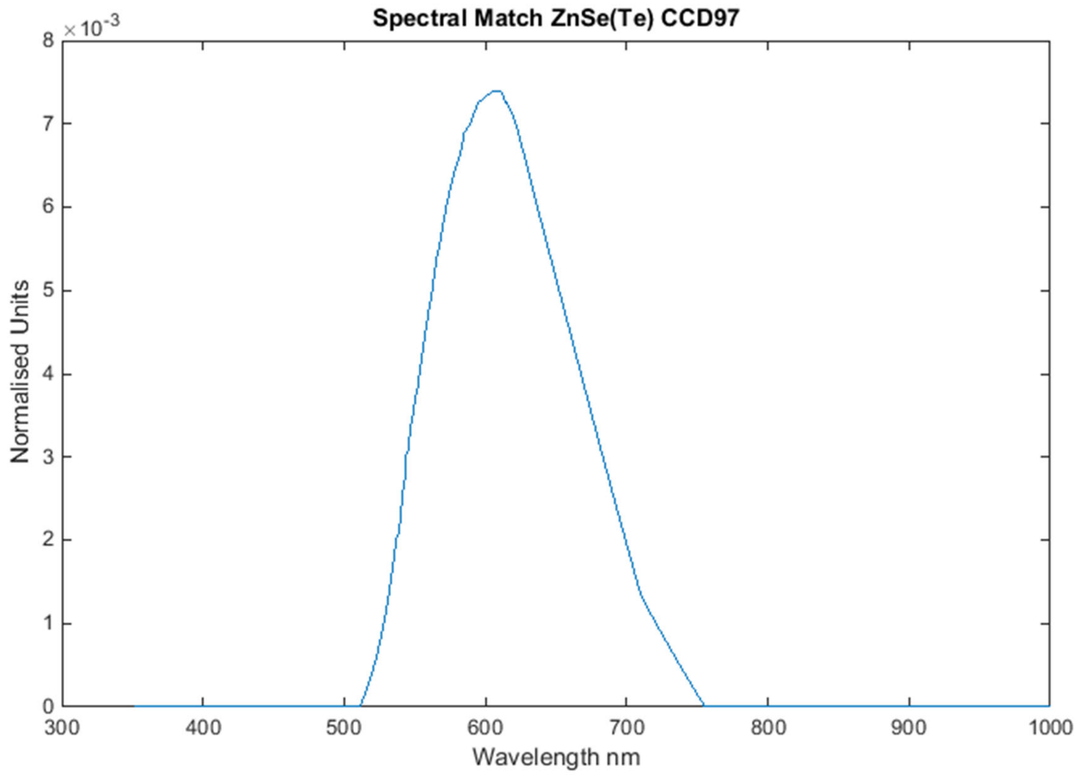

Figure 82 Spectral Matching ZnSe(Te) - CCD97

The matching factor η_{CCD}, introduced in chapter 3, is given by the area of the spectral match curve, and has a value of 0.907 for ZnSe coupled to a CCD97, so a loss of only of 10%.

The Lanex spectral match is shown in Figure 83.

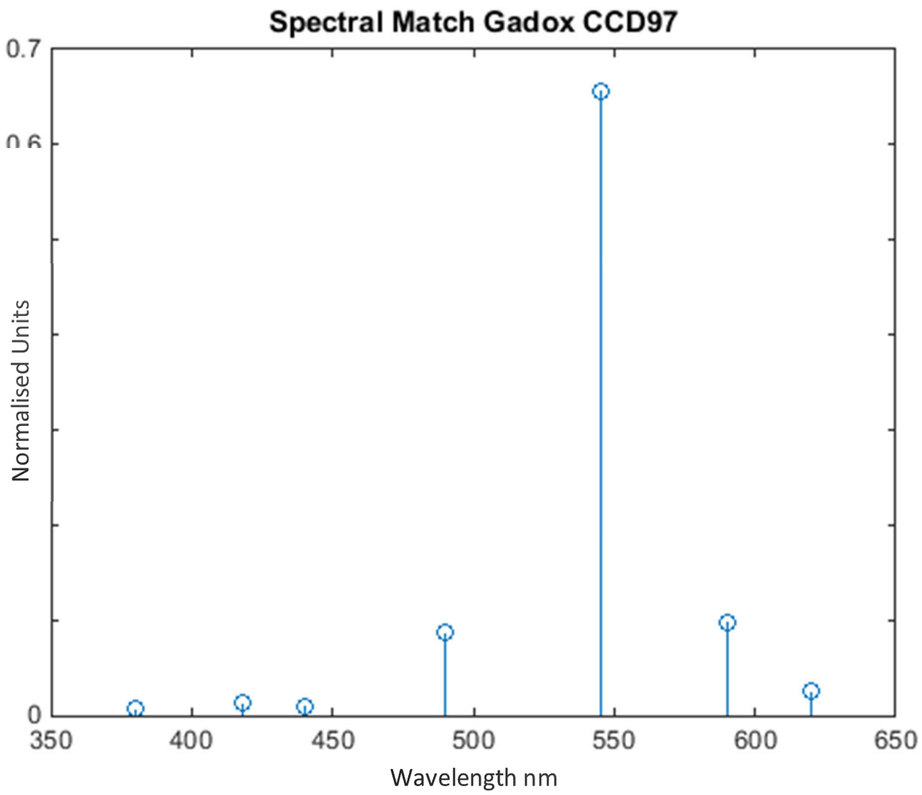

Figure 83 Spectral Matching Lanex - CCD97

The Lanex matching factor has a value of 0.898 so a value very close to the ZnSe scintillator.

At this point a number of flat field images under the same incident flux condition, for integration times up to three hours long, were collected for each scintillator and the mean value of electron/(pix·s) was assessed at the centre of the image, in the area of the scintillator corresponding to the position of the PN sensor used for calibration of the flux.

Table 14 summarises the experimental findings.

	ZnSe(Te) 0.7 mm	ZnSe(Te) 0.3 mm	Lanex regular	HB screen
$\Gamma_{CCDreal}$ (electron/(pix·s))	0.1986	0.1722	0.1944	0.2312

Table 14 X-ray Experimental Results

The results relative to the simulation reveal higher values than expected, likely due to the presence of higher energy X-rays above 27 keV. For instance, the simulation gave a value of Γ_{CCD} = 0.1433 electron/(pix·s) up to 27 keV of energy for Lanex against a real $\Gamma_{CCDreal}$ of 0.19. The simulated behaviour of the ZnSe would match the measured values but considering the higher amount of X-rays at high energy, which experience less attenuation through the 0.7 mm Al vacuum flange, results in an overestimation for the ZnSe screen. However, Litichevskyi et al. (2011) confirm similar results in terms of light yield for the Lanex screen. This is also confirmed by the fact that the HB screen has the best performance (Tyrrell, 2005) indicating the presence of higher energy X-rays because the screen would have given better performance compared to the Lanex regular for energies above 25 to 30 keV (AST, 2015). The thickness and coating of the HB screen would have prevented better performance if only energies below 20 keV were present.

To compare the performance of the scintillators in terms of spatial resolution, the MTF response to a slanted edge of tungsten, with thickness 1 mm and polished at the edge with a Struers diamond wheel (Struers, 2017) to a roughness of 50 μm measured by Scanning Electron Microscope (SEM), was calculated.

The well-known method by Samei et al. (1998) with the tungsten edge tilted at 3° relative to the vertical pixel line was adopted to calculate the MTF.

The method can be summarised in the following steps:

Sampling the edge spread function, fitting the resulting curve and differentiating to give the line spread function, up sampling the LSF and finally discrete Fourier transforming gives the Optical Transfer Function (OTF), represented by:

$$OTF(k_x, k_y) = MTF(k_x, k_y) \cdot \exp(j \cdot \Phi)(x, y) \tag{5.5}$$

Where k_x, k_y are the spatial frequencies, $\Phi(k_x,k_y)$ is the phase and the modulus of the OTF is called modulation transfer function (MTF).

Spatial frequencies are measured in units of cycles per mm (cy/mm) or also named as line pairs per mm (lp/mm), meaning the number of white and black vertical parallel stripes that fit in one mm, the higher the number of white and black pairs the higher the spatial frequency. The MTF curve characterises an optical system in terms of the spatial resolution that the system is able to resolve and process, as a linear system is characterised in frequency by the frequency transfer function. A value of one for the MTF means that the system reproduces perfectly the related spatial frequency, lower values of MTF mean that the optical system is not able to reproduce with fidelity the spatial frequency pattern of interest. The MTF curve of the complete optical system can be seen as the product of the MTF curves of each component along the chain, e.g. scintillator, mirror, lens, detector, and has the shape of a low pass transfer function meaning that low frequency spatial details are represented better than high frequency details. Usually a value of 0.1 for the MTF can be accepted as a mean to compare the performance of an optical system in terms of its capability to reproduce spatial details.

A sample of one of the acquired images is shown from Figure 84 to Figure 86 for each of the ZnSe, Lanex regular and HB AST screens respectively.

The lighter part of the images corresponds to the area where the scintillator is directly exposed to X-rays while the right part of the image is the unexposed area because of the attenuation of the tungsten sheet with its edge passing through the centre and inclined of 3°. The aluminium holder for the Lanex and ZnSe scintillators has an aperture of 50 mm by 50 mm with a recession of 1 mm in thickness by 2.5 mm wide with rounded corners to position the screen. The holder for the HB screen has an overall aperture of 70 mm by 70 mm. The visible patterns at the bottom left corner of the images, especially detectable for the Lanex and HB screens, correspond to wiring and support structures at the internal side of the vacuum chamber external aluminium flange.

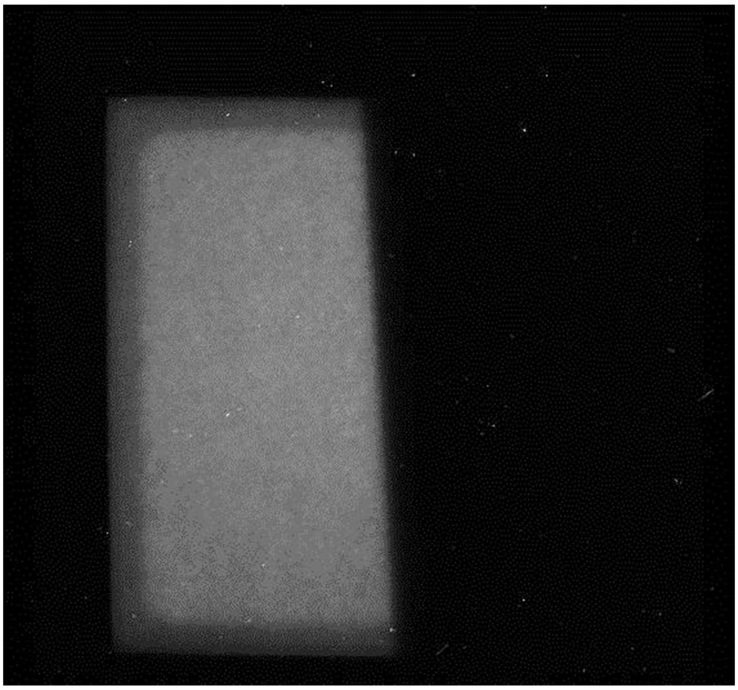

Figure 84 Edge - ZnSe(Te)

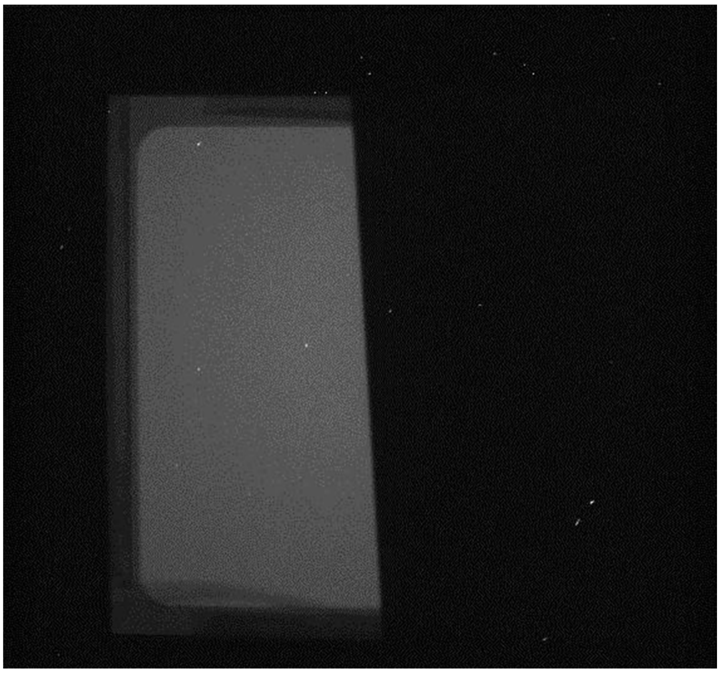

Figure 85 Edge - Lanex

Figure 86 Edge - HB Screen

From the collected images the higher sharpness of the Gadox based scintillators, namely Lanex and the HB screen, is visually noticeable observing the representation of the tungsten edge in the image.

The granular structure of the ZnSe screen plays a major role; dependency from the granularity/powder of the screen has been studied by Litichevskyi (2013) for ZnSe with results that vary from 2 to 7 line pairs per mm (lp/mm) using standard test objects for X-ray radiography.

Analytical comparison of the spatial resolution among the four screens is carried out analysing the respective MTF curves. MTF was calculated using an adapted Matlab code by Burns (2000) and the MTF plots are shown from Figure 87 to Figure 90.

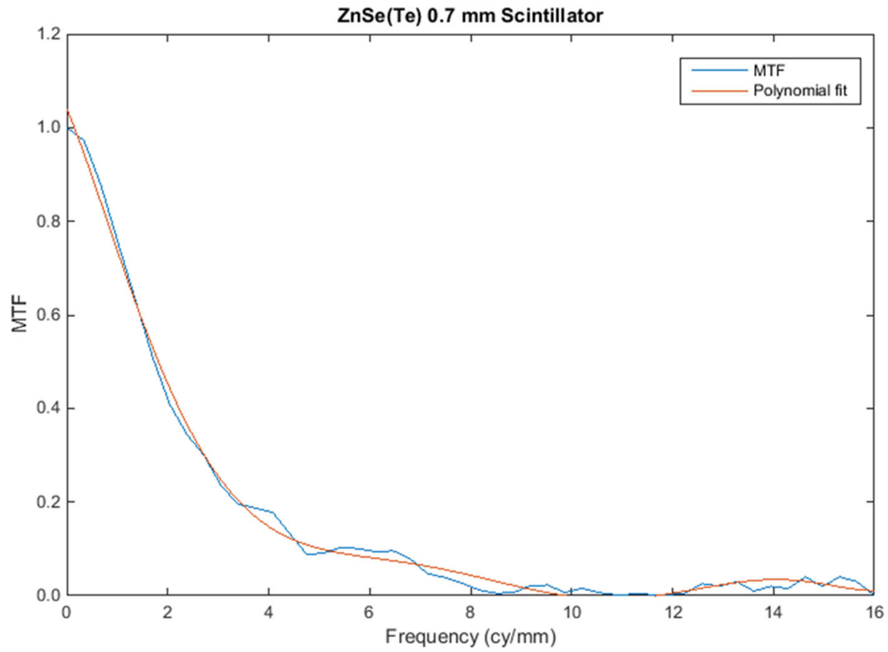

Figure 87 MTF - ZnSe 0.7 mm

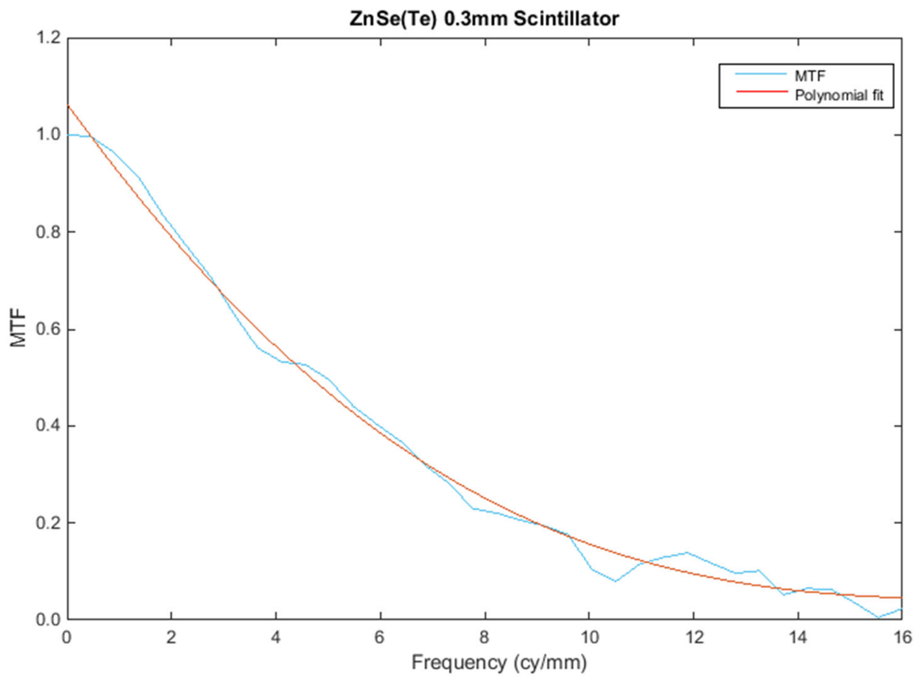

Figure 88 MTF - ZnSe 0.3 mm

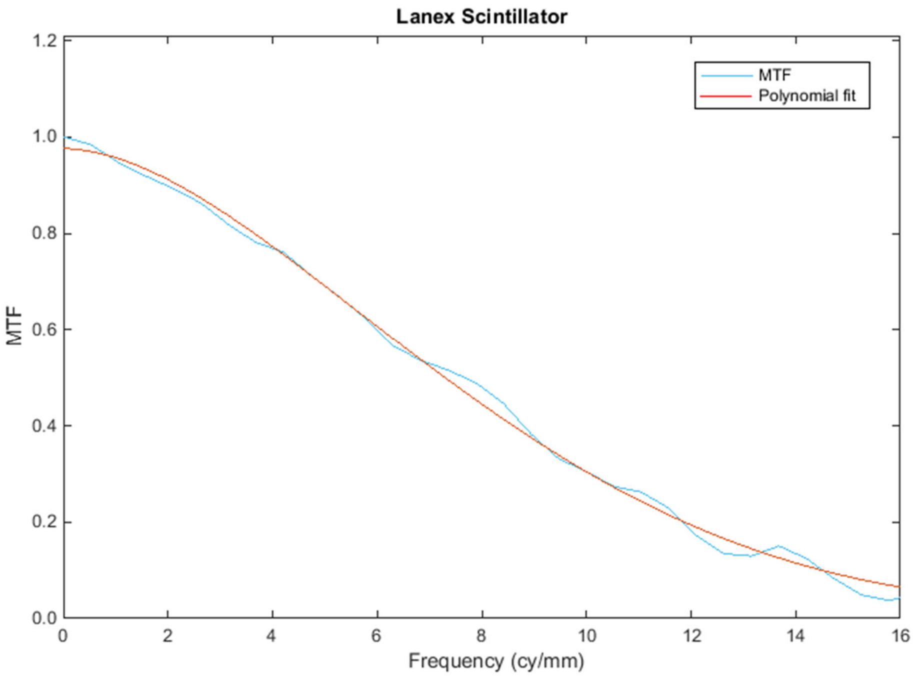

Figure 89 MTF - Lanex

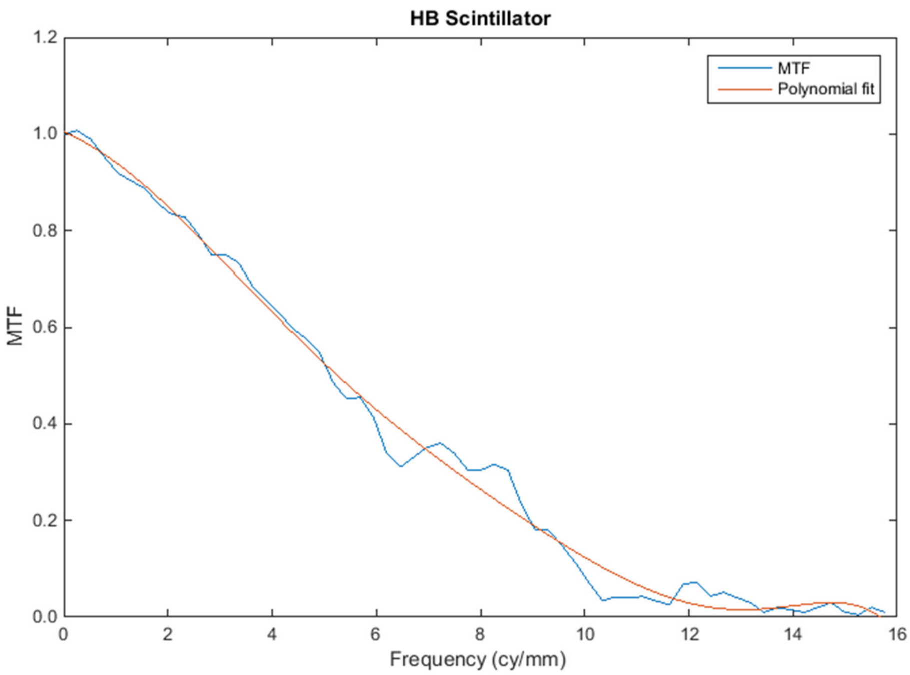

Figure 90 MTF - HB Screen

Assuming a resolution at 10% contrast, calculated on the 7th degree polynomial fit curve to the MTF raw data as shown in the MTF figures, Table 15 summarises the results.

	ZnSe(Te) 0.7 mm	ZnSe(Te) 0.3 mm	Lanex regular	HB screen
MTF at 10%	4.8 cy/mm	11.4 cy/mm	14 cy/mm	10 cy/mm

Table 15 MTF Measurements

The results confirm the first visual impression and the HB screen although having higher light responsivity has a lower resolution as confirmed also in literature (Tyrrell, 2005). Interestingly, but not surprisingly, the thinner ZnSe has better a better performance than the thicker one given the smaller optical path of light through the screen. Normally, for better resolution and at the energy of Mo lines, finer screens, like Kodak Fine, give the best performance as used in mammography diagnostics.

The overall resolution performance confirms the goodness of the camera in comparison with high end systems using similar scintillators (Graeve et al., 2001).

A more exhaustive understanding of the quantum detection processes could have been done considering the detection quantum efficiency (*DQE*) of the system (Cunningham, 2000):

$$DQE(f) = \frac{\Phi(K \cdot MTF(f))^2}{NPS(f)} \tag{5.6}$$

Where:

- K is the gain factor of the system
- Φ is the X-ray fluence
- *NPS(f)* is the noise power spectrum giving information of the noise distribution in the image with spatial frequency

DQE express the ratio of the $(SNR_{out})^2/(SNR_{in})^2$ and can be interpreted as the effective quantum utilisation efficiency as if the detector acts as an ideal photon counter taking into account the degraded performance along the transformation chain from X-ray to readout electrons in the sensor.

A possible future development of the work of the thesis could be to assess the impact that enabling avalanche multiplication on the CCD97 has on the performance of the system expressed in terms of the quality parameters above mentioned, namely MTF and DQE assuming an accurate measurement of the total X-ray fluence is available.

5.3 Micro-Channel Plates Imaging

5.3.1 Introduction

Micro-channel plates are made of lead glass with closely packed microscopic channels manufactured by chemical etching.

MCPs were originally used as electron intensifiers by the means of avalanche multiplication. A single electron at the entrance of the channel striking the channel surface excites secondary electrons; a bias voltage applied between the walls accelerates the electrons down the channel liberating more secondary electrons on its way through the walls, to the extent to make detectable a single incident event.

Angel (1979) proposed its application for X-ray telescopes. At X-ray energies, photons can be reflected if they impact the sides of a glass at an angle less than their critical angle at a given energy.

MCPs can be distinguished into two types, flat and slumped. Flat MCPs can be considered point to point focusing systems while slumped MCPs behave with the optical reflection characteristics of a spherical mirror for incident particles below their critical angle.

Figure 91 shows the two types of MCP. Where l_s is the source distance, l_i is the image distance and R_{MCP} is the curvature radius of the slumped MCP.

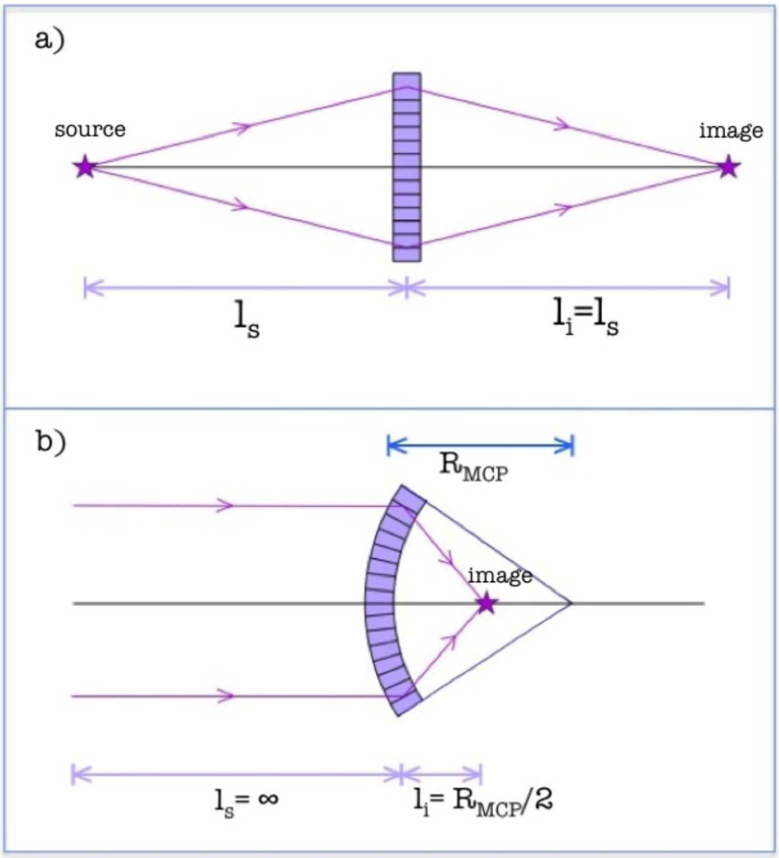

Figure 91 MCP Reflection (Courtesy of Pippa Moyenex, SRC University of Leicester)

The benefit of MCP technology is that telescopes can achieve larger fields of view than more traditional optics at significantly lower mass and volume requirements (Fraser, 1997). Rays, depending on the angle of incidence at the walls, get reflected a different number of times on each set of parallel walls within a channel. Rays reflected once for each wall (odd,odd) will be directed to the focal square area at the optical axis. The term focal square will be used from this point on for this specific case.

Rays reflected once in one direction only will be concentrated only in that direction as cross arms in the focal plane. Rays not reflected will contribute to the diffuse background (Angel, 1979).

MCPs achieve a resolution related to the size of the channel but deformations due to misalignments between the channels and distortions in the structure strongly affect the final performance.

The collection area efficiency depends on the energy of the rays, grazing angle, and the aspect ratio of the plates.

The ratio between the focal square area, cross arms and diffused background depends on the aspect ratio and critical angle.

For a flat square MCP the optimal ratio is expressed by (Chapman et al., 1991):

$$\frac{D}{L} = \frac{\theta_c}{\sqrt{2}} \tag{5.7}$$

Where D is the side of the square, L is the length of the channel and θ_c is the critical angle. This means 34.3% of the photons are focused into the central square, 24.3% in each of the one- dimensional cross arms and 17.2% in the unfocused background.

In the presented study flat MCPs as a point to point focusing system were investigated first in terms of their focusing capability in the focal square as concentrators of flux.

The average count of photons in the focal square for a flat MCP can be expressed as (Chapman et al., 1991):

$$I_{00} = \frac{4 \cdot \theta_c^2 \cdot \Omega_{00} \cdot \eta}{b_{\max}^2} \tag{5.8}$$

Where:

- Θ_c is the critical angle
- b_{max} is the area of the focal region
- η is the aperture efficiency
- Ω_{00} is the collection efficiency focal square

The equation expressing I_{00} has been inserted in an analytical model to assess the performance of the focusing system together with the experimental equation to calculate the critical angle for hard X-rays as a function of energy, expressed by (Willingale et al., 1998):

$\Theta_c = a \cdot \exp^{-1.04}$

Where the constant a has the value 144 and the unit of angle is the arc-minute and the unit of energy is the keV.

The simulation of the system was supported by a Monte Carlo sequential ray tracing method (Brunton, 1997) developed at University of Leicester.

For the necessity of extrapolating specific information from the results of the simulation a number of Matlab routines were developed to process the raw information from the detected rays in the focal plane.

A facility was designed to test a flat square MCP at the energy of 17.5 keV. The same flat MCP had already been the object of testing at the University of Leicester (Price et al., 2002). The facility is shown in Figure 92.

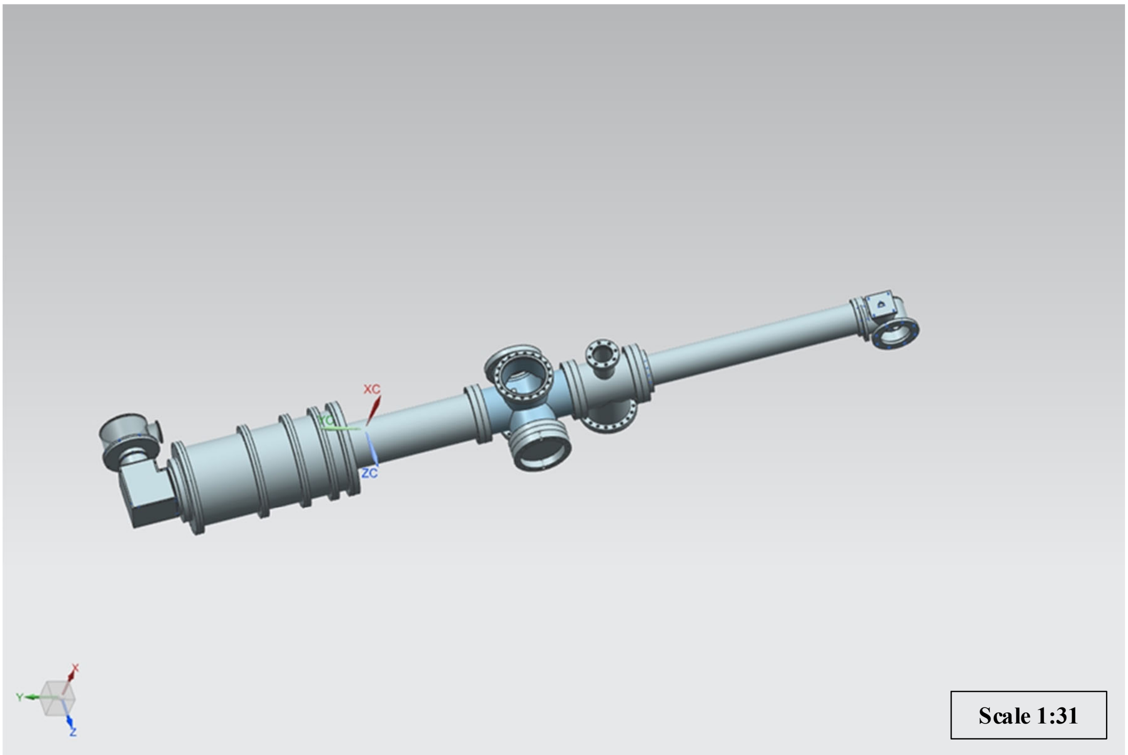

Figure 92 MCP Test Facility Design

The facility allows testing of the MCP optics at a distance of 150 cm from detector to optic and the same distance from optic to X-ray point source.

The optic and its characteristics are shown in Figure 93.

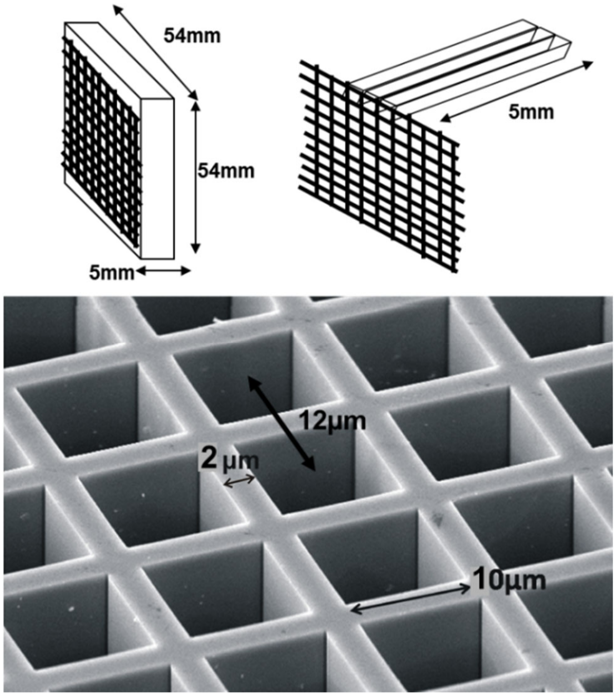

Figure 93 Flat MCP Geometry

The conceptual setup of the measurement through the camera developed under the scope of the thesis is shown in Figure 94.

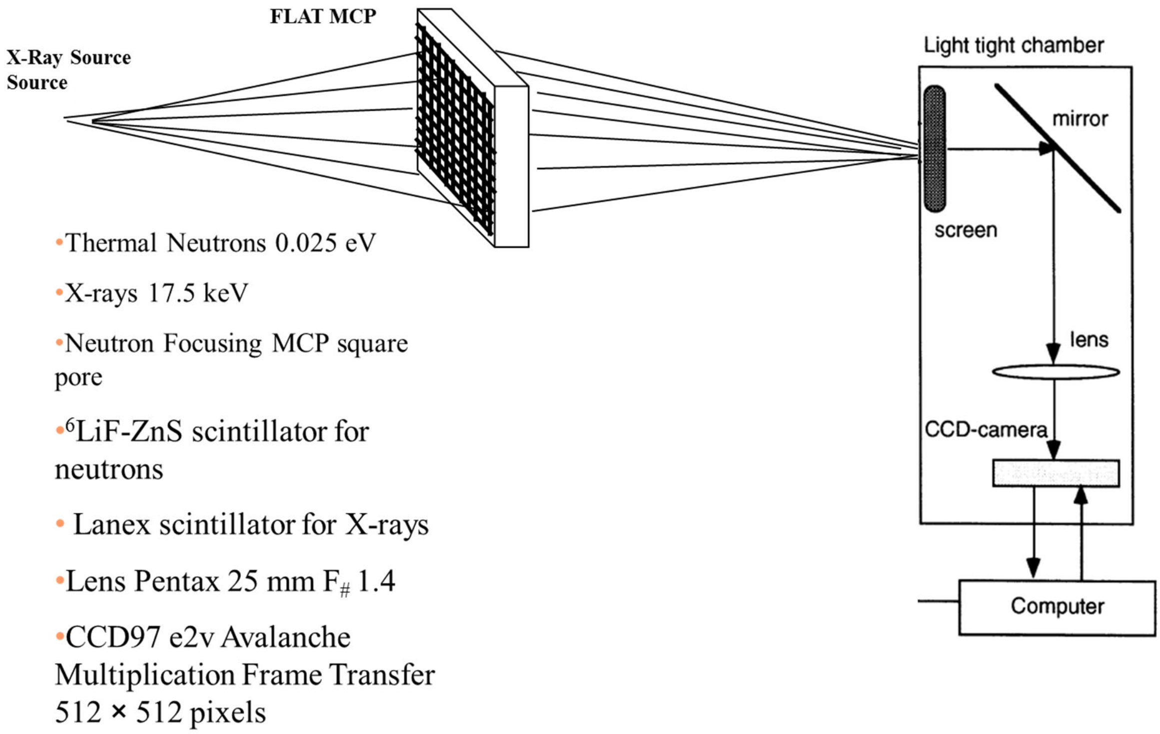

Figure 94 Conceptual Experiment Setup

It is to note that at first predicted measurements are simulated for X-rays and then subsequently for the case of neutrons. The data from the real measurements carried out by Price et al. (2002) for the optics are analysed to get an estimation for the measurements that will be done at 13.5 keV for X-rays as a follow up to the work of the thesis. Subsequently, the optic will be characterized at a nuclear research reactor for the interaction with thermal neutrons, the objective of the last part of this chapter.

5.3.2 MCP Modelling for X-Rays

The comparison of the optics has been done considering at first what would be the behaviour of the optic for an energy representing the optimal case given the aspect ratio $L/D = 500$. The energy that meets the requirement from the empirical formula introduced is 13.5 keV, maximising the collection area in the focal square.

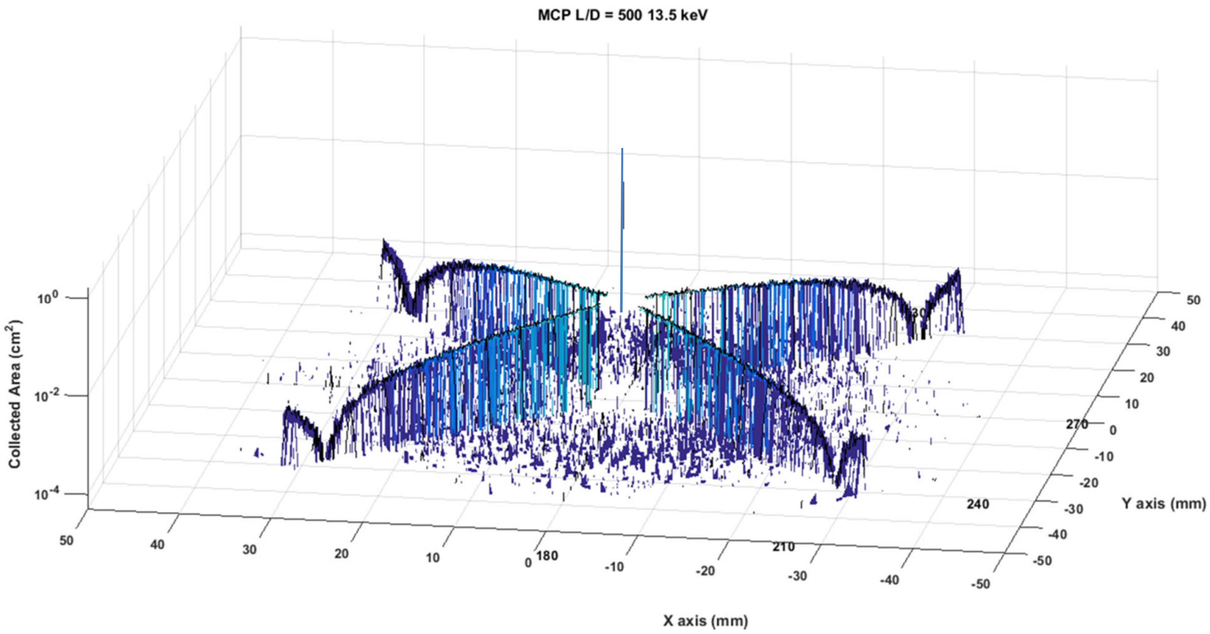

Figure 95 Point Spread Function for Optimal MCP/Energy

Figure 95 shows the typical cruciform point spread function and the arms, represented in figure as a tri-dimensional polar plot with a catchment radius of 45 mm, half of the side of the square detection area of 90 × 90 mm used in the presented calculations. The central focus square ideally has a geometrical area of $(2 \cdot D)^2$ with a collected area of 6.9 cm^2, equivalent to the 34% of the counts. The area at the detection plane represents the part of the area of the optic entrance plane that is projected on the detector plane as a consequence of the focusing action of the optic. The vertical axis in the plot is the 'collection area' that photons will have interacted with on their journey through the MCP to the focal plane. Each detected event transports the same fraction of the optic aperture area, which depends on the number of rays used in the Monte Carlo simulation.

In comparison, the simulation for the measurement at low energy conducted by Price et al. (2002) at University of Leicester is shown in Figure 96.

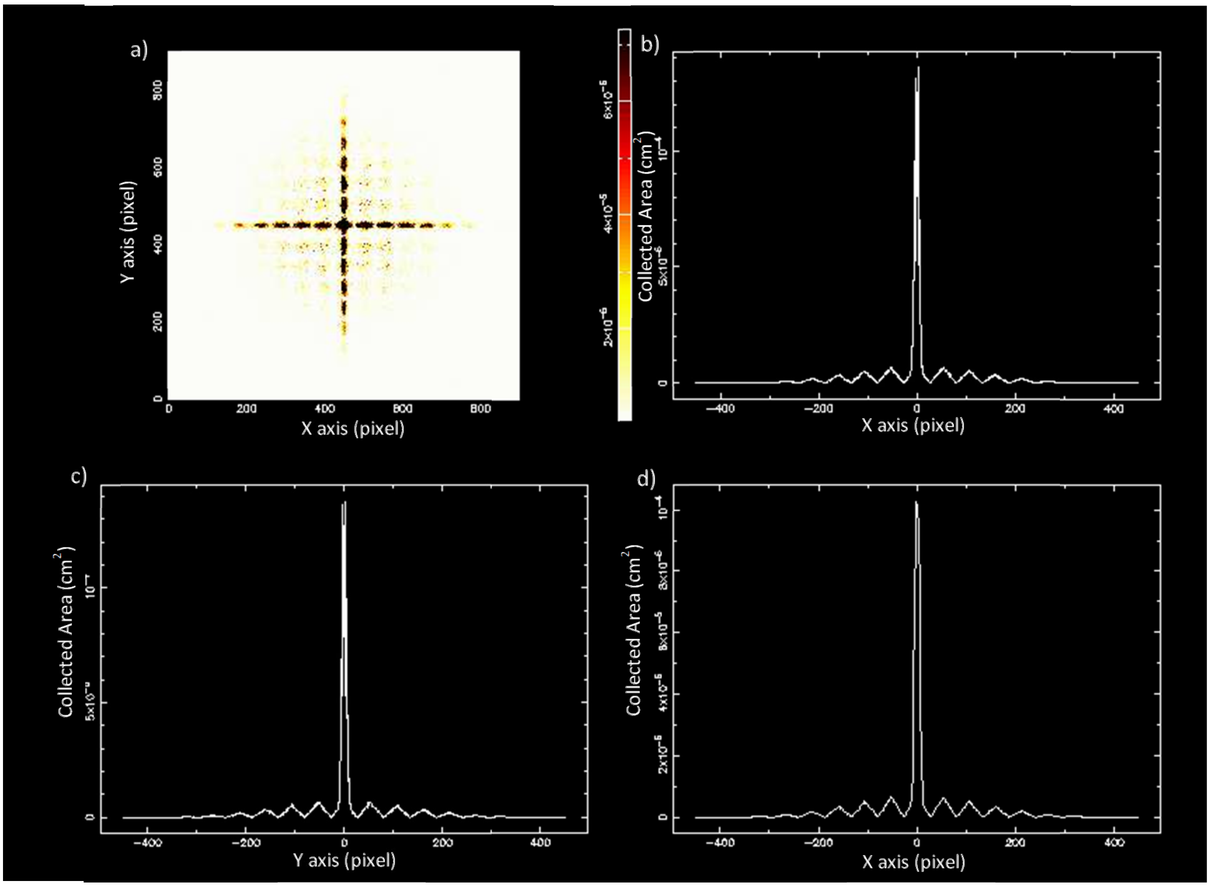

Figure 96 SRT Simulation at 0.93 keV

The plots are extracted directly from the sequential ray tracing (SRT) code developed by Brunton (1997) and represent, in a point to point focusing configuration, the amount of area collected by the optic and the relative spatial distribution. The detection plane in the simulation is represented by a detector made of 900 × 900 pixels with 100 μm × 100 μm per pixel. Subplot a) shows the spatial distribution of the collected area on the detector along the X and Y pixel directions, while subplots b) to d) represent a cut along the X direction on the detection plane binning the collected area in the Y direction, a cut along the Y direction with binning in the X direction and a cut as in subplot b) along the X direction but binning only half of the pixels respectively.

The percentage of hits in the focal square is only 4.6% as shown in Figure 97, compared to 34% for the optimum case.

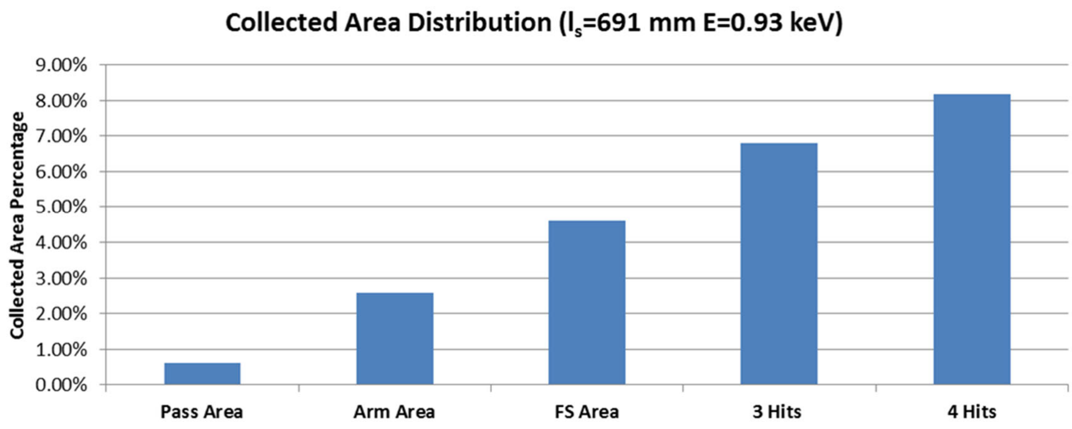

Figure 97 Collected Area Distribution by Ray Path l_s = 691 mm E = 0.93 keV

Multiple reflection becomes dominant given the low energy of the rays, hence a higher critical angle.

Figure 98 shows an overall comparison of the areas in the focal plane, processed by the ray tracing method output through the developed Matlab code.

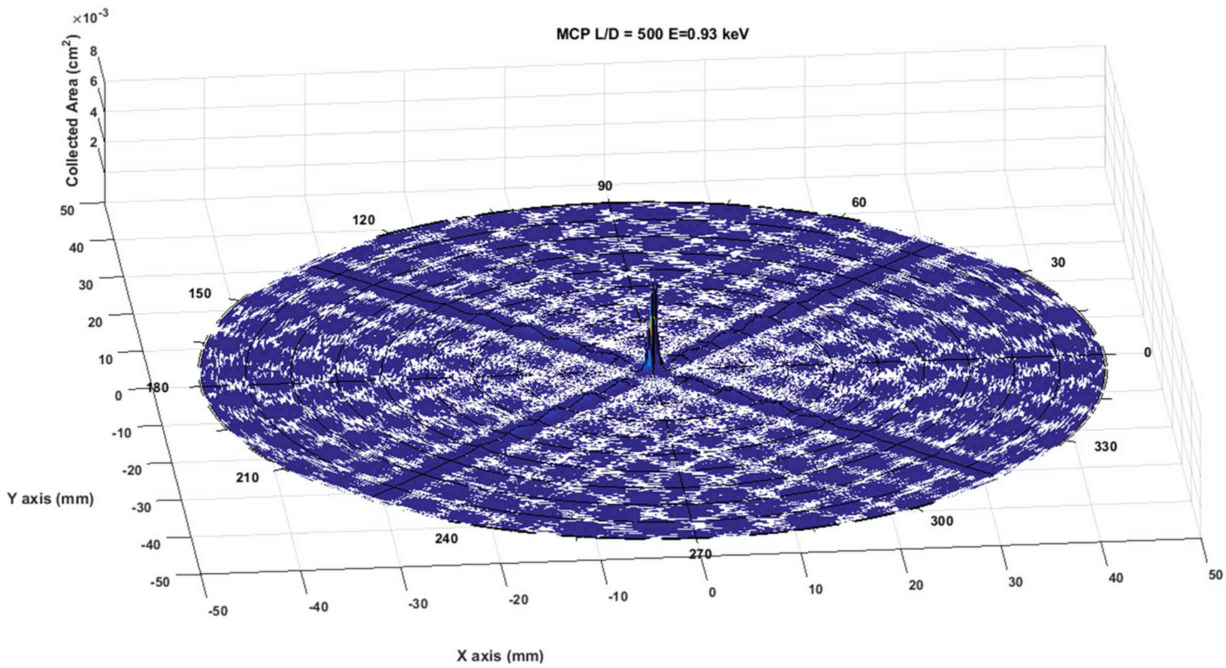

Figure 98 Point Spread Function l_s = 691 mm E = 0.93 keV

Note that the vertical scale is linear in Figure 98, relative to the log scale for the optimum case shown in Figure 95.

Defining the gain as the ratio between the collected area at the detector in a certain radius over the same physical area at the optic plane, the difference in gain between the model output at 0.93 keV and the optimum case is shown in Figure 99.

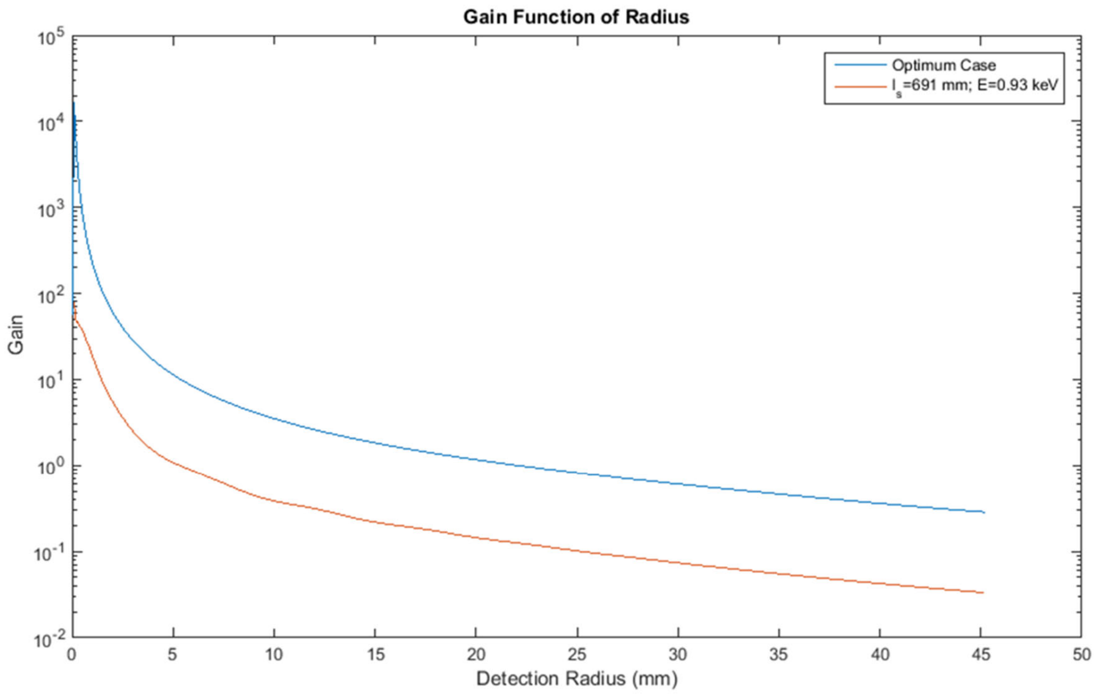

Figure 99 Gain Comparison as Function of Integration Area

Figure 99 shows nearly two orders of magnitude of difference; a gain value of 20 was experimentally measured by Price et al. (2002) at the pixel with the peak value. Note that the gain definition adopted in the above mentioned work is different from the definition adopted in this thesis. The gain as calculated by Price et al. (2002) was calculated as the ratio of the collected area by the optic at the detection plane to the area at the detection plane when the optic is not in place.

In order to reconcile the two definitions of gain, assuming a point source flux, the gain defined in this thesis should be multiplied by 4 (ratio between the square of the distance $2R$ at the detection plane and the distance R at the optic aperture plane) to allow for a comparison with the definition of gain adopted in the mentioned work. The simulated peak gain in Figure 99 for E = 0.93 keV has a value of 78, hence to compare it with the experimental gain value found by Price et al. (2002) $Gain_d = 4 \cdot 78 = 312$. The loss of gain due to MCP defects can be estimated as the ratio between the experimental and the simulated gain, namely 20/312 resulting in a factor 0.064 of the theoretical simulated case at the peak. Generally, to characterise the optic's focusing advantage by only the gain at the peak pixel value would not be a wise choice. In fact as in Willingale et al. (1998) the focusing advantage F_a is defined as the ratio of the collecting area over a square with side B_{HEW}, containing 50% of detected flux from source calculated in a radius of 10 mm from the centre of the detector.

Furthermore, an estimate for the gain over a more meaningful area can be derived analysing the experimental data by Price et al. (2002). The reported collected area is calculated over a radius 3σ, with $\sigma = 0.424 \cdot FWHM_{exp}$, the area has about half the value compared with the value of the collected area $Flux_{3\sigma Sim}$ calculated from the theoretical simulation on the same radius $R = 3\sigma = 1.27 \cdot FWHM_{exp}$; hence a gain for the radius corresponding to the FWHM experimental value, equal to 5.9' arc minutes, is calculated as:

$$G_{3\sigma} = 0.5 \cdot Flux_{3\sigma Sim} / (\pi \cdot R^2) \tag{5.9}$$

$R = 1.27 \cdot l_i \cdot 2 \cdot \tan(FWHM_{exp}/2) = 1.5$ mm, l_i is the distance from optics to detector.

For the above low energy case $G_{3\sigma} = 5.37$, compared to the theoretical gain of 9.48 as shown in Figure 99 for a detection radius of 1.5 mm, a factor of loss of gain of 0.56. A further model will account for the MCP deformation as a follow up to this thesis.

To allow comparison between optics, and at different energy levels, a different parameter can be defined: the radius where the gain drops to unity, $R_{G=1}$.

Adopting the above definition $R_{G=1}$ is 22 mm for the optimal case and $R_{G=1}$ is 5.3 mm for the low energy case, where the larger the radius the better the system.

Further characterisation of the quality of the focusing system can be given by looking at the surface brightness as a density of area per mm of circumference radius ($2 \cdot \pi \cdot$radius) as shown in Figure 100 for the optimal case and in Figure 101 for the low energy case.

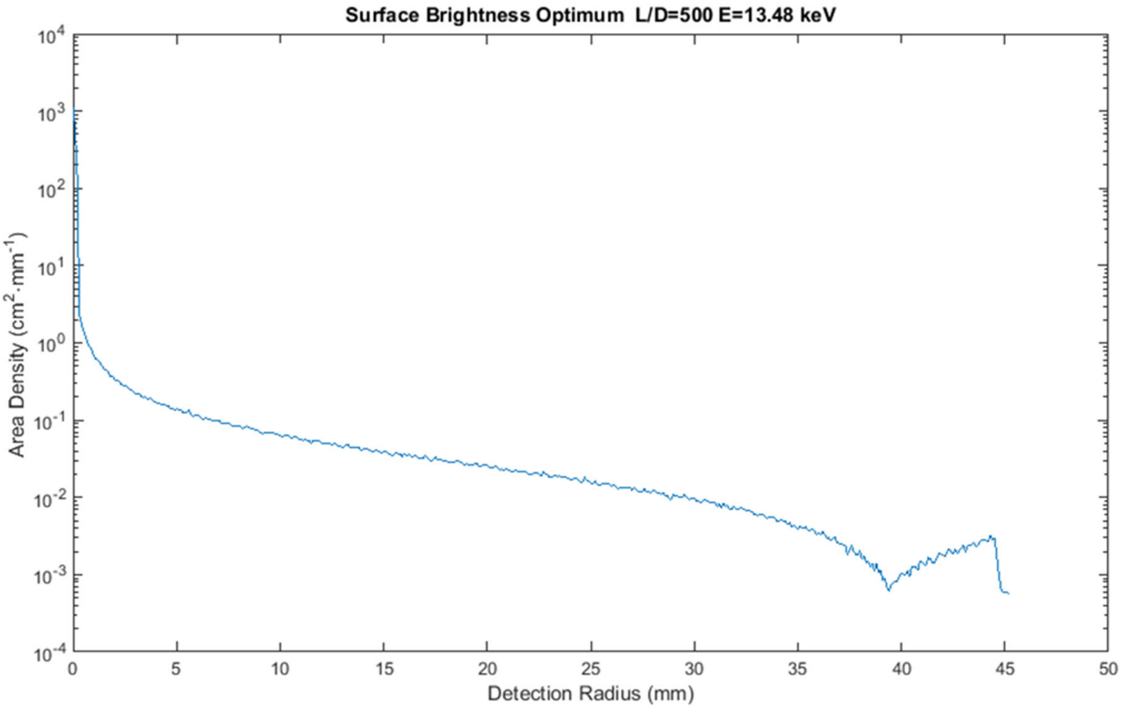

Figure 100 Surface Brightness Optimal MCP/Energy

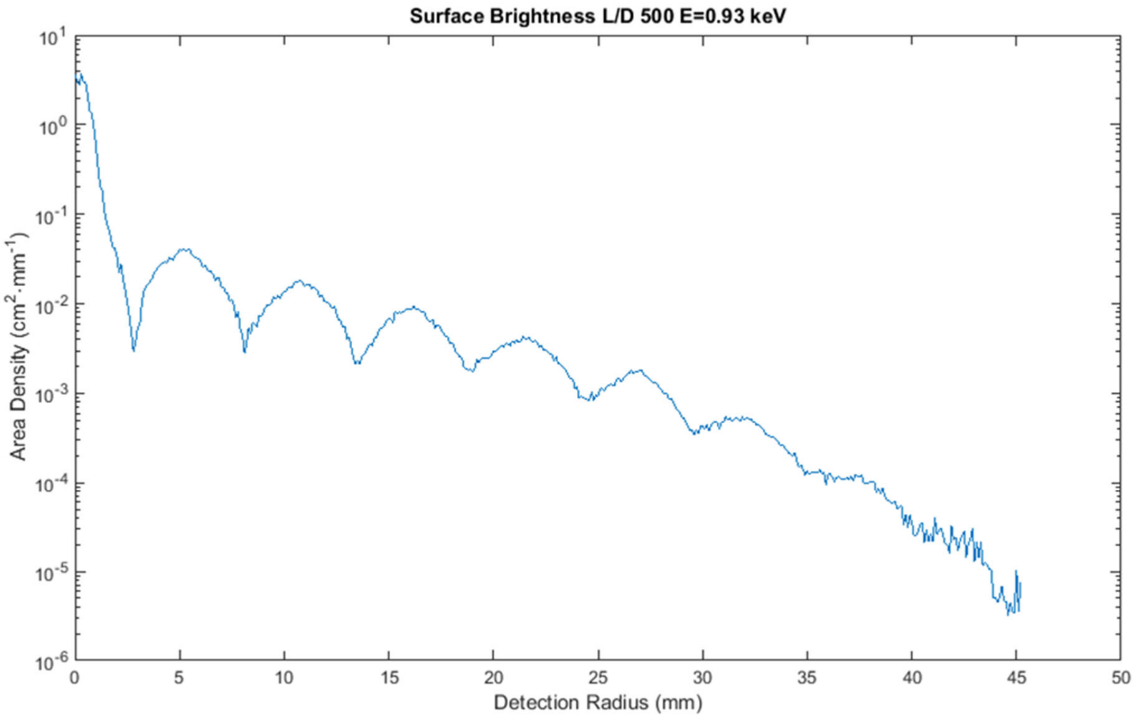

Figure 101 Surface Brightness MCP l_s = 691 mm E = 0.93 keV

The simulation results in Figure 102 show the data from the MCP optic at the energy of the Mo line, in the designed arrangement distance of 1500 mm as shown in Figure 92.

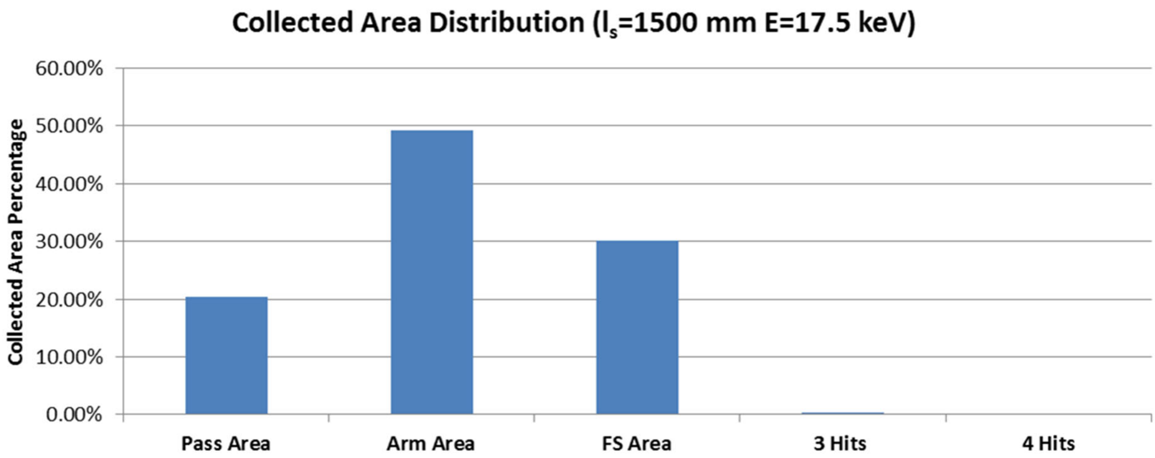

Figure 102 Collected Area Distribution by Ray Path l_s = 1500 mm E = 17.5 keV

The FS area counts for the 30% of the total flux of 0.308 cm^2 and from Figure 103 $R_{G=1}$ is 2.7 mm. An estimate of the gain compatible with the spatial resolution of the Lanex scintillator-CCD camera system can be given. The limit of the spatial resolution from MTF measurements of the camera system is an area of 0.6 mm × 0.6 mm, and a gain loss factor can be estimated taking into account the previously calculated losses of gain due to MCP defects for the peak pixel and for a 1.5 mm detection radius. These gain loss factors are 0.064 and 0.56 respectively, and an estimate of the loss factor for a 0.3 mm detection radius is estimated to be 0.1 over the theoretical value due to MCP deformations. The theoretical gain from the simulation at a detection radius of 0.3 mm is 38.29 as shown in Figure 103, hence an estimated gain $G_{RealEst} = 38.29 \cdot 0.1 = 3.82$ is expected.

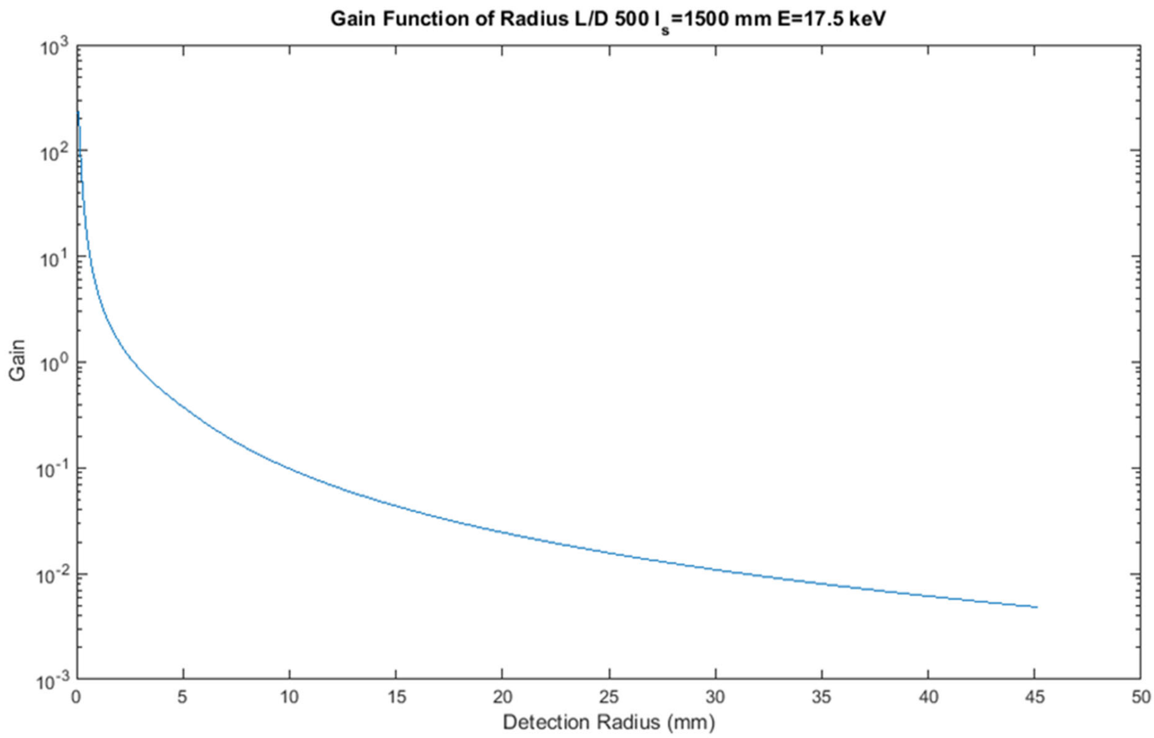

Figure 103 Gain Function of Integration Area l_s = 1500 mm E = 17.5 keV

In terms of X-ray flux, for a similar X-ray source setup as used for the camera characterisation, the flux per mm^2 at the MCP optic plane for a source at 150 cm, as shown in Figure 92, will be 0.16 times the experimental value calculated previously for the scintillators' characterisation, given the different distance from the source.

It is then possible to deduce the value of electron per second at the CCD given the previous results and under the same spectral energy of the X-ray flux:

$$\Gamma mcp_{CCD}\,(\text{electron}/(\text{pix}\cdot\text{s})) = \Gamma_{CCDreal} \cdot 0.16 \cdot G_{RealEst} \tag{5.10}$$

Adopting the Lanex scintillator and with the Al 0.7 mm flange, Γmcp_{CCD} is estimated to 0.1188 electron/(pix·s). In the case of no Al flange present this value needs to be multiplied by nearly a factor of two but then also the contribution of X-rays below 10 keV should be taken into account both for the scintillator response and also for the MCP optic response in the presence of a multispectral X-ray flux. Ideally, the experiment should also be carried out with a Mo filter to filter out energies above 20 keV and below 10 keV to isolate the Mo lines.

Considering that a signal could be read out when the signal was at least three times the level of noise, assuming the noise at first approximation could be considered as the photon shot noise and readout noise σ_{Read} of 10 electrons r.m.s., a number of electrons N_{el} that satisfies the following relationship is necessary:

N_{el} / (3·sqrt(σ_{Read}^2 +N_{el})) > 1 equivalent to a SNR = 3;

N_{el} = 35 electrons are necessary to reach the required level of SNR. The above considerations, assuming the estimated value for Γmcp_{CCD}, determine an integration time of at least 300 seconds.

A proper calculation should rely on the equation as expressed in Willingale et al. (1998) and similarly the SNR on the detected flux from a point source is given by the ratio of the source counts in the beam to the square root of the total counts in the beam:

$$\frac{S}{N}(E) = \frac{G \cdot A \cdot S \cdot T \cdot W}{\sqrt{G \cdot A \cdot S \cdot T \cdot W + (\eta \cdot S + B) \cdot A \cdot W}} \tag{5.11}$$

Where:

E = the photon energy (keV)

S = the incident source photon flux (cm^2/s·keV)

G = Gain

$A = \pi \cdot R^2$ the physical area (cm^2)

T = the observation time (s)

W = the energy band width (keV)

η = the unfocused fraction of source flux detected

B = the detector background photon rate (cm^2/s·keV)

R = the radius of the beam on the detector (cm).

The above equation, excluding the detector background rate term, has been implemented in a spreadsheet, which accepts as input the parameters of the X-ray energy beam considered in the order of $\Phi(Ph/s{\cdot}\Omega) = 4258000$ for only the energy of the Mo line at E = 17.5 keV, CCD characteristics, demagnification, CCD readout noise and dark current noise as function of temperature, integration time, as well as the parameters of the scintillator and MCP optic. Hence following the expression of I_{00} to calculate the collection area in the focal square, the number of electrons per pixel·s in the focal square is calculated for different focal square collection efficiencies Ω_{00} and different sizes of focal square or FWHM due to MCP deformations decreasing the performance of the focusing optic. Figure 104 shows a section of the spreadsheet data.

CCDs	Detector size	0,8192		Xray Atten	0,372						
CCRreadout	Read out noise e-	10									
Multiplication	Avalanche multiplication	100									
Pixels	Number of pixels	512									
M	Demagnification	6,83									
s	Seconds	796		218							
N	Ph/s/sr	1583976	4258000		1						
Energy	Kev	17,5									
Thetac	Critical angle rad	7,338426038	0,122307101	0,002134662							
Ωcr	Critical angle sr	1,82271E-05									
Chi	Form factor	1	0,5								
Ω	Collection eff	0,34	0,32	0,3	0,28	0,26	0,24	0,22	0,2	0,15	0,03
eta	aperture eff	0,69									
Bmax	size focal square	0,002	0,004	0,006	0,008	0,01	0,012	0,014	0,016	0,018	0,055
Mt	Magnification	1									
d	Channel pore size cm	0,001									
t	Channel length cm	0,5									
R	Distance from MCP cm	150									
FS	Focal square area	0,000004	0,000016	0,000036	0,000064	0,0001	0,000144	0,000196	0,000256	0,000324	0,003025
Ωsd	Sr with no MCP on Detector	4,44444E-11	1,77778E-10	4E-10	7,11E-10	1,11E-09	1,6E-09	2,18E-09	2,84E-09	3,6E-09	3,36E-08
Ioo	Counts in Focal square	6,773212067	6,374787828	5,976363588	5,577939	5,179515	4,781091	4,382667	3,984242	2,988182	0,597636
Iooavg	Av counts in Focal square	1693303,017	1593696,957	1494090,897	1394485	1294879	1195273	1095667	996060,6	747045,4	149409,1
		423325,7542	398424,2392	373522,7243	348621,2	323719,7	298818,2	273916,7	249015,1	186761,4	37352,27
		188144,7796	177077,4397	166010,0997	154942,8	143875,4	132808,1	121740,7	110673,4	83005,05	16601,01
		105831,4385	99606,05981	93380,68107	87155,3	80929,92	74704,54	68479,17	62253,79	46690,34	9338,068
		67732,12067	63747,87828	59763,63588	55779,39	51795,15	47810,91	43826,67	39842,42	29881,82	5976,364
		47036,19491	44269,35991	41502,52492	38735,69	35968,85	33202,02	30435,18	27668,35	20751,26	4150,252
		34557,20442	32524,42769	30491,65096	28458,87	26426,1	24393,32	22360,54	20327,77	15245,83	3049,165
		26457,85964	24901,51495	23345,17027	21788,83	20232,48	18676,14	17119,79	15563,45	11672,59	2334,517
		20904,97552	19675,27107	18445,56663	17215,86	15986,16	14756,45	13526,75	12297,04	9222,783	1844,557
		2239,078369	2107,367877	1975,657385	1843,947	1712,236	1580,526	1448,815	1317,105	987,8287	197,5657
Inomcpp	count in focal square with no MCP	7,03989E-05	0,000281596	0,00063359	0,001126	0,00176	0,002534	0,00345	0,004506	0,005702	0,053239
Inomcppavg	Avg count in focal square with no MCP	17,59973333	17,59973333	17,59973333	17,59973	17,59973	17,59973	17,59973	17,59973	17,59973	17,59973
Ap	Area per pixel on scintillator	0,000119421									
Npx	Photoelectrons per x-ray	1,3523									
Npix	Electrons per pixel no MCP	0,002842238									
NpixMCP	Electrons per pixel MCP in focal square per sec.	273,4570364	257,3713284	241,2856204	225,1999	209,1142	193,0285	176,9428	160,8571	120,6428	24,12856
		68,3642591	64,34283209	60,32140509	56,29998	52,27855	48,25712	44,2357	40,21427	30,1607	6,032141
		30,38411516	28,59681426	26,80951337	25,02221	23,23491	21,44761	19,66031	17,87301	13,40476	2,680951
		17,09106478	16,08570802	15,08035127	14,07499	13,06964	12,06428	11,05892	10,05357	7,540176	1,508035
		10,93828146	10,29485314	9,651424814	9,007996	8,364568	7,72114	7,077712	6,434283	4,825712	0,965142
		7,596028789	7,149203566	6,702378343	6,255553	5,808728	5,361903	4,915077	4,468252	3,351189	0,670238
		5,580755845	5,252476089	4,924196334	4,595917	4,267637	3,939357	3,611077	3,282798	2,462098	0,49242
		4,272766194	4,021427006	3,770087818	3,518749	3,267409	3,01607	2,764731	2,513392	1,885044	0,377009
		3,376012795	3,177423807	2,978834819	2,780246	2,581657	2,383068	2,184479	1,98589	1,489417	0,297883
		0,361596081	0,340325723	0,319055366	0,297785	0,276515	0,255244	0,233974	0,212704	0,159528	0,031906
Sthreshold	Pixel signal higher 3(sigma^2)^1/2	1399,987065	1358,206822	1315,099904	1270,531	1224,341	1176,339	1126,293	1073,917	930,1627	416,8628
		700,4849222	679,6099052	658,0730356	635,8071	612,7325	588,7543	563,7571	537,5989	465,8206	210,0758
		467,5354265	453,6354831	439,2959457	424,4723	409,1118	393,1517	376,5156	359,1097	311,3667	141,8588
		351,2235216	340,8160594	330,0806123	318,9841	307,4873	295,5437	283,0966	270,0765	234,383	108,2642
		281,5660179	273,2579403	264,6892167	255,8337	246,6604	237,1325	227,2054	216,8243	188,3852	88,49777
		235,2350406	228,3297362	221,2089793	213,8512	206,2312	198,3185	190,0768	181,4611	157,8781	75,62511
		202,2328088	196,3321492	190,2485654	183,9639	177,4568	170,7019	163,6684	156,3187	136,2206	66,67285
		177,5603309	172,4154203	167,1121875	161,635	155,9657	150,0823	143,9587	137,5628	120,0918	60,15368
		158,4403035	153,8851463	149,1909741	144,3442	139,329	134,1263	128,7136	123,0629	107,6465	55,24139
		59,22878033	57,92812423	56,59758594	55,23501	53,83795	52,40367	50,929	49,41035	45,39196	33,85477
Sdelta	Signal FS - threshold	216271,8139	203509,3706	190748,2539	177988,6	165230,6	152474,3	139720,2	126968,3	95101,51	18789,47
		53717,46532	50537,28444	47357,76541	44178,98	41000,99	37823,92	34647,86	31472,96	23542,1	4591,508
		23718,22024	22309,42867	20901,0767	19493,21	18085,88	16679,15	15273,09	13867,81	10358,82	1992,178
		13253,26404	12463,40753	11673,879	10884,71	10095,94	9307,624	8519,807	7732,563	5767,597	1092,132
		8425,306021	7921,445155	7417,844935	6914,532	6411,536	5908,895	5406,653	4904,865	3652,882	679,7556
		5811,203875	5462,436302	5113,884182	4765,569	4417,516	4069,756	3722,325	3375,268	2509,668	457,8842
		4240,048844	3984,638818	3729,411716	3474,386	3219,582	2965,026	2710,749	2456,788	1823,61	325,2932
		3223,561559	3028,640476	2833,877716	2639,289	2444,892	2250,71	2056,767	1863,097	1380,403	239,9453
		2528,865881	2375,344204	2221,961542	2068,731	1915,67	1762,796	1610,132	1457,705	1077,93	181,8739
		228,6017003	212,9711517	197,3704852	181,8019	166,2677	150,7708	135,3142	119,9017	81,59207	-8,45796

Figure 104 Spreadsheet for Analytical Evaluation

Ω_{00} Collection Efficiency

466,4474	452,5141	438,1378	423,2736	407,868	391,8572	375,1638	357,6921	309,7308	138,2325
233,0654	226,0939	218,9004	211,4624	203,7531	195,7404	187,3853	178,6399	154,6276	68,59311
155,2016	150,5485	145,747	140,7819	135,6351	130,2852	124,7061	118,8654	102,8226	45,16573
116,2178	112,7225	109,1153	105,3848	101,5173	97,49652	93,30274	88,91148	76,84401	33,31009
92,78676	89,98492	87,09304	84,10184	81,00035	77,77539	74,41094	70,88719	61,19807	26,10159
77,13268	74,79224	72,37624	69,87688	67,28489	64,58915	61,77615	58,82912	50,72057	21,2334
65,92326	63,91168	61,83483	59,68594	57,45697	55,13825	52,71804	50,18177	43,19862	17,71682
57,49246	55,72695	53,90385	52,01716	50,05975	48,02305	45,89663	43,66755	37,52598	15,05667
50,91473	49,34017	47,71397	46,03071	44,28399	42,46608	40,56757	38,57681	33,08825	12,97664
14,67062	14,12355	13,55854	12,97388	12,36762	11,73744	11,08065	10,39403	8,519409	2,43936

Focal square Area

Figure 105 SNR Analytical Assessment

The model data sample shown in Figure 105 represents the SNR for the MCP optic for different values of collection efficiency and area of integration.

The advantage of the model is in the direct visual snapshot of the results.

A comparison of this analytical model with the results derived by estimating the value of Γmcp_{CCD} requires a correction to take into account only the 17.5 keV line of the Mo, the previously estimated Γmcp_{CCD} of 0.1188 electron/(pix·s) also includes other energy components; from the simulation and measurements for the scintillators' characterisation, $\Gamma mcp_{CCDE17.5}$ can be assumed to be 37% of the total value.

Hence, the value of Γmcp_{CCD} gets to a value $\Gamma mcp_{CCDE17.5}$ = 0.0439 electron/(pix·s). In order to get to a SNR= N_{el} / sqrt(σ_{Read}^2 +N_{el}) = 3, an integration time of 797 s is needed.

Considering this integration time and integrating over the same area of the spatial resolution of the camera system, around 0.6 × 0.6 mm, and assuming a loss of collection efficiency Ω_{00} due to MCP deformation of the same entity as the adopted gain loss factor of 0.1 over the theoretical simulation, namely Ω_{00} from a simulated value of 30% gets to 3%, the analytical model predicts a value of SNR= 2.43.

This value is in good agreement with the estimation from the experimental findings, the lower value is also justified by other noise components being added in the model.

The model also predicts the level of SNR with/without MCP optics, with/without binning 2 × 2 and with/without avalanche multiplication, including the excess noise factor for CCD multiplication.

Interestingly, the SNR without the MCP would be only 0.22 and with avalanche multiplication rises to 0.89. Adopting avalanche multiplication with the MCP, given the low level of signal, results in a beneficial contribution to the SNR which rises to 3.65.
Table 16 summarises the SNR values for different options.

	MCP	**No MCP**	**MCP L3**	**No MCP L3**	**Binning 2×2**	**Binning 2×2 L3**
SNR	2.43	0.22	3.65	0.89	7.55	7.31

Table 16 SNR Comparison

Given the low level of signal over the readout noise of 10 electrons r.m.s., binning is clearly a beneficial way to increase SNR but at a loss of spatial resolution.

5.3.3 MCP modelling for Thermal Neutrons

In the following study the use of a MCP square pore optic as a focusing system for thermal neutron imaging will be investigated. In the past, long established research activity has been carried out for detection of thermal neutrons by imaging micro-channel plate systems (Fraser et al, 1990) (Fraser et al., 1993). In the study presented the MCP optic will be considered only as a focusing element, namely no bias voltages will be applied to the walls and the optical behaviour of the neutron will be exploited.
For example, given the basic constants of neutron optics, such as the index of refraction and the coherent and incoherent scattering amplitudes, the behaviour of thermal neutrons in terms of reflection follows similar roles to those for light and X-rays (Hughes, 1954).
Research on the focusing of neutrons relies on the available methods on capillary optics or aspherical super-mirrors with layers of NiC/Ti achieving a focusing gain of 52 (Nagano et al., 2012) or Kirkpatrick–Baez micro-focusing optics (Ice, 2005) achieving a gain of 27.
The reflectivity at specific neutron energies over the typical material composition of MCP glasses has been considered, in particular the same structure as for the Mercury Imaging X-

ray Spectrometer (MIXS) imagers on the Bepi Colombo mission to Mercury (Martindale, 2015).

As an aid to this study the IMD software (Windt, 1998) for modelling and analysis of multilayer films has been adopted.

Figure 106 shows the simulated reflectivity for thermal neutrons on standard MCP glass resulting in a critical angle of around 0.2°.

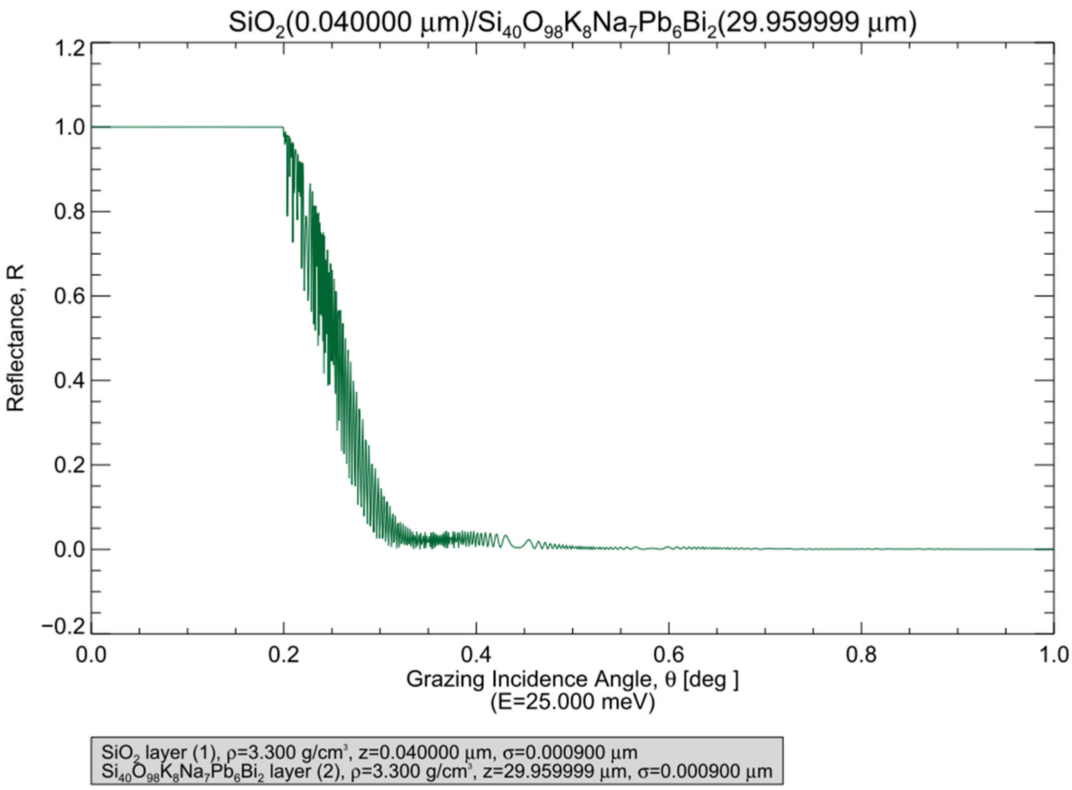

Figure 106 Thermal Neutron Reflection over Standard Glass

Adding a layer of ^{58}Ni has also been considered and results in an improvement of nearly 0.05° as shown in Figure 107.

The Monte Carlo sequential ray tracing software has been modified to accept as a look up table the value of reflectivity from the IMD software.

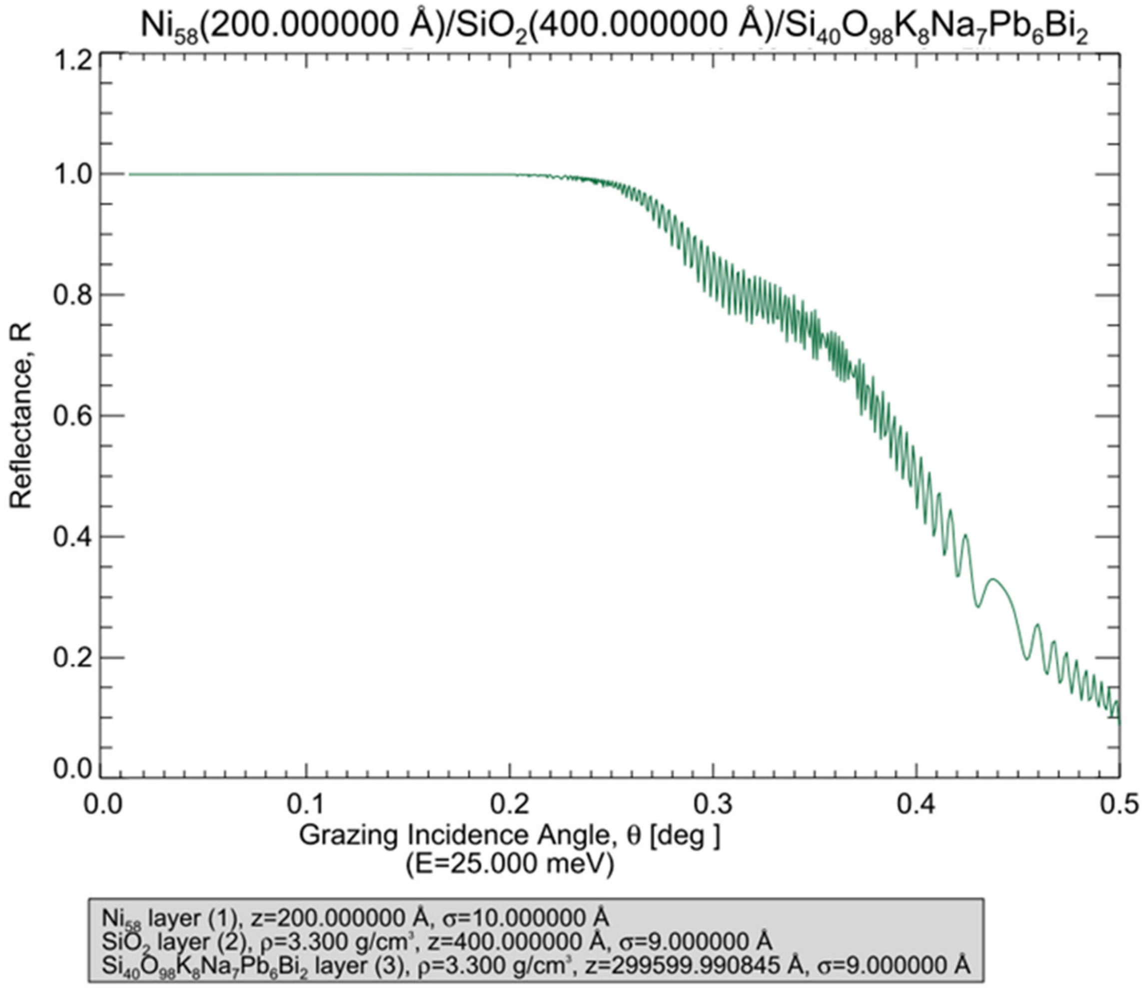

Figure 107 Thermal Neutron Reflection over 200 Å ^{58}Ni over Standard Glass

Figure 108 is the simulation for the given MCP in linear scale and shows the high collection area at the focal square at a distance of 10 m from the optics to the detector.

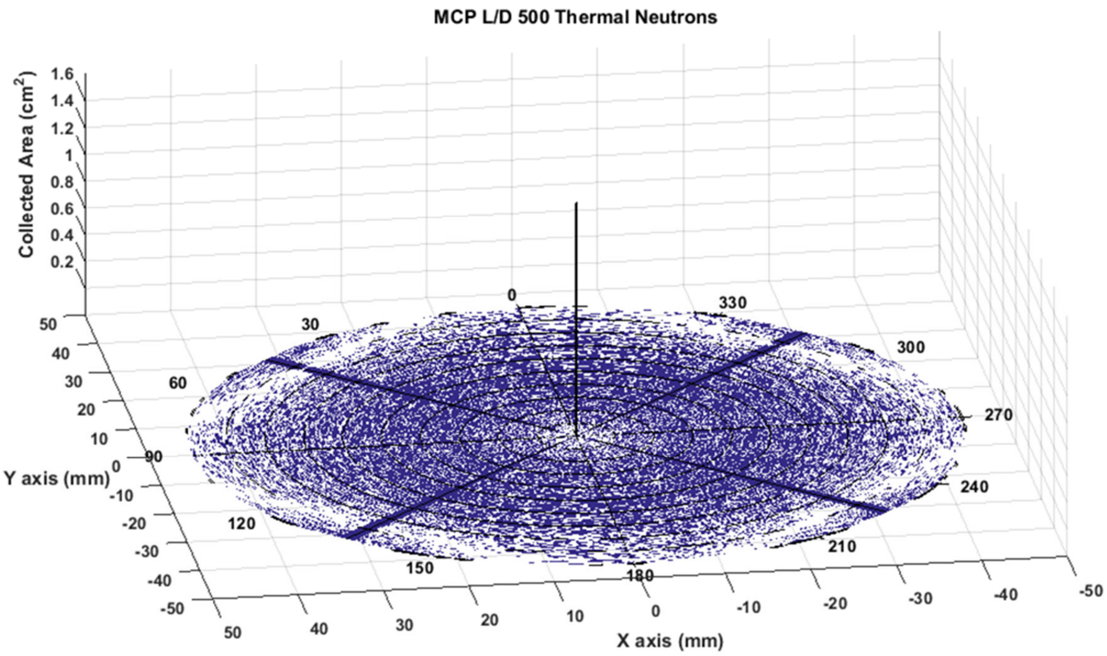

Figure 108 MCP Flat at 10 m for Thermal Neutrons

At such a distance all the neutrons, assuming a perfect point source diffusion, hit at an angle lower than the critical angle. The total collection area ratios are then shown in Figure 109.

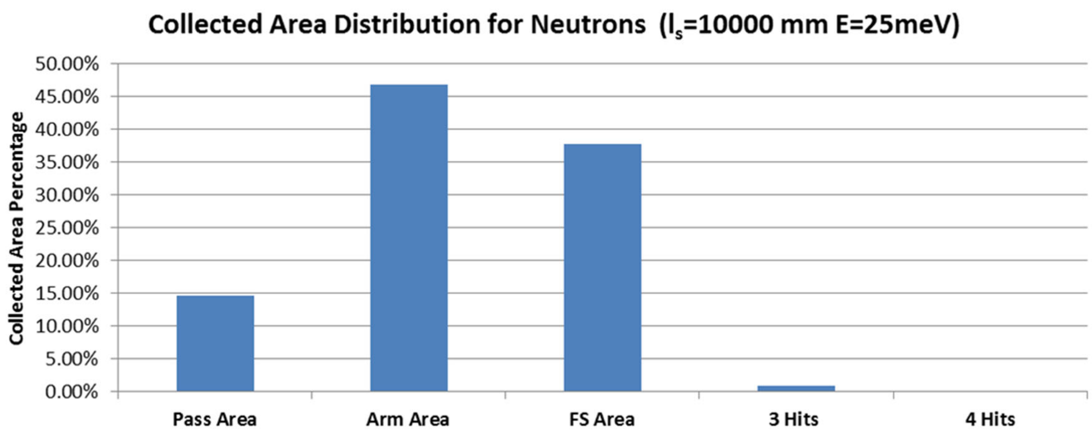

Figure 109 Collected Area Distribution by Ray Path for Neutrons at 10 m

The gain will be very high as can be predicted by the above ratios, for a focal square area of 7 cm^2 as shown in Figure 110.

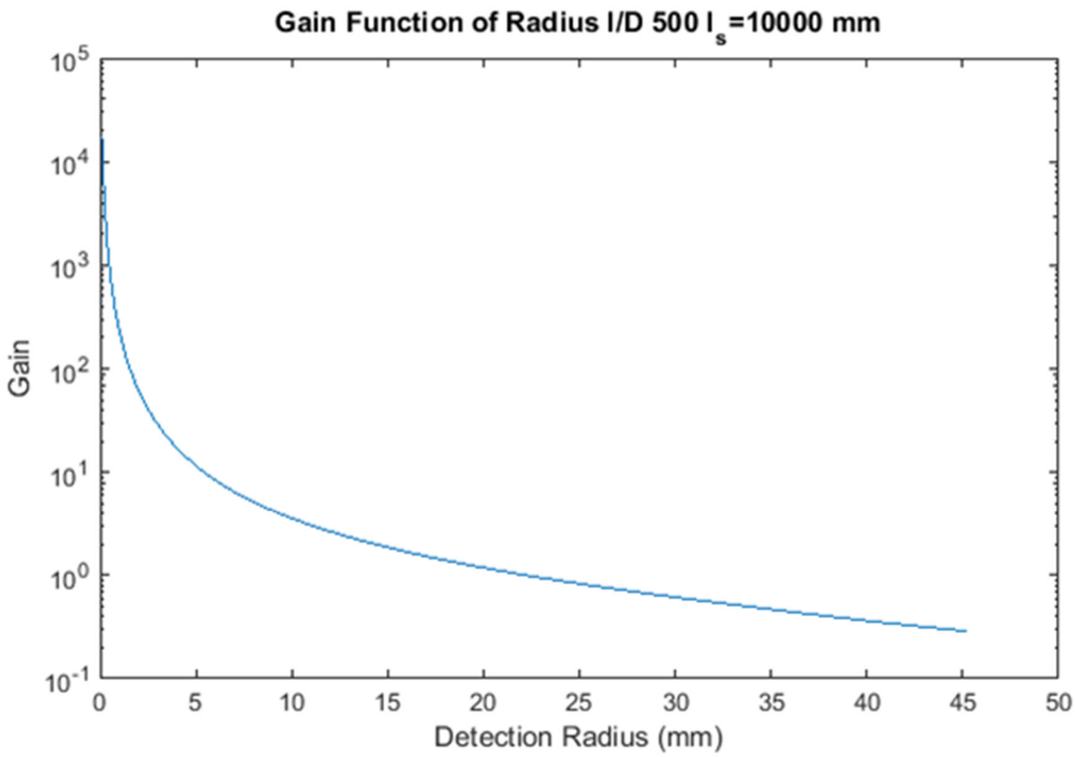

Figure 110 Gain Function of Integration Area Thermal Neutrons at 10 m

Ideally a gain of 2496 for a detection radius of 0.3 mm should be obtained. This is a very high value but because of deformation of the optics it is unrealistically achievable given the long distance. To get to an estimate of an achievable gain at that distance a comparison with the experimental measurements carried out by Price et al. (2002) has been done.

Specifically, in order to estimate the gain loss for the peak value, the measured peak value by Price et al. (2002) has been compared with the corresponding theoretical simulation value, whose collected area distribution is shown in Figure 111. The same loss ratio has been applied to the ideal simulation for neutrons with l_s = 10 m, resulting in an estimated peak gain $G_{Neutrons}$ = 2.31 at the peak pixel.

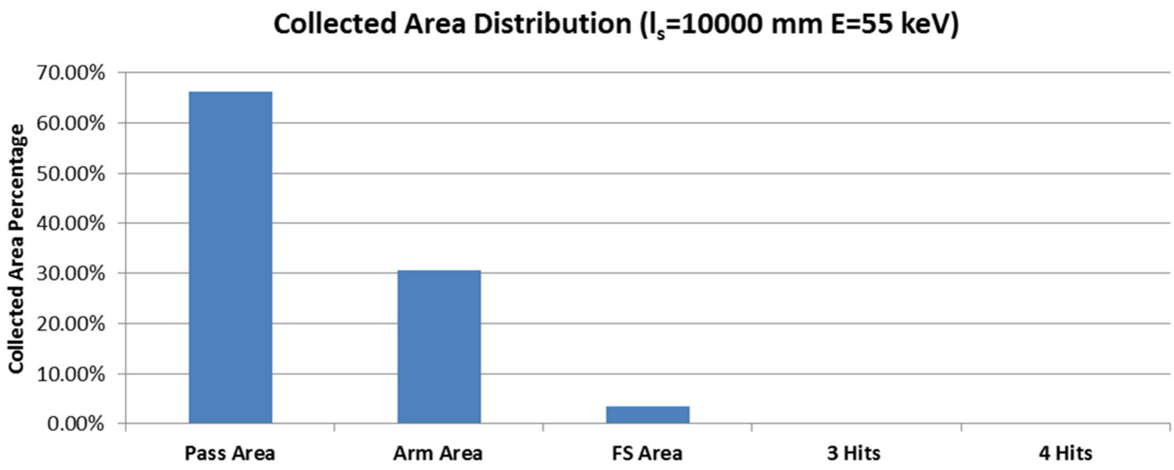

Figure 111 Collected Area Distribution by Ray Path for X-Rays E = 55 keV l_s = 10m

In the same geometrical conditions for the simulation for X-rays at 17.5 keV previously described, the simulated reflection of neutrons over the mentioned glass structure reported a focal square area of 4 cm^2, a value similar to the first MCP simulation for X-rays at 13.5 keV, which was the optimal geometric energy matching for the optics.

The same identical estimation for the peak gain has been done for the case where the MCP optic was placed at 691 mm, whose collection statistics are shown in Figure 112, giving a total focal square area of 0.22 cm^2, due to the low percentage of interacting neutrons because of the short distance and low critical angle.

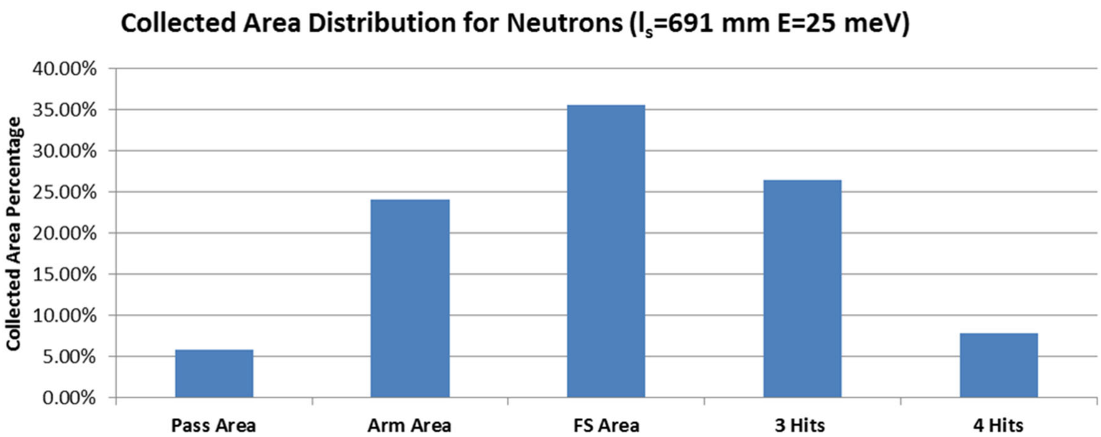

Figure 112 Collected Area Distribution by Ray Path for Neutrons l_s = 691mm

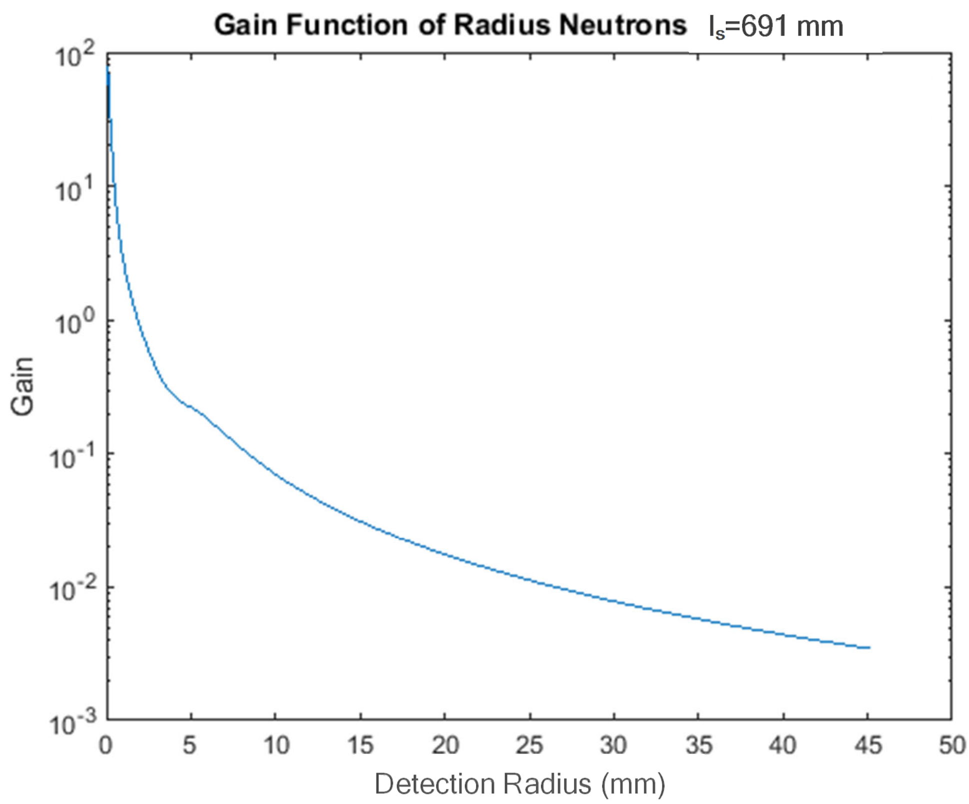

Figure 113 Gain Function of Integration Area Thermal Neutrons l_s = 691 mm

Figure 113 features the gain function of detection radius for l_s = 691 mm, and applying the previously derived gain loss factor of 0.064 for the peak value, the theoretical peak gain of 77 drops to an estimated peak gain of 4.9.

Comparing with the results in Allman et al. (1998) which adopted an MCP with ratio L/D of 30 at l_s = 110 cm and square pores of 200 μm for focusing 7.5 Å neutrons, the authors obtained a gain of 10 in a focal spot of 1 mm × 1 mm. In order to compare this value with the gain defined in this thesis, which is the gain related to the flux in front of the optics, the estimated gain of 4.9 should therefore be multiplied by four to be compared with the gain defined for the area at the detector with no optic in between.

The same MCP optic was tested for focusing X-rays at 1.5 keV by Peele et al. (1996), obtaining a peak gain of 27 against the simulated gain of 83. The FWHM angular resolution of that MCP optic was reported to be of 3.3’ arc minutes compared to the 5.5’ of the MCP under consideration.

The technical capability to manufacture MCP optics in the past 20 years has reached levels for which it is possible at least to double the value of the estimated gain, reaching values of peak gain of 40 to 50.

In order to get an estimate of the signal that the CCD camera system would detect, a ^{6}LiF/ZnS:Ag screen scintillator for neutron detection (van Eijk, 2004) has been considered. Assuming a 0.6 × 0.8 mm pinhole to realize a point source from a flux of $1.3 \cdot 10^5$ N/(cm^2·s) with a divergence of 10°, a flux Φ per stereo radiant of 20,800 N/s·Ω can be assumed.

When a neutron is captured in the ^{6}Li nucleus, two ^{4}He and one ^{3}H particles are emitted with a liberated total kinetic energy of $4.79 \cdot 10^6$ eV.

The absorption length for the screen is about 1 mm (van Eijk, 2004), it means an absorption of 63% for 1 mm thick scintillator and of 36% for a 0.5 mm thick screen, which would benefit spatial resolution.

The number of light photons, $N_{photons}$, emitted per incident thermal neutron by the scintillator can be expressed as:

$$N_{photons} = \eta_{screen} \cdot \frac{E_s}{E_{\bar{\lambda}}} \cdot \alpha_s \tag{5.12}$$

Where:

- η_{screen} is the conversion efficiency of the scintillator equal to 28%
- E_s is the liberated energy by the nuclear reaction at the scintillator $4.79 \cdot 10^6$ eV
- $E_{\bar{\lambda}}$ is the average energy of a light photon emitted by Zn equal to 3 eV
- α_s is the absorption of the 0.5 mm screen equal to 36%

Considering the above numerical values $N_{photons}$ = 160,000 photons, which is consistent with the findings in van Eijk (2004).

Adopting the same method as for the X-ray case, the number of photo-electrons collected by the CCD detector per incident neutron is expressed by:

$$N_{phelectrons} = N_{photons} \cdot \rho_R \cdot \eta_L \cdot \eta_{CCD} \tag{5.13}$$

Where:

- ρ_R is equal to 0.6 and takes into account the contribution of the back light reflection layer of the screen and the assumption that half of the light photons are emitted in the direction of the detector
- η_L is the optical coupling efficiency for a Lambertian source, which is equal to 0.002 in the actual setting
- η_{CCD} is the CCD QE which is equal to 85% at 460 nm, typical average emission wavelength for the screen

Given the above considerations, the number $N_{phelectrons}$ of photo-electrons per incident neutron is estimated to 160 photo-electron/neutron.

At this point a spreadsheet similar to the one shown in Figure 104 and Figure 105 for the X-ray calculation has been used to calculate N_{el}, the number of electrons per pixel, to achieve the desired level of SNR.

An integration time of 82 s is necessary to achieve a $SNR_{MCP} = 3$ with the focusing advantage of the MCP optic. In the same condition of flux without the MCP optic between the source and the detector a $SNR = 0.88$ is predicted.

In case avalanche multiplication is enabled on the CCD97 and with the focusing advantage of the MCP, an integration time of 42 s is necessary to achieve a $SNR_{MCP\_L3} = 3$; interestingly, for this integration time when no MCP and no multiplication were adopted a $SNR = 0.087$ would be forecast, as a consequence the peak signal would be completely unperceivable.

In this last case the adoption of a flat MCP in the hypothesised experimental setup allows an SNR increase of 34 times.

The higher SNR determines an improved sensitivity, which plays a fundamental role to detect photon limited signals, where the quantum nature of the source limits the achievable SNR.

5.3.4 Neutron Telescope

An example of an application using the neutron reflectivity model as previously introduced can be given in planetary remote sensing science where the characteristics of reflectivity of MCP structures can be exploited for the conceptual design of a neutron telescope.

The telescope structure does not rely on the classical lobster eye optic for X-ray astronomy (Angel, 1979) but on its evolution based on Wolter I type approximation optics as described in Willingale et al. (1998).

Following the same geometrical structure and focal length as for the Mercury Imaging X-ray Spectrometer-Telescope (MIXS-T) (Fraser et al., 2010) a neutron imaging telescope is proposed relying on the geometry of the square packet MCP considered in paragraph 5.3: pitch 12 μm, wall 2 μm, *L*/*D* 500 at maximum at the centre to a ratio of *L*/*D* 38 at the edges because of the Wolter type conic approximation (Willingale et al., 1998).

Focal length is 1 m, determined by the 4 m and 1.33 m slump radii of the front and rear MCP plates respectively.

Simulations were run relying on the reflection model of neutrons over the standard glass with no specific coating, and with an on axis parallel ray source placed at an infinite distance.

The point spread function of the optic is shown in Figure 114, and as expected the typical cruciform of a lobster eye optic disappeared.

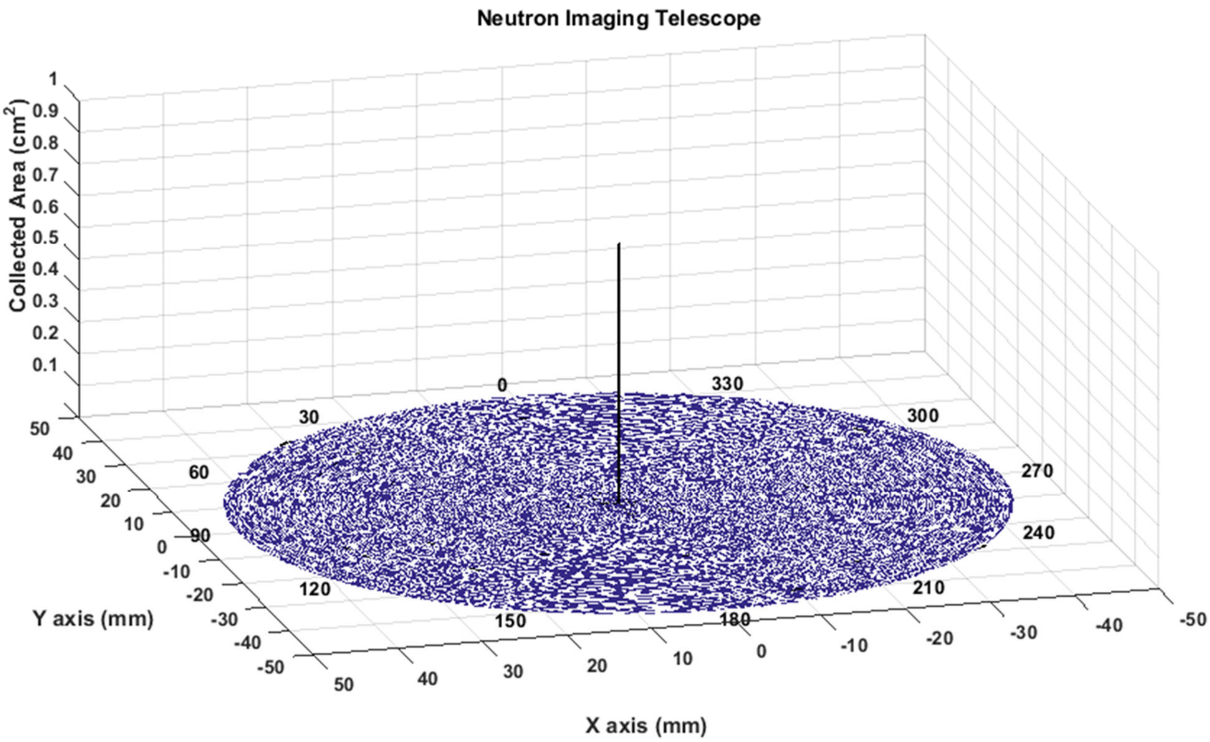

Figure 114 Point Spread Function for Neutron Telescope

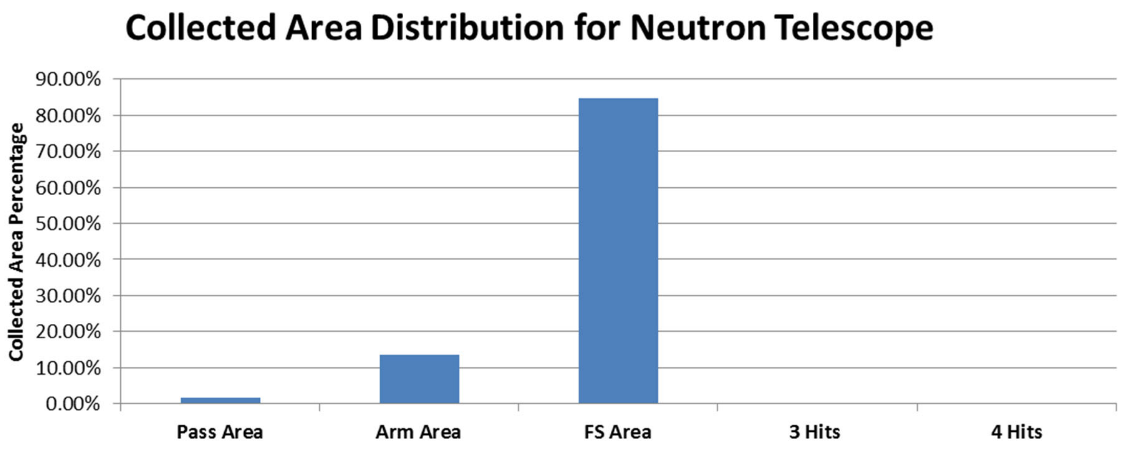

Figure 115 Collected Area Distribution by Ray Path for Neutron Telescope

Almost all the rays hitting the detector are focused in the focal square with the ratios given Figure 115.

A focal square area of 3.49 cm^2 over a total collected area at the focal plane of 4.12 cm^2 is reported, in comparison to MIXS-T (Fraser et al., 2010) with effective areas depending on energy from 46 cm^2 up to 1.5 keV and to 6 cm^2 at 8 keV for the focus area.

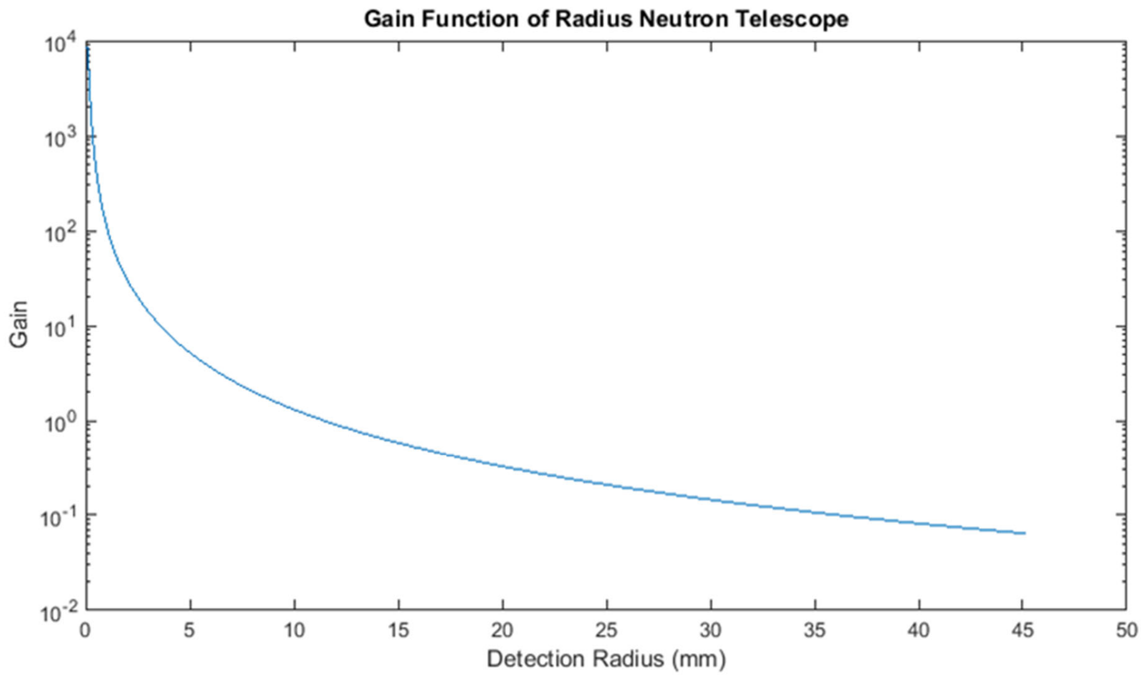

Figure 116 Gain Function of Integration Area for Neutron Telescope

From the analysis of the collected area, Figure 116 shows the gain as function of the detection radius and Figure 117, the surface brightness plot, shows that the area in the focal square is reached in a radius of less than 200 μm.

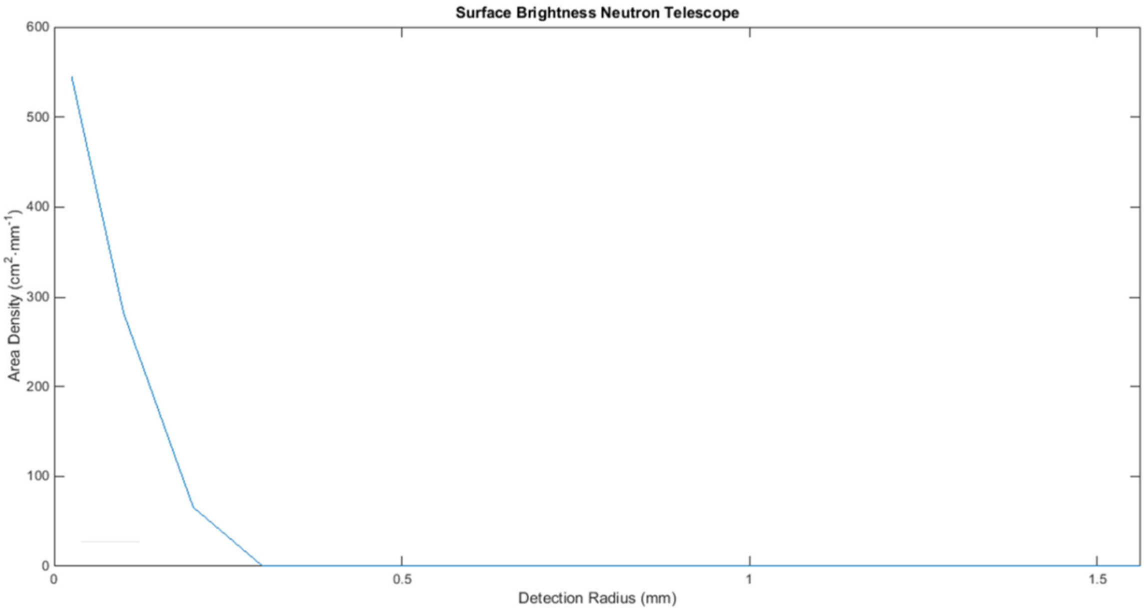

Figure 117 Surface Brightness for Neutron Telescope

Figure 117 confirms a theoretical angular resolution comparable with the MIXS-T of around 1' arc minute with a goal to achieve 2' arc minute (Fraser et al., 2010).

Considering a planetary orbit around Mercury similar to the Bepi Colombo mission, the neutron telescope could aim to resolve spatial details with a resolution between 1 km and 4 km.

A correct analysis to determine the neutron flux at the planetary surface, as well as the minimum detectable flux, requires calculation of the telescope grasp (cm^2·sr) and hence of the variation of the effective area with the off-axis incident angle, namely the vignetting function and consequent assessment of the field of view (FOV).

A follow up to this thesis will address these issues as well as conduct a simulation of neutron emission at the surface by GCR induced reactions, transport from the surface to the spacecraft including the effect that a planetary gravitational field has on the trajectory of emitted neutrons and its impact on the spatial resolving capability of the telescope.

Achieving spatial resolutions below 10 km would be very competitive compared to previous instruments like the MESSENGER Gamma-Ray and Neutron Spectrometer (Goldsten et al., 2007), where the effective FOV has hemispherical response to thermal neutrons along and opposite the spacecraft velocity direction and the Mercury Gamma and Neutron Spectrometer (MGNS) on Bepi Colombo with surface resolution of 400 km (Kozyrev et al., 2009).

In this context only thermal neutrons could be detected by the proposed instrument. The actual methods to detect the abundance of hydrogen compounds rely on the determination of the difference in fluxes between epithermal, fast and thermal neutrons over a specific collection area. The critical angle of reflection of epithermal neutrons is much lower than the angle for thermal neutrons, resulting in a collected area by the MCP optic likely not sufficient for them to be detected. This goes out of the scope of this thesis. The detection of thermal neutrons could be exploited to map abundances of the rare earth elements as a group, given their higher thermal neutron absorption cross-sections, if their abundance is sufficient to determine a depression of the neutron flux to a detectable level (Goldsten et al., 2007).

All the possible applications and constraints of spatially resolved thermal neutron measurements in orbit could be a follow up study to the present work.

6. Conclusions

The work in this thesis addressed the challenges of the opto-mechanical, thermal and electronic design to develop a versatile CCD imaging system. Furthermore, optimization and analytical modelling of the performance of the system supported by simulation and laboratory characterisation have been carried out. Relying on these findings, the design and prediction of the performance of CCD camera systems adopting MCP focusing optics has been considered.

The constructed CCD camera system has been operated for long hours at -70 °C via liquid nitrogen cooling. To improve usability and for future applications it would be appropriate to replace this cooling system with a double TEG system to operate at -45 to -50 °C, which would simplify the design and facilitate the camera integration in a space based remote sensing system.

The collected data in terms of CCD readout noise demonstrated a need to improve the PCB layout design and camera head shielding. The assessment of the noise for the digital readout method introduced by only the digital processing electronic chain has shown a contribution of only 0.19 electrons r.m.s..

The CCD time domain simulation model has demonstrated how digital signal processing methods can help to reduce the low frequency noise components otherwise not treatable by classical analogue CDS methods. A shaping filter to model flicker noise has been proposed and as an evolution to the present work it can be embedded in the realisation of a Kalman filtering algorithm to estimate low frequency noise components.

The importance of the simulation model developed stands in the capability to assess the impact that different design choices and noise processing algorithms have on the performance of the readout process.

The optical coupling between sensor and scintillator is the biggest drawback in terms of efficiency in the conversion chain from incident particles to electrons in the CCD. In a future evolution of the camera system a fibre optic bundle coupling would be desirable, allowing one order of magnitude of improvement in optical collection efficiency.

For what concerns the performance of MCP focusing systems, estimating data from real measurements and supported by simulations and an analytical model it was concluded that gains above 20 are achievable and likely gains up to 40 to 50 with the latest MCP manufacturing technologies. As a future task the geometric deformation of the optic will be included in the MCP simulation.
Theoretical gains orders of magnitude higher could be achievable, fabrication technology and the limits in the calibration and alignment phase posing a limit to the current results.

Relying on the same principles of reflectivity for neutrons on a flat MCP as for X-rays, the analysis of a neutron remote sensing telescope was carried out. Assuming a conceptual design similar to the MIXS-T imager on Bepi Colombo, the analysis has shown to be able to achieve in an ideal scenario an effective collection area of about 4 cm^2. The proposed telescope could be considered as an answer to the request for spatially resolved neutron remote sensing.
Further efforts are necessary to validate the deployability of the instrument. Calculation of the telescope grasp and vignetting function are necessary to assess the instrument detection capability and the minimum detectable flux of emitted thermal neutrons from a planetary surface. A simulation of the instrument in an orbital remote sensing scenario is desirable to model gravitational effects on thermal neutrons and optimise spacecraft attitude control strategies, as well as to validate remote sensing science objectives.

A neutron telescope can be envisaged where a large area CCD detector is coupled via a fibre optic bundle to the scintillator, in such a way that it is not the pixel size that determines the resolution of the instrument, determining a trade-off between the area of the detector and the tapering ratio of the bundle. In this way the sensor would not be in line with the neutron flux and proper shielding would be assured for the sensor and readout electronics against radiation damage. The availability of avalanche multiplication in the CCD detector could be exploited in areas where the flux is too low, a level where multiplication gain would be advantageous. On the other hand, in areas where a sufficient flux is detected, a high quality acquisition via low noise digital readout electronics would ensure the best performance in terms of spatial resolution.

All the above findings suggest, especially for space applications with faint flux sources or where short integration times are necessary, for instance to get higher temporal/spatial resolution, the matching between high quality avalanche multiplication CCD sensors and MCP imaging/focusing systems can bring about remarkable levels of sensitivity.
Furthermore, digital readout methods can help to reduce noise to a sub electron level, which for specific conditions and high quality applications is fundamental as in the detection of dark matter.

7. References

- Alefeld, J., et al., ”New developments of small angle neutron scattering instruments with focusing” Nuclear Instruments and Methods in Physics Research Section A, Vol. 274, Issues 1–2, 1989

- Allman, B.E., et al., ”Focusing Neutrons with a "Lobster-Eye" Optic” Proc. SPIE, Vol. 3449, 1998

- Ambily, S., et al., “Near UV Imager with an MCP Based Photon Counting Detector” Proc. SPIE, Space Telescopes and Instrumentation, Vol. 9905, 2016

- Ambrosi, R.M., “A model for the physics of image formation in Fast Neutron Radiography” Ph.D. Thesis, 2000

- Angel, J.R.P., “Lobster eyes as X-rays telescopes” The Astrophysical Journal, Vol. 233, 1979

- AST Private Email Communication Applied Scintilation Technologies

- Barrett, H., et al., “Radiological Imaging” Academic Press, 1981

- Bendat, J.S., et al., “Random Data: Analysis and Measurement Procedures” John Wiley & Sons, 1986

- Bigas, M., et al., “Review of CMOS imagers” Microelectronics Journal, Vol. 37, Issue 5, 2006

- Boyle, W., et al., “Charge coupled devices” Bell Syst. Tech. J., Vol. 49, 1970

- Bredthauer, R., K. Boggs, G. Bredthauer, “STA CCD Detector, Controller and System - Developments” Scientific Detector Workshop, Astrophysics and Space Science Library, 2013

- Brigati, S., et al., ”SDtoolbox” University of Pavia, 2009

- Brown, R.G., et al., “Introduction to Random Signals and Applied Kalman Filtering” Wiley, 2012

- Brunton, A.N., et al., “Metrology and modeling of microchannel plate x-ray optics” Applied Optics, Vol. 36, No. 22, 1997

- Bugby, S., et al., "A comparison of CsI:Tl and GOS in a scintillator-CCD detector for nuclear medicine imaging" J. Instrumentation, Vol. 11, 2016

- Burns, P.D., "Slanted-Edge MTF for Digital Camera and Scanner Analysis" Proc. IS&T PICS Conference, 2000
- Cancelo, G., et al., ”Deep sub electron noise readout in CCD systems using digital filtering techniques” Experimental Astronomy, Vol. 34, No. 1, 2012
- Chapman, H.N., et al., “X-Ray Focusing Using Square Channel-Capillary Arrays” Review of Scientific Instruments, Vol. 62, 1991
- Chen, C.T., "Introduction to Linear System Theory". New York: Holt, Rinehart and Winston, Inc., 1970
- Clapp, M.J., “Development of a test system for the characterization of DCDS CCD readout techniques ” Proc. SPIE, High Energy, Optical, and Infrared Detectors for Astronomy V, Vol. 8453, 2012
- CubeSense, “CubeSense_Specsheet”, CubeSpace, 2016
- Cunningham, I.A., "Applied Linear-Systems Theory", Handbook of Medical Imaging, Vol. 1, SPIE Press, Bellingham WA, 2000
- Davis, J.A., et al., ”A Kalman Filter Clock Algorithm for Use in the Presence of Flicker Frequency Modulation Noise” 35th Annual Precise Time and Time Interval (PTTI) Meeting, 2005
- Desert, S., “Focusing neutrons with a combination of parabolic and elliptical supermirrors” J. Appl. Cryst., Vol. 46, 2013
- Elphic, A., et al., “Determination of lunar global rare earth element abundances using Lunar Prospector neutron spectrometer observations” J. Geophys. Res, Vol. 105, 2000
- Endicott, J., et al., “Charge-Coupled Devices for the ESA PLATO M-class Mission” Proc. SPIE, High Energy, Optical, and Infrared Detectors for Astronomy V, Vol. 8453, 2012.
- Fornasari, P., Malcovati “SDtoolbox” University of Pavia, 2009
- Franco, S., “Design with Operational Amplifiers”, 1990
- Fraser, G.W., et al., ”The mercury imaging X-ray spectrometer (MIXS) on Bepicolombo” Planetary and Space Science, Vol. 58, Issue 1-2, 2010
- Fraser, G.W., et al., "The direct detection of thermal-neutrons by imaging microchannel-plate detectors" Nuclear Instruments and Methods in Physics Research Section A, Vol. 293, Issue 3, 1990

- Fraser, G.W., et al., “Thermal neutron imaging using microchannel plates” Proc. SPIE, Neutrons, X Rays, and Gamma Rays: Imaging Detectors, Material Characterization Techniques, and Applications, Vol. 1737, 1993
- Fraser, G.W., “Microchannel plate X-ray optics”, The Next Generation of X-ray Observatories, XRA97/02 Leicester X-ray Astronomy Group Special Report, Vol. 191, 1997
- Gach, J.L., et al., “A New Digital CCD Readout Technique for Ultra-Low-Noise CCDs” Publications of the Astronomical Society of the Pacific, Vol. 115, 2003
- Gatti, E., V. Svelto, C. Cottini "A new method of analog to digital conversion" Nuclear Instruments and Methods, Vol. 24, 1963.
- Ginzburg, A., ”Image information transfer properties of X-ray intensifying screens in the energy range from 17 to 320 keV” Med. Phys., Vol. 20, No. 4, 1993
- Goldsten, J.O., ”The MESSENGER Gamma-Ray and Neutron Spectrometer” Space Sci. Rev., Vol. 131, Issue 1, 2007
- Graeve, T., et al., “High-resolution CMOS imaging detector” Proc. SPIE, Medical Imaging 2001, Physics of Medical Imaging, Vol. 4320, 2001
- Gray Meyer, ”Analysis and Design of Analog Integrated Circuits” 4th ed. John Wiley & Sons, 2001
- Hansford, G., “Astrosat Calibration Report” University of Leicester, 2012
- Hartmann, R., et al., “The radiation entrance window of pn junction detectors” Metrologia, Vol. 32, Issue 6, 1996
- Heinzel, G., et al., “Spectrum and spectral density estimation by the Discrete Fourier transform (DFT), including a comprehensive list of window functions and some new flat-top windows” Max-Planck-Institut fur Gravitationsphysik, 2002
- Hejazi, S., et al., “System considerations in CCD-based x-ray imaging for digital chest radiography and digital mammography” Med. Phys., Vol. 24, No. 2, 1997
- Holst, G.C., "CCD Arrays, Cameras, and Displays" SPIE Press, 1998
- Hopkinson, G.R., D.H. Lumb, “Noise reduction techniques for CCD image sensors” Journal of Physics E: Scientific Instruments, Vol. 15, No. 11, 1982
- Hughes, D.J., “Neutron Optics” New York: Interscience Publishers, 1954

- Hynecek, J., “Impactron—A New Solid State Image Intensifier” IEEE Transactions on Electron Devices, Vol. 48, 2001
- Ice, G.E., “Kirkpatrick–Baez microfocusing optics for thermal neutrons” Nuclear Instruments and Methods in Physics Research Section A, Vol. 539, issue 1-2, 2005
- In Soo, A., “State Modeling of Clocks Noises and its Application” PhD Thesis, Iowa State University, 1986
- Janesick, J., “Photo Transfer”, SPIE Press, 2007
- Janesick, J., ”Scientific Charge-Coupled Devices” SPIE Press, 2001
- Jerram, P., et al., “The LLLCCD: Low Light Imaging without the need for an intensifier. “ Proc. SPIE, The International Society for Optical Engineering, Vol. 4306, 2001
- Jerram, P., et al., “Recent Sensor Designs for Earth Observation” Proc. SPIE, Earth Observing Missions and Sensors: Development, Implementation, and Characterization IV, Vol. 9881, 2016
- Kapany, N.S., "Fiber optics, Principles and Applications” Academic Press, New York, 1967
- Khaykovich, B., et al., “From x-ray telescopes to neutron scattering: Using axisymmetric mirrors to focus a neutron beam.” Nuclear Instruments and Methods in Physics Research Section A, Vol. 631, Issue 1, 2011
- Konnik, M., et al., “High-level numerical simulations of noise in CCD and CMOS photosensors: review and tutorial” http://arxiv.org/abs/1412.4031v1, 2014
- Kozyrev, A.S, et al., “Studying Mercury surface Composition by Mercury Gamma-Rays and Neutrons” Conference: 40th Lunar and Planetary Science Conference, Vol. 40, 2009
- Kuhls-Gilcrist, A., et al., "The Solid-State X-Ray Image Intensifier (SSXII): An EMCCD-Based X-Ray Detector” Proc. SPIE, Int. Soc. Opt. Eng., Vol. 6913, 2008
- Lawrence, D.J., et al., “Performance of Orbital Neutron Instruments for Spatially Resolved Hydrogen Measurements of Airless Planetary Bodies” Astrobiology, Vol. 10, Issue 2, 2010
- Lees, J.E., et al., “A high resolution Small Field Of View (SFOV) gamma camera: a columnar scintillator coated CCD imager for medical applications” J. Instrumentation, Vol. 6, 2011

- Litichevskyi, V., “Composite Scintillation of Panels and Elements based on fine-grained granules of crushed crystals” Functional Materials, Vol. 20, No. 4, 2013
- Litichevskyi, V., et al., “Scintillation panels based on zinc selenide and oxide scintillators” Functional Materials, Vol. 18, No. 3, 2011
- Martindale, A., private email, University of Leicester, 2015
- Maurice, S., et al., “Reduction of neutron data from Lunar Prospector” J. Geophys. Res., Vol. 109, Issue E7, 2004
- Miller, K., et al., “Advanced charge injection devices for space instruments” Proc. SPIE, Focal Plane Arrays for Space Telescopes, Vol. 5167, 2004
- Mitrofanov, I.G., ”Lunar Exploration Neutron Detector for the NASA Lunar Reconnaissance Orbiter” Space Sci. Rev., Vol. 150, Issue 1-4, 2010
- Motchenbacher, C.D., J.A. Conelly, “Low Noise Electronic System Design” New York, NY, USA: Wiley, 1993
- MT-050 “Op Amp Noise” Analog Devices Tutorial, 2008
- Nagano, M., et al., “One-dimensional neutron focusing with large beam divergence by 400mm-long elliptical supermirror” Journal of Physics: Conference Series, Vol. 340, 2012
- Opolonin, O., et al., “Increasing informativity of digital radiographic systems” Functional Materials, Vol. 20, Issue 4, 2013
- Oppenheim, A.V., et al., "Discrete-Time Signal Processing". Upper Saddle River, NJ, Prentice Hall, 1999
- Peele, A.G., et al., “X-ray focusing with lobster-eye optics: a comparison of theory with experiment” Applied Optics Vol. 35, Issue 22, 1996
- Pimbley, J.M., et al., “The output power spectrum produced by correlated double sampling” IEEE Trans. Circuit Syst., Vol. 38, No. 9, 1991
- Prettyman, T.H., et al., ”Composition and structure of the martian surface at high southern latitudes from neutron spectroscopy” J. Geophys. Res., Vol. 109, Issue E5, 2004
- Price, G.J., et al., ”Hard X-ray imaging with microchannel plate optics”, Nuclear Instruments and Methods in Physics Research Section A, Vol. 490, Issue 1-2, 2002
- ProEM-HS, Princeton Instruments, “Princeton-Instruments-ProEM-HS-512BX3” datasheet Rev P4, July 2016

- Rawley, C., “On-orbit performance of the Gaia CCDs at L2” Astronomy & Astrophysics, Vol. 595, 2016
- Robbins, M.S., et al., "The Noise Performance of Electron Multiplying Charge-Coupled Devices", IEEE Transactions On Electron Devices, Vol. 50, Issue 5, 2003
- Rudolph, M., “http://it.mathworks.com/matlabcentral/newsreader/view_thread/336939”, 2014
- Ryzhikov, V., et al., “New semiconductor scintillators ZnSe(Te,O) and integrated radiation detectors based thereon” IEEE Transactions on Nuclear Science, Vol. 48, Issue 3, 2001
- Samei, E., et al., "Measuring the presampled MTF of digital radiographic systems" Med. Phys., Vol. 25, No.1, 1998
- Schreier, R., G. Temes, “Understanding Delta-Sigma Converters” IEEE Press, 2005
- Serrano-Finetti, E., et al., “Noise Reduction in AC-Coupled Amplifiers” IEEE Transaction on Instrumentation and Measurement, Vol. 63, No. 7, 2014
- SLOA054D, Texas Instruments “Fully-Differential Amplifiers” Application Report – January, 2002
- SLVA043B, Texas Instruments “Noise Analysis in Operational Amplifier Circuits” Application Report, 2007
- Smith, R., et al., “Digital Correlated Double Sampling for ZTF” Proc. Scientific Detector Workshop 2013, California Institute of Technology, Astrophysics and Space Science Library, 2013
- Stefanov, K.D., et al., “Optimal digital correlated double sampling for CCD signals” Electronics Letters, Vol. 50, Issue 14, 2014
- Stern, R.A., et al., “EUV and Soft X-Ray Quantum Efficiency Measurements of a Thinned Back-Illuminated CMOS Active Pixel Sensor” IEEE Electron Device Letters, Vol. 32, Issue 3, 2011
- Struers “http://www.struers.com/en/Products/Grinding-and-Polishing/Grinding-and-polishing-equipment”, 2017
- Swindell, W., “The lens coupling efficiency in megavoltage imaging" Med. Phys., Vol. 18, No. 6, 1991

- Szafraniec, M., et al., “On-ground characterization of the Euclid low noise CCD273 sensor for precise galaxy shape measurements” J. Instrumentation, Vol. 10, 2014
- Takayanagi, I., et al., “A Four-Transistor Capacitive Feedback Reset Active Pixel and its Reset Noise Reduction Capability” IEEE Workshop on CCDs, 2008
- Terry, S.C., et al., “Time-Domain Noise Analysis of Linear Time-Invariant and Linear Time-Variant Systems Using MATLAB and HSPICE” Nuclear Science Symposium Conference Record, 2004
- Trauger, J.T., “Sensors for the Hubble Space Telescope wide field and planetary cameras (1 and 2)” Proc. of the Conference CCDs in astronomy, Tucson, AZ, 1989
- Tsoulfanidis, N., “Measurement and Detection of radiation”, CRC Press Book, 1990
- Turner, M.J.L., ”The European Photon Imaging Camera on XMM-Newton: The MOS cameras” Astronomy & Astrophysics, Vol. 365, 2001
- Tyrrell, G.C., ”Phosphors and scintillators in radiation imaging detectors” Nuclear Instruments and Methods in Physics Research Section A, Vol. 546, Issue 1-2, 2005
- Usdin, N.J., “Discrete Simulation of Colored Noise and Stochastic Processes and l/f Power Law Noise Generation” Proc. IEEE, Vol. 83, No. 5, May, 1995
- van Eijk, C.W.E., “Inorganic thermal-neutron scintillators” Nuclear Instruments and Methods in Physics Research Section A, Vol. 529, Issue 1-3, 2004
- Vargas, M., et al., “The Seemingly Paradoxical Noise Behavior of Some Active Circuits” IEEE Transactions on Instrumentation and Measurements, Vol. 43, No.5, 1994
- White, M., et al., “Characterization of surface channel CCD image arrays at low light levels” IEEE Journal of Solid-State Circuits, Vol. 9, Issue 1, 1974.
- Willingale, R., et al., “Hard X-ray Imaging with Micro-channel Plate Optics” Experimental Astronomy, Vol. 8, Issue 4, 1998
- Windt, D.L., “IMD-software for modelling the optical properties of multilayer films” Computers in Physics, Vol. 12, No. 4, 1998
- Wiza, J.L., “Micro Channel Plate Detectors” Nuclear Instruments and Methods, Vol. 162, 1979
- Yadid-Pecht, O., et al., "CMOS Imagers: From Phototransduction to Image Processing" Springer, 2004

- Yibin, B., et al., “Teledyne Imaging Sensors: Silicon CMOS imaging technologies for X-ray, UV, visible and near infrared” Proc. SPIE, High Energy, Optical, and Infrared Detectors for Astronomy III, Vol. 7021, 2008
- Yu, T., "Lens coupling efficiency: Derivation and application under differing geometrical assumptions” Med. Phys., Vol. 24, No. 4, 1997